PHOTODEGRADATION OF POLYSTYRENE BY NANO TITANIUM DIOXIDE AND PHOTOSENSITIZERS

Thesis submitted to the University of Calicut
in partial fulfillment of the requirements
for the award of the Degree of
Doctor of Philosophy in Chemistry

By

DINOOP LAL S

Under the guidance of

Dr. Sunil Jose T

Assistant Professor, Research & Postgraduate Department of
Chemistry, St. Thomas' College (Autonomous), Thrissur

Co-Guide

Dr. Rajesh C

Assistant Professor, Department of Chemistry,
MES Keveeyam College, Valanchery

University of Calicut, Kerala, India

December 2020

Date: 26/06/2021

CERTIFICATE

We hereby certify that, this is the revised version of the thesis entitled *"Photodegradation of Polystyrene by Nano Titanium dioxide and Photosensitizers"* submitted by **Mr. Dinoop lal S,** under our guidance after incorporating the necessary corrections/suggestions made by the adjudicators. The content of the CD is the same as in the hard copy.

Dr. Sunil Jose T

(Research Guide)

Dr. SUNIL JOSE T., M.Sc., M.Tech, Ph.D.
Assistant Professor
Research & PG Department of Chemistry
St. Thomas' College (Autonomous)
Thrissur - 680 001

PHOTODEGRADATION OF POLYSTYRENE BY NANO TITANIUM DIOXIDE AND PHOTOSENSITIZERS

Thesis submitted to the University of Calicut
in partial fulfillment of the requirements
for the award of the Degree of
Doctor of Philosophy in Chemistry

By

DINOOP LAL S

Under the guidance of

Dr. Sunil Jose T

Assistant Professor, Research & Postgraduate Department of
Chemistry, St. Thomas' College (Autonomous), Thrissur

Co-Guide

Dr. Rajesh C

Assistant Professor, Department of Chemistry,
MES Keveeyam College, Valanchery

University of Calicut, Kerala, India

December 2020

Date: 07/12/2020

CERTIFICATE

This is to certify that the thesis entitled *"Photodegradation of Polystyrene by Nano Titanium dioxide and Photosensitizers"* is an authentic record of original research carried out by **Mr. Dinoop lal S** under our supervision in partial fulfillment of the requirements for the award of the degree of Doctor of Philosophy in Chemistry of University of Calicut and further that no part thereof has been presented before for any other degree.

Dr. Rajesh C

(Research Co-Guide)

Dr. Sunil Jose T

(Research Guide)

DECLARATION

I hereby declare that the thesis entitled **"Photodegradation of Polystyrene by Nano Titanium dioxide and Photosensitzers"**, submitted to the University of Calicut in partial fulfillment of the requirement for the award of the Degree of Doctor of Philosophy in Chemistry is a bonafied research work done by me under the supervisions of **Dr. Sunil Jose T**, Assistant Professor, Research and Post graduate Department of Chemistry, St.Thomas' College (Autonomous), Thrissur and **Dr. Rajesh C**, Assistant Professor, Department of Chemistry, MES Keveeyam College, Valanchery.

I also declare that the material presented in this thesis is original and does not form the basis for the award of any other degree, diploma or other similar titles of any other university.

Date: 07.12.2020

DINOOP LAL S

Acknowledgement

Dedicated to

Our Environment

Celebrating the 100th anniversary of polymer science, let the humanity be more concerned about the potential threats posed by the plastic debris to our environment along with the innovative techniques for the development of future polymer technology.

Let us sacrifice our today so that our children can have a better tomorrow

- A.P.J. Abdul Kalam

Preface

The increasing demand of plastic commodities resulted in their mass production worldwide. The accumulation of the used and thrown away plastics over land and water bodies has contributed to plastic pollution. The past few decades witnessed a steep increase in the total quantity of plastic debris that has affected the eco system badly. Photo degradation is considered as an ecofriendly and cheap method that could be employed for the demolition of such plastic debris. The disadvantage of photo degradation is that, it is a slow process. Application of suitable methods to accelerate the photodegradation process is our research problem. Photodegradation can be enhanced in the presence of photocatalysts. The entire thesis reports the studies conducted in order to accelerate the rate of photodegradation of polystyrene (PS) using different photocatalysts, under controlled ultraviolet (UV) radiation. The mechanical, electrical and thermal properties of the PS-photocatalyst composites are also studied. Nano TiO_2 has been chosen as the core photocatalyst for the degradation of PS considering its efficiency, non-toxicity, photostability, low cost and ease for synthesis. The full-fledged photocatalytic efficiency could not be exhibited by this semiconductor metal oxide due to its faster charge recombination. Modification of TiO_2 using suitable photosensitizers can alter its surface chemistry, resulting in better charge separation, thereby improving its photocatalytic efficiency. In addition to Nano TiO_2, we have also studied the photocatalytic efficiency of ZnO and modified ZnO for the degradation of PS under UV radiation.

The thesis as a whole is divided into eight chapters. A general introduction along with the literature review of PS chemistry, TiO_2, surface modified TiO_2 and ZnO are discussed in chapter 1.

The preparation of PS and PS-photocatalyst composite specimens for their photodegradation studies is explained in chapter 2. PS and PS composite sheets prepared by solvent casting methods were subjected to controlled UV irradiation using a UV tube of power 30 W, emitting UV radiation of wavelength 253 nm. All the specimens were irradiated for a total time period of 1000 hours and monitored at regular intervals of 200 hours, using various analysis techniques. The monitoring techniques included gel permeation chromatography, FTIR and UV spectroscopies, SEM, weight loss measurements etc. Specimens were also moulded for the

determination of electrical and mechanical studies as per ISO standards and these specimens were also subjected to UV irradiation. Electrical properties studied include the break down voltage (BDV) and dielectric constant. The mechanical properties included measurement of tensile and flexural strength. Thermo gravimetric analysis (TGA) of the specimens was also conducted. All these studies were conducted for the non-irradiated as well as UV irradiated PS-composite specimens.

The synthesis and characterization of TiO_2 and ZnO photocatalysts are described in chapter 3. Nano TiO_2 has been synthesized by sonication assisted sol-gel technique. ZnO has been synthesized by three different methods- sonication assisted precipitation, hydrothermal method with uncontrolled hydrolysis and hydrothermal method with controlled hydrolysis. ZnO nanospheres obtained via hydrothermal method with controlled hydrolysis were used as photocatalyst. A comparison of photodegradation of PS in the absence and presence of TiO_2 and ZnO photocatalysts were studied under UV radiation. A possible mechanism was proposed for the UV initiated photodegradation of PS in the presence and absence of TiO_2 and ZnO.

Chapter 4 describes the study of photodegradation of PS in the presence of TiO_2 and ZnO modified by graphene oxide (GO) photocatalyst. The synthesis and characterisation of GO by modified Hummer's method and the preparation of GO-modified TiO_2 and ZnO by sonication assisted hydrothermal method are discussed. Different sets of TiO_2-GO and ZnO-GO composites were prepared with varying percentages of GO. The interaction of GO with TiO_2 or ZnO is investigated. All these photocatalysts were loaded into the PS matrix whose photodegradation was studied.

Chapter 5 deals with the study of photodegradation of PS using polyaniline (PANI) modified TiO_2 and ZnO as photocatalysts. Polyaniline has been synthesised by chemical oxidative polymerization. TiO_2-PANI as well as ZnO-PANI composites were also developed by chemical oxidative polymerization method where insitu polymerization of aniline was done over the surface of dispersed TiO_2 or ZnO particles. The mole percentage of aniline was varied in order to obtain TiO_2-PANI/ ZnO-PANI composites of different composition. The interaction between TiO_2/ZnO with PANI is also investigated.

The role of a few benzophenone derivatives and tryphenylmethane dyes as photosensitizers for the degradation of PS is discussed in chapter 6. The benzophenone derivatives chosen as photosensitizers were 4-methoxybenzophenone 2-hydroxy-4-methoxybenzophenone, 2-chlorobenzophenone, 4-nitrobenzophenone and benzophenone itself. The dye photosensitizers included malachite green and methyl blue. Photodegradation of PS was studied by loading these photosensitizers directly or in coupled state with nano TiO_2. The mechanism of photodegradation of PS in the presence of these photocatalysts is discussed.

Photodegradation of PS catalysed by metal doped TiO_2 is discussed in chapter 7. TiO_2 was doped with Cu, Fe and Ag separately. The mole percentage of the dopant metal used was varied in order to obtain TiO_2-metal photocatalysts of varying composition. The phase change occurred in TiO_2 a result of increasing metal percentages is discussed. The mechanism of improved photocatalytic efficiency of metal doped TiO_2, for the photodegradation of PS is also discussed.

The entire work is summarised in chapter 8. The possible application of PS-composites that depends on the type of photocatalysts loaded is discussed. The significance of the work along with its environmental friendliness and future scope is also discussed.

Abbreviations

PS	Polystyrene
UV	Ultraviolet
GPC	Gel permeation chromatography
UV-DRS	UV-visible diffused reflectance spectroscopy
BDV	Breakdown voltage
PANI	Polyaniline
GO	Graphene oxide
BP	Benzophenone
2HO4MOBP	2-hydroxy-4-methoxybenzophenone
4MOBP	4-methoxybenzophenone
2ClBP	2-chlorobenzophenone
4NBP	4-nitrobenzophenone
MG	Malachite green
MB	Methyl blue

Table of Contents

Chapter 6: UV degradation of Polystyrene using Organic Photosensitisers coupled and uncoupled with Nano TiO₂

List of Tables

Table no:	Table heading	Page No
Chapter 1: Introduction and Review of Literature		
1.1	*Expected properties of TiO₂ related to its structural dimensionality......*	21
Chapter 3: Photodegradation of Polystyrene using Nano TiO₂ and Nano ZnO Catalysts under UV irradiation - a Comparison		
3.1	*Interplanar distance d corresponding to each 2θ angles of TiO₂ and ZnO…………………………………………………………………*	65
3.2	*Optical bandgap energies (Egs) of nano TiO₂ and nano ZnO…………….*	70
3.3	*Important observations made from FTIR spectra of PS and PS-TiO₂ composites………………………………………………………….....*	76
3.4	*Observations and conclusions made from GPC, FTIR spectroscopy, UV-DRS spectroscopy, electrical studies, weight loss measurements and SEM…………………………………………………………….*	87
Chapter 4: Accelerated photodegradation of Polystyrene Using nano TiO₂ and ZnO surface modified with Polyaniline		
4.1.1	*Mole percentages and weights of the components in TiO₂-PANI composites………………………………………………………….....*	98
4.1.2	*Mole percentages and weights of the components in ZnO-PANI composites………………………………………………………….....*	98
4.2.1	*Tabulated values of crystallite sizes of TiO₂-PANI and ZnO-PANI composites………………………………………………………….....*	102
4.2.2	*Interplanar distance d corresponding to each 2θ angles of TiO₂-PANI composites in comparison to pristine TiO₂…………………………….....*	102
4.2.3	*Interplanar distance d corresponding to each 2θ angles of ZnO-PANI composites in comparison to pristine ZnO…………………………….....*	103
4.2.4	*Values of optical bandgap energies of TiO₂-PANI composites………….*	111
4.2.5	*Values of optical bandgap energies of ZnO- PANI composites………….*	112
Chapter 5: Accelerated photodegradation of Polystyrene Using TiO₂ and ZnO surface modified with Graphene oxide		
5.1.1	*Inter planar distances (d) corresponding to 2θ peaks of TiO₂ and TiO₂-GO composites………………………………………………………….*	141
5.1.2	*Inter planar distances (d) corresponding to 2θ peaks of ZnO and TiO₂-GO composites………………………………………………………….*	142
5.1.3	*Crystallite size of TiO₂-GO and ZnO-GO composites calculated using*	

Chapter 6: UV degradation of Polystyrene using Organic Photosensitisers coupled and uncoupled with Nano TiO$_2$

Chapter 7: Enhanced photocatalytic activity of metal doped TiO$_2$ in the UV light initiated photodegradation of Polystyrene

Chapter 1

Introduction and Review of Literature

1.1 A glimpse into the polymer history

Human beings have been enjoying the benefits of polymer materials since 1600 BC when Mesoamericans processed natural rubber for their specific uses. They moulded several materials ranging from bands to sculptures using natural rubber[1]. Human beings have been experimenting on various natural resources for developing rubbers, resins and waxes for their uses. 19th century witnessed some advances in the polymer chemistry with the invention of vulcanized rubber in 1839 AD by Charles Goodyear by heating natural rubber with sulphur at 132°C[2]. Polystyrene was discovered by Eduard Simon in the same year. In 1907, a Belgian-American chemist named Leo Baekeland condensed phenol with formaldehyde and developed phenol formaldehyde resin most commonly called bakelite. It is hard and used as insulators in electrical appliances even today especially in switch boards. The new era of polymer technology began in 1922 when an Austrian-American Chemist Herman Francis Mark proved that polymers are made up of macromolecules instead of aggregations of small molecules. This was very much in support to the ideas of the German Chemist Hermann Staudinger. Staudinger published a paper in 1920 titled as "Über Polymerisation" based on the modern polymer theories[3]. During the 19th century many classes of polymers were synthesized and developed which found applications in various sectors replacing wood, metals, stones, bones, glasses etc. Polymers including polystyrene (PS), polycarbonates (PC), polyvinyl chloride (PVC), polypropylene (PP), polyphenylene oxide (PO), polyesters (PES), acrylonitrile-butadiene-styrene copolymer (ABS), polyurethane (PU) etc., were commercialized during the 19th and 20th centuries[4]. Polymers were classified as natural, synthetic and semi-synthetic based upon their origin. Development of new types of polymers further widened their classification based on their structures (linear, branched and cross-linked), mode of polymerization (addition and condensation polymers), molecular forces as (elastomers, thermosetting plastics, thermoplastics and fibers) and so on. Polymers with the property of plasticity were in good demand. Such polymers began

to be known as "plastics" in general. Plasticizers were developed which enhanced the properties of some rigid plastics. The so called plastics exhibited superior properties compared to other materials where ever it was applied.

The past few decades witnessed a steep rise in the amount of plastics consumed by the humanity. The global plastic production which was estimated to be around 2 metric tons in 1950 increased to 7300 metric tons in 2015. 92% of the plastics ever made include PE, PP, PVC, PS, PET, PU etc. These plastics are very much in demand for construction works, packing and so on[5]. The demand of polymer plastics are still increasing in such a way that we are unable to think of a world without them.

1.2 Polystyrene (PS)
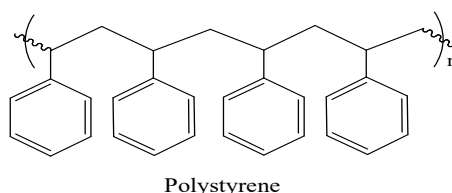
Polystyrene

Polystyrene (PS) could be considered one of the most widely used polymer material meeting the needs of human society in the form of various commodities[6,7]. Styrene monomer units polymerise to form a colourless thermoplastic resin - PS whose tacticity depends upon the mechanism adopted or catalyst used in the polymerisation process. The wide use of PS in industries, constructions, packing, automobiles and common house hold goods began when PS was commercialised in 1930s after its accidental discovery by Eduard Simon (German apothecary) in 1839. In order for PS to be useful commercially, its weight average molecular weight ($\overline{M}_w$) should be ten times its chain entanglement molecular weight ($\overline{M}_e$). Like most other polymers, the mechanical properties (tensile, flexural, impact etc.) of PS depends very much on $\overline{M}_w$. PS having $\overline{M}_w$ lesser than $\overline{M}_e$ has not much industrial significance as it remains just in white powdery form that cannot be moulded into desired commodities or useful parts owing to its week mechanical properties. The $\overline{M}_e$ of PS is ~18100 and hence PS with $\overline{M}_w$ lesser than this value is not used [8,9].

1.2.1. Tacticity in PS and its significance

The orientation of phenyl rings in PS chain determines its tacticity. If the phenyl rings are arranged in the same side of the chain we have *isotactic* PS (Figure 1.1).

Alternate arrangement of phenyl groups result in *syndiotactic* PS. Random arrangement of phenyl groups give *atactic* PS.

Atactic   Isotactic   Syndiotactic
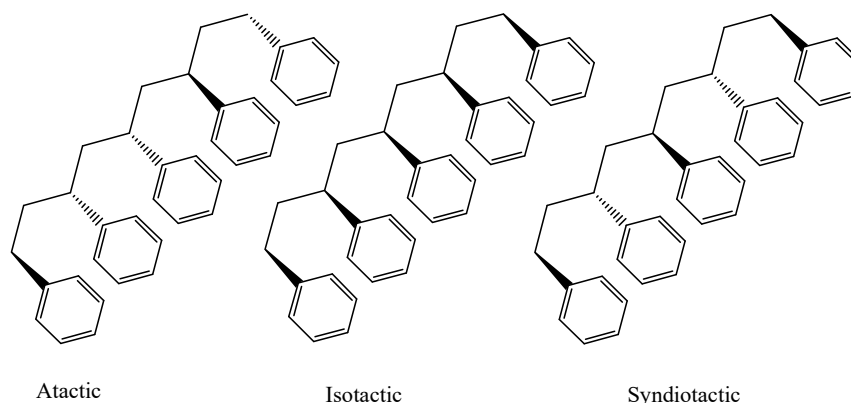
Figure 1.1. *Illustration of tacticity in PS*

The commercially produced *general purpose polystyrenes (GPPS)* are atactic. They are amorphous in nature and hard. Free-radical polymerisation results in atactic PS. The glass transition temperature (T_g) of atactic PS is around 100°C. Isotatic PS is not produced commercially. They are more crystalline compared to atactic PS. They are prepared by coordination polymerisation (Ziegler-Natta type) using stereospecific catalysts such as $TiCl_3$ activated by triethylaluminium. They melt at a temperature around 240°C[10]. Even though the catalyst used for the preparation of isotactic PS was reported in 1986[11], they are not produced due to their commercial insignificance. The reason for this is their slow crystallisation and difficulty in preparation (compared to atactic PS and syndiotactic PS). Syndiotactic PS is also crystalline with Tg around 270°C[10]. The method of preparation of sydiotactic PS also involves polymerisation using Ziegler-Natta type catalysts. Soluble complexes of titanium combined with alkyl aluminium (say (η^5-C_5H_5)$TiCl_3$ with methylaluminoxane ($Al(CH_3)_xO_y)_n$) gives syndiotactic PS. Crystallisation of syndiotactic PS is relatively fast. This type of PS is also not produced commercially (however some industries produce syndiotactic PS for special purposes).

Soon after the discovery of isotactic PS by Natta (1955), studies regarding the stereospecific process of PS preparation was put into practice[12]. Several authors have reported articles related to the determination of tacticity of PS through various techniques. NMR spectroscopy was an important tool used to determine the tacticity of PS during those days. The NMR proton chemical shifts could be accessed in order

to determine the tacticity of the PS chain. Even though separate peaks corresponding to α-proton of isotactic PS have been identified, attempts to resolve this peak from that of other protons of the polymer remained almost impossible. In 1962, Brownstein et al. resolved the α-proton of PS by deuteriating the β- protons and hence nullifying the spin-spin coupling of the chain by which isotactic, syndiotactic as well as heterotactic PS could be distinguished[13]. In order to minimise the solvent effect Brownstein and co-workers used benzene as solvent. Benzene solvent unlike other solvents maximised the chemical shift of α-protons. Separate peaks corresponding to α-protons of isotactic, syndiotactic and heterotactic PS were identified. Bovey et al. (1965) reported that the ^{1}H NMR signal of methylene proton of atactic PS appeared as a broad resonance[14]. Heatly and Bovey (1968) showed that the ^{1}H NMR signal of methylene proton of isotactic PS appeared as distinguishable non equivalent peaks[15]. Matsuzaki et al. (1974) reported that signals of methyl protons showed a chemical shift in the order isotactic>atactic>syndiotactic PS towards higher magnetic field in their ^{1}H NMR spectra [16]. In 1986, Ishihara and co-workers studied the stereoregularity in syndiotactic PS through XRD, ^{1}H NMR, ^{13}C NMR and IR spectroscopy[11]. The ^{1}H NMR and ^{13}C NMR spectra made it easy to distinguish between the PS of different tacticity just by observing the chemical shifts and splitting patterns of the peaks. IR spectra of syndiotactic PS as reported by Ishihara et al showed the absence of helical conformation of PS chain, as reported earlier in the case of isotactic PS by Tadokoro et al. (1961)[17]. Even though several authors have studied the NMR spectra of PS [18–21] the assignment of methylene carbon of PS backbone faced a big divergence in opinion until in 1996 Cheng and Lee deconvoluted the broad overlapped resonance of methylene carbon assisted by computer analysis[22]. With the development of various analytical tools the characterisation of tacticity of PS became much easier. Lots of articles were published on this topic recently and many works are in progress.

Tacticity of PS has a lot to tell about the physical and chemical properties of PS. Researchers worldwide have studied the dependence of tacticity of PS in its chemical and physical properties. Several authors including Tan et al. (1983)[23], Clark et al (1983)[24], Gan et al. (1985) [25] and Gan et al. (1986)[26] studied the gelation property of atactic PS. Even though polymers that have appreciable crystallinity or stereo regular sequence are the only ones that are supposed to exhibit gelation, the contrary has taken place in the case of amorphous PS (by showing gelation property). The problem

was solved in 1987 by Jeanne François and co-workers who studied the phenomenon of gelation of atactic as well as isotactic PS in CS$_2$ and reported that gelation observed in the solution of amorphous atactic PS was due to the presence of certain amount of syndiotactic sequence in it[27]. David et al. (1973) reported that the fluorescence yield increased with crystallinity of PS at room temperature. The excimer fluorescence followed the order isotactic crystallised>isotactic amorphous>atactic oriented>atactic amorphous[28]. Chen et al. (2003) compared the thermal stability of atactic, syndiotactic and isotactic PS and concluded that isotactic PS exhibited far better thermal stability compared to the other two. Higher activation energy required to degrade isotactic PS, supported by restricted molecular mobility explained this observation[29]. The viscoelastic property of isotactic PS was found to be lower than that of atactic and syndiotactic PS by one order of magnitude. This was due to the difference in entanglement molecular weight ($\overline{M}_e$) at a fixed weight average molecular weight ($\overline{M}_w$) as reported by Huange et al. (2011)[30]. Grigoriadi et al. (2019) studied the ageing kinetics of PS using flash-differential scanning calorimetry. He reported that the ageing kinetics followed the order isotactic PS>atactic PS>syndiotactic PS[31].

1.2.2. Polymerisation techniques for PS production

PS is prepared through addition polymerisation. The different kinds of addition polymerisation techniques that could be employed are (i) anionic (ii) cationic (iii) free-radical and (iv) coordination (Ziegler-Natta) polymerisation[9,32].

(i) **Anionic polymerisation**: Sequential steps of initiation, propagation and termination take place. The polymer formed have polydispersity index (PDI) less than 1.1 [PDI= weight average molecular weight ($\overline{M}_w$)/number average molecular weight ($\overline{M}_n$)]. One of the advantages of this method is that the structure of end-groups could be controlled by controlling the chain termination step. The disadvantage is that the polymerisation feed needs purification which determines the purity of the polymer product.

(ii) **Cationic polymerisation**: This process is generally not employed due to the difficulty in the production of high molecular weight PS. The cation intermediate (polystyrylcarbocation) is not much stable and results in fast termination of the

polymerisation process leading to low molecular weight PS. In addition to this the polymerisation feed needs purification.

(iii) **Free-radical polymerisation**: The process takes place through simultaneous initiation, propagation and termination steps. The polymer formed will have a PDI greater than 2. Variety of end products is formed in this process due to multiple termination steps. These facts confirm that free-radical polymerisation is not as organised as anionic polymerisation. The advantage of free-radical polymerisation is that the polymerisation feed requires no purification.

(iv) **Coordination polymerisation (Ziegler-Natta polymerisation):** This type of polymerisation is generally employed where polymer of high crystallinity is in demand. Catalysts are introduced in this process. The polymerisation takes place on the surface of the catalysts used. The resulting polymer product formed will have higher melting temperatures compared to their amorphous counter parts. Ziegler-Natta polymerisation is not employed in the production of cheap PS for daily usages. The polymer formed through this method will have a PDI $\approx$2.

Out of the above mentioned methods, the most widely used one by the industries for the production of commercial polystyrene is free-radical polymerisation. The process needs less effort as the monomer need not be cleaned during the process as mentioned above. Since the initiator residues left behind has less impact on the properties of PS formed, they (initiator) need not be removed[33]. The mechanism of free-radical polymerisation of PS formation was studied by Florey (1937)[34]. According to Florey, PS is formed when molecules of styrene are involved in a bond forming reaction through 1, 4-diradical formation as illustrated in Figure 1.2.1. Later in 1968, Mayo proposed another mechanism in which he describes the formation of a dimer through the Diels-Alder reaction involving two styrene monomers followed by the reaction between dimer and styrene to form PS (Figure 1.2.2)[35]. Later in 1988, Mulzer and co-workers proposed a mechanism where the diradical suggested by Florey could lead to the dimer suggested by Mayo (Figure 1.2.3)[36].
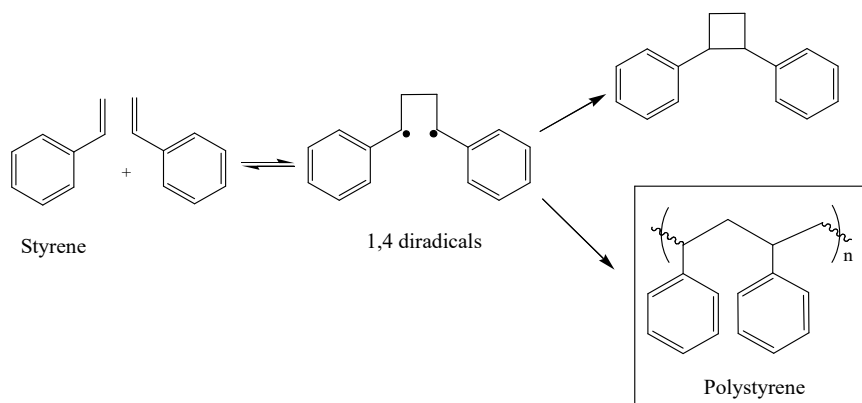
Figure 1.2.1. *Mechanism of PS polymerisation via free-radical polymerisation as proposed by P.J. Florey (1937).*
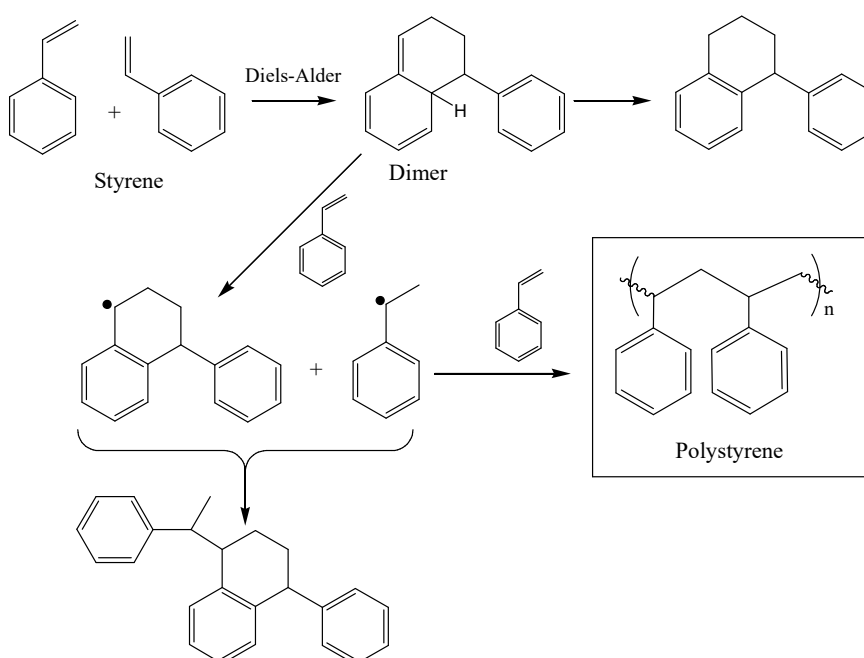
Figure 1.2.2. *Mechanism of PS polymerisation via free-radical polymerisation as proposed by F.R. Mayo (1968).*
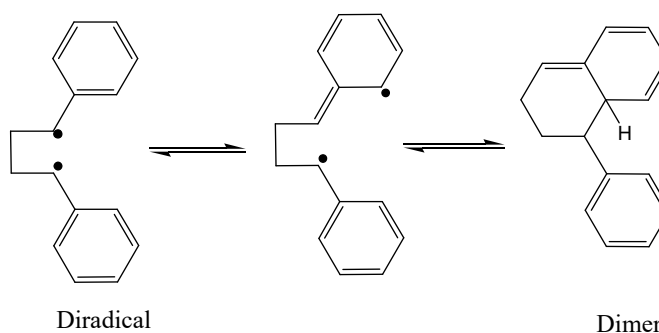
Figure 1.2.3. *Formation of dimer (F.R. Mayo) from diradical (P.J.Florey) as explained by J.Mulzer (1988)*

1.2.3. Classification of PS

Based on the production and processing techniques applied, different forms of PS could be obtained. These forms of PS differ from each other in physical, mechanical and electrical properties and hence in their applications too. General purpose polystyrene (GPPS), PS forms, expanded polystyrene (EPS), extruded polystyrene (XPS) and oriented polystyrene (OPS) cover these classifications.

- **General purpose polystyrene (GPPS):** These types of PS with $\overline{M}_w$ ranging between 2,00,000 to 3,00,000 are produced by free-radical polymerisation as discussed above. GPPS are hard and colourless. They have low specific gravity and are cheap. As the name implies, GPPS is the most common PS that we meet in our daily life for common usage. They are the type of PS hence produced by industries in large scale. They can be moulded into thin flexible films. They are electrical insulators and serve the purpose of insulation in electric devices too. GPPS is amorphous and has a glass transition temperature (T_g) around 100°C. GPPS could be moulded into various commodities of the users' choice, easily through injection moulding at a temperature below 200°C. GPPS has several disadvantages such as low heat resistant, low impact resistant and are soluble in some of the organic solvents. It should also be noted that the commercially available PS are not pure. They may contain oligomers of styrene and traces of initiators[33].

- **PS foams:** PS foams are made by the assembly of particles of PS containing air voids (volume fraction of air ≈8% and PS ≈2%). Suspension radical polymerisation is used to prepare PS beads, using blowing agents. The beads are subjected to steam and moulded to desired products. They serve the application of light weight water proof packing materials, insulators, surfboards etc. Insulating concrete form (ICF) that we see commonly is made up of PS forms. Structures like ornamental pillars that should be light weight are also made up of PS forms.

- **Expanded polystyrene (EPS):** are developed from pre-expanded beads of PS. They are very low dense white material, commonly termed as "Styrofoam". They are brittle and soft and are generally used as cushions to protect delicate appliances. The high thermal insulation property of EPS also makes them available for the use of packing frozen food items. They also serve as disposable plates and cups. Injection moulding is employed to manufacture the products of EPS.

- **Extruded polystyrene (XPS):** As the name implies, XPS are processed by extrusion method. Unlike EPS, XPS are closely packed and denser. They have a rough surface with reduced thermal conductivity. XPS finds their application in model making (especially architecture models).

- **Oriented polystyrene (OPS):** OPS are specially developed for packing purposes. XPS discussed above is opaque. On stretching XPS the haziness is reduced and transparency is increased. This is OPS. The advantage of OPS as packing material is that they are relatively cheap, at the same time stiff.

1.2.4. PS blends or copolymers

In order to enhance the properties of PS for specific applications, the PS is blended with some other polymers or molecules. Blending soft rubber with PS for example results in acrylonitrile-butadiene-styrene copolymer (ABS) and high impact polystyrene (HIPS) which shows superior impact resistance. ABS also shows enhanced chemical resistance. Styrene-acrylonitrile (SAN) obtained on copolymerization of styrene and acrylonitrile is resistant to chemicals and heat and also shows better mechanical properties.

1.3 Plastic Debris and environmental issues

1.3.1 Causes and consequences of plastic pollution

Increased consumption of plastic commodities including PS worldwide has led to a steep rise in the amount of plastic debris. The uncontrollable spread of plastic wastes which has adverse effects on the environment has become one of the primary concerns of most of the countries[37–39]. Plastics have touched almost all the sectors of human need replacing natural resources due to its magnificent properties. The use and throw system practiced by the humanity causes a huge deposit of hazardous PS debris have adverse effects on the bio system. Plastics like PS as we know are resistant to environmental weathering over a long period of time[40]. It takes a period of few decades for low density polymer materials like bags, wrappers etc., to degrade completely. Degradation of plastic bottles takes around half a millennium. Plastic products of higher size and density cost nearly a millennium to vanish completely from earth. This is of course too long for the bio systems of the environment. In

addition to this, studies are being conducted in order to increase the stability of polymers from environmental weathering[41–45]. Such polymers with incorporated stabilizers, further increases the life span of polymer debris. Some of the plastic debris ends up in land fillings. Lack of enough land for waste plastic deposition leads most of the debris exposed to the eco system and hence causing pollution.

Plastic which end up in the oceans are broken down and spread over a large area[46–49]. These debris are serious threat to the marine eco system and may even result in deaths of several marine life forms[50–53]. In addition to this various plasticizers added into the polymer matrix also contribute to the marine pollution[54–56]. Plastic debris spread over soil affects the soil fertility which has serious adverse effects on the bio system depended on soil[57–59]. Plastic debris are often unknowingly taken by animals and birds as food and are ingested causing various disorders or ultimate death[60,61]. The food safety of human being too is affected due to soil pollution caused by the plastic debris[62]. Plastic debris like PS forms or extruded PS are easily carried away by the wind to far-away places and spread the plastic pollution over a wider range.

1.3.2 Remedial measures against plastic pollution

Measures to treat pollution due to plastic debris are actively being thought of and implemented throughout the world. An effective method for plastic waste treatment is yet to be developed. Plastics cannot be banned all of a sudden as they have turned out to be a part of human life. The only way left is to find out a proper route to assemble the plastic debris and demolish them or recycle them at a very low cost.

In most cases, the primary idea for the demolition of plastic debris that originates in our mind is to burn plastics. Burning plastics is of course not a wise idea as the outcome of burning is toxic gases that can be lethal to the creatures including human beings who inhale them[63]. Burning plastics therefore results in air pollution. Controlled burning of plastics is done in municipalities or industries using incinerators. Incineration also produces acidic gases and other gases that lead to secondary air pollution causing various health issues. In addition to this, auxiliary fuels should be used for maintaining proper temperature that consumes energy[64,65].

Another method for the treatment of plastic wastes is recycling[66]. Even though this method sounds good theoretically, its scope is limited practically. The process called recycling is in fact a combination of several steps starting with the separation of plastic debris from other waste and sorting them (segregation). The next step is compaction which involves reduction in the volume of the plastics (up to 98% of the total volume). Shredding follows compaction where plastic pieces are changed into small flakes. Finally the flakes are pelletized using an extruder, melted and cooled. The resultant recycled plastics are used for manufacturing various commonly used commodities. The major disadvantage of recycling is its limited application and cost. Expanded polystyrene (EPS) for example occupies larger volume compared to its mass. This makes the transport of bulk EPS debris costly. The recycling process compresses EPS into smaller volumes. The recycled compressed EPS finally obtained does not worth much compared to the cost of recycling and transporting EPS. Another disadvantage of recycled PS is that it cannot be used for food storing/ packing for the sake of hygiene.

Biodegradation could not be thought of for polymers like PS, PVC, PE, PES, PP etc., as the enzymes of microbes are unable to digest these polymers. Polymers like PS could be degraded thermally[67].Thermal degradation of polymers is also not safe due to the formation of toxic gases and energy consumption. Chemical degradation[68] that is done in the presence of reagents could not be applied for large PS debris. The use of chemicals is not ecofriendly in some cases and is costly too. Radiolytic degradation is another effective process for the degradation of PS[69]. In this technique, the polymers are exposed to high energy gamma radiation. This technique too requires large amount of energy and are costly too. Photodegradation could be considered for the demolition of polymers as the process is cheap and ecofriendly. Methods to accelerate the process of photodegradation by loading it with suitable photocatalysts are being discussed in this thesis.

1.4 Photodegradation

Photodegradation refers to the decomposition of a material in the presence of electromagnetic radiations. Most of the polymers including PS undergo photodegradation in the presence of sunlight (mostly in the UV region)[70]. The main advantage of photodegradation over other methods of polymer remediation is that, it

is ecofriendly, cheap, produces no toxic gases and no artificial external energy is required (the process takes place in renewable natural sunlight). In simple words, we can call photodegradation, a "green" process. The disadvantage of photodegradation is that it takes long time for completion. Photodegradation depend upon the nature of polymers. High molecular weight polymers require a longer time to degrade completely and the samples should be exposed to more intense electromagnetic radiations.

1.4.1   Photodegradation of PS

PS undergoes photodegradation in the presence of UV radiation of the solar spectra. Photodegradation of PS is through photo-oxidation pathway in the presence of air. Slight yellowing is noticed as a result of photodegradation of PS due to the formation of conjugated double bonds that absorbs in the visible region. The mechanical properties of PS are deteriorated as a result of photodegradation. The flexibility of chain also decreases rendering it as a brittle useless material which is easily decomposed after photodegradation. Photodegradation of PS depends upon the mobility of ions through the matrix, impurities present within the polymer and interaction with atmospheric oxygen, water etc.

The phenyl rings which absorb UV radiations are excited to singlet followed by triplet states producing radicals initiating the degradation process. The degradation however depends upon the mobility of the radicals through the PS matrix. It should be noted that the mobility of radicals through solid phase via diffusion is hindered due to steric effect. Hydrogen radicals can find an easy way through the polymer matrix and interact with other molecules creating macromolecular radicals or combine with other hydrogen molecules or radicals. Bulky macromolecular radicals including the phenyl radicals cannot diffuse easily. These bulky molecular radicals however can abstract hydrogen radicals from their vicinity or can cleave the associated or neighbouring bonds leading to the relay of radical propagation until it is quenched[71]. The interaction of macromolecular radicals formed over the PS chain with the atmospheric gases or water molecules play a vital role in photo-oxidative degradation. Secondary radicals formed on interaction of macromolecular PS radicals with atmospheric oxygen or water molecules are responsible for oxidation over the PS chain. Formation of carbon-

carbon double bonds or conjugated double bonds due to cleavage of adjacent carbon-hydrogen bonds also results in oxidation.

The study of photodegradation of PS dated back in the 20th century. Matheson and Boyler in 1952 reported the yellow colouration on PS surface when exposed to light[72]. The yellow colouration of light exposed PS was due to the oxidation of PS leading to the affixation of some chromophoric groups according to the report. The formation of carbonyl groups on the PS chain upon light exposure was also reported. According to Matheson and Boyler, the yellow colouration of light exposed PS specimens could be washed off easily but they were not soluble in the solvents where PS was normally soluble. This could be due to the cross linking of PS polymer chains. In 1965 Grassie and Weir corrected the belief that the reason for yellowing of PS upon exposure to light was due to oxidation leading to the formation of colour absorbing groups[73]. According to the study, the formation of conjugated double bonds when PS was exposed to light radiation was responsible for the yellow colouration. Grassie and weir explained the theory of conjugated carbon-carbon double bond formation as illustrated below (Figure 1.3). UV radiation absorbed by the PS leads to the cleavage of α-C-H bond (marked as C_1) through homolytic fission. The hydrogen atom cleaved from C_1 now abstracts another hydrogen atom associated with the adjacent carbon atom (C_2) of the same chain. This ultimately leads to the formation of carbon-carbon double bond (>C=C<). The >C=C< formed between C_1 and C_2 renders the α-hydrogen (tertiary H atom) present on C_3 more labile. This triggers the homolytic cleavage of C-H bond (of C_2) followed by hydrogen abstraction from C_4 leading to the formation of >C=C< (between C_3 and C_4). Conjugated double bonds are thus formed. Three such conjugation results in the absorption of visible light (yellow region).
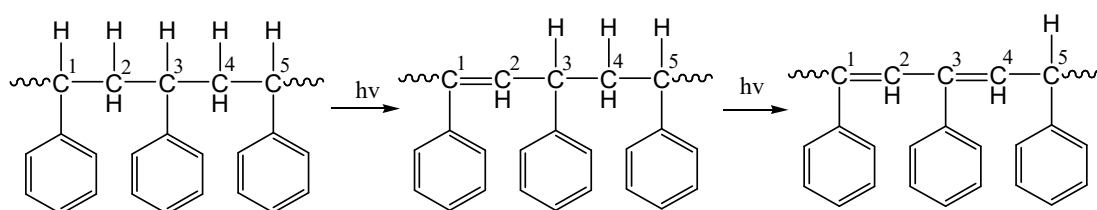
Figure 1.3. *Mechanism of conjugated double bond formation in PS chain under UV irradiation proposed by Grassie and Weir (1965)*

The intensity of the yellow colour is increased as a result of prolonged exposure to light radiations. However red shift to higher wavelength was not observed. This was explained by Grassie and weir by the limitation of extended conjugation due to the lack of coplanarity of PS matrix which restricts the mobility of molecules. George (1974) investigated the photodegradation of PS and reported that the presence of aromatic carbonyl groups as impurities in the PS matrix enhances the oxidation process[74]. Chain scission was observed in PS through Norrish type II reaction under UV exposure. Singlet oxygen was formed when UV radiation interacted with the impurities or air which further attacks the PS chain leading to the introduction of hydroperoxy group in the chain. The increase in the intensity of >C=O absorption bands in the IR spectra of PS upon UV irradiation was observed. The effect of temperature on photodegradation was studied by Torikai et al. (1986)[75]. The degradation of PS was studied under a mercury lamp at temperatures 30°C, 100°C and 120°C which were below, equal to and above the glass transition temperature (T_g) of PS respectively. Photo-oxidation increased as the temperature increased. The concentration of polystyryl radicals formed initially decreased as the temperature increased. The conclusion was that, at higher temperatures, cross linking between the adjacent chains of PS matrix resulted by the combination of polystyryl radicals assisted by the segmental motion of the chains.

Photodegradation as explained is a slow process. Photodegradation could be implemented as a common system of plastic waste treatment only if the entire process proceeds in a stipulated amount of time. Introducing photocatalysts/ photosensitizers that could efficiently accelerate photodegradation has been thought of and investigated by many researchers worldwide.

Acceleration in polymer degradation could be achieved by the use of metal oxides[76–79], modified metal oxides[80], organic photosensitisers[81–84] etc. loaded into the polymer matrix. Of late the enhancement of photodegradation of polymers coupled systems like metal doped metal oxides[85], organo-inorganic systems[80] etc. is also being studied. Photodegradation studies have also been done by modifying the chain of a particular polymer by copolymerizing it with another polymer [86]. It has been observed that inorganic metal oxide semiconductors like TiO_2, ZnO etc showed superior photocatalytic activity. Our study presented in this thesis includes the

photodegradation of PS in the presence of nano TiO_2 as well as TiO_2-photosensitizer couples under UV radiation. TiO_2 have been chosen as core catalyst in this work, considering its superior photocatalytic activity, photostability, non toxicity, ease of preparation and better thermal stability. ZnO and photosensitizer-coupled ZnO have also been used in our study. Importance has been given to TiO_2 however considering superior photocatalytic activity and photostability of TiO_2 compared to ZnO.

1.5 Titanium dioxide (TiO_2)

TiO_2- an oxide of the transition metal titanium, has been commercialized in 1920s since its discovery by William Gregor in 1791 in black magnetic sand followed by its isolation from the mineral rutile by Klaproth in 1795. The first products developed out of TiO_2 were pigments[87]. The application of TiO_2 has extended from the level of pigments to that of a catalyst within a short span of time[88,89]. One notable work includes the study of Fujishima and Honda (1971) who used TiO_2 as an anode in the electrochemical photolysis of water[90]. The use of TiO_2 has increased commercially as well as in catalysis in the following years.

1.5.1 Polymorphs of TiO_2

TiO_2 exists in three different morphologies namely anatase, rutile and brookite. These three polymorphs differ by the sequence in which the TiO_6 octahedral units are arranged (Figure 1.4). Anatase and rutile phases are used in photocatalysis[91]. Anatase phase shows superior photocatalytic activity compared to rutile phase TiO_2[92].
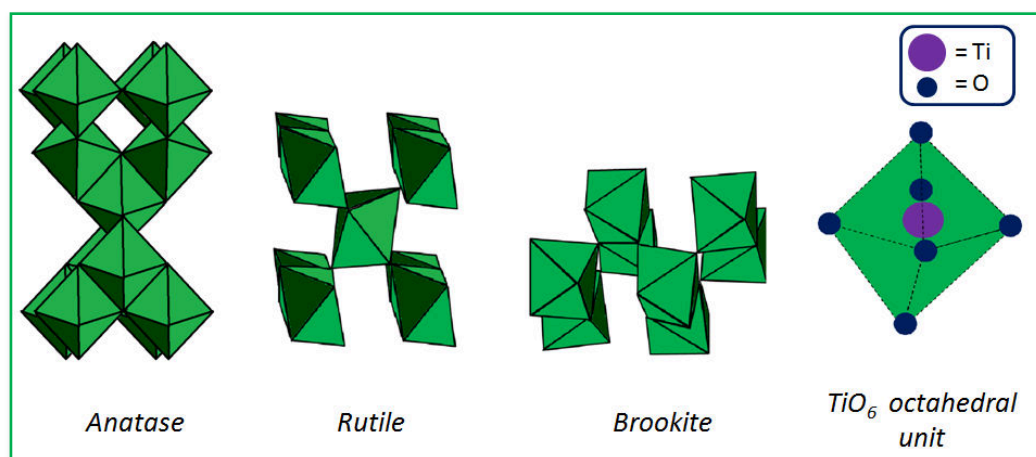
Figure 1.4. *Arrangement of TiO_2 octahedral units in anatase, rutile and brookite*
polymorphs of TiO_2

TiO$_2$ also have several metastable forms such as hollandite oxide (TiO$_2$(H))[93], TiO$_2$ (B)[94] and ramsdellite type (TiO$_2$(R))[95] structures. TiO$_2$ also exists in high pressure forms namely cubic[96], orthorhombic columbite (TiO$_2$ II)[97] type, intermediate orthorhombic (TiO$_2$ OI)[98], orthorhombic cotunnite (TiO$_2$ OII)[99] type, and monoclinic baddeleyite (MI) type[100] structures. TiO$_2$ OII with cotunnite PbCl$_2$ like structure holds the credit of being the hardest oxide known. When octahedral TiO$_6$ (O$_h$ symmetry) units combine in different ways to form different oxides of titanium, a distortion in its regular octahedral structure occurs. This leads to a change in O$_h$ symmetry of the TiO$_6$ units. As a consequence of the distortion in the regular O$_h$ symmetry of TiO$_6$ units, further splitting in the t$_2$g and e$_g$ bands are observed in the electronic spectra as sub-bands[101]. The perfect O$_h$ symmetry of TiO$_6$ (as observed in cubic structure) undergoes tetragonal distortion into D$_{2d}$ symmetry in anatase and D$_{2h}$ symmetry in rutile structures. Similar distortions are observed in other structures (say Ti$_2$O$_3$ → trigonal distortion; Ti$_4$O$_7$ & Ti$_5$O$_9$→ orthorhombic distortion and so on). The splitting patterns of octahedral, tetragonal, trigonal and orthorhombic symmetries are as represented below (Figure 1.5)[102].
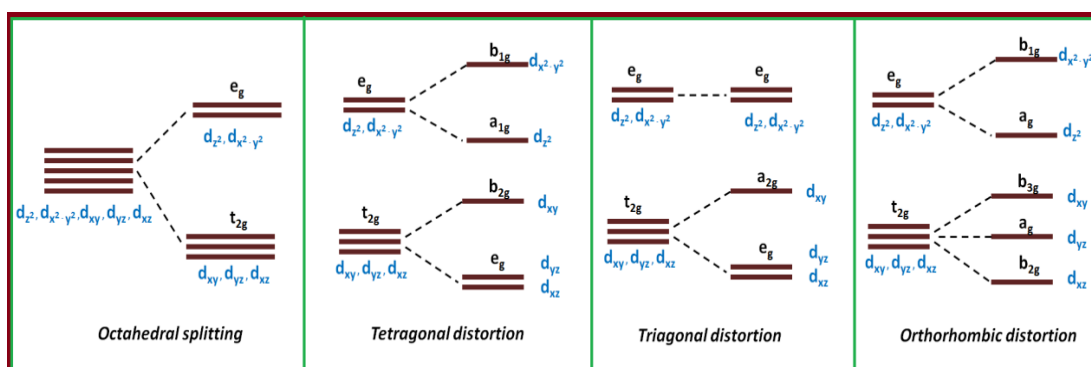
Figure 1.5. *Bands and sub-bands in the electronic structure due to octahedral splitting, tetragonal, trigonal and orthorhombic distortions*

1.5.2   General methods for TiO$_2$ synthesis

TiO$_2$ was reported to be synthesised using several methods. Some methods employed for the synthesis of TiO$_2$ are discussed below.

➤ **Sol-gel method**

In sol-gel method, the precursor used for the preparation of a particular compound is hydrolysed in solution to form sols. These sols are then transformed into gel on

polymerisation. The gel so formed is transformed into products on heat treatment. TiO_2 have been synthesised through sol-gel technique from Ti(IV) alkoxides in acidic pH[103–105]. The amount of water used in the process controls the hydrolysis rate and thereby the structure of TiO_2 formed. When the water content is less in the reaction mixture (titanium alkoxide is in excess) the rate of hydrolysis will be lower facilitating the growth of Ti-O-Ti chains. The growth of Ti-O-Ti would be in such a way that close packed three dimensional structures are formed. In the reaction mixture where the amount of water is comparatively higher, the rate of hydrolysis would also be higher favouring the development of $Ti(OH)_4$ which ultimately results in particles which are loosely packed (first order particles). This is due to the fact that three dimensional structures of Ti-O-Ti are not developed appreciably in the intermediate step. When the water content in the reaction mixture is in excess the growth of three dimensional Ti-O-Ti chains in the gel are favoured resulting in first ordered particles that are closely packed[106–108].

Sugimoto et al. have conducted several studies regarding the synthesis of TiO_2 through sol-gel route. The precursor used was titanium(IV) isopropoxide (TTIP) mixed with triethanolamine (TEOA) in the ratio 1:2. Amines were used as surfactants that controlled the shape of the particles. pH of the system was tuned and it was found that the shape of nano TiO_2 at acidic pH was cuboidal and at basic pH (above 11) it was ellipsoidal. When TEOA was replaced with diethylenetriamine, ellipsoidal shape was obtained at a pH just above 9[109–111]. Sodium oleate and Sodium stearate used in the reaction mixture could tune the shape of the TiO_2 particles from distorted cubes to perfect cubes having sharp edges[110]. The studies of Uekawa et al. (2002)[112] and Le et al (2004)[113] showed that the agglomeration of TiO_2 particles could be prevented during the crystallisation process by heating the gel to a temperature below 100° C for a prolonged time. Zhang and Banfiled obtained anatase nano TiO_2 with size below 50 nm by heating amorphous TiO_2 aerobically in the series of their work done on TiO_2 synthesis through sol-gel route[114–117]. In order to obtain TiO_2 particles of high crystallinity, Kim et al.[118,119] modified the sol-gel method as continuous reaction as well as two stages mixing methods. Znaidi et al. (2001) on the other hand adopted semicontinuous method for the same purpose[118]. Synthesis of TiO_2 nano tubes were also reported by several authors using sol-gel route[120–122].

➢ **Hydrothermal method**

The advantage of hydrothermal method is that the temperature of the aqueous reaction mixture can be elevated much above 100° C (>boiling point of water) at an elevated pressure. The morphology and size of the product formed can be controlled by adjusting the parameters such as reaction temperature and the quantity of solvent used. The process is done using steel hydrothermal autoclaves (which may or may not be teflon lined). Many authors have reported the synthesis of nano TiO_2 particles using hydrothermal technique[123–125]. Yang et al. (2001) for example reported the synthesis of nano TiO_2 by subjecting the peptized precursor of TiO_2 to hydrothermal process[126]. Chae et al. (2003) reported the synthesis of TiO_2 by the hydrothermal treatment of titanium alkoxide in ethanol water mixture adjusting to acidic pH[125]. Hydrothermal method have also been adopted for the synthesis of nano rods[127–129], nano wires and nano tubes[130,131]. Zhang et al. (2002) reported the conversion of TiO_2 particles into TiO_2 nano wires by treating it with NaOH hydrothermally at a temperature range 150-200°C[132]. Wei et al. (2004) synthesised TiO_2 nano wires from layered titanate[133]. Kasuga et al. were the first to introduce the synthesis of TiO_2 nano tubes through hydrothermal process in (1998)[134]. Nano tubes were also developed from the hydrothermal process of TiO_2 powder in the presence of NaOH. An interesting mechanism was suggested by Kasuga et al. in 1999 for the formation of TiO_2 rods[135]. NaOH treatment leads to the cleavage of Ti-O-Ti bonds of TiO_2 leading to the formation of Ti-O-Na as well as Ti-O-H bonds. Reaction of these newly formed bonds with water and HCl results in the formation of sheets of Ti-O-H linkage which on dehydration converts into Ti-O-H-O-Ti sheets. These sheets finally folds to form TiO_2 tubes.

➢ **Solvothermal method**

The difference between hydrothermal and solvothermal processes lies in the solvent used during the course of reaction. When aqueous medium used in hydrothermal process is replaced by organic solvents, the process is called solvothermal process. The advantage of solvothermal process over hydrothermal process is that the temperature of the system could be elevated much higher than that of hydrothermal process depending upon the solvents chosen. As a result of this the

particles produced via solvothermal approach could be better controlled in their size, shape and distribution compared to the product of hydrothermal synthesis.

Several authors have reported the synthesis of nano TiO_2 (particles, rods etc) using solvothermal methods[136,137]. Kim et al. (2003) used toluene as the solvent for the preparation of TiO_2 from TTIP precursor at a temperature of 250°C by solvothermal method[138]. Li et al. (2006) prepared TiO_2 nano particles and rods from titanium tetraisobutoxide precursor using linoleic acid as solvent[139]. TiO_2 nano rods were synthesised from TTIP precursor in toluene solvent and surfactants at 250° C by Kim et al. (2003)[140]. TiO_2 nano wires have also been prepared using solvothermal method[136,141]. The TiO_2 rods and NaOH were autoclaved in ethanol-water mixture at temperature between 170 and 200°C (Wen et al. 2005)[141].

➢ **Chemical vapour deposition (CVD) method**

Materials are converted into vapour state followed by condensation to obtain the required product in CVD approach. CVD is a versatile method adopted for the preparation of coated materials over a substrate. Surface coating of substrates with other materials are employed in varied applications to tune their electrical, corrosion resistant, optical, thermal etc. properties. Other than for coating purpose, CVD method is employed for the preparation of nano particles, fibers, films etc.

TiO_2 has been prepared using CVD in oxygen-helium atmosphere from TTIP precursor (Seifried et al; 2000)[142]. Sung et al (2018) used CVD for TiO_2 ultrathin coating on boron particles from TTIP[143]. Alotaibi et al. (2018) synthesised TiO_2 brookite thin films and found that its photocatalytic activity was superior compared to anatase TiO_2 particles[144]. Nagasawa et al. (2018) prepared TiO_2-coated polymethylmethacrylate polymer which exhibited excellent UV shielding effect[145].

➢ **Sonochemical method**

Sonochemistry utilizes the acoustic cavitation originating from the interference of ultrasound with reaction media. High pressures and localized heat results as a consequence of the bubbles formed during cavitation. This in turn drives a chemical reaction through improved interaction between the molecules. Nano TiO_2 has been synthesised using sonochemical method[146,147]. Huang et al. (2000) synthesised

anatase, rutile and mixed phase nano TiO_2 using different precursors at varying temperature by sonochemical method[146]. TiO_2 nanotubes were prepared through sonochemical method by Zhu et al. (2001) by sonicating TiO_2 in the presence of $NaOH$[147]. Yu et al. (2001) sonicated TTIP in ethanol water mixture and reported the formation of TiO_2 with a mixture of anatase and brookite phases that exhibited photocatalytic activity[148].

1.5.3 TiO_2 as a photocatalyst

TiO_2 is a well celebrated photocatalyst used in various applications related to energy conversions, water purification, air purification, defogging, hydrogen generation, self-cleaning, sterilization etc. What makes TiO_2 such a satisfying photocatalyst is its superior efficiency, non-toxicity, photostability, ease for synthesis and low cost compared to other metal oxides[149–151].

TiO_2 is a semiconductor metal oxide having a band gap energy (E_g) above 3.0 eV (band gap varies in different polymorphs of TiO_2 and also depends upon the particle size). Such a large value of E_g restricts its absorbance to the UV region of spectra. UV irradiation of TiO_2 results in the formation of electron-hole pairs (if $h\upsilon \geq E_g$). The photogenerated electrons in the valence band (VB) are transferred into the conduction band (CB) through the band gap leaving behind positive charged holes in the VB. The photocatalytic activity of TiO_2 depends upon the fate of these photogenerated electrons and holes. The electron in the VB interacts with the adsorbed oxygen leading to the formation of reactive superoxide ($O_2^{\bullet-}$). The holes left behind in the CB on the other hand react with adsorbed water or hydroxyl ion (OH^-) to form reactive hydroxyl radical $OH\bullet$[152–154]. The $O_2^{\bullet-}$ and $OH\bullet$ further interacts with the reactant molecules including polymers, pollutants etc. if present in their vicinity to initiate various reactions[155]. If polymers like PS, are attacked by these reactive radical species, oxidation of the polymer chain takes place. In such cases $>C=O$, -OH and -OOH groups are introduced in the polymer chain termed as photo-oxidation[156]. It should also be noted that all these possible reactions occur if the photo generated electrons and holes either have appreciable life time or they are transferred into another system associated with TiO_2. If the photo generated charges recombine before having a chance for the interaction with other molecules, the photocatalytic activity is

quenched. The entire mechanism of photocatalysis of TiO_2 is pictorially depicted in Figure 1.6.
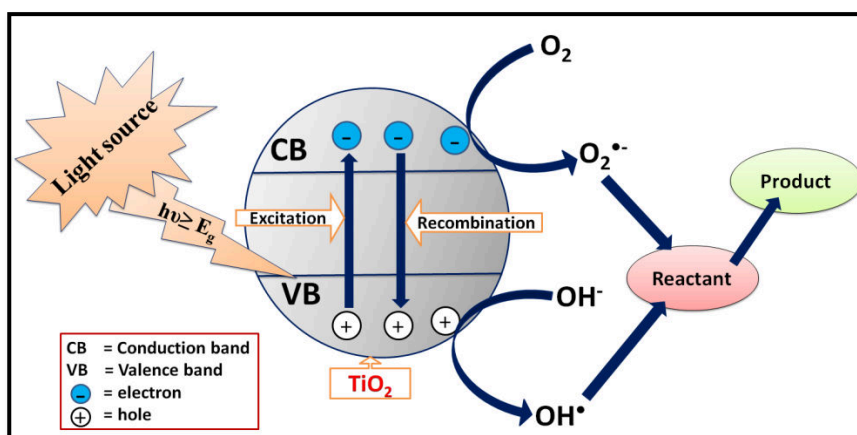
Figure 1.6. *Mechanism of photocatalysis of TiO_2*

The holes left behind in the VB may not combine with water directly in all the cases. They may get trapped in the oxygen sites within TiO_2 and may weaken the Ti-O bond existing in the lattice. The adsorbed water molecules now get a chance to react with these loosely bounded Ti-O bonds leading to the formation of -OH groups on the surface of TiO_2 through coordination. These less stable bonds make the TiO_2 surface superhydrophilic[157].

Table 1.1. *Expected properties of TiO_2 related to its structural dimensionality*

Structures	Names	Dimensions	Properties
	spheres	0D	• High surface area
	Rods		• Delayed charge recombination.
	Tubes	1D	• Light scattering.
	Wires		• Fabricated into nonwoven mat
	Sheets	2D	• High adhesion. • Smooth surface.
	Interconnected structures	3D	• Better mobility of charge carriers.

The structure of TiO_2 assembly exhibits variant properties suitable for different choice of photocatalytic application. Zero-dimensional (0D) TiO_2 nano spheres, for

example, due to its high surface area could be used in photocatalytic decomposition/ photodegradation of pollutants[158]. One-dimensional (1D) TiO_2 rods, tubes and fibers show better light scattering[159] and delayed electron-hole recombination[160] properties. The enhanced diffusion of charge carriers in these 1D structures is the reason for this delayed recombination of charges[160]. They also could be fabricated into mats which are self stabilised[161]. Two-dimensional (2D) TiO_2 sheets have the characteristic property of high adhesion with smooth surface[162]. Three-dimensional (3D) structures of TiO_2 bears interconnected architecture that enables easy mobility of charge carriers. 3D TiO_2 monoliths find their application in environmental purification[157].

TiO_2 is being widely used as photocatalyst in water treatment for the degradation of various contaminants. Organic dyes exposed to water could be successively removed using TiO_2 photocatalyst in the presence of UV light. These dyes include Procion yellow H-ELX[163], Methylene blue[164], Amaranth[165], acridine orange[166] etc whose removal efficiency depended upon pH. An enhancement in the dye removal using TiO_2 was achieved by the addition of H_2O_2 for dyes like Rodhamin 6G[167], direct dye 40 [168], etc. Tang et al. reported that the increase in azo linkage decreased the rate of dye degradation in the presence of TiO_2 catalyst and UV radiation. The rate of degradation of the azo dyes followed the order Direct blue 87 > Basic Yellow 15 > Acid Blue 40[169]. The degradation of Reactive Black 5 under UV irradiation and TiO_2 increased in the presence of dissolved oxygen and NaCl, and was independent of pH[170]. An inhibition in the degradation of Reactive Red 198 dye was reported in the presence of ethanol[171]. Photodegradation of some phenolic compounds including phenol [172–174], 2-chlorophenol[175], 2,4-dinitrophenol[176], bisphenol A[177,178] in the presence of TiO_2 and application of TiO_2 based on its superhydrophilicity[179–181] and wettability[182,183] has also been reported.

TiO_2 has also been used as catalyst in polymer degradation with appreciable results. Cho and Choi (2001)[184] studied the photodegradation of PVC in the presence of TiO_2 under UV radiation of wavelength (λ) 300 nm and ambient supply of air. PVC-TiO_2 composite underwent better photodegradation compared to pure PVC. Mass loss, decrease in average molecular weights, increase in the formation of carbonyl groups and evolution of CO_2 and water vapour upon UV irradiation was monitored. Photodegradation of polyethylene (PE) loaded with TiO_2 under solar light

and artificial UV radiation in ambient air supply was investigated by Zhao et al. (2007)[185]. The photodegradation of PE increased as the percentage of TiO_2 loading increased with the evolution of CO_2 and water. The degradation initiated in the PE-TiO_2 interface was extended over the PS matrix. The reactive oxygen produced on TiO_2 photocatalyst diffused through the PE matrix causing the oxidative- degradation of rest of the PE chain. Thomas et al. (2013)[186] reported that the size of TiO_2 photocatalyst used, affected the rate of photodegradation of low density polyethylene under UV radiation. TiO_2 with smaller particle size exhibited better photocatalytic activity compared to the larger sized TiO_2. The photodegradation of polycarbonate (PC) in the presence of TiO_2 as reported by Hwang et al. (2014)[76] resulted in various side products including aliphatic and aromatic ketones. The weight loss observed in the PC-TiO_2 composite was double as observed in pristine PC under UV irradiation. Shang et al. (2003) studied the photodegradation of PS-TiO_2 composites under UV radiation and observed better photo-oxidation, weight loss, decrease in molecular weight etc. for the composites compared to pristine PS[187]. Diffusion of reactive oxygen- by the interaction of photogenerated electrons in TiO_2, through the PS matrix extended the range of degradation along the PS chain. In 2011, Jaleh et al. investigated the photodegradation of spin coated PS-TiO_2 composite films and reported that the hydrophilicity and contact angles were affected by photodegradation process[188].

1.6 Modified TiO_2 for enhanced photocatalysis

TiO_2 is a versatile photocatalyst used in many areas including environmental and energy related applications. The full-fledged photocatalytic activity of TiO_2 however cannot be utilised due to its rapid charge recombination. The meagre response of TiO_2 towards visible spectra too limits its application. It should be noted that TiO_2 is photo catalytically active only in the UV region of the spectra that comprises only about 3 to 5% of the total radiation reaching the earth. In addition to this, the photocatalytic efficiency of TiO_2 also depends on the separation of photo carriers and their transportation to the reactant associated with TiO_2. Weaker separation efficiency also restricts its photocatalytical activity[189]. In order to overcome these limitations of TiO_2, modifications are done. Modification refers to the processes like doping, sensitizing, composite fabrication etc. Modification of TiO_2 reduces the possibility of charge

recombination and/or narrows the band gap energy. When charge recombination is delayed, better photocatalytic activity is exhibited by TiO_2 and modifying TiO_2 with suitable materials extends its activity to the visible region of the spectra[190].

1.6.1 Metal doping

Some of the methods adopted for the preparation of metal doped TiO_2 include hydrothermal[191,192], sol-gel[193,194], sol-gel/microemulsion[195], impregnation[196], impregnation/photodeposition[197], photochemical deposition[198], photochemical reduction[199], reflux[200] etc. Many studies have been done on the structure and properties of TiO_2 doped with alkaline metals[201], alkaline earth metals[202], 3d-transition metals[203],4d-transition metals[204] and rare earth metals[205]. All the studies showed that the enhancement in the photocatalytic property of metal-doped TiO_2 could be achieved by lower concentration of metal doping (<10%). Metal doping facilitates the transport of photogenerated electrons from the CB into the metal. Redox potential of the radical species created during photocatalysis at the vicinity of TiO_2 is increased as a consequence of metal doping. These species can easily trigger photochemical reactions, reducing the time of charge recombination within TiO_2[206].

Transition metal doped TiO_2 has been most widely used by various research groups in several applications especially environmental purification. Transition metals can disturb the electronic properties of TiO_2 causing a shift in its absorption from UV to visible region. The photocatalyst so developed using transition metal doped TiO_2 may be active in the visible region too[207]. Inturi et al. (2014)[208] studied the photocatalytic efficiency of transition metals V, Cr, Mn, Fe, Co, Ni, Cu, Mo, Y, Ce, or Zr doped TiO_2. Better conversion in the visible region was observed in V, Cr or Fe doped TiO_2. The photocatalytic activity of Cr doped TiO_2 was found to be superior compared to TiO_2 doped with other metals. Doping Cr with TiO_2 increased the reduction potential of Ti and Cr leading to the formation of Ti-O-Cr bond that increased the photo response of the system.

Several authors have reported the enhancement in the photocatalytic activity of metal doped TiO_2 for the removal of environmental pollutants [193,209,218,210–217]. Mogal et al. (2014)[219] conducted a detailed study with regards to the structure of Ag-doped TiO_2 of varying Ag concentrations and its efficiency for the photodegradation of

phthalic acid under UV radiation. Even at 0.75% Ag doping, better thermal stability and degradation efficiency was achieved for Ag-TiO$_2$. Increased Ag doping percentage decreased the photocatalytic efficiency of Ag-TiO$_2$. Ag metal was found to agglomerate at the surface of TiO$_2$ as the percentage of Ag doping increased. Chiang et al. (2002) reported the oxidative degradation of cyanide ions using Cu doped TiO$_2$ catalysts with different Cu doping percentage under UV radiation. The rate of oxidation of cyanide was maximum at 0.1 % Cu doping and higher percentage of Cu retarded the reaction[220]. Superhydrophilic Cu doped TiO$_2$ catalysed photodegradation of Methylene blue was reported by Wang et al (2014)[221]. The Cu doped TiO$_2$ also exhibited antifogging property.

1.6.2   TiO$_2$ modified by carbonaceous materials

Carbonaceous compounds like activated carbons[222,223], carbon nanotubes (CNTs)[224,225], fullerene[226], graphenes/ graphene oxides[227,228] are used to modify TiO$_2$ photocatalyst owing to the unique properties exhibited by them. The advantages of such carbonaceous compounds modified TiO$_2$ lie on their special abilities to tune the electrical, structural and optical properties. Such composites are observed to exhibit superior chemical and thermal stability too[229,230]. Another advantage of carbonaceous compounds lies in their ability to hold TiO$_2$ within their matrix taking advantage of their large surface area. Better transfer of charge carriers along their surface is also facilitated[231]. The application of carbonaceous materials modified TiO$_2$ photocatalysts depend on the type of carbon structure used as different carbon allotropes have their own unique properties. Enhancement in the mechanism of photocatalytic activity of TiO$_2$ coupled carbonaceous materials lie in their superior adsorption property[232]. The carbon materials can adsorb various dyes like ecotoxic pollutants on their surface and can relay the photogenerated charge carriers originating from TiO$_2$ to these pollutants[233]. Ti-O-C bonds could be formed in the TiO$_2$ coupled with carbonaceous compounds[228,234,235] thereby extending their photo response towards the visible region[236]. Carbon materials also play the role of electron reservoirs that accepts and stores the photogenerated electrons from the CB of TiO$_2$ thus reducing the chance of electron hole recombination within TiO$_2$[237]. The electrons stored in the carbon materials associated with TiO$_2$ are utilized for the photochemical process.

Activated carbons have the special property of high surface area due to its porous nature. The pores could be classified as micro, meso and macro depending on the sizes. This porous nature helps activated carbon to adsorb impurities on its surface. Zhang et al. (2004) reported an interesting scheme by which municipal sewage sludge was utilized for the development of activated carbon. The activated carbon so developed was coupled with TiO_2 for the removal of Hg(II) ions from contaminated water photochemically. The TiO_2-activated carbon photocatalyst adsorbed the Hg(II) ions and reduced them into Hg(0) which was then recovered from the solution[222]. Wang et al. (2007)[223] prepared TiO_2-activated carbon couple by developing TiO_2 crystals over activated carbon. The photocatalyst so produced through sol-gel technique exhibited an appreciable activity in the UV region for the photodegradation of Chromotrope 2R in aqueous media. Activated carbon was coated on the surface of TiO_2 via hydrolytic precipitation method by Li and coworkers (2006)[238] using tetrabutylorthotitanate as precursor. The modified TiO_2 so produced showed enhanced photochemical activity for the degradation of methyl orange obeying pseudo-first order rate law. Deqing Mo and Dai Qi Ye. (2009) devised a setup by which activated carbon fibers were first modified using nitrogen plasma followed by loading it with TiO_2. TiO_2 loading into the developed carbon fibers was accomplished using tertiary butyl titanate via hydrolysis. The photocatalyst so produced could degrade formaldehyde much efficiently[239]. Slimen et al. (2011)[240] further heated TiO_2-activated carbon composite in air at 700°C which was developed through sol-gel technique. The photocatalyst was used for the degradation of methyl orange under visible light irradiation. Orha et al. (2017)[241] adopted microwave supported hydrothermal process for the preparation of granular activated carbon modified TiO_2. The photocatalyst so developed actively degraded humic acid under UV radiation.

Carbon nanotubes (CNT) with its one-dimensional rolled network like structure offer better surface area. They can stabilise TiO_2 associated with them. The properties of CNT could be tuned by functionalisation. Better thermal and electronic properties are exhibited by CNTs[242]. CNTs could be classified based upon the number of the of concentric carbon network rolled to form tubes. Single walled carbon nano tubes (SWCNTs) and multi walled carbon nanotubes (MWCNTs) consist of single carbon tube and multiple concentric carbon tubes rolls respectively[243]. Better photosensitization is promised by CNTs coupled with TiO_2 structures.

Yen et al. (2008) reported that the photocatalytic activity of TiO_2-MWCNT photocatalyst prepared through sol-gel route was found to be superior to those synthesised through hydrothermal route for the photodegradation of NOx and phenol[244]. Sol gel process was used by Gao and co-workers (2009)[245] to coat anatase mesoporous TiO_2 nano layers over MWCNT. Uniform coating of TiO_2 over MWCNT was accomplished with the air of surfactants. The developed photocatalyst showed improved efficiency for the photodegradation of methylene blue. Ashkarran and co-workers (2015)[246] developed TiO_2-CNT composites via different approaches like simple mixing, mixing followed by heating and mixing followed by UV irradiation. The UV irradiated composite exhibited superior photocatalytic activity compared to the others. TiO_2-CNT nano fibers were prepared by Wongaree et al. (2016)[247] using electrospinning method which showed effective activity for the photodegradation of methylene blue and benzene gas. Ahmad et al (2017)[248] prepared hair like TiO_2-CNT wires via CVD technique that could completely degrade methyl orange solution from the aqueous solution within 30 minutes.

The most widely used type of fullerene for photocatalytic applications is C_{60} with 60 p-electrons and C_{70} with 70 p-electrons[249]. C_{70} is less symmetric compared to C_{60}. As result of this, better ability for free radical creation is observed in C_{70} compared to C_{60}. Electron affinity of C_{70} is higher compared to C_{60} [250]. Superior visible light response observed in C_{70} compared to C_{60} could be explained by its larger photo cross-sectional area[251]. Most of the studies are however based on C_{60} TiO_2 couple. C_{70} has been into the picture recently. The conjugated close-shell structure with delocalised electrons has added to its unique physicochemical properties[252,253]. Fullerenes can act as sensitizer when coupled with materials like TiO_2 separating the photogenerated charge carriers much efficiently[254]. This is accomplished by its electron accepting property[254]. They can absorb mainly in UV region and moderately in the visible region[255]. The properties of fullerene can further be tuned by functionalisation.

Arrays of TiO_2-fullerene nanotubes[256], TiO_2-fullerene prepared via refluxing method[257] and TiO_2-fullerene prepared via hydrothermal method[258] were reported to show better photocatalytic property for the photodegradation of Methylene blue, Cr(IV) and Rhodamine B. Functionalised fullerene-TiO_2 composites like water

soluble polyhydroxyl fullerene coupled with TiO_2[259] and carboxylic acid functionalized fullerene coupled with TiO_2[260] efficiently degraded Procion red and Rhodamine B dyes photochemically. Out of these the carboxylic acid functionalized fullerene could shift the photocatalytic activity of TiO_2 towards visible region and the degradation of Rhodamine B took place under the visible light. Monolayer dispersion of C_{60} over mesoporous TiO_2 was achieved by hydrothermal method as reported by Yu et al. (2011)[261] which catalysed acetone oxidation. Qi and co-workers[262] reported that the optimum loading of 2% C_{60} into TiO_2 prepared through solution phase method catalysed the photodegradation of Methylene blue more efficiently. A comparison between the photocatalytic activities of C_{60} and C_{70} coupled with TiO_2 was made by Cho and co-workers (2015)[263] for the photodegradation of Methylene blue. C_{70} incorporated TiO_2 was found to show better activity for the photodegradation of Methylene blue under visible light irradiation.

Graphene is another significant material which is widely being studied accounting its outstanding unique properties. The sp^2 hybridized two dimensional hexagonal array of carbon atoms could be extracted from graphite[264]. In fact graphene is nothing but a single layer 2D sheet exfoliated from 3D structured graphite by chemical or physical methods[264]. Graphene has been of quite interest for the researchers owing to its electrical[265,266], mechanical[267], interfacial[268], photosensitizing[227], capacitance[269] and thermal[270] properties. Graphene also have high charge mobility along its structure[265]. Graphene find application in photocatalysis[271], composite materials[272], medicine[273], energy conversions[274], electronic devices[275], molecular sensors[276], liquid crystal devices[277], quantum hall devices[278], ultracapacitors [279] etc. The properties of graphene are quite tunable by doping[280] and functionalisation[281].

Graphene oxide (GO) as the name implies, is the oxidized form of graphene. In GO the oxygen atoms are bonded covalently to some of its carbon atoms resulting in the formation of hydroxyl or epoxy bonds[282–286]. Peripheral carbon atoms in GO may also contain carboxylic acid functional groups attached in addition to hydroxyl and epoxy groups[287]. The presence of these functional groups decrease the delocalisation of electrons through the graphene backbone of GO[288] and increase the hydrophilicity of the material. GO is in fact highly dispersible in water whereas graphene is not [234,289]. Hummers method[290] is most widely used for the preparation of graphene oxide

(GO) from graphite. During the process, oxidising agents used (H_2SO_4, $NaNO_3$ and $KMnO_4$) penetrate through the graphite layer and oxidizes the layers of graphite. This weakens the bond between each layers of graphite[291]. Process like sonication can lead to exfoliation of each layers into GO. The GO hence formed can be reduced into reduced graphene oxide (rGO) using simple chemical process. UV irradiation of GO catalysed by TiO_2 in ethanol media can also reduce it into rGO[289].

Zhang et al. (2011)[271] compared the photocatalytic activity of TiO_2-graphene and TiO_2-CNT photocatalysts for the selective oxidation of alcohols. Better photocatalytic efficiency was observed in TiO_2-graphene composites compared to that of TiO_2-CNT. The photocatalytic activity of TiO_2 was further tuned by controlling the morphology of TiO_2-graphene composite. Huang et al. (2013)[292] reported that the enhanced photocatalytic activity exhibited by TiO_2-graphene for the photodegradation of formaldehyde in air was due to the formation of Ti-C bond between TiO_2 and graphene. The formation of Ti-C bond facilitated the easy charge transfer from TiO_2 to graphene thereby reducing the charge recombination in TiO_2. Liu and co-workers (2013)[228] developed a core shell structure in which TiO_2 was encapsulated by GO. The condensation reaction between the -OH groups on TiO_2 surface and -COOH functional groups on GO resulted in the core shell structure. Enhanced photodegradation of Rhodamine B dye under UV as well as visible light was observed in the presence of the core shell TiO_2-GO structure, compared to pure TiO_2 photocatalyst. Umrao et al. (2014)[293] reported that the formation of Ti-O-C between TiO_2 and graphene in TiO_2-graphene composite minimised its band gap energy. The easy movement of charge carriers along the Ti-O-C bridge between TiO_2 resulted in better electron-hole separation and lowering of band gap energy. The composite catalysed the photodegradation of Methylene blue dye under visible light radiation. Rakkesh et al. (2014)[294] studied the photodegradation of Methylene blue dye catalysed by TiO_2-graphene and ZnO-graphene photocatalysts. Both the photocatalysts exhibited better efficiency for the photodegradation of the dye in sunlight due to the formation of heterojunction between the metal oxides and graphene. Increased interfacial charge transfer resulted in better electron hole separation in TiO_2 as well as ZnO in the presence of graphene. Hi and co-workers (2016)[295] developed bipyramidal structured TiO_2-rGO photocatalyst. The structure

consisted of one to five layers of rGO encapsulating TiO_2. The composites acted as better photocatalysts for the photodegradation of Methyl orange.

1.6.3 TiO₂ modified by conjugated polymers

The idea of coupling a metal oxide photocatalyst with a polymer system was introduced in order to develop a system that could support the metal oxide for better activity. Such an immobilized system with polymer supported inorganic photocatalysts find its application in water purification systems. Polymer supported inorganic heterogeneous photocatalyst particles eliminate the troubles faced while retracting the catalyst from water after the reaction. In other words the highly dispersed catalyst particles require more time to settle after purification process and this drawback is nullified by polymer support. Based on this idea numerous polymer supports[296] were introduced, with PE being the first reported polymer for TiO_2 support[297].

The most remarkable advantage in photocatalysis was achieved with the introduction of conducting polymers having extended conjugation such as polyaniline (PANI)[298], polythiophene (PTh)[299], poly(3,4-ethylenedioxythiophene) (PEDOT)[300], Poly(3-hexylthiophene) (P3HT)[301], polypyrrole (PPy)[302], poly-(fluorene-co-thiophene) (PFT)[303] etc. These conducting conjugated polymers act as co-catalyst to enhance the activity of the photocatalyst associated with them[304]. Conducting polymers that have extended π-conjugation are quiet stable and can also absorb in UV and visible region (190 to 800 nm)[305]. The introduction of such conjugated systems coupled with photocatalysts like TiO_2 can hence extend their activity in the visible region [306].

PANI offers a better choice of conjugated conducting polymers that could be coupled with TiO_2 like photocatalysts. The characteristic property of PANI includes high charge carrier mobility along the matrix, better absorption in visible region, environmental stability and easy synthetic approach making the material cheap. PANI is a hole transporting polymer[307]. PANI can be considered as p-type material that forms p-n heterojunction with n-type TiO_2 semiconductor that further enhances the charge carrier mobility[308].

Wang et al (2007)[305] reported the preparation of TiO_2-PANI nano composite via chemical oxidative polymerisation of aniline. The prepared composite catalysed the photodegradation of Methylene blue dye, utilizing UV as well as visible region of natural light. Pure TiO_2 photocatalyst on the other hand was active only in the UV region. Min et al (2007)[309] reported the existence of coordination bond between titanium atom of TiO_2 and nitrogen atom of PANI, prepared through oxidative polymerisation method. The composite catalysed enhanced degradation of methylene blue dye under natural light compared to pure TiO_2 catalyst. Zhang and co-workers (2008)[306] reported that the improved photocatalytic activity of the synthesised TiO_2-PANI composite for the photodegradation of Methylene blue and Rhodamine B under visible light was facilitated by the $\pi \rightarrow \pi^*$ transition in PANI. The $\pi \rightarrow \pi^*$ transition caused transportation of electrons from PANI to the CB of TiO_2 and further to the adsorbed molecules (O_2 and H_2O/-OH) producing radical species. These species initiated the degradation mechanism of the dyes. Wang and co-workers (2010)[310] prepared PANI doped with camphorsulfonic acid (CSA) by dispersion polymerisation method. Composite of TiO_2-PANI-CSA was developed by dissolving PANI-CSA in THF. The photodegradation of methylene blue was studied using TiO_2 and TiO_2-PANI-CSA photocatalysts. It was concluded that PANI-CSA extended the activity of TiO_2 towards visible region of the spectra. Olad (2011)[311] developed core shell structures of TiO_2-PANI composite with PANI encapsulating TiO_2. The composite showed improved activity for the photodegradation of Methyl orange under visible light radiation. Reddy et al. (2016)[298] prepared TiO_2-PANI through oxidative polymerisation and reported that the composite showed improved photocatalytic activity under UV radiation for the photodegradation of Rhodamine B, Methylene Blue and phenol. The extent of photodegradation of Reactive red (azo dye) from waste water under UV radiation was greater in the presence of TiO_2-PANI compared to pristine TiO_2 as reported by Gilja (2017)[312].

1.7 Organic compounds as photosensitizers

Some simple organic compounds have the ability to absorb electromagnetic radiations, get excited and dissipate their energy by transferring it into another system without quenching. Such compounds come under the category of photosensitizers. Photosensitizers transfer its triplet energy into the reactant compounds coupled with

them. The use of photosensitizers hence finds their application when the triplet state yield of a particular compound is not satisfactory. In addition to triplet energy transfer, photosensitizers also involve in photocatalysis in some cases[313]. The efficiency of a molecule to act as an efficient photosensitizer depends upon the efficiency of its inter system crossing (ISC) which determines its triplet state production[314,315]. Based on the triplet state energy transfer efficiency, the choice of photosensitizers spread to a wide variety including organic compounds, organic dyes, organo-metallic compounds, transition metallic complexes etc. The application of photosensitizers is also extended to therapy, disinfection, hydrogen production, environmental remediation, luminescent oxygen sensing[316,317] and other photochemical reactions[318,319]. In polymer degradation chemistry, the photosensitisers work by producing free radicals that interacts with the polymer chains initiating photodegradation[320]. The region of light absorption and thereby the photo-reactivity/degradation of a polymer could be tuned by coupling it with suitable photosensitizer[321].

Eltayeb and co-workers (2009)[83] investigated the photodegradation of LDPE using 2-hydroxy-4-methoxybenzophenone and cobalt naphthenate photosensitizers, under UV radiation. It was observed that the rate of photodegradation of LDPE increased in the presence of cobalt naphthenate. 2-hydroxy-4-methoxybenzophenone on the other hand showed retardation in photo-oxidative degradation. In 2011 Eltayeb et al.[82] again compared the degradation of LDPE using cobalt naphthenate and 2-benzoylbenzoic acid under UV radiation. Even though the rate of photodegradation of LDPE increased as the percentage of cobalt naphthenate increased, the increase in the concentration of 2-benzoylbenzoic acid retarded the photodegradation. Manangan et al. (2010)[320] investigated the photodegradation of PE and PP using derivatives of benzophenone and acetophenone. Two different light sources (λ= 254 nm and 366 nm) were used. The photodegradation was efficient under 254 nm UV radiation. 3-nitroacetophenone showed better photosensitization for the effective degradation of PE and PP compared to the others. Pinto et al. (2013)[322] investigated the photodegradation of PS film in the presence of organic photosensitizers, thioxanthone and benzophenone. Both the photosensitizers caused oxidative degradation with the formation of double bonds in the PS chain. The photosensitization of thioxanthone was found to be superior compared to that of benzophenone. Flash photolysis proved

that both the photosensitizers exhibited same triplet state reactivity. The larger absorptivity of thioxanthone compared to benzophenone was the reason behind its superior photosensitizing efficiency. Nguyen et al. (2018)[80] developed a hybrid photocatalyst TiO$_2$-benzophenone-ethylene vinyl acetate by mixing process. Photodegradation of LDPE film was studied using this catalyst. The catalyst showed improved efficiency for the photodegradation of LDPE with increasing carbonyl index and decrease in the mechanical property with respect to degradation time.

1.8 Zinc oxide (ZnO)

Zinc oxide (ZnO) is a transition metal semiconductor whose photochemistry resembles that of TiO$_2$ in several aspects[323]. The band gap energy (E$_g$) of ZnO is almost equal to TiO$_2$ (generally E$_g$ of ZnO is slightly greater than that of TiO$_2$)[324]. ZnO is also non-toxic, cheap and efficient photocatalyst just like TiO$_2$[325]. It is an n-type semiconductor like TiO$_2$[326]. ZnO has also been widely used in many applications[327,328]. Disadvantages like faster charge recombination and inactivity towards visible region is also observed in ZnO. Another disadvantage is that the photostability of ZnO is not as much pronounced as TiO$_2$. ZnO undergoes photo-corrosion to form Zn(OH)$_2$ when exposed to UV radiation for a prolonged time interval[329]. ZnO is also soluble in strong acidic and strong alkaline medium[329,330]. This limits the use of ZnO compared to TiO$_2$ in most of the cases. Some authors reported that ZnO is less efficient compared to TiO$_2$ as a photocatalyst. Several modification strategies have been practiced in order to increase the photocatalytic efficiency of ZnO[331–333] as explained in the case of TiO$_2$ in previous sections. ZnO commonly exists in zinc blende and wurtzite phases. Wurtzite phase is mostly used as photocatalysts especially in environmental cleaning processes[334,335].

Out of several studies reported using ZnO initiated photochemical reactions, recent ones include the work of Denisyuk et al. (2016)[336] who studied the photodegradation of p-type semiconductor doped acrylic polymer film. The photodegradation of the polymer was explained by the development of bubbles due to the formation of various photolysis products. Suryavanshi et al. (2018)[337] adopted spray pyrolysis method for the deposition of ZnO films over glass substrates. The photodegradation of methyl blue and benzoic acid dye were studied using these ZnO coated electrodes. Methyl blue underwent better photodegradation. Zhang et al.

(2018)[338] dried ZnO particles in vacuum in order to develop nano ZnO particles with oxygen vacancies. Photodegradation of methylene blue was studied using this nano ZnO as catalyst under UV radiation. Superior photocatalytic efficiency exhibited by the synthesised nano ZnO was reported to be due to the reduction of electron hole recombination by the oxygen vacancies, increased surface area and better photostability.

Application of ZnO catalyst modified by several techniques was also reported. Some of the recent works include the study of Ngaloy et al. (2019)[339] where chemical vapour decomposition method was used for the preparation of ZnO-rGO photocatalyst that showed improved activity for the degradation of methylene blue under UV radiation. The formation of Zn-O-C bond between ZnO and rGO improved the separation of charge carriers generated within ZnO and hence better photocatalytic activity. Asgar et al. (2019)[340] developed ZnO-PANI photocatalyst via chemical oxidative polymerisation method for the study of degradation of metronidazole under UV radiation. The photodegradation of metronidazole was accelerated by ZnO-PANI photocatalyst by the formation of highly reactive $O_2^{\bullet-}$ and $OH^{\bullet}$ radicals which interacted with metronidazole. Qi and co-workers (2019) [341] modified ZnO by doping it with some transition metals Fe, Ni, Co, Mn and Cu. The transition metal doped ZnO existed in wurtzite phase. The metal doping was 3% versus ZnO. Cu doped ZnO showed superior photocatalytic activity for the degradation of methylene blue under light radiation (λ=365 nm). Ismael et al. (2019)[342] developed ZnO modified with graphitic carbon nitride via calcination method. The composite efficiently catalysed the photodegradation of 4-chlorophenol and methyl orange in the presence of visible light. The improved degradation efficiency of the composite attributed to the easy charge transfer through the interface between the heterojunctions of the composite. Neelgud and Oki (2020)[343] developed graphene nanosheets deposited by ZnO nanotrapezoids. The composite exhibited better photostability and improved efficiency for the photodegradation of different types of dye contaminants in sunlight. The mechanism of enhancement of photocatalytic activity is due to the formation of heterojunctions formed between ZnO and graphene nanosheets that facilitated better charge transfer and reduced the charge carrier recombination.

1.9 Objectives of the present study

1. To prepare and characterise modified TiO_2/ZnO photocatalysts.

2. To study the photodegradation of PS in the presence of these photocatalysts and other photosensitizers under UV radiation.

3. To investigate the change in electrical, mechanical and thermal properties of PS-composites due to photodegradation.

4. To propose a suitable mechanism for photodegradation of PS composites.

5. To optimise the degradation conditions of PS under UV radiation.

References

1. Hosler, D., Burkett, S. L. & Tarkanian, M. J. Prehistoric Polymers: Rubber Processing in Ancient Mesoamerica. *Science (80-.).* **284**, 1988–1991 (1999).
2. Andrady, A. L. & Neal, M. A. Applications and societal benefits of plastics. *Philos. Trans. R. Soc. B Biol. Sci.* **364**, 1977–1984 (2009).
3. Staudinger, H. Über Polymerisation. *Berichte der Dtsch. Chem. Gesellschaft (A B Ser.* **53**, 1073–1085 (1920).
4. Mulder, K. F. Sustainable Consumption and Production of Plastics? *Technol. Forecast. Soc. Change* **58**, 105–124 (1998).
5. Geyer, R., Jambeck, J. R. & Law, K. L. Production, use, and fate of all plastics ever made. *Sci. Adv.* **3**, (2017).
6. Rabie, S., Mahran, A., M Kamel, E. & H Abdel Hamid, N. Photodegradation of Polystyrene Stabilized with Uracil Derivatives. *J. Appl. Sci. Res.* **4**, 2018–2026 (2008).
7. Chaukura, N., Gwenzi, W., Bunhu, T., Ruziwa, D. T. & Pumure, I. Potential uses and value-added products derived from waste polystyrene in developing countries: A review. *Resour. Conserv. Recycl.* **107**, 157–165 (2016).
8. Hocking, M. B. Paper versus polystyrene: a complex choice. *Science (80-.).* **251**, 504 (1991).
9. Priddy, D. Styrene Polymers. in *Encyclopedia of Polymer Science and Technology* 241–336 (American Cancer Society, 2001). doi:10.1002/0471440264.pst354.
10. Pasztor, A. J., Landes, B. G. & Karjala, P. J. Thermal properties of syndiotactic polystyrene. *Thermochim. Acta* **177**, 187–195 (1991).
11. Ishihara, N., Seimiya, T., Kuramoto, M. & Uoi, M. Crystalline syndiotactic polystyrene. *Macromolecules* **19**, 2464–2465 (1986).
12. Natta, G. *et al.* Crystalline High Polymers of α-olefins. *J. Am. Chem. Soc.* **77**, 1708–1710 (1955).
13. Brownstein, S., Bywater, S. & Worsfold, D. J. Proton Resonance Spectra and Tacticity of Polystyrene and Deuteriopolystyrenes. *J. Phys. Chem.* **66**, 2067–2068 (1962).
14. Bovey, F. A., Hood, F. P., Anderson, E. W. & Snyder, L. C. Polymer NMR Spectroscopy. XI. Polystyrene and Polystyrene Model Compounds. *J. Chem. Phys.* **42**, 3900–3910 (1965).
15. Heatley, F. & Bovey, F. A. Polymer Nuclear Magnetic Resonance Spectroscopy. XIII. Polystyrene at 220 MHz. *Macromolecules* **1**, 301–303 (1968).
16. Matsuzaki, K., Uryu, T., Osada, K. & Kawamura, T. Stereoregularity of polystyrene-β,β-d2. *J. Polym. Sci. Polym. Chem. Ed.* **12**, 2873–2879 (1974).
17. Tadokoro, H., Nishiyama, Y., Nozakura, S. & Murahashi, S. Stereoregular Polymers. VII. Infrared Spectra of Isotactic Polystyrene, Isotactic Poly-α, β, β-trideuterostyrene and Isotactic Poly-p- deuterostyrene. *Bull. Chem. Soc. Jpn.* **34**, 381–391 (1961).
18. Trumbo, D. L., Chen, T. K. & Harwood, H. J. Observation of triad stereosequences in a

polystyrene derivative. *Macromolecules* **14**, 1138–1139 (1981).

19. Ray, G. J., Pauls, R. E., Lewis, J. J. & Rogers, L. B. Structure determination by two-dimensional NMR of α-hydro-ω-butyloligostyrenes fractionated by liquid chromatography. *Die Makromol. Chemie* **186**, 1135–1149 (1985).

20. Johnson, L. F., Heatley, F. & Bovey, F. A. Polymer Nuclear Magnetic Resonance Spectroscopy. XIX. Carbon-13 Resonance Observations of Stereochemical Configuration. *Macromolecules* **3**, 175–177 (1970).

21. Randall, J. C. The distribution of stereochemical configurations in polystyrene as observed with 13C NMR. *J. Polym. Sci. Polym. Phys. Ed.* **13**, 889–899 (1975).

22. Cheng, H. N. & Lee, G. H. NMR Studies of Polystyrene Tacticity. *Int. J. Polym. Anal. Charact.* **2**, 439–455 (1996).

23. Tan, H., Moet, A., Hiltner, A. & Baer, E. Thermoreversible gelation of atactic polystyrene solutions. *Macromolecules* **16**, 28–34 (1983).

24. Clark, J. C., Wellinghoff, S. T. & Miller, W. G. Rheological Properties of Polystyrene Carbon-Disulfide Gels. in *Abstracts of Papers of the American Chemical Society* vol. 186 41--POLY (1983).

25. Gan, Y.-S., François, J., Guenet, J.-M., Gauthier-Manuel, B. & Allain, C. A direct demonstration of the occurrence of physical gelation in atactic polystyrene solutions. *Die Makromol. Chemie, Rapid Commun.* **6**, 225–230 (1985).

26. Gan, J. Y. S., Francois, J. & Guenet, J. M. Enhanced low-angle scattering from moderately concentrated solutions of atactic polystyrene and its relation to physical gelation. *Macromolecules* **19**, 173–178 (1986).

27. François, J., Gan, J., Sarazin, D. & Guenet, J.-M. Relation between physical gelation and tacticity in polystyrene. *Polymer (Guildf).* **29**, 898–903 (1988).

28. David, C., Putman-de Lavareille, N. & Geuskens, G. Luminescence studies in polymers—IV. Effect of orientation, tacticity and crystallinity on polystyrene and polyvinylcarbazole fluorescence. *Eur. Polym. J.* **10**, 617–621 (1974).

29. Chen, K., Harris, K. & Vyazovkin, S. Tacticity as a Factor Contributing to the Thermal Stability of Polystyrene. *Macromol. Chem. Phys.* **208**, 2525–2532 (2007).

30. Huang, C.-L., Chen, Y.-C., Hsiao, T.-J., Tsai, J.-C. & Wang, C. Effect of Tacticity on Viscoelastic Properties of Polystyrene. *Macromolecules* **44**, 6155–6161 (2011).

31. Grigoriadi, K. *et al.* Physical Ageing of Polystyrene: Does Tacticity Play a Role? *Macromolecules* **52**, 5948–5954 (2019).

32. Terashima, T. Polystyrene (PSt). in *Encyclopedia of Polymeric Nanomaterials* (eds. Kobayashi, S. & Müllen, K.) 2077–2091 (Springer Berlin Heidelberg, 2015). doi:10.1007/978-3-642-29648-2_255.

33. Priddy, D. B. Recent advances in styrene polymerization. in *Polymer Synthesis* 67–114 (Springer Berlin Heidelberg, 1994). doi:10.1007/BFb0024127.

34. Flory, P. J. The Mechanism of Vinyl Polymerizations1. *J. Am. Chem. Soc.* **59**, 241–253 (1937).

35. Mayo, F. R. The dimerization of styrene. *J. Am. Chem. Soc.* **90**, 1289–1295 (1968).

36. Mulzer, J., Kühl, U., Huttner, G. & Evertz, K. Facial selectivities and rate effects in the thermal [4+2] dimerization of arylated 1,3-dienes. 1,5-H shift versus dimerization of (Z)-1,3-Dienes. *Chem. Ber.* **121**, 2231–2238 (1988).

37. Gibbs, B. F. & Mulligan, C. N. Styrene Toxicity: An Ecotoxicological Assessment. *Ecotoxicol. Environ. Saf.* **38**, 181–194 (1997).

38. Kwon, B. G. *et al.* Regional distribution of styrene analogues generated from polystyrene degradation along the coastlines of the North-East Pacific Ocean and Hawaii. *Environ. Pollut.* **188**, 45–49 (2014).

39. LI, W. C., TSE, H. F. & FOK, L. Plastic waste in the marine environment: A review of sources, occurrence and effects. *Sci. Total Environ.* **566–567**, 333–349 (2016).

40. Singh, B. & Sharma, N. Mechanistic implications of plastic degradation. *Polym Degrad Stab* **93**, (2008).

41. Xiao, L. *et al.* Synthesis of novel ultraviolet stabilizers based on [60]fullerene and their

effects on photo-oxidative degradation of polystyrene. *Fullerenes, Nanotub. Carbon Nanostructures* **28**, 465–473 (2020).

42. Al-Khazraji, A. M. A., Hassani, R. A. M. Al & Ahmed, A. Studies on the Photostability of Polystyrene Films with New Metals Complex of 1, 2, 4-triazole-3-thione Derivate. *Syst. Rev. Pharm.* **11**, 525–534 (2020).

43. Alotaibi, M. H. *et al.* Evaluation of the use of polyphosphates as photostabilizers and in the formation of ball-like polystyrene materials. *J. Polym. Res.* **26**, 161 (2019).

44. Hadi, A. G. *et al.* Photostabilization of Poly(vinyl chloride) by Organotin(IV) Compounds against Photodegradation. *Molecules* **24**, (2019).

45. Ali, G. Q. *et al.* Photostability and Performance of Polystyrene Films Containing 1,2,4-Triazole-3-thiol Ring System Schiff Bases. *Molecules* **21**, (2016).

46. Kwon, B. G., Chung, S.-Y., Park, S.-S. & Saido, K. Qualitative assessment to determine internal and external factors influencing the origin of styrene oligomers pollution by polystyrene plastic in coastal marine environments. *Environ. Pollut.* **234**, 167–173 (2018).

47. Barnes, D. K. A., Galgani, F., Thompson, R. C. & Barlaz, M. Accumulation and fragmentation of plastic debris in global environments. *Philos. Trans. R. Soc. B Biol. Sci.* **364**, 1985–1998 (2009).

48. Cole, M., Lindeque, P., Halsband, C. & Galloway, T. S. Microplastics as contaminants in the marine environment: a review. *Mar. Pollut. Bull.* **62**, 2588–2597 (2011).

49. Eriksen, M. *et al.* Plastic pollution in the South Pacific subtropical gyre. *Mar. Pollut. Bull.* **68**, 71–76 (2013).

50. Bergami, E. *et al.* Nano-sized polystyrene affects feeding, behavior and physiology of brine shrimp Artemia franciscana larvae. *Ecotoxicol. Environ. Saf.* **123**, 18–25 (2016).

51. Barboza, L. G. A. & Gimenez, B. C. G. Microplastics in the marine environment: Current trends and future perspectives. *Mar. Pollut. Bull.* **97**, 5–12 (2015).

52. de Stephanis, R., Giménez, J., Carpinelli, E., Gutierrez-Exposito, C. & Cañadas, A. As main meal for sperm whales: plastics debris. *Mar. Pollut. Bull.* **69**, 206–214 (2013).

53. Hidalgo-Ruz, V., Gutow, L., Thompson, R. C. & Thiel, M. Microplastics in the marine environment: a review of the methods used for identification and quantification. *Environ. Sci. Technol.* **46**, 3060–3075 (2012).

54. Koelmans, A. A., Besseling, E., Wegner, A. & Foekema, E. M. Plastic as a carrier of POPs to aquatic organisms: a model analysis. *Environ. Sci. Technol.* **47**, 7812–7820 (2013).

55. Koelmans, A. A., Besseling, E. & Foekema, E. M. Leaching of plastic additives to marine organisms. *Environ. Pollut.* **187**, 49–54 (2014).

56. Thompson, R. C. *et al.* Lost at Sea: Where Is All the Plastic? *Science (80-.).* **304**, 838 (2004).

57. Chae, Y. & An, Y.-J. Current research trends on plastic pollution and ecological impacts on the soil ecosystem: A review. *Environ. Pollut.* **240**, 387–395 (2018).

58. Nizzetto, L., Bussi, G., Futter, M. N., Butterfield, D. & Whitehead, P. G. A theoretical assessment of microplastic transport in river catchments and their retention by soils and river sediments. *Environ. Sci. Process. Impacts* **18**, 1050–1059 (2016).

59. Rillig, M. C. Microplastic in terrestrial ecosystems and the soil? *Environ. Sci. Technol.* **46**, 6453–6454 (2012).

60. Liu, E. K., He, W. Q. & Yan, C. R. `White revolution' to `white pollution'{\textemdash}agricultural plastic film mulch in China. *Environ. Res. Lett.* **9**, 91001 (2014).

61. Rochman, C. M. *et al.* Scientific Evidence Supports a Ban on Microbeads. *Environ. Sci. Technol.* **49**, 10759–10761 (2015).

62. Akhtar, S. Food Safety Challenges—A Pakistan's Perspective. *Crit. Rev. Food Sci. Nutr.* **55**, 219–226 (2015).

63. Morikawa, T. & Yanai, E. Toxic Gases and Smoke Evolution from Foam Plastic Building Materials Burning in Fire Environments. *J. Fire Sci.* **7**, 131–141 (1989).

64. Gao, X., Ji, B., Yan, D., Huang, Q. & Zhu, X. A full-scale study on thermal degradation of polychlorinated dibenzo- p-dioxins and dibenzofurans in municipal solid waste incinerator fly ash and its secondary air pollution control in China. *Waste Manag. Res. J. Int. Solid Wastes Public Clean. Assoc. ISWA* **35**, 437–443 (2017).

65. Ji, L. *et al.* Municipal solid waste incineration in China and the issue of acidification: A review. *Waste Manag. Res. J. Int. Solid Wastes Public Clean. Assoc. ISWA* **34**, 280–297 (2016).

66. Ragaert, K., Delva, L. & Van Geem, K. Mechanical and chemical recycling of solid plastic waste. *Waste Manag.* **69**, 24–58 (2017).

67. Guaita, M., Chiantore, O. & Costa, L. Changes in degree of polymerization in the thermal degradation of polystyrene. *Polym. Degrad. Stab.* **12**, (1985).

68. Weidner, S., Kühn, G., Friedrich, J. & Schröder, H. Plasmaoxidative and Chemical Degradation of Poly(ethylene terephthalate) Studied by Matrix-assisted Laser Desorption/Ionization Mass Spectrometry. *Rapid Commun. Mass Spectrom.* **10**, 40–46 (1996).

69. Vinhas, G. M., Souto-Maior, R. M., Lapa, C. M. & Almeida, Y. M. B. de. Degradation studies on plasticized PVC films submited to gamma radiation. *Mater. Res.* **6**, 497–500 (2003).

70. Fotopoulou, K. N. & Karapanagioti, H. K. Degradation of Various Plastics in the Environment. in *Hazardous Chemicals Associated with Plastics in the Marine Environment* (eds. Takada, H. & Karapanagioti, H. K.) 71–92 (Springer International Publishing, 2019). doi:10.1007/698_2017_11.

71. Yousif, E. & Haddad, R. Photodegradation and photostabilization of polymers, especially polystyrene: review. *Springerplus* **2**, 398 (2013).

72. Matheson, L. A. & Boyer, R. F. Light Stability of Polystyrene and Polyvinylidene Chloride. *Ind. Eng. Chem.* **44**, 867–874 (1952).

73. Grassie, N. & Weir, N. A. The photooxidation of polymers. IV. A note on the coloration of polystyrene. *J. Appl. Polym. Sci.* **9**, 999–1003 (1965).

74. George, G. A. The phosphorescence spectrum and photodegradation of polystyrene films. *J. Appl. Polym. Sci.* **18**, 419–426 (1974).

75. Torikai, A., Takeuchi, A. & Fueki, K. The effect of temperature on the photo-degradation of polystyrene. *Polym. Degrad. Stab.* **14**, 367–375 (1986).

76. Hwang, D., Shul, Y. & Chu, Y. Photodegradation behavior of the polycarbonate/TiO2 composite films under the UV irradiation in ambient air condition. *Polym. Compos.* **36**, 1462–1468 (2014).

77. Zhao, X. u, Li, Z., Chen, Y., Shi, L. & Zhu, Y. Solid-phase photocatalytic degradation of polyethylene plastic under UV and solar light irradiation. *J. Mol. Catal. A Chem.* **268**, 101–106 (2007).

78. Al Safi, S. A., Al Mouamin, T. M., Al Sieadi, W. N. & Al Ani, K. E. Irradiation Effect on Photodegradation of Pure and Plasticized Poly (4-Methylstyrene) in Solid Films. *Mater. Sci. Appl.* **5**, 300 (2014).

79. Shawaphun, S., Sangsansiri, D., Changcharoen, J. & Wacharawichanant, S. Nano-Sized Titanium Dioxides as Photo-Catalysts in Degradation of Polyethylene and Polypropylene Packagings. *Sci. J. Ubon Ratchathani Univ.* **1**, (2010).

80. Nguyen, T. K. N. *et al.* Titanium dioxide-benzophenone hybrid as an effective catalyst for enhanced photochemical degradation of low density polyethylene. *e-Polymers* **18**, (2018).

81. Amin, M. U. & Scott, G. Photo-initiated oxidation of polyethylene effect of photo-sensitizers. *Eur. Polym. J.* **10**, 1019–1028 (1974).

82. Eltayeb, E. A., Mahdavian, A. R. & Barikani, M. The Effect of Cobalt Naphthenate and 2-benzoylbenzoic Acid on UV-Degradation Of LDPE. *Iran. J. Chem. Eng.* **8**, 31–42 (2011).

83. Eltayeb, E., Barikani, M., Mahdavian, A. R. & Honarkar, H. The Effect of Cobalt Naphthenate and 2-Hydroxy-4-Methoxybenzophenone on Photo-oxidative Degradation

of LDPE. *Iran. Polym. J.* **18**, 753–760 (2009).

84. Barboiu, V. & Avadanei, M. I. Chemical reactions of benzophenone photoirradiated in 1,2-polybutadiene. *J. Photochem. Photobiol. A Chem.* **222**, 170–179 (2011).

85. Asghar, W. *et al.* Comparative Solid Phase Photocatalytic Degradation of Polythene Films with Doped and Undoped TiO 2 Nanoparticles. **2011**, (2011).

86. Shanti, R. *et al.* Degradation of ultra-high molecular weight poly(methyl methacrylate-co-butyl acrylate-co-acrylic acid) under ultra violet irradiation. *RSC Adv.* **v. 7**, 112-120– 2016 v.7 no.1 (2016).

87. Oil and Colour Chemists' Association, A. Titanium Dioxide Pigments. in *Surface Coatings: Vol I-Raw Materials and Their Usage* 305–312 (Springer Netherlands, 1983). doi:10.1007/978-94-011-6940-0_26.

88. Renz, C. Lichtreaktionen der Oxyde des Titans, Cers und der Erdsäuren. *Helv. Chim. Acta* **4**, 961–968 (1921).

89. Goodeve, C. F. & Kitchener, J. A. The mechanism of photosensitisation by solids. *Trans. Faraday Soc.* **34**, 902–908 (1938).

90. FUJISHIMA, A. & HONDA, K. Electrochemical Photolysis of Water at a Semiconductor Electrode. *Nature* **238**, 37–38 (1972).

91. Bickley, R. I., Gonzalez-Carreno, T., Lees, J. S., Palmisano, L. & Tilley, R. J. D. A structural investigation of titanium dioxide photocatalysts. *J. Solid State Chem.* **92**, 178–190 (1991).

92. Luttrell, T. *et al.* Why is anatase a better photocatalyst than rutile? - Model studies on epitaxial TiO2 films. *Sci. Rep.* **4**, 4043 (2014).

93. Latroche, M., Brohan, L., Marchand, R. & Tournoux, M. New hollandite oxides: TiO2(H) and K0.06TiO2. *J. Solid State Chem.* **81**, 78–82 (1989).

94. Marchand, R., Brohan, L. & Tournoux, M. TiO2(B) a new form of titanium dioxide and the potassium octatitanate K2Ti8O17. *Mater. Res. Bull.* **15**, 1129–1133 (1980).

95. Akimoto, J. *et al.* Topotactic Oxidation of Ramsdellite-Type Li0.5TiO2, a New Polymorph of Titanium Dioxide: TiO2(R). *J. Solid State Chem.* **113**, 27–36 (1994).

96. Mattesini, M. *et al.* High-pressure and high-temperature synthesis of the cubic TiO2 polymorph. *Phys. Rev. B* **70**, 212101 (2004).

97. Simons, P. Y. & Dachille, F. The structure of TiO2II, a high-pressure phase of TiO2. *Acta Crystallogr.* **23**, 334–336 (1967).

98. Dubrovinskaia, N. A. *et al.* Experimental and Theoretical Identification of a New High-Pressure TiO2 Polymorph. *Phys. Rev. Lett.* **87**, 275501 (2001).

99. Dubrovinsky, L. S. *et al.* The hardest known oxide. *Nature* **410**, 653–654 (2001).

100. Sato, H. *et al.* Baddeleyite-Type High-Pressure Phase of TiO2. *Science (80-.).* **251**, 786–788 (1991).

101. Tian, M. *et al.* Recent progress in characterization of the core–shell structure of black titania. *J. Mater. Res.* 1–16 (2019) doi:10.1557/jmr.2019.46.

102. Stoyanov, E., Langenhorst, F. & Steinle-Neumann, G. The effect of valence state and site geometry on Ti L 3, 2 and O K electron energy-loss spectra of TixOy phases. *Am. Mineral.* **92**, 577–586 (2007).

103. Bessekhouad, Y., Robert, D. & Weber, J. V. Synthesis of photocatalytic TiO2 nanoparticles: optimization of the preparation conditions. *J. Photochem. Photobiol. A Chem.* **157**, 47–53 (2003).

104. Oskam, G., Nellore, A., Penn, R. L. & Searson, P. C. The Growth Kinetics of TiO2 Nanoparticles from Titanium(IV) Alkoxide at High Water/Titanium Ratio. *J. Phys. Chem. B* **107**, 1734–1738 (2003).

105. Sugimoto, T. Preparation of monodispersed colloidal particles. *Adv. Colloid Interface Sci.* **28**, 65–108 (1987).

106. Anderson, M. A., Gieselmann, M. J. & Xu, Q. Titania and alumina ceramic membranes. *J. Memb. Sci.* **39**, 243–258 (1988).

107. Barringer, E. A. & Bowen, H. K. High-purity, monodisperse TiO2 powders by hydrolysis of titanium tetratethoxide. 2. Aqueous interfacial electrochemistry and

dispersion stability. *Langmuir* **1**, 420–428 (1985).

108. Kormann, C., Bahnemann, D. W. & Hoffmann, M. R. Preparation and characterization of quantum-size titanium dioxide. *J. Phys. Chem.* **92**, 5196–5201 (1988).

109. Sugimoto, T., Zhou, X. & Muramatsu, A. Synthesis of uniform anatase TiO2 nanoparticles by gel–sol method: 3. Formation process and size control. *J. Colloid Interface Sci.* **259**, 43–52 (2003).

110. Sugimoto, T., Zhou, X. & Muramatsu, A. Synthesis of uniform anatase TiO2 nanoparticles by gel–sol method: 4. Shape control. *J. Colloid Interface Sci.* **259**, 53–61 (2003).

111. Sugimoto, T., Zhou, X. & Muramatsu, A. Synthesis of Uniform Anatase TiO2 Nanoparticles by Gel–Sol Method: 1. Solution Chemistry of Ti(OH)n(4−n)+ Complexes. *J. Colloid Interface Sci.* **252**, 339–346 (2002).

112. Uekawa, N., Kajiwara, J., Kakegawa, K. & Sasaki, Y. Low Temperature Synthesis and Characterization of Porous Anatase TiO2 Nanoparticles. *J. Colloid Interface Sci.* **250**, 285–290 (2002).

113. Li, Y., White, T. J. & Lim, S. H. Low-temperature synthesis and microstructural control of titania nano-particles. *J. Solid State Chem.* **177**, 1372–1381 (2004).

114. Zhang, H. & Banfield, J. F. Understanding Polymorphic Phase Transformation Behavior during Growth of Nanocrystalline Aggregates: Insights from TiO2. *J. Phys. Chem. B* **104**, 3481–3487 (2000).

115. Zhang, H. & Banfield, J. F. Kinetics of Crystallization and Crystal Growth of Nanocrystalline Anatase in Nanometer-Sized Amorphous Titania. *Chem. Mater.* **14**, 4145–4154 (2002).

116. Zhang, H. & Banfield, J. F. Size Dependence of the Kinetic Rate Constant for Phase Transformation in TiO2 Nanoparticles. *Chem. Mater.* **17**, 3421–3425 (2005).

117. Zhang, H., Finnegan, M. & Banfield, J. F. Preparing Single-Phase Nanocrystalline Anatase from Amorphous Titania with Particle Sizes Tailored by Temperature. *Nano Lett.* **1**, 81–85 (2001).

118. Kim, K. Do & Kim, H. T. Synthesis of TiO2 nanoparticles by hydrolysis of TEOT and decrease of particle size using a two-stage mixed method. *Powder Technol.* **119**, 164–172 (2001).

119. Kim, K. Do & Kim, H. T. Synthesis of titanium dioxide nanoparticles using a continuous reaction method. *Colloids Surfaces A Physicochem. Eng. Asp.* **207**, 263–269 (2002).

120. Chen, Y., Crittenden, J. C., Hackney, S., Sutter, L. & Hand, D. W. Preparation of a Novel TiO2-Based p−n Junction Nanotube Photocatalyst. *Environ. Sci. Technol.* **39**, 1201–1208 (2005).

121. Lee, S., Jeon, C. & Park, Y. Fabrication of TiO2 Tubules by Template Synthesis and Hydrolysis with Water Vapor. *Chem. Mater.* **16**, 4292–4295 (2004).

122. Jung, J. H., Shimizu, T. & Shinkai, S. Self-assembling structures of steroidal derivatives in organic solvents and their sol–gel transcription into double-walled transition-metal oxide nanotubes. *J. Mater. Chem.* **15**, 3979–3986 (2005).

123. Yang, J., Mei, S. & Ferreira, J. M. F. Hydrothermal Fabrication of Rod-Like Rutile Nano-Particles. in *Advanced Materials Forum II* vol. 455 556–559 (Trans Tech Publications Ltd, 2004).

124. Yang, J., Mei, S. & Ferreira, J. M. F. In situ preparation of weakly flocculated aqueous anatase suspensions by a hydrothermal technique. *J. Colloid Interface Sci.* **260**, 82–88 (2003).

125. Chae, S. Y. *et al.* Preparation of Size-Controlled TiO2 Nanoparticles and Derivation of Optically Transparent Photocatalytic Films. *Chem. Mater.* **15**, 3326–3331 (2003).

126. Yang, J., Mei, S. & Ferreira, J. M. F. Hydrothermal synthesis of TiO2 nanopowders from tetraalkylammonium hydroxide peptized sols. *Mater. Sci. Eng. C* **15**, 183–185 (2001).

127. Yang, S. & Gao, L. Low-temperature Synthesis of Crystalline TiO2 Nanorods: Mass

Production Assisted by Surfactant. *Chem. Lett.* **34**, 964–965 (2005).

128. Zhang, Q. & Gao, L. Preparation of Oxide Nanocrystals with Tunable Morphologies by the Moderate Hydrothermal Method: Insights from Rutile TiO2. *Langmuir* **19**, 967–971 (2003).

129. Feng, X., Zhai, J. & Jiang, L. The Fabrication and Switchable Superhydrophobicity of TiO2 Nanorod Films. *Angew. Chemie Int. Ed.* **44**, 5115–5118 (2005).

130. Bavykin, D. V, Friedrich, J. M. & Walsh, F. C. Protonated Titanates and TiO2 Nanostructured Materials: Synthesis, Properties, and Applications. *Adv. Mater.* **18**, 2807–2824 (2006).

131. Miyauchi, M., Tokudome, H., Toda, Y., Kamiya, T. & Hosono, H. Electron field emission from TiO2 nanotube arrays synthesized by hydrothermal reaction. *Appl. Phys. Lett.* **89**, 43114 (2006).

132. Zhang, Y. X. *et al.* Hydrothermal synthesis and photoluminescence of TiO2 nanowires. *Chem. Phys. Lett.* **365**, 300–304 (2002).

133. Wei, M., Konishi, Y., Zhou, H., Sugihara, H. & Arakawa, H. A simple method to synthesize nanowires titanium dioxide from layered titanate particles. *Chem. Phys. Lett.* **400**, 231–234 (2004).

134. Kasuga, T., Hiramatsu, M., Hoson, A., Sekino, T. & Niihara, K. Formation of Titanium Oxide Nanotube. *Langmuir* **14**, 3160–3163 (1998).

135. Kasuga, T., Hiramatsu, M., Hoson, A., Sekino, T. & Niihara, K. Titania Nanotubes Prepared by Chemical Processing. *Adv. Mater.* **11**, 1307–1311 (1999).

136. Wen, B., Liu, C. & Liu, Y. Bamboo-Shaped Ag-Doped TiO2 Nanowires with Heterojunctions. *Inorg. Chem.* **44**, 6503–6505 (2005).

137. Yang, S. & Gao, L. Fabrication and shape-evolution of nanostructured TiO2 via a sol–solvothermal process based on benzene–water interfaces. *Mater. Chem. Phys.* **99**, 437–440 (2006).

138. Kim, C.-S., Moon, B. K., Park, J.-H., Tae Chung, S. & Son, S.-M. Synthesis of nanocrystalline TiO2 in toluene by a solvothermal route. *J. Cryst. Growth* **254**, 405–410 (2003).

139. Li, X.-L., Peng, Q., Yi, J.-X., Wang, X. & Li, Y. Near Monodisperse TiO2 Nanoparticles and Nanorods. *Chem. – A Eur. J.* **12**, 2383–2391 (2006).

140. Kim, C.-S., Moon, B. K., Park, J.-H., Choi, B.-C. & Seo, H.-J. Solvothermal synthesis of nanocrystalline TiO2 in toluene with surfactant. *J. Cryst. Growth* **257**, 309–315 (2003).

141. Wen, B.-M., Liu, C.-Y. & Liu, Y. Solvothermal synthesis of ultralong single-crystalline TiO2 nanowires. *New J. Chem.* **29**, 969–971 (2005).

142. Seifried, S., Winterer, M. & Hahn, H. Nanocrystalline Titania Films and Particles by Chemical Vapor Synthesis. *Chem. Vap. Depos.* **6**, 239–244 (2000).

143. Sung, J. *et al.* Preparation of ultrathin TiO2 coating on boron particles by thermal chemical vapor deposition and their oxidation-resistance performance. *J. Alloys Compd.* **767**, 924–931 (2018).

144. Alotaibi, A. M. *et al.* Chemical Vapor Deposition of Photocatalytically Active Pure Brookite TiO2 Thin Films. *Chem. Mater.* **30**, 1353–1361 (2018).

145. Nagasawa, H., Xu, J., Kanezashi, M. & Tsuru, T. Atmospheric-pressure plasma-enhanced chemical vapor deposition of UV-shielding TiO2 coatings on transparent plastics. *Mater. Lett.* **228**, 479–481 (2018).

146. Huang, W., Tang, X., Wang, Y., Koltypin, Y. & Gedanken, A. Selective synthesis of anatase and rutile via ultrasound irradiation. *Chem. Commun.* 1415–1416 (2000) doi:10.1039/B003349I.

147. Zhu, Y., Li, H., Koltypin, Y., Hacohen, Y. R. & Gedanken, A. Sonochemical synthesis of titania whiskers and nanotubes. *Chem. Commun.* 2616–2617 (2001) doi:10.1039/B108968B.

148. Yu, J. C., Yu, J., Ho, W. & Zhang, L. Preparation of highly photocatalytic active nano-sized TiO2 particles via ultrasonic irradiation. *Chem. Commun.* 1942–1943 (2001)

doi:10.1039/B105471F.

149. Yadav, H. M. *et al.* Preparation and characterization of copper-doped anatase TiO2 nanoparticles with visible light photocatalytic antibacterial activity. *J. Photochem. Photobiol. A Chem.* **280**, 32–38 (2014).

150. Marami, M. B., Farahmandjou, M. & Khoshnevisan, B. Sol-Gel Synthesis of Fe-Doped TiO2 Nanocrystals. *J. Electron. Mater.* **47**, 3741–3748 (2018).

151. Hassanjani-Roshan, A., Kazemzadeh, S. M., Vaezi, M. R. & Shokuhfar, A. Effect of sonication power on the sonochemical synthesis of titania nanoparticles. *J. Ceram. Process. Res.* **12**, 299–303 (2011).

152. Fujishima, A., Zhang, X. & Tryk, D. A. TiO2 photocatalysis and related surface phenomena. *Surf. Sci. Rep.* **63**, 515–582 (2008).

153. Fujishima, A., Rao, T. N. & Tryk, D. A. Titanium dioxide photocatalysis. *J. Photochem. Photobiol. C Photochem. Rev.* **1**, 1–21 (2000).

154. Ikeda, K., Sakai, H., Baba, R., Hashimoto, K. & Fujishima, A. Photocatalytic Reactions Involving Radical Chain Reactions Using Microelectrodes. *J. Phys. Chem. B* **101**, 2617–2620 (1997).

155. Kashif, N. & Ouyang, F. Parameters effect on heterogeneous photocatalysed degradation of phenol in aqueous dispersion of TiO2. *J. Environ. Sci.* **21**, 527–533 (2009).

156. lal S, D., T, S. J. & C, R. Solid-phase photodegradation of polystyrene by nano TiO2 under ultraviolet radiation. *Environ. Nanotechnology, Monit. Manag.* **12**, 100229 (2019).

157. Nakata, K. & Fujishima, A. TiO2 photocatalysis: Design and applications. *J. Photochem. Photobiol. C Photochem. Rev.* **13**, 169–189 (2012).

158. Liu, B. *et al.* Mesoporous TiO2 Core–Shell Spheres Composed of Nanocrystals with Exposed High-Energy Facets: Facile Synthesis and Formation Mechanism. *Langmuir* **27**, 8500–8508 (2011).

159. Yao, L. *et al.* Electrospinning and Stabilization of Fully Hydrolyzed Poly(Vinyl Alcohol) Fibers. *Chem. Mater.* **15**, 1860–1864 (2003).

160. Nakata, K. *et al.* Fabrication and Photocatalytic Properties of TiO2 Nanotube Arrays Modified with Phosphate. *Chem. Lett.* **40**, 1107–1109 (2011).

161. Lee, K. H., Kim, H. Y., Khil, M. S., Ra, Y. M. & Lee, D. R. Characterization of nano-structured poly(ε-caprolactone) nonwoven mats via electrospinning. *Polymer (Guildf).* **44**, 1287–1294 (2003).

162. Katsumata, K. *et al.* Preparation and Characterization of Self-Cleaning Glass for Vehicle with Niobia Nanosheets. *ACS Appl. Mater. Interfaces* **2**, 1236–1241 (2010).

163. Barakat, M. A. Adsorption and photodegradation of Procion yellow H-EXL dye in textile wastewater over TiO2 suspension. *J. Hydro-environment Res.* **5**, 137–142 (2011).

164. Zhang, T. *et al.* Photooxidative N-demethylation of methylene blue in aqueous TiO2 dispersions under UV irradiation. *J. Photochem. Photobiol. A Chem.* **140**, 163–172 (2001).

165. Gupta, V. K. *et al.* Photo-catalytic degradation of toxic dye amaranth on TiO2/UV in aqueous suspensions. *Mater. Sci. Eng. C* **32**, 12–17 (2012).

166. Faisal, M., Abu Tariq, M. & Muneer, M. Photocatalysed degradation of two selected dyes in UV-irradiated aqueous suspensions of titania. *Dye. Pigment.* **72**, 233–239 (2007).

167. Chen, J., Liu, M., Zhang, J., Ying, X. & Jin, L. Photocatalytic degradation of organic wastes by electrochemically assisted TiO2 photocatalytic system. *J. Environ. Manage.* **70**, 43–47 (2004).

168. Mahmoodi, N. M., Arami, M., Limaee, N. Y. & Tabrizi, N. S. Decolorization and aromatic ring degradation kinetics of Direct Red 80 by UV oxidation in the presence of hydrogen peroxide utilizing TiO2 as a photocatalyst. *Chem. Eng. J.* **112**, 191–196 (2005).

169. Tang, W. Z. & Huren An. UV/TiO2 photocatalytic oxidation of commercial dyes in aqueous solutions. *Chemosphere* **31**, 4157–4170 (1995).

170. Tang, C. & Chen, V. The photocatalytic degradation of reactive black 5 using TiO2/UV in an annular photoreactor. *Water Res.* **38**, 2775–2781 (2004).

171. Wu, C.-H. Effects of operational parameters on the decolorization of C.I. Reactive Red 198 in UV/TiO2-based systems. *Dye. Pigment.* **77**, 31–38 (2008).

172. Naeem, K. & Feng, O. Parameters e ff ect on heterogeneous photocatalysed degradation of phenol in aqueous dispersion of TiO 2. **21**, 527–533 (2009).

173. Liu, S., Jaffrezic, N. & Guillard, C. Size effects in liquid-phase photo-oxidation of phenol using nanometer-sized TiO2 catalysts. *Appl. Surf. Sci.* **255**, 2704–2709 (2008).

174. Górska, P. *et al.* TiO2 photoactivity in vis and UV light: The influence of calcination temperature and surface properties. *Appl. Catal. B Environ.* **84**, 440–447 (2008).

175. Ruppert, G., Bauer, R. & Heisler, G. UV-O3, UV-H2O2, UV-TiO2 and the photo-Fenton reaction - comparison of advanced oxidation processes for wastewater treatment. *Chemosphere* **28**, 1447–1454 (1994).

176. Shukla, S. S., Dorris, K. L. & Chikkaveeraiah, B. V. Photocatalytic degradation of 2,4-dinitrophenol. *J. Hazard. Mater.* **164**, 310–314 (2009).

177. Tsai, W.-T., Lee, M.-K., Su, T.-Y. & Chang, Y.-M. Photodegradation of bisphenol-A in a batch TiO2 suspension reactor. *J. Hazard. Mater.* **168**, 269–275 (2009).

178. Kaneco, S., Rahman, M. A., Suzuki, T., Katsumata, H. & Ohta, K. Optimization of solar photocatalytic degradation conditions of bisphenol A in water using titanium dioxide. *J. Photochem. Photobiol. A Chem.* **163**, 419–424 (2004).

179. Nakata, K. *et al.* Antireflection and Self-Cleaning Properties of a Moth-Eye-Like Surface Coated with TiO2 Particles. *Langmuir* **27**, 3275–3278 (2011).

180. Wang, R. *et al.* Light-induced amphiphilic surfaces. *Nature* **388**, 431–432 (1997).

181. Nakata, K. *et al.* Fabrication and Application of TiO2-Based Superhydrophilic–Superhydrophobic Patterns on Titanium Substrates for Offset Printing. *Chem. – An Asian J.* **4**, 984–988 (2009).

182. Nishimoto, S. *et al.* TiO2-based superhydrophobic–superhydrophilic patterns: Fabrication via an ink-jet technique and application in offset printing. *Appl. Surf. Sci.* **255**, 6221–6225 (2009).

183. Nakata, K. *et al.* Fabrication of micro-patterned TiO2 thin films incorporating Ag nanoparticles. *Mater. Lett.* **63**, 1628–1630 (2009).

184. Cho, S. & Choi, W. Solid-phase photocatalytic degradation of PVC–TiO2 polymer composites. *J. Photochem. Photobiol. A Chem.* **143**, 221–228 (2001).

185. Zhao, X., Li, Z., Chen, Y., Shi, L. & Zhu, Y. Enhancement of photocatalytic degradation of polyethylene plastic with CuPc modified TiO2 photocatalyst under solar light irradiation. *Appl. Surf. Sci.* **254**, 1825–1829 (2008).

186. Thomas, R. T., Nair, V. & Sandhyarani, N. TiO2 nanoparticle assisted solid phase photocatalytic degradation of polythene film: A mechanistic investigation. *Colloids Surfaces A Physicochem. Eng. Asp.* **422**, 1–9 (2013).

187. Shang, J., Chai, M. & Zhu, Y. Solid-phase photocatalytic degradation of polystyrene plastic with TiO2 as photocatalyst. *J. Solid State Chem.* **174**, 104–110 (2003).

188. Jaleh, B. *et al.* UV-degradation effect on optical and surface properties of polystyrene-TiO2 nanocomposite film. *J. Iran. Chem. Soc.* **8**, S161--S168 (2011).

189. Huang, F., Yan, A. & Zhao, H. Influences of doping on photocatalytic properties of TiO2 photocatalyst. *Semicond. Photocatal. Mech. Appl. Cao, W., Ed* 31–80 (2016).

190. Zaleska, A. Doped-TiO2: A Review. *Recent Patents Eng.* **2**, 156–164 (2008).

191. Tong, T., Zhang, J., Tian, B., Chen, F. & He, D. Preparation of Fe3+-doped TiO2 catalysts by controlled hydrolysis of titanium alkoxide and study on their photocatalytic activity for methyl orange degradation. *J. Hazard. Mater.* **155**, 572–579 (2008).

192. Xiao, J., Peng, T., Li, R., Peng, Z. & Yan, C. Preparation, phase transformation and photocatalytic activities of cerium-doped mesoporous titania nanoparticles. *J. Solid State Chem.* **179**, 1161–1170 (2006).

193. Asiltürk, M., Sayılkan, F. & Arpaç, E. Effect of Fe3+ ion doping to TiO2 on the photocatalytic degradation of Malachite Green dye under UV and vis-irradiation. *J. Photochem. Photobiol. A Chem.* **203**, 64–71 (2009).

194. Bettinelli, M. *et al.* Photocatalytic activity of TiO2 doped with boron and vanadium. *J. Hazard. Mater.* **146**, 529–534 (2007).

195. Adán, C., Carbajo, J., Bahamonde, A. & Martínez-Arias, A. Phenol photodegradation with oxygen and hydrogen peroxide over TiO2 and Fe-doped TiO2. *Catal. Today* **143**, 247–252 (2009).

196. Sakthivel, S. *et al.* Enhancement of photocatalytic activity by metal deposition: characterisation and photonic efficiency of Pt, Au and Pd deposited on TiO2 catalyst. *Water Res.* **38**, 3001–3008 (2004).

197. Kozlova, E. A. & Vorontsov, A. V. Influence of mesoporous and platinum-modified titanium dioxide preparation methods on photocatalytic activity in liquid and gas phase. *Appl. Catal. B Environ.* **77**, 35–45 (2007).

198. Sun, W., Zhang, S., Liu, Z., Wang, C. & Mao, Z. Studies on the enhanced photocatalytic hydrogen evolution over Pt/PEG-modified TiO2 photocatalysts. *Int. J. Hydrogen Energy* **33**, 1112–1117 (2008).

199. Huang, M. *et al.* Photocatalytic discolorization of methyl orange solution by Pt modified TiO2 loaded on natural zeolite. *Dye. Pigment.* **77**, 327–334 (2008).

200. Wang, C. *et al.* Preparation, characterization, photocatalytic properties of titania hollow sphere doped with cerium. *J. Hazard. Mater.* **178**, 517–521 (2010).

201. Bessekhouad, Y., Robert, D., Weber, J.-V. & Chaoui, N. Effect of alkaline-doped TiO2 on photocatalytic efficiency. *J. Photochem. Photobiol. A Chem.* **167**, 49–57 (2004).

202. Panagiotopoulou, P. & Kondarides, D. I. Effects of promotion of TiO2 with alkaline earth metals on the chemisorptive properties and water–gas shift activity of supported platinum catalysts. *Appl. Catal. B Environ.* **101**, 738–746 (2011).

203. Matsumoto, Y. Photoelectrochemical Properties of Polycrystalline TiO 2 Doped with 3d Transition Metals. *J. Electrochem. Soc.* **128**, 1040 (1981).

204. Song, K., Han, X. & Shao, G. Electronic properties of rutile TiO2 doped with 4d transition metals: First-principles study. *J. Alloys Compd.* **551**, 118–124 (2013).

205. Chen, W. *et al.* Electronic properties of anatase TiO2 doped by lanthanides: A DFT+U study. *Phys. B Condens. Matter* **407**, 1038–1043 (2012).

206. Barakat, M. A. & Kumar, R. Photocatalytic Activity Enhancement of Titanium Dioxide Nanoparticles. in *Photocatalytic Activity Enhancement of Titanium Dioxide Nanoparticles: Degradation of Pollutants in Wastewater* 1–29 (Springer International Publishing, 2016). doi:10.1007/978-3-319-24271-2_1.

207. Moma, J. & Baloyi, J. Modified titanium dioxide for photocatalytic applications. in *Photocatalysts-Applications and Attributes* (IntechOpen, 2018). doi:http://dx.doi.org/10.5772/intechopen.79374.

208. Inturi, S. N. R., Boningari, T., Suidan, M. & Smirniotis, P. G. Visible-light-induced photodegradation of gas phase acetonitrile using aerosol-made transition metal (V, Cr, Fe, Co, Mn, Mo, Ni, Cu, Y, Ce, and Zr) doped TiO2. *Appl. Catal. B Environ.* **144**, 333–342 (2014).

209. Wang, Y. *et al.* The Effects of Doping Copper and Mesoporous Structure on Photocatalytic Properties of TiO$_2$. *J. Nanomater.* **2014**, 178152 (2014).

210. Lin, J. C.-T., Sopajaree, K., Jitjanesuwan, T. & Lu, M.-C. Application of visible light on copper-doped titanium dioxide catalyzing degradation of chlorophenols. *Sep. Purif. Technol.* **191**, 233–243 (2018).

211. Garcidueñas-Piña, C. *et al.* Evaluation of the Antimicrobial Activity of Nanostructured Materials of Titanium Dioxide Doped with Silver and/or Copper and Their Effects on *Arabidopsis thaliana*. *Int. J. Photoenergy* **2016**, 8060847 (2016).

212. Kavitha, V., Ramesh, P. S. & Geetha, D. Synthesis of Cu Loaded TiO2 Nanoparticles for the Improved Photocatalytic Degradation of Rhodamine B. *Int. J. Nanosci.* **15**, 1660002 (2016).

213. Sahoo, C., Gupta, A. K. & Pal, A. Photocatalytic degradation of Crystal Violet (C.I. Basic Violet 3) on silver ion doped TiO2. *Dye. Pigment.* **66**, 189–196 (2005).

214. Sobana, N., Muruganadham, M. & Swaminathan, M. Nano-Ag particles doped TiO2 for efficient photodegradation of Direct azo dyes. *J. Mol. Catal. A Chem.* **258**, 124–132 (2006).

215. Sobana, N., Selvam, K. & Swaminathan, M. Optimization of photocatalytic degradation conditions of Direct Red 23 using nano-Ag doped TiO2. *Sep. Purif. Technol.* **62**, 648–653 (2008).

216. Sung-Suh, H. M., Choi, J. R., Hah, H. J., Koo, S. M. & Bae, Y. C. Comparison of Ag deposition effects on the photocatalytic activity of nanoparticulate TiO2 under visible and UV light irradiation. *J. Photochem. Photobiol. A Chem.* **163**, 37–44 (2004).

217. Behnajady, M. A., Modirshahla, N., Shokri, M. & Rad, B. Enhancement of photocatalytic activity of TiO2 nanoparticles by silver doping: photodeposition versus liquid impregnation methods. (2008).

218. Ambrus, Z. *et al.* Synthesis, structure and photocatalytic properties of Fe(III)-doped TiO2 prepared from TiCl3. *Appl. Catal. B Environ.* **81**, 27–37 (2008).

219. Mogal, S. I. *et al.* Single-Step Synthesis of Silver-Doped Titanium Dioxide : In fl uence of Silver on Structural , Textural , and Photocatalytic Properties. *Ind. Eng. Chem. Res.* **53**, 5749−5758 (2014).

220. Chiang, K., Amal, R. & Tran, T. Photocatalytic degradation of cyanide using titanium dioxide modified with copper oxide. *Adv. Environ. Res.* **6**, 471–485 (2002).

221. Wang, S., Meng, K. K., Zhao, L., Jiang, Q. & Lian, J. S. Superhydrophilic Cu-doped TiO2 thin film for solar-driven photocatalysis. *Ceram. Int.* **40**, 5107–5110 (2014).

222. Zhang, F.-S., Nriagu, J. O. & Itoh, H. Photocatalytic removal and recovery of mercury from water using TiO2-modified sewage sludge carbon. *J. Photochem. Photobiol. A Chem.* **167**, 223–228 (2004).

223. Wang, W., Silva, C. G. & Faria, J. L. Photocatalytic degradation of Chromotrope 2R using nanocrystalline TiO2/activated-carbon composite catalysts. *Appl. Catal. B Environ.* **70**, 470–478 (2007).

224. Woan, K., Pyrgiotakis, G. & Sigmund, W. Photocatalytic Carbon-Nanotube–TiO2 Composites. *Adv. Mater.* **21**, 2233–2239 (2009).

225. Yu, J., Ma, T. & Liu, S. Enhanced photocatalytic activity of mesoporous TiO2 aggregates by embedding carbon nanotubes as electron-transfer channel. *Phys. Chem. Chem. Phys.* **13**, 3491–3501 (2011).

226. Meng, Z.-D., Zhu, L., Choi, J.-G., Chen, M.-L. & Oh, W.-C. Effect of Pt treated fullerene/TiO2 on the photocatalytic degradation of MO under visible light. *J. Mater. Chem.* **21**, 7596–7603 (2011).

227. Liang, Y., Wang, H., Sanchez Casalongue, H., Chen, Z. & Dai, H. TiO2 nanocrystals grown on graphene as advanced photocatalytic hybrid materials. *Nano Res.* **3**, 701–705 (2010).

228. Liu, H. *et al.* A green and direct synthesis of graphene oxide encapsulated TiO2 core/shell structures with enhanced photoactivity. *Chem. Eng. J.* **230**, 279–285 (2013).

229. Bamba, D. *et al.* Synthesis and characterization of TiO2/C nanomaterials: Applications in water treatment. *Phys. status solidi* **252**, 2503–2511 (2015).

230. Chen, J., Qiu, F., Xu, W., Cao, S. & Zhu, H. Recent progress in enhancing photocatalytic efficiency of TiO2-based materials. *Appl. Catal. A Gen.* **495**, 131–140 (2015).

231. Nouri, E., Mohammadi, M. R. & Lianos, P. Impact of preparation method of TiO2-RGO nanocomposite photoanodes on the performance of dye-sensitized solar cells. *Electrochim. Acta* **219**, 38–48 (2016).

232. Perera, S. D. *et al.* Hydrothermal Synthesis of Graphene-TiO2 Nanotube Composites with Enhanced Photocatalytic Activity. *ACS Catal.* **2**, 949–956 (2012).

233. Kamat, P. V. Graphene-Based Nanoassemblies for Energy Conversion. *J. Phys. Chem. Lett.* **2**, 242–251 (2011).

234. Naknikham, U. *et al.* Mutual-stabilization in chemically bonded graphene oxide–TiO2 heterostructures synthesized by a sol–gel approach. *RSC Adv.* **7**, 41217–41227 (2017).

235. Zhang, H., Lv, X., Li, Y., Wang, Y. & Li, J. P25-graphene composite as a high performance photocatalyst. *ACS Nano* **4**, 380–386 (2009).

236. Khannam, M., Sharma, S., Dolui, S. & Dolui, S. K. A graphene oxide incorporated TiO2 photoanode for high efficiency quasi solid state dye sensitized solar cells based on a poly-vinyl alcohol gel electrolyte. *RSC Adv.* **6**, 55406–55414 (2016).

237. Shi, J. On the Synergetic Catalytic Effect in Heterogeneous Nanocomposite Catalysts. *Chem. Rev.* **113**, 2139–2181 (2013).

238. Li, Y., Li, X., Li, J. & Yin, J. Photocatalytic degradation of methyl orange by TiO2-coated activated carbon and kinetic study. *Water Res.* **40**, 1119–1126 (2006).

239. Mo, D. & Ye, D. Surface study of composite photocatalyst based on plasma modified activated carbon fibers with TiO2. *Surf. Coatings Technol.* **203**, 1154–1160 (2009).

240. Slimen, H., Houas, A. & Nogier, J. P. Elaboration of stable anatase TiO2 through activated carbon addition with high photocatalytic activity under visible light. *J. Photochem. Photobiol. A Chem.* **221**, 13–21 (2011).

241. Orha, C., Pode, R., Manea, F., Lazau, C. & Bandas, C. Titanium dioxide-modified activated carbon for advanced drinking water treatment. *Process Saf. Environ. Prot.* **108**, 26–33 (2017).

242. Wang, W., Serp, P., Kalck, P., Silva, C. G. & Faria, J. L. Preparation and characterization of nanostructured MWCNT-TiO2 composite materials for photocatalytic water treatment applications. *Mater. Res. Bull.* **43**, 958–967 (2008).

243. Lee, K.-Y., Yeoh, W.-M., Chai, S.-P., Ichikawa, S. & Mohamed, A. R. Optimization of Carbon Nanotubes Synthesis via Methane Decomposition over Alumina-Based Catalyst. *Fullerenes, Nanotub. Carbon Nanostructures* **18**, 273–284 (2010).

244. Yen, C.-Y. *et al.* The effects of synthesis procedures on the morphology and photocatalytic activity of multi-walled carbon nanotubes/TiO2 nanocomposites. *Nanotechnology* **19**, 45604 (2008).

245. Gao, B., Chen, G. Z. & Li Puma, G. Carbon nanotubes/titanium dioxide (CNTs/TiO2) nanocomposites prepared by conventional and novel surfactant wrapping sol–gel methods exhibiting enhanced photocatalytic activity. *Appl. Catal. B Environ.* **89**, 503–509 (2009).

246. Ashkarran, A. A., Fakhari, M., Hamidinezhad, H., Haddadi, H. & Nourani, M. R. TiO2 nanoparticles immobilized on carbon nanotubes for enhanced visible-light photo-induced activity. *J. Mater. Res. Technol.* **4**, 126–132 (2015).

247. Wongaree, M., Chiarakorn, S., Chuangchote, S. & Sagawa, T. Photocatalytic performance of electrospun CNT/TiO2 nanofibers in a simulated air purifier under visible light irradiation. *Environ. Sci. Pollut. Res.* **23**, 21395–21406 (2016).

248. Ahmad, A., Razali, M. H., Mamat, M., Mehamod, F. S. B. & Anuar Mat Amin, K. Adsorption of methyl orange by synthesized and functionalized-CNTs with 3-aminopropyltriethoxysilane loaded TiO2 nanocomposites. *Chemosphere* **168**, 474–482 (2017).

249. Scuseria, G. E. The equilibrium structure of C70. An ab initio Hartree-Fock study. *Chem. Phys. Lett.* **180**, 451–456 (1991).

250. Wang, X. *et al.* Enhanced Photocurrent Spectral Response in Low-Bandgap Polyfluorene and C70-Derivative-Based Solar Cells. *Adv. Funct. Mater.* **15**, 1665–1670 (2005).

251. He, Y. *et al.* High performance low band gap polymer solar cells with a non-conventional acceptor. *Chem. Commun.* **48**, 7616–7618 (2012).

252. Zhu, S., Xu, T., Fu, H., Zhao, J. & Zhu, Y. Synergetic Effect of Bi2WO6 Photocatalyst with C60 and Enhanced Photoactivity under Visible Irradiation. *Environ. Sci. Technol.* **41**, 6234–6239 (2007).

253. Hasobe, T., Hattori, S., Kamat, P. V & Fukuzumi, S. Supramolecular nanostructured assemblies of different types of porphyrins with fullerene using TiO2 nanoparticles for

light energy conversion. *Tetrahedron* **62**, 1937–1946 (2006).

254. Kamat, P. V, Haria, M. & Hotchandani, S. C60 Cluster as an Electron Shuttle in a Ru(II)-Polypyridyl Sensitizer-Based Photochemical Solar Cell. *J. Phys. Chem. B* **108**, 5166–5170 (2004).

255. Sibley, S. P., Argentine, S. M. & Francis, A. H. A photoluminescence study of C60 and C70. *Chem. Phys. Lett.* **188**, 187–193 (1992).

256. Lin, J., Zong, R., Zhou, M. & Zhu, Y. Photoelectric catalytic degradation of methylene blue by C60-modified TiO2 nanotube array. *Appl. Catal. B Environ.* **89**, 425–431 (2009).

257. Mu, S., Long, Y., Kang, S.-Z. & Mu, J. Surface modification of TiO2 nanoparticles with a C60 derivative and enhanced photocatalytic activity for the reduction of aqueous Cr(VI) ions. *Catal. Commun.* **11**, 741–744 (2010).

258. Long, Y. *et al.* Effect of C60 on the Photocatalytic Activity of TiO2 Nanorods. *J. Phys. Chem. C* **113**, 13899–13905 (2009).

259. Krishna, V., Noguchi, N., Koopman, B. & Moudgil, B. Enhancement of titanium dioxide photocatalysis by water-soluble fullerenes. *J. Colloid Interface Sci.* **304**, 166–171 (2006).

260. Zhang, X., Wang, Q., Zou, L.-H. & You, J.-W. Facile fabrication of titanium dioxide/fullerene nanocomposite and its enhanced visible photocatalytic activity. *J. Colloid Interface Sci.* **466**, 56–61 (2016).

261. Yu, J., Ma, T., Liu, G. & Cheng, B. Enhanced photocatalytic activity of bimodal mesoporous titania powders by C60 modification. *Dalt. Trans.* **40**, 6635–6644 (2011).

262. Qi, K. *et al.* Enhanced photocatalytic activity of anatase-TiO2 nanoparticles by fullerene modification: A theoretical and experimental study. *Appl. Surf. Sci.* **387**, 750–758 (2016).

263. Cho, E.-C. *et al.* Fullerene C70 decorated TiO2 nanowires for visible-light-responsive photocatalyst. *Appl. Surf. Sci.* **355**, 536–546 (2015).

264. Marcano, D. C. *et al.* Improved Synthesis of Graphene Oxide. *ACS Nano* **4**, 4806–4814 (2010).

265. Novoselov, K. S. *et al.* Two-dimensional gas of massless Dirac fermions in graphene. *Nature* **438**, 197–200 (2005).

266. Novoselov, K. S. *et al.* Electric Field Effect in Atomically Thin Carbon Films. *Science (80-.).* **306**, 666–669 (2004).

267. Lee, C., Wei, X., Kysar, J. W. & Hone, J. Measurement of the elastic properties and intrinsic strength of monolayer graphene. *Science (80-.).* **321**, 385–388 (2008).

268. Mohanty, N. & Berry, V. Graphene-Based Single-Bacterium Resolution Biodevice and DNA Transistor: Interfacing Graphene Derivatives with Nanoscale and Microscale Biocomponents. *Nano Lett.* **8**, 4469–4476 (2008).

269. Geim, A. K. & Novoselov, K. S. The rise of graphene. *Nat. Mater.* **6**, 183–191 (2007).

270. Balandin, A. A. *et al.* Superior Thermal Conductivity of Single-Layer Graphene. *Nano Lett.* **8**, 902–907 (2008).

271. Zhang, Y., Tang, Z.-R., Fu, X. & Xu, Y.-J. Engineering the Unique 2D Mat of Graphene to Achieve Graphene-TiO2 Nanocomposite for Photocatalytic Selective Transformation: What Advantage does Graphene Have over Its Forebear Carbon Nanotube? *ACS Nano* **5**, 7426–7435 (2011).

272. Stankovich, S. *et al.* Graphene-based composite materials. *Nature* **442**, 282–286 (2006).

273. Liu, Z., Robinson, J. T., Sun, X. & Dai, H. PEGylated Nanographene Oxide for Delivery of Water-Insoluble Cancer Drugs. *J. Am. Chem. Soc.* **130**, 10876–10877 (2008).

274. Wang, X., Zhi, L. & Müllen, K. Transparent, Conductive Graphene Electrodes for Dye-Sensitized Solar Cells. *Nano Lett.* **8**, 323–327 (2008).

275. Novoselov, K. S. *et al.* Room-Temperature Quantum Hall Effect in Graphene. *Science (80-.).* **315**, 1379 (2007).

276. Robinson, J. T., Perkins, F. K., Snow, E. S., Wei, Z. & Sheehan, P. E. Reduced

graphene oxide molecular sensors. *Nano Lett.* **8**, 3137–3140 (2008).

277. Blake, P. *et al.* Graphene-Based Liquid Crystal Device. *Nano Lett.* **8**, 1704–1708 (2008).

278. Abanin, D. A. *et al.* Dissipative Quantum Hall Effect in Graphene near the Dirac Point. *Phys. Rev. Lett.* **98**, 196806 (2007).

279. Stoller, M. D., Park, S., Zhu, Y., An, J. & Ruoff, R. S. Graphene-based ultracapacitors. *Nano Lett.* **8**, 3498–3502 (2008).

280. Wehling, T. O. *et al.* Molecular Doping of Graphene. *Nano Lett.* **8**, 173–177 (2008).

281. Sundaram, R. S., Gómez-Navarro, C., Balasubramanian, K., Burghard, M. & Kern, K. Electrochemical Modification of Graphene. *Adv. Mater.* **20**, 3050–3053 (2008).

282. Park, S. & Ruoff, R. S. Chemical methods for the production of graphenes. *Nat. Nanotechnol.* **4**, 217–224 (2009).

283. He, H., Riedl, T., Lerf, A. & Klinowski, J. Solid-State NMR Studies of the Structure of Graphite Oxide. *J. Phys. Chem.* **100**, 19954–19958 (1996).

284. He, H., Klinowski, J., Forster, M. & Lerf, A. A new structural model for graphite oxide. *Chem. Phys. Lett.* **287**, 53–56 (1998).

285. Lerf, A., He, H., Forster, M. & Klinowski, J. Structure of Graphite Oxide Revisited. *J. Phys. Chem. B* **102**, 4477–4482 (1998).

286. Cai, W. *et al.* Synthesis and Solid-State NMR Structural Characterization of 13C-Labeled Graphite Oxide. *Science (80-.).* **321**, 1815–1817 (2008).

287. Dreyer, D. R., Park, S., Bielawski, C. W. & Ruoff, R. S. The chemistry of graphene oxide. *Chem. Soc. Rev.* **39**, 228–240 (2010).

288. Kamat, P. V. Graphene-Based Nanoarchitectures. Anchoring Semiconductor and Metal Nanoparticles on a Two-Dimensional Carbon Support. 520–527 (2010) doi:10.1021/jz900265j.

289. Williams, G., Seger, B. & Kamat, P. V. TiO2-Graphene Nanocomposites. UV-Assisted Photocatalytic Reduction of Graphene Oxide. *ACS Nano* **2**, 1487–1491 (2008).

290. Hummers, W. S. & Offeman, R. E. Preparation of Graphitic Oxide. *J. Am. Chem. Soc.* **80**, 1339 (1958).

291. Kang, J. H. *et al.* Hidden Second Oxidation Step of Hummers Method. *Chem. Mater.* **28**, 756–764 (2016).

292. Huang, Q. *et al.* Enhanced Photocatalytic Activity of Chemically Bonded TiO2/Graphene Composites Based on the Effective Interfacial Charge Transfer through the C–Ti Bond. *ACS Catal.* **3**, 1477–1485 (2013).

293. Umrao, S. *et al.* A possible mechanism for the emergence of an additional band gap due to a Ti–O–C bond in the TiO2–graphene hybrid system for enhanced photodegradation of methylene blue under visible light. *RSC Adv.* **4**, 59890–59901 (2014).

294. Rakkesh, R. A., Durgalakshmi, D. & Balakumar, S. Efficient sunlight-driven photocatalytic activity of chemically bonded GNS–TiO2 and GNS–ZnO heterostructures. *J. Mater. Chem. C* **2**, 6827–6834 (2014).

295. He, D., Li, Y., Wang, J., Yang, Y. & An, and Q. Tunable Nanostructure of TiO2/Reduced Graphene Oxide Composite for High Photocatalysis. *Appl. Microsc.* **46**, 37–44 (2016).

296. Singh, S., Mahalingam, H. & Singh, P. K. Polymer-supported titanium dioxide photocatalysts for environmental remediation: A review. *Appl. Catal. A Gen.* **462–463**, 178–195 (2013).

297. Tennakone, K., Tilakaratne, C. T. K. & Kottegoda, I. R. M. Photocatalytic degradation of organic contaminants in water with TiO2 supported on polythene films. *J. Photochem. Photobiol. A Chem.* **87**, 177–179 (1995).

298. Raghava, K., Karthik, K. V, Prasad, S. B. B., Soni, S. K. & Jeong, H. M. Enhanced photocatalytic activity of nanostructured titanium dioxide / polyaniline hybrid photocatalysts Enhanced photocatalytic activity of nanostructured titanium dioxide / polyaniline hybrid photocatalysts. *Polyhedron* **120**, 169–174 (2016).

299. Ansari, M. O., Khan, M. M., Ansari, S. A. & Cho, M. H. Polythiophene

nanocomposites for photodegradation applications: Past, present and future. *J. Saudi Chem. Soc.* **19**, 494–504 (2015).

300. Abdiryim, T., Ali, A., Jamal, R., Osman, Y. & Zhang, Y. A facile solid-state heating method for preparation of poly(3,4-ethelenedioxythiophene)/ZnO nanocomposite and photocatalytic activity. *Nanoscale Res. Lett.* **9**, 89 (2014).

301. Duan, Y. *et al.* An efficient visible light photocatalyst poly(3-hexylthiophene)/CdS nanocomposite with enhanced antiphotocorrosion property. *Superlattices Microstruct.* **67**, 61–71 (2014).

302. Dimitrijevic, N. M. *et al.* Nanostructured TiO2/Polypyrrole for Visible Light Photocatalysis. *J. Phys. Chem. C* **117**, 15540–15544 (2013).

303. Qiu, R. *et al.* Photocatalytic activity of polymer-modified ZnO under visible light irradiation. *J. Hazard. Mater.* **156**, 80–85 (2008).

304. Su, Y.-W., Lin, W.-H., Hsu, Y.-J. & Wei, K.-H. Conjugated Polymer/Nanocrystal Nanocomposites for Renewable Energy Applications in Photovoltaics and Photocatalysis. *Small* **10**, 4427–4442 (2014).

305. Wang, F. & Min, S. X. TiO2/polyaniline composites: An efficient photocatalyst for the degradation of methylene blue under natural light. *Chinese Chem. Lett.* **18**, 1273–1277 (2007).

306. Zhang, H., Zong, R., Zhao, J. & Zhu, Y. Dramatic Visible Photocatalytic Degradation Performances Due to Synergetic Effect of TiO2 with PANI. *Environ. Sci. Technol.* **42**, 3803–3807 (2008).

307. Zhang, H., Zong, R. & Zhu, Y. Photocorrosion Inhibition and Photoactivity Enhancement for Zinc Oxide via Hybridization with Monolayer Polyaniline. *J. Phys. Chem.* **113**, 4605–4611 (2009).

308. Ganesan, R. & Gedanken, A. Organic-organic hybrid materials based on polyaniline/TiO2 nanocomposites for ascorbic acid fuel cell systems. *Nanotechnology* **19**, 435709 (2008).

309. Min, S., Wang, F. & Han, Y. An investigation on synthesis and photocatalytic activity of polyaniline sensitized nanocrystalline TiO2 composites. *J. Mater. Sci.* **42**, 9966–9972 (2007).

310. Wang, F., Min, S., Han, Y. & Feng, L. Visible-light-induced photocatalytic degradation of methylene blue with polyaniline-sensitized TiO2 composite photocatalysts. *Superlattices Microstruct.* **48**, 170–180 (2010).

311. Olad, A. li, Behboudi, S. & Entezami, A. li A. Preparation, characterization and photocatalytic activity of TiO2/polyaniline core-shell nanocomposite. *Bull. Mater. Sci.* **35**, 801–809 (2012).

312. Gilja, V. *et al.* Stability and synergistic effect of polyaniline/TiO2 photocatalysts in degradation of azo dye in wastewater. *Nanomaterials* **7**, 412 (2017).

313. Zhao, J., Wu, W., Sun, J. & Guo, S. Triplet photosensitizers: from molecular design to applications. *Chem. Soc. Rev.* **42**, 5323–5351 (2013).

314. Zhao, J. *et al.* Transition metal complexes with strong absorption of visible light and long-lived triplet excited states: from molecular design to applications. *RSC Adv.* **2**, 1712–1728 (2012).

315. Goldsmith, J. I., Hudson, W. R., Lowry, M. S., Anderson, T. H. & Bernhard, S. Discovery and High-Throughput Screening of Heteroleptic Iridium Complexes for Photoinduced Hydrogen Production. *J. Am. Chem. Soc.* **127**, 7502–7510 (2005).

316. Schäferling, M. The Art of Fluorescence Imaging with Chemical Sensors. *Angew. Chemie Int. Ed.* **51**, 3532–3554 (2012).

317. Fischer, L. H. *et al.* Referenced Dual Pressure- and Temperature-Sensitive Paint for Digital Color Camera Read Out. *Chem. – A Eur. J.* **18**, 15706–15713 (2012).

318. Tucker, J. W. & Stephenson, C. R. J. Shining Light on Photoredox Catalysis: Theory and Synthetic Applications. *J. Org. Chem.* **77**, 1617–1622 (2012).

319. Zou, Y.-Q. *et al.* Highly Efficient Aerobic Oxidative Hydroxylation of Arylboronic Acids: Photoredox Catalysis Using Visible Light. *Angew. Chemie Int. Ed.* **51**, 784–788

(2012).

320. Manangan, T., Shawaphun, S. & Wacharawichanant, S. Acetophenone and Benzophenone Derivatives as Catalysts in Photodegradation of PE and PP Films. in *Functionalized and Sensing Materials* vol. 93 284–287 (Trans Tech Publications Ltd, 2010).

321. Yousif, E., Salimon, J. & Salih, N. New stabilizers for polystyrene based on 2-N-salicylidene-5-(substituted)-1,3,4-thiadiazole compounds. *J. Saudi Chem. Soc.* **16**, 299–306 (2012).

322. Pinto, L. F. A., Goi, B. E., Schmitt, C. C. & Neumann, M. G. Photodegradation of polystyrene films containing UV-visible sensitizers. *J. Res. Updat. Polym. Sci.* **2**, 39–47 (2013).

323. Ong, C. B., Ng, L. Y. & Mohammad, A. W. A review of ZnO nanoparticles as solar photocatalysts: Synthesis, mechanisms and applications. *Renew. Sustain. Energy Rev.* **81**, 536–551 (2018).

324. Sharma, B. K., Gupta, A. K., Khare, N., Dhawan, S. K. & Gupta, H. C. Synthesis and characterization of polyaniline – ZnO composite and its dielectric behavior. **159**, 391–395 (2009).

325. Ameen, S., Akhtar, M. S. & Kim, Y. S. An effective nanocomposite of polyaniline and ZnO : preparation , characterizations , and its photocatalytic activity. *Colloid Polym Sci* **289**, 415–421 (2011).

326. Daikh, S., Zeggai, F. Z., Bellil, A. & Benyoucef, A. Chemical polymerization, characterization and electrochemical studies of PANI/ZnO doped with hydrochloric acid and/or zinc chloride: Differences between the synthesized nanocomposites. *J. Phys. Chem. Solids* **121**, 78–84 (2018).

327. Khan, A. A. & Khalid, M. Synthesis of Nano-Sized ZnO and Polyaniline-Zinc Oxide Composite : Characterization , Stability in Terms of DC Electrical Conductivity Retention and Application in Ammonia Vapor Detection. (2010) doi:10.1002/app.

328. Patil, S. L. *et al.* Structural, Morphological, Optical, and Electrical Properties of PANi-ZnO Nanocomposites. *Int. J. Polym. Mater. Polym. Biomater.* **61**, 809–820 (2012).

329. Gilja, V., Vrban, I., Mandić, V., Žic, M. & Hrnjak-Murgić, Z. Preparation of a PANI/ZnO composite for efficient photocatalytic degradation of acid blue. *Polymers (Basel).* **10**, 940 (2018).

330. Kumar, S. G. & Rao, K. S. R. K. Comparison of modification strategies towards enhanced charge carrier separation and photocatalytic degradation activity of metal oxide semiconductors (TiO2, WO3 and ZnO). *Appl. Surf. Sci.* **31517**–**3**, S0169-4332 (2016).

331. Chen, C. *et al.* Effect of Transition Metal Ions on the TiO2-Assisted Photodegradation of Dyes under Visible Irradiation: A Probe for the Interfacial Electron Transfer Process and Reaction Mechanism. *J. Phys. Chem. B* **106**, 318–324 (2002).

332. Sun, Q. & Xu, Y. Sensitization of TiO2 with Aluminum Phthalocyanine: Factors Influencing the Efficiency for Chlorophenol Degradation in Water under Visible Light. *J. Phys. Chem. C* **113**, 12387–12394 (2009).

333. Olad, A. & Nosrati, R. Preparation, characterization, and photocatalytic activity of polyaniline/ZnO nanocomposite. *Res Chem Intermed* **38**, 323–336 (2012).

334. Girish Kumar, S. & Koteswara Rao, K. S. R. Tungsten-based nanomaterials (WO3 & Bi2WO6): Modifications related to charge carrier transfer mechanisms and photocatalytic applications. *Appl. Surf. Sci.* **355**, 939–958 (2015).

335. Rajbongshi, B. M. & Samdarshi, S. K. Cobalt-doped zincblende–wurtzite mixed-phase ZnO photocatalyst nanoparticles with high activity in visible spectrum. *Appl. Catal. B Environ.* **144**, 435–441 (2014).

336. Denisyuk, I. Y., Pozdnyakova, S. A., Koryakina, I. G., Uspenskaya, M. V & Volkova, K. V. Polymer photodegradation initiated by ZnO nanoparticles. *Opt. Spectrosc.* **121**, 778–781 (2016).

337. Suryavanshi, R. D. *et al.* Nanocrystalline immobilised ZnO photocatalyst for

degradation of benzoic acid and methyl blue dye. *Mater. Res. Bull.* **101**, 324–333 (2018).

338. Zhang, Q. *et al.* Oxygen vacancy-mediated ZnO nanoparticle photocatalyst for degradation of methylene blue. *Appl. Sci.* **8**, 353 (2018).

339. Ngaloy, R. T. *et al.* Highly Efficient Photocatalysis by Zinc Oxide-Reduced Graphene Oxide (ZnO-rGO) Composite Synthesized via One-Pot Room-Temperature Chemical Deposition Method. *J. Nanotechnol.* **2019**, 1895043 (2019).

340. Asgari, E. *et al.* The comparison of ZnO/polyaniline nanocomposite under UV and visible radiations for decomposition of metronidazole: Degradation rate, mechanism and mineralization. *Process Saf. Environ. Prot.* **128**, 65–76 (2019).

341. Qi, K. *et al.* Transition metal doped ZnO nanoparticles with enhanced photocatalytic and antibacterial performances: Experimental and DFT studies. *Ceram. Int.* **46**, 1494–1502 (2020).

342. Ismael, M. The photocatalytic performance of the ZnO/g-C3N4 composite photocatalyst toward degradation of organic pollutants and its inactivity toward hydrogen evolution: The influence of light irradiation and charge transfer. *Chem. Phys. Lett.* **739**, 136992 (2020).

343. Neelgund, G. M. & Oki, A. ZnO conjugated graphene: An efficient sunlight driven photocatalyst for degradation of organic dyes. *Mater. Res. Bull.* **129**, 110911 (2020).

Chapter 2

Materials and Methods

2.1 Materials

The following chemicals were used for the preparation of various photocatalysts.

Chemicals	Manufacturer
• Titanium(IV)isopropoxide	: Sigma Aldrich
• Zinc nitrate hexahydrate ($Zn(NO_3)_2.6H_2O$)	: Sigma Aldrich
• Aniline	: Merk, India
• Ammonium peroxodisulphate	: Merk, India
• Graphite (150 mesh)	: Merk, India
• Sodium nitrate ($NaNO_3$)	: Merk, India
• Hydrogen peroxide (H_2O_2) (30% W/V)	: Merk, India
• Potassium permanganate ($KMnO_4$)	: Merk, India
• Silver nitrate ($AgNO_3$)	: Sigma Aldrich
• Iron (III) nitrate nonahydrate ($Fe(NO_3)_3.9H_2O$)	: Sigma Aldrich
• Copper sulphate pentahydrate ($CuSO_4.5H_2O$)	: Sigma Aldrich
• Benzophenone	: TCI chemicals, India
• 2-hydroxy-4-methoxybenzophenone	: TCI chemicals, India
• 4-methoxybenzophenone	: TCI chemicals, India
• 2-chlorobenzophenone	: TCI chemicals, India
• 4-nitrobenzophenone	: TCI chemicals, India
• Malachite green	: TCI chemicals, India
• Methyl blue	: TCI chemicals, India
• Sulphuric acid	: Merk, India
• Hydrochloric acid	: Merk, India
• Nitric acid	: Merk, India
• Ammonium hydroxide	: Merk, India

All the above chemicals were used directly without further purifications for the photocatalyst preparation. Ethanol was distilled in the presence of magnesium ribbon and iodine solution in order to remove the water content.

Detailed Methods of preparation of various photocatalysts are described in the corresponding chapters (chapters 3-7)

PS specimens for photodegradation studies were prepared using the following chemicals.

Chemicals	Manufacturer
• Polystyrene beads	: LG Polymer India Pvt. Ltd
• Toluene	: Merk,India

UV tube (253 nm. 30 W, Phillips Holland) fit inside a wooden chamber (96 cm x 26cm x 34cm) was used as UV light source for the photodegradation studies.

2.2 Preparation of PS and PS-photocatalyst composite sheets

2.2.1 Preparation of PS sheets

PS sheets were prepared through the method of solvent casting. Typically 5g of PS beads were dissolved in 20 ml toluene and the resulting viscous solution was homogenized using ultrasonic probe sonicator (750 W) for 30 minutes. The solution was immediately poured into petri dishes of uniform dimensions and kept overnight in a vacuum oven. The obtained PS sheets were allowed to dry at room temperature for seven days. The PS sheets hence obtained were subjected to photodegradation studies.

2.2.2 Preparation of PS-composite sheets

PS-composite sheets were also prepared through solvent casting method. Photocatalysts of varying weight percentages were loaded into 5g PS dissolved in 20 ml toluene. The viscous solutions were sonicated for 30 minutes, casted in petri dishes, dried in a vacuum oven followed by room temperature drying as explained above. The polymer composite sheets were subjected to UV irradiation for photodegradation studies.

2.2.3 Preparation of PS and PS-composites for mechanical studies

Mechanical tests included determination of tensile and flexural properties. Polymer composites for mechanical studies were prepared by injection moulding technique. Finely chopped PS and PS composite sheets- prepared by solvent casting method discussed above, were fed into injection moulder (Windsor, India) which consisted of moulds corresponding to tensile and flexural test specimens. Dimension of polymer specimens for tensile test was as per *ISO-527-2-1A* standard while that of flexural was as per *ISO-178* standard (Figure 2.1). Two other duplicates were also moulded for each sample. The samples were subjected to UV irradiation after which their tensile and flexural properties were measured using a universal testing machine (UTM).

Tensile test specimen -Dimension-(ISO-527-2-1A)		
L1	Total length	75 mm
L2	Gauge length	30 mm
B1	Width of grip end	10 mm
B2	Width of center	05 mm
H	Thickness	02 mm
Flexural test specimen -Dimension-ISO-178		
L	Length	80 mm
B	Breadth	10 mm
H	Thickness	40 mm
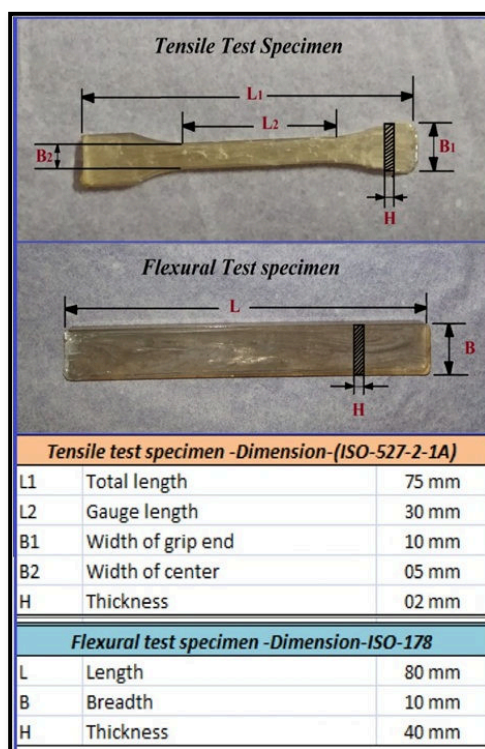
Figure 2.1. Dimensions of injection moulded specimens for tensile and flexural measurements as per ISO standards.

2.2.4 Preparation of PS and PS-composites for electrical studies

Electrical studies included dielectric breakdown (break down voltage) (BDV) measurement and determination of dielectric permittivity (ε_r) through capacitance

measurement. Specimens for BDV were moulded by the aid of hydraulic hot press to obtain uniform discs of thickness 1 mm and diameter 75 mm. Polymer sheets were cut out into small circular button shaped discs of diameter 10 mm for the determination of dielectric permittivity. The samples were then exposed to UV irradiation for photodegradation studies followed by electrical testing along with their duplicates.

2.3 Photodegradation reaction setup

Photodegradation of PS and PS composites were studied under artificial UV irradiation. Artificial UV irradiation of the polymer specimens in an isolated chamber avoided the possibility of their degradation through any other weathering process. UV chamber also protected the polymer specimens from natural harsh conditions and hence the impact of UV radiations alone, on photodegradation of PS could be investigated. The polymer specimens were subjected to a uniform UV exposure throughout the study and the rate of photodegradation of each specimen were compared.
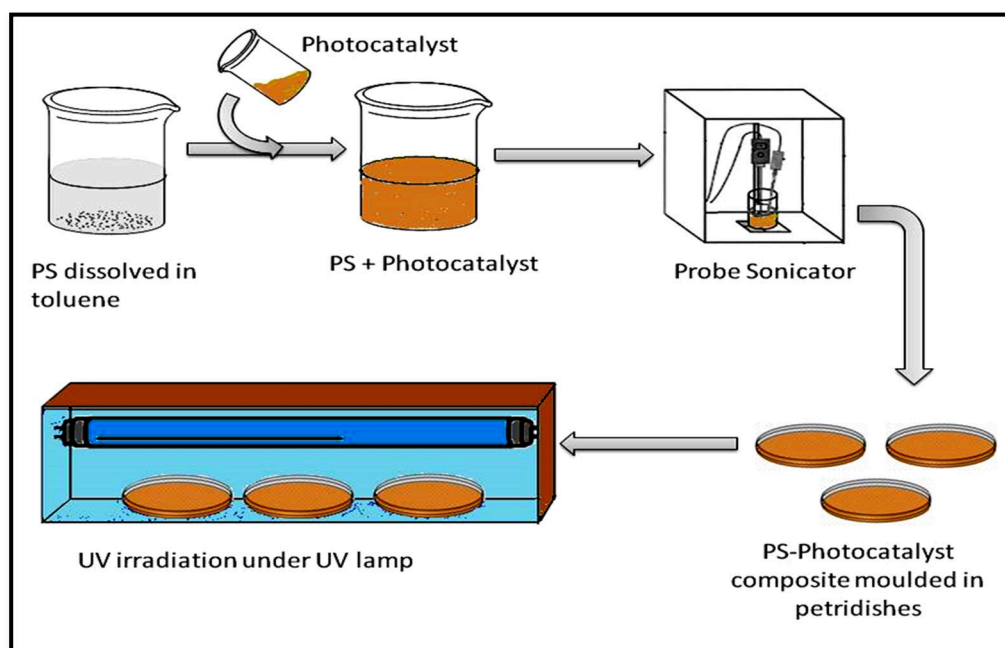
Figure 2.2. *Illustration of PS composites preparation and their photodegradation setup*

The UV irradiation chamber contained a UV tube (30 W, Philips Holland) of wavelength 253 nm and the specimens were irradiated maintaining an exact distance

of 8 cm from the tube. Irradiation was carried out continuously for 1000 hours. The specimens were subjected to various analyses at regular intervals of 200 hours. Figure 2.2 illustrates the scheme starting from polymer composite preparation to their UV exposure.

2.4 Characterisation techniques

Powder XRD analysis of the photocatalysts was done using X-Ray diffractometer Aeris, Panalytical -with Copper-K alpha radiation (1.5406Å wavelength) as the source. The particle size and morphology of the prepared photocatalysts were determined using Scanning Electron Microscope (FESEM) Hitachi SU6600 Variable Pressure Field Emission. Elemental analyses were done using energy dispersive X-ray (EDX) instrument JED 2300, Jeol. The surface morphology of PS-composite sheets was determined through SEM instrument, JSM-6390LV, JEOL. High resolution transmission electron microscope (HRTEM) and selected area electron diffraction (SAED) analysis were done using JEM 2100, Jeol. Molecular weight determination of the PS-composites was done using Gel Permeation Chromatography (GPC) LC-20AD, Shimadzu, Japan, with stationary phase silica gel and mobile phase tetrahydrofuran. The samples were dissolved in tetrahydrofuran for GPC analysis. IR spectroscopic analysis was done using FTIR-ATR spectrometer IRAffinity-1S, Shimadzu, Japan. PS composite sheets as such were used for FTIR analysis. UV-DRS analyses were conducted using UV-visible spectrometer UV-2600, Shimadzu, Japan. PS sheets were directly loaded into the instrument for UV-visible spectroscopic analysis. Thermal studies were conducted in a thermogravimetric analyzer (TGA), STA 6000, Perkin Elmer. The TG analysis was done in nitrogen atmosphere. Mechanical measurements were taken using universal testing machine (UTM), Autograph AG-X plus, Shimadzu. The samples moulded as per ISO standard as mentioned above were tested for tensile and flexural properties. Capacitance was measured using LCR meter of frequency range 20 to 10^7 Hz. The value of dielectric constant was determined using the measured value of capacitance. Dielectric breakdown or Breakdown voltage (BDV) was measured using specially designed wooden chamber with two copper electrodes aligned in a head to head fashion with respect to each other (Figure 2.3). The electrodes were connected to the two terminals

of a high power alternating current (AC) voltage source. The disc shaped sample (1 mm thickness) was placed in between the round heads of the electrodes. The chamber was filled with transformer oil so as to immerse the electrodes and sample completely. Transformer oil served as insulator in order to suppress arcing or discharges of electricity which may lead to current leakage and false measurement. Voltage needed to break the sample (BDV) was measured for the polymer samples and their duplicates.
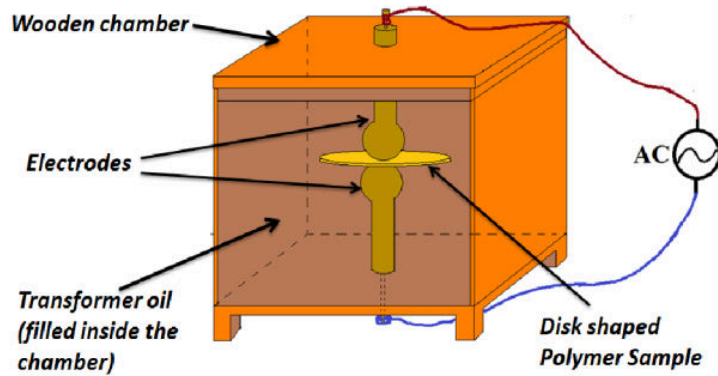
Figure 2.3. *Setup for BDV measurement*

Chapter 3

Photodegradation of Polystyrene using Nano TiO$_2$ and Nano ZnO Catalysts under UV Irradiation - a Comparison

Abstract

Nano TiO$_2$ has been synthesised by ultrasonication assisted sol-gel technique from Titanium (IV) isopropoxide (TTIP) precursor. ZnO have been synthesised using three methods viz., Sonication assisted precipitation method, hydrothermal method with uncontrolled hydrolysis and hydrothermal method with controlled hydrolysis. TiO$_2$ and ZnO were characterized using XRD, FTIR spectroscopy, UV-DRS, SEM and EDX. TiO$_2$ existed as spherical nanoparticles having diameter ≈25 nm. ZnO synthesised through three different techniques resulted in particles of varying size and morphology. XRD analysis revealed that nano TiO$_2$ existed predominantly in anatase phase with a fewer rutile phase where as ZnO existed in hexagonal wurtzite structure. Photodegradation of PS was studied in the presence of TiO$_2$ and ZnO under UV radiation. GPC analysis showed a decrease in average molecular weights and increase in chain scission as the time of UV irradiation increased in the PS-composites. FTIR spectra showed that photo-oxidation has taken place in all the composites upon UV irradiation. UV-DRS further supported photodegradation. The mechanical (tensile and flexural) strength of the composites decreased upon UV irradiation. The observed variations in electrical properties (breakdown voltage and dielectric permittivity) of the composites revealed the formation of charged species on UV exposure. Thermal stability of the composites too decreased upon UV irradiation. Based on all the observations it was concluded that PS loaded with TiO$_2$ or ZnO underwent accelerated UV degradation compared to pristine PS. Photocatalytic efficiency of TiO$_2$ was found to be superior compared to ZnO for the photodegradation of PS.

3.1 Introduction

The study of photodegradation of solid phase polystyrene (PS) in the presence and absence of nano titanium dioxide (TiO_2) and nano zinc oxide (ZnO) as photocatalysts under UV radiation is reported in this chapter. Even though PS is not a biodegradable polymer and withstands environmental weathering for a long span of time it undergoes photodegradation in the presence of UV radiation from the sunlight[1,2]. Radiations, especially in the UV region are absorbed by polystyrene during photodegradation which causes change in its original properties. Polystyrene undergoes photo-oxidative degradation when exposed to ultraviolet (UV) radiation[3–5]. Photo dissociation (chain scission), formation of carbonyl groups, isolated and conjugated double bonds and slight yellowing occurs due to radical initiated mechanism. Photodegradation cause changes in the original properties of polymer with depleted mechanical properties resulting in weight loss and brittleness[6–11].

Naturally occurring photodegradation of PS is of course a slow process. The rate of photodegradation further depends upon its type (density). High impact polystyrene (HIPS) and general purpose polystyrene (GPPS) takes much longer time to degrade compared to their low density counterparts such as expanded polystyrene (EPS). Difficulty faced by photons to reach the inner layers of high density PS matrix and difficulty to conduct reactive radicals across the tightly packed PS macromolecules are the main reasons responsible for this. This problem could be overcome by the incorporation of photocatalysts into the PS matrix.[12] Loading photocatalysts into PS furnishes more radicals, ions or free electrons in the presence of UV radiation which could further accelerate degradation. Photocatalysts can interact with each other and transfer electrons through the PS matrix where the UV light cannot reach much efficiently. One of the criteria of choosing photocatalysts is that they should have high surface area and very small size[13,14]. Nano particles satisfy these needs. The small size of nano particles resulting in high surface to volume ratio not only enables good and uniform dispersion along the PS matrix but also provides an easy platform for the charge carriers to migrate from the surface of the particles resulting in high photocatalytic activity[15].

Nano metal oxide semiconductor photocatalysts have been celebrated as satisfying photocatalysts for their multi advantages including better efficiency, photostability,

thermal stability, non toxicity, relative cheapness and so on[16–19]. In general semiconductor metal oxides absorb UV or visible radiations of solar spectra resulting to the transfer of electrons from valence to conduction band[20]. The electron hole pair formed further interacts with adsorbed molecules over the surface of these metal oxides resulting in the formation of secondary radicals or ions. These highly reactive species now interacts with the reactant, initiating several radical reactions. Nano TiO_2 and nano ZnO has been the most popular among semiconductor metal oxide especially while dealing with polymer degradation and water purification[21–24]. Herein, a comparative study of nano TiO_2 and nano ZnO on the photodegradation of PS in the presence of UV irradiation is reported.

TiO_2 and ZnO could easily be synthesised in laboratory under normal conditions. The morphology and particle size of these metal oxides could easily be tuned by adjusting the parameters or reaction conditions. In our work, we have used ultra sonication during the formation stage of these metal oxides through which the particle size could be reduced to nano scale. Nano TiO_2 was synthesised by sonication assisted sol-gel route while ZnO was synthesised via sonication assisted hydrothermal and precipitation methods. The synthesised nano particles were used as photocatalysts for the photodegradation of PS. The samples were irradiated using an artificial UV irradiation source and analysed at regular intervals of 200 hour. A comparison of photodegradation of pristine PS with that of PS-TiO_2 and PS-ZnO composites were studied. Variation in mechanical, electrical and thermal properties of the specimens was also studied at regular intervals of UV irradiation.

This chapter is presented in two sections. *Section I* includes the synthesis and characterization of nano TiO_2 and ZnO photocatalysts. *Section II* covers comparative study of photodegradation of PS in the presence and absence of nano TiO_2 and nano ZnO photocatalysts.

Section I

Synthesis and characterisation of nano TiO₂ and ZnO

3.2 Methods

3.2.1 Synthesis of nano TiO₂

Sonication assisted sol-gel method was adopted for the synthesis of nano TiO_2 particles. The precursor used was Titanium (IV) isopropoxide (TTIP). About 0.5 ml of TTIP was added to a mixture of 2 ml ethanol and 2ml deionized water in a boiling tube with constant stirring using a magnetic stirrer. The temperature of the system was set to 50°C. pH 4 was maintained by adding drops of HNO_3. The system was now moved to an ultrasonic probe sonicator (750 W), sonicated for two hours and centrifuged. The settled white precipitate was separated and washed with deionized water several times. Nano particles of TiO_2 collected were dried and calcined at 400°C for 5 hours. The synthesised nano TiO_2 was characterized and used as the photocatalyst for the photodegradation of PS[25–28].

3.2.2 Synthesis of ZnO

Synthesis of ZnO was carried out by three different techniques which resulted in ZnO structures with three different morphologies and particle dimensions. Sonication assisted precipitation method; hydrothermal method with uncontrolled hydrolysis and hydrothermal method with controlled hydrolysis were employed for the synthesis of ZnO as explained below.

Sonication assisted precipitation method:- 0.65 g of $Zn(NO_3)_2.6H_2O$ was dissolved in 25 ml distilled water. The solution was stirred over a magnetic stirrer vigorously to which liquid ammonia was added dropwise. Slow addition of ammonia solution was carried out until the pH of the solution turned out to be 7.5 where precipitation of $Zn(OH)_2$ was assumed to be complete. The system was now subjected to ultrasonic probe sonication for an hour followed by filtration and washing with distilled water. The ZnO powder hence obtained was dried at 80°C for 24 hours and calcinated at 400°C for 5 hours.

Hydrothermal method with uncontrolled hydrolysis:- The same procedure used in precipitation method was repeated in order to obtain turbid solution at pH 7.5. The solution was now transferred into a 50 litre vertical autoclave with distilled water filled up to optimum level. The system was autoclaved for 12 hours at temperature 130 °C. This was now filtered, dried at 80°C for 24 hours and calcinated at 400°C for 5 hours.

Hydrothermal method with controlled hydrolysis:- The same procedure mentioned above was repeated with a change in the autoclave setup. The turbid solution at pH 7.5 was autoclaved in a 25 ml Teflon lined hydrothermal autoclave. The quantity of water in the autoclave was exactly 25 ml. The solution was autoclaved for 12 hours at 130°C followed by filtration, drying and calcination under the same condition as mentioned above to obtain white powder of ZnO[29].

ZnO synthesised through all the three techniques were characterized.

3.3 Results and Discussion

3.3.1 Powder XRD
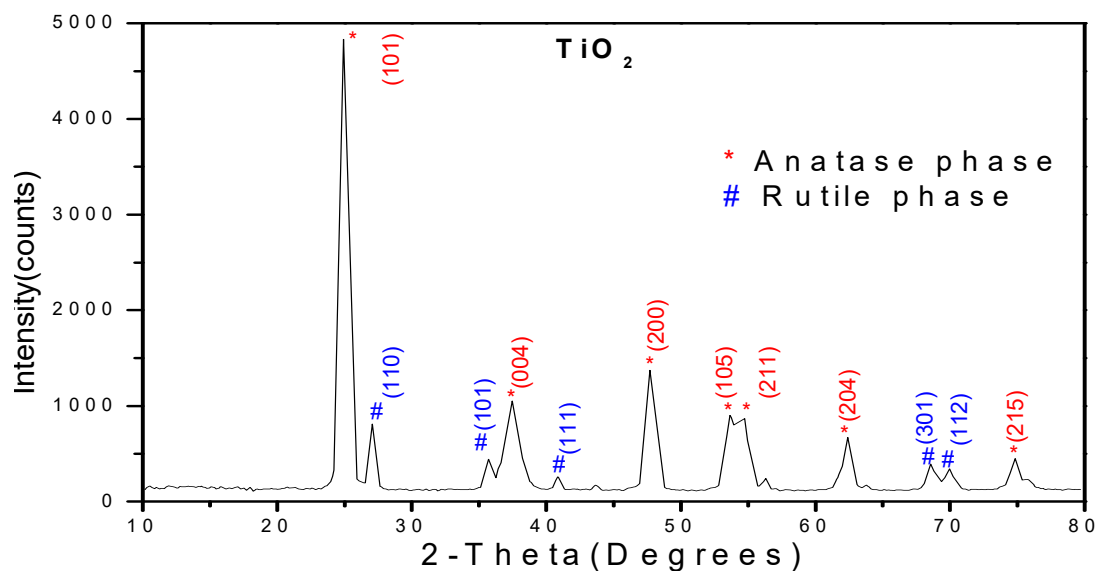
***Figure 3.1.1**. XRD pattern of nano TiO₂ particles*

The powder XRD pattern of TiO_2 synthesised by sol-gel method (Figure.3.1.1) exhibited strong diffraction peaks at 2θ = 24.94° (101), 37.44° (004), 47.70° (200), 53.64° (105), 54.73° (211), 62.40° (204) and 74.80° (215) corresponding to the

anatase phase of TiO_2. The diffraction peaks observed at $2\theta = 27.07°$ (110), $35.71°$ (101), $40.89°$ (111), $68.50°$ (301) and $69.95°$ (112) indicated the presence of rutile phase of TiO_2 in a lower percentage[30–32]. The percentage of anatase and rutile phases of TiO_2 existing in the composites were determined by Spurr equations (equation 3.1 and 3.2)[33].

$$\text{Percentage of anatase phase, } A\% = {100}\Big/{\{1 + 1.265\left(\frac{I_R}{I_A}\right)\}} \tag{3.1}$$

$$\text{Percentage of rutile phase, } R\% = {1}\Big/{\{1 + 0.8\left(\frac{I_A}{I_R}\right)\}} \tag{3.2}$$

Where I_A represents the intensity of anatase (101) peak and I_R represents the rutile (110) peak of TiO_2. The percentage of anatase phase TiO_2 obtained was 91.8 and that of rutile phase was 8.2 %.
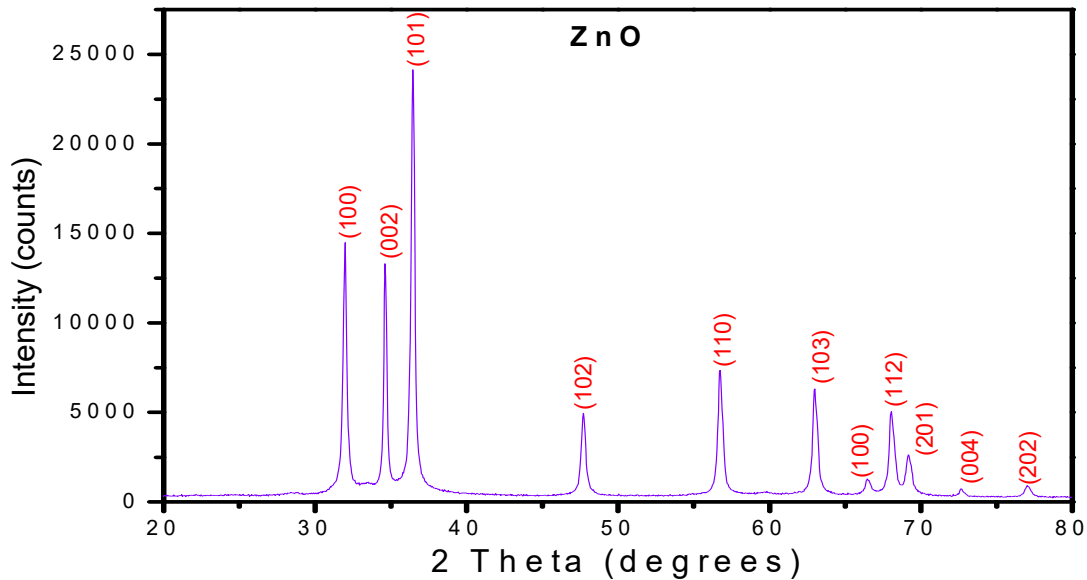
Figure 3.1.2. *XRD pattern of nano ZnO particles*

ZnO powder synthesised through precipitation as well as hydrothermal methods gave similar XRD patterns (Figure 3.1.2). The XRD pattern of ZnO consisted of peaks at 2θ= $31.97°$ (100), $34.62°$ (022), $36.45°$ (101), $47.71°$ (102), $56.75°$ (110), $63.01°$ (103), $66.48°$ (100), $68.05°$ (112), $69.18°$ (201), $72.70°$ (004), $77.00°$ (202). The pattern corresponds to hexagonal wurtzite structure of ZnO. Crystallite sizes of the synthesised TiO_2 and ZnO particles were calculated using the Debye Scherrer's formula (Equation 3.3)[34,35].

$$D = (k.\lambda)/(\beta.Cos\theta) \qquad\qquad (3.3)$$

Where

D = Crystallite size (nm)

k = Shape-sensitive coefficient (0.89- For spherical spheres)

λ = Wavelength of the X-ray beam (0.15406 nm for Cu-Kα radiation)

β = Full width at half maximum (FWHM) of the peak under consideration

θ = Diffracting angle

The average crystallite size of TiO$_2$ particles calculated using Debye Scherrer's formula was 18.9 nm and that of ZnO was 30.7 nm.

Interplanar distance (d spacing) was calculated for each plane of the synthesised TiO$_2$ and ZnO using Bragg's equation (equation 3.4)

$$\lambda = 2dsin\theta \qquad\qquad (3.4)$$

The values of d spacing are as tabulated below (Table 3.1).

Table 3.1*. Interplanar distance d corresponding to each 2θ angles of TiO$_2$ and ZnO*

TiO$_2$		ZnO	
2 θ°	**d (Å)**	**2 θ°**	**d (Å)**
24.94	3.57	31.97	2.80
27.07	3.29	34.62	2.59
35.71	2.51	36.45	2.46
37.44	2.40	47.71	1.90
40.89	2.21	56.75	1.62
47.70	1.91	63.01	1.47
53.64	1.71	66.48	1.41
54.73	1.68	68.05	1.38
62.40	1.49	69.18	1.36
68.50	1.37	72.70	1.30
69.95	1.34	77.00	1.24
74.80	1.27		

3.3.2   FESEM-EDX

From the FESEM image of the synthesised TiO$_2$ it could be observed that the synthesised TiO$_2$ existed as nano particles. The spherical morphology adopted by TiO$_2$ particles with particle diameter ≈25 nm (as determined through *image j* software) is given in Figure 3.2.1 A. Energy dispersive X-ray (EDX) pattern clearly

confirmed the fact that the synthesised nano TiO_2 particles contained no other impurities (Figure 3.2.1 B). The EDX peaks corresponding to titanium were observed at 4.51 (Kα1), 4.93 (Kβ1) and 0.45 (Lα1) keV and that of oxygen at 0.53 (Kα1) keV. Atomic percentages of titanium and oxygen present in TiO_2 were 19.94 % and 83.06 % respectively according to the EDX pattern.
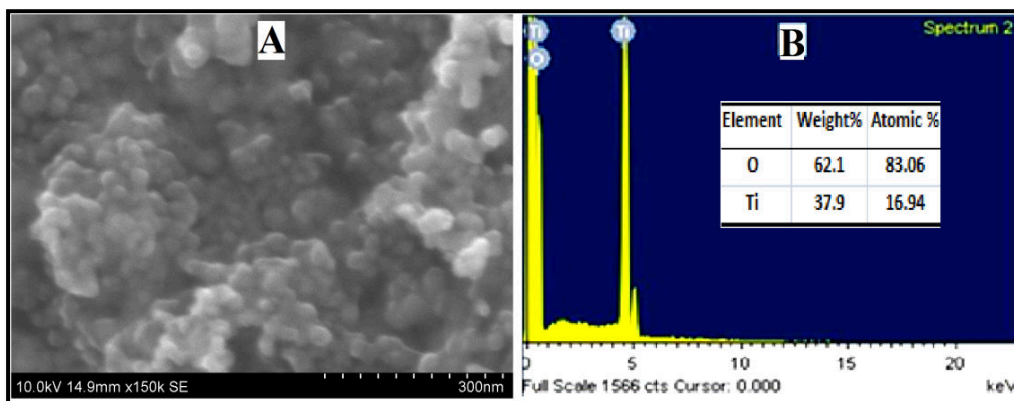
Figure 3.2.1. *FESEM image (A) and EDX pattern (B) of nano TiO₂*
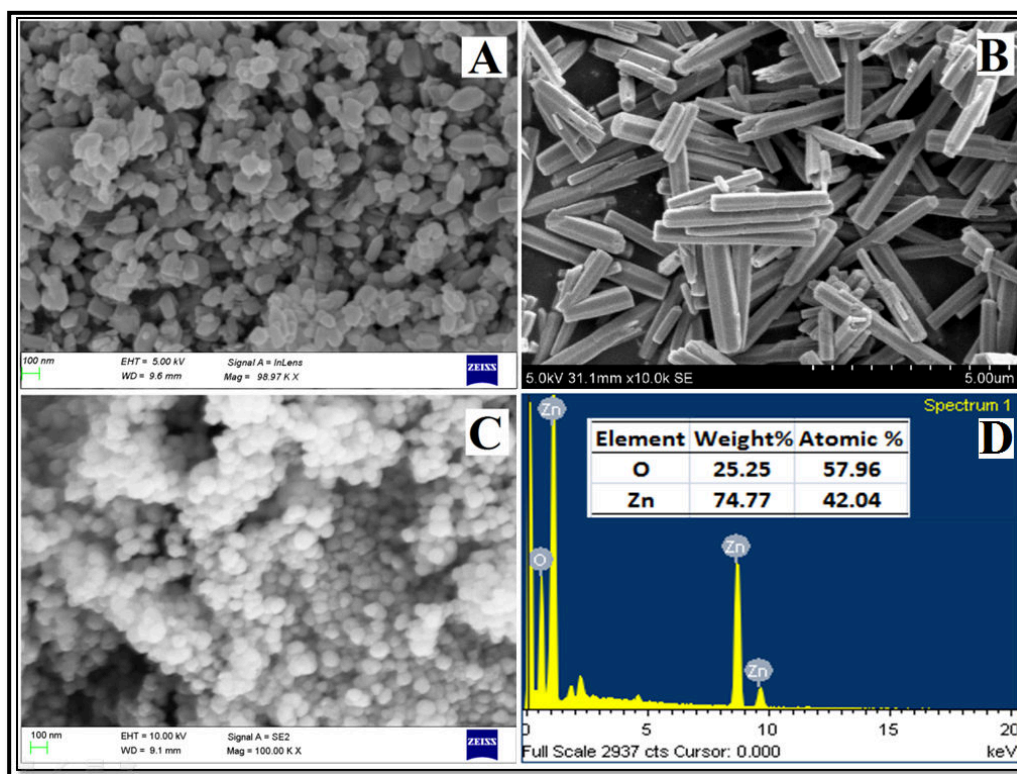
Figure 3.2.2. *FESEM image of ZnO synthesised through: Precipitation method (A) Hydrothermal method (uncontrolled hydrolysis) (B) Hydrothermal method (controlled hydrolysis)(C) and EDX pattern of nano ZnO (D).*

ZnO synthesised through three different synthetic approaches were analysed through FESEM. ZnO synthesised through precipitation method resulted in particles which resembled spheres with irregular edges. As could be seen in Figure 3.2.2 A, the size of the ZnO particles synthesised through this method ranged from 50 to 110 nm with majority of the particles lying in nanometer dimension (<100 nm). Hydrothermal method with excess of water (uncontrolled hydrolysis) adopted for the synthesis of ZnO on the other hand resulted in perfect hexagonal rod shaped structures (Figure 3.2.2 B). Lengths of the ZnO rods were non-uniform and ranges between 0.4 to 5 μm while the thickness of the rods ranges from 250 to 445 nm. ZnO synthesised using hydrothermal method with controlled hydrolysis resulted in nano particles of spherical morphology with diameter ≈70 nm (Figure 3.2.2 C). Controlled hydrolysis was done in a Teflon lined autoclave at a temperature of 120°C. The fact that uncontrolled hydrolysis lead to crystal growth of ZnO whereas controlled hydrolysis resulted in spherical nano structures at 120° C under high pressure were hence clear from the FESEM images. EDX analysis of all synthesised ZnO gave similar pattern which confirmed the presence of zinc and oxygen atoms with no other impurities (figure 3.2.2 D). EDX peaks corresponding to zinc were observed at 1.02 (Lα1, Lβ1 and Lβ3 overlap), 8.62 (overlap of Kα1 and Kα2 overlap) and 9.58 (Kβ1 and Kβ2 overlap) keV. Peak corresponding to oxygen was observed at 0.53 (Kα1) keV.

3.3.3 FTIR Analysis
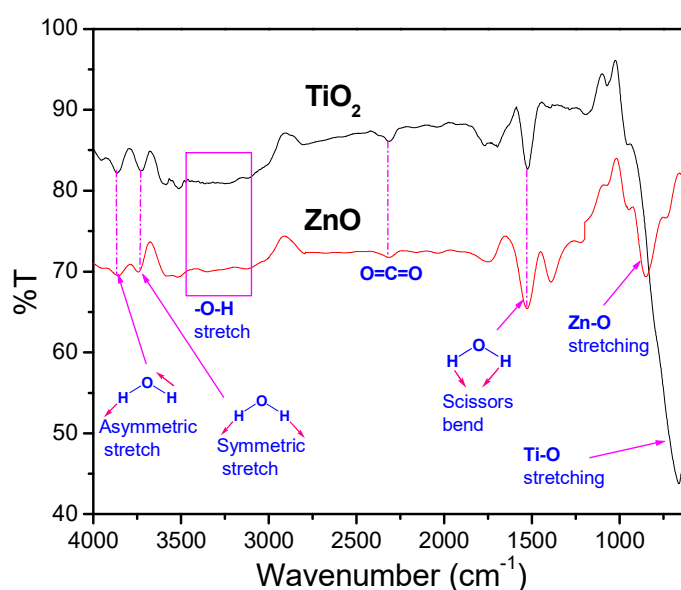
Figure 3.3*. FTIR spectra of nano TiO₂ and nano ZnO*

FTIR spectra of synthesised nano TiO_2 and nano ZnO is as given in the figure below (Figure 3.3). In addition to Ti-O stretching band (in TiO_2) and Zn-O stretching band (in ZnO), bands corresponding to H_2O, -OH and CO_2 were also observed. The fact that nano ZnO and nano TiO_2 adsorb water, carbon dioxide and hydroxyl ions from the atmosphere was hence clear. The adsorbed H_2O, OH and CO_2 played an important role in the photocatalytic activity of these nano particles under UV radiation (explained section 3.5)

3.3.4 UV- visible Diffused reflectance spectroscopy (UV-DRS)
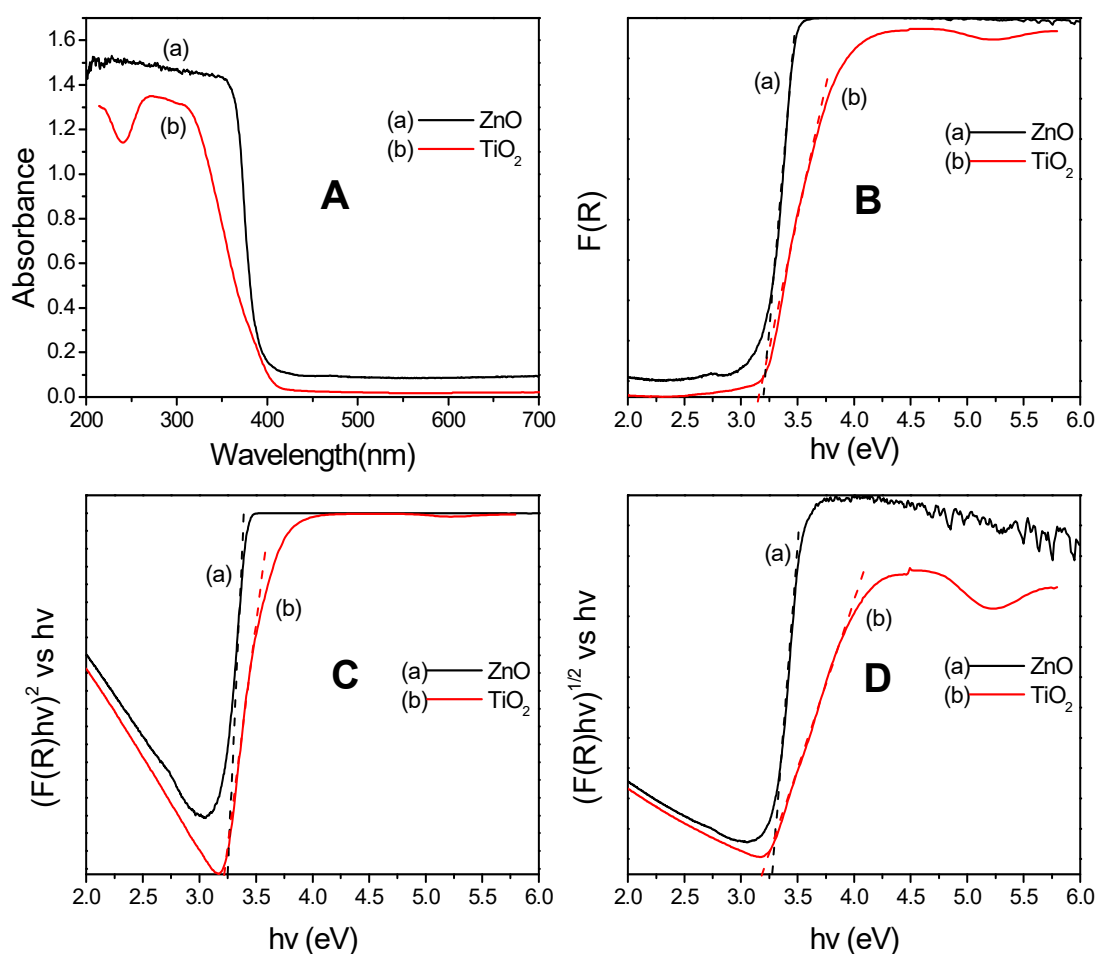
Figure 3.4*. A): Absorption spectra of TiO_2 and ZnO, **B):** Plot of F(R) versus hv **C):** $(F(R)hv)^2$ versus hv representing the direct allowed Eg and **D):** $(F(R)hv)^{1/2}$ versus hv representing the indirect allowed Eg of TiO_2 and ZnO.*

UV-DRS of synthesised TiO_2 as well as ZnO exhibited its characteristic absorption in the UV region (λ<400 nm). No absorption was observed in the visible region (400-800 nm) (Figure 3.4 A). Determination of optical bandgap energies (E_g)

of TiO$_2$ and ZnO was done by the application of Kubelka-Munk function (K-M or F(R)) in Tauc method[36–38]. Reflectance spectra of the composites obtained through UV-DRS were used for E$_g$ determination. Kubelka-Munk function (F(R)) is given by

$$F(R) = \frac{(1-R)^2}{2R} \qquad (3.5)$$

where 'R' is the reflectance.

F(R) was plotted against energy (hυ) in eV and the bandgap energy (E$_g$) was determined from the plot obtained by extrapolating the linear portion of the curve to the x-axis (Figure 3.4 B). The E$_g$ determined from the plot F(R) v/s hυ was irrespective of transitions (direct/indirect, allowed/forbidden).

In order to determine the E$_g$ of a particular type of transition, F(R) is substituted in Tauc method. Extinction coefficient (α) is related to photon energy and optical bandgap through equation (3.6) according to Tauc method.

$$\alpha = \frac{A(h\upsilon - E_g)^n}{h\upsilon} \qquad (3.6)$$

Where A is a constant, hυ represents the energy of photons, coefficient (n) is associated with corresponding electronic transition (n=2 for indirect allowed and n=1/2 for direct allowed Eg). F(R) being proportional to α, the following equation (equation 3.7) could be arrived.

$$F(R) = \frac{A(h\upsilon - E_g)^n}{h\upsilon} \qquad (3.7)$$

Equation 3.5, known as modified Kubelka-Munk function were used to determine the E$_g$ of TiO$_2$ of particular transition through the plot of (F(R)hυ)^n v/s hυ. The plot (F(R)hυ)^2 versus hυ represents direct allowed transition (Figure 3.4 C) whereas (F(R)hυ)$^{1/2}$ versus hυ represents indirect allowed transition (Figure 3.4D). Modified Kubelka-Munk function also holds further scope for determination of E$_g$s corresponding to other type transitions just by substituting the exponential factor n with corresponding values which is insignificant in this piece of work. The tabulated values of E$_g$s determined for TiO$_2$ and ZnO particles using the three methods were as tabulated in the following table (Table 3.2).

Table 3.2. *Optical bandgap energies (E_gs) of nano TiO$_2$ and nano ZnO*

Method	Transition Type	Optical Bandgap energy in eV	
		Nano TiO$_2$	Nano ZnO
F(R) vs hυ	Irrespective of transitions	3.16	3.2
(F(R)hυ)^2 vs hυ	Direct allowed	3.22	3.25
(F(R)hυ)$^{1/2}$ vs hυ	Indirect allowed	3.18	3.27

It could be concluded from the comparative values of E_gs that nano TiO$_2$ has lower E_g compared to nano ZnO. The excitation of electrons from valence band to conduction band in TiO$_2$ requires lesser energy compared to that of nano ZnO.

Section II

Photodegradation of polystyrene using nano TiO$_2$ and nano ZnO

PS and PS loaded with TiO$_2$ or ZnO were prepared using solvent casting method as described in chapter 2. PS, PS-TiO$_2$ and PS-ZnO composite specimens were also moulded for mechanical and electrical measurements. All the specimens were subjected to UV irradiation. The samples were monitored at regular intervals and the results are as presented below.

3.4   Results and Discussion

3.4.1   Gel permeation chromatography (GPC) analysis

Gel permeation Chromatography analysis of PS, PS-ZnO and PS-TiO$_2$ was used to determine their average molecular weights ie., weight average molecular weight ($\overline{M}_w$) and number average molecular weight ($\overline{M}_n$). PS, PS-ZnO and PS-TiO$_2$ composites were subjected to GPC measurements after regular intervals (200 hours) of UV exposure. Average molecular weights of the specimens were measured by GPC and from these data, polydispersity index (PDI), chain scission per macro molecule (S) and number of scission events per gram (N_t) were determined using the equations given below (Equations 3.8, 3.9 and 310).

Average chain scission per polymer macro molecule $S = \left[\dfrac{(\overline{M}_n)_0}{(\overline{M}_n)_t} - 1\right]$ (3.8)

Number of scission events per gram of polymer $N_t = \left[\dfrac{1}{(\overline{M}_n)_t} - \dfrac{1}{(\overline{M}_n)_0}\right]$ (3.9)

Polydispersity index $PDI = \dfrac{\overline{M}_w}{\overline{M}_n}$ (3.10)

Where $\overline{M}_n$ and $\overline{M}_w$ represents number average and weight average molecular weights of PS respectively. $(\overline{M}_n)_0$ and $(\overline{M}_n)_t$ represents number average molecular weight before and after *t* hours of UV irradiation respectively.

Decrease in average molecular weights were observed in PS as well as PS-composites under study (figure 3.5.1 A & B). Decrease in molecular weights of the polymer specimens could be attributed to the polymer chain scission which in turn was a consequence of polymer degradation on UV exposure.
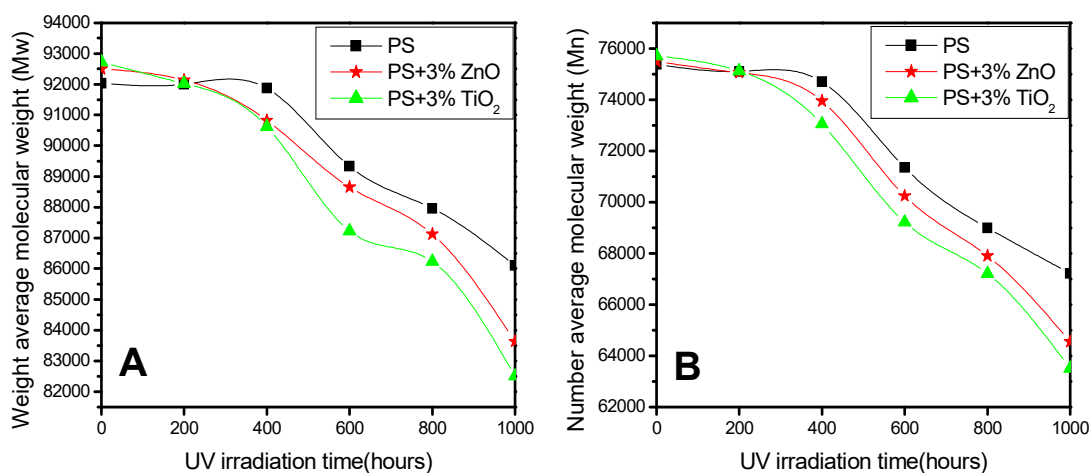
Figure 3.5.1. A): *Weight average ($\overline{M}_w$) and **B):** number average ($\overline{M}_n$) molecular weights of PS and PS-3% TiO$_2$ composite under different UV irradiation time*

The increasing value of S and N_t on irradiation (determined using equations 3.8 and 3.9) pointed out the extent to which chain scission had taken place in the polymer specimens on different UV exposure time intervals (Figure 3.5.2 A and B). Decrease in average molecular weights and increase in polymer chain scission were more predominant in PS-TiO$_2$ composites compared to pristine PS and PS-ZnO composites.

The polydispersity index PDI (calculated from equation 3.10) of the polymer specimens increased with the increase in UV exposure time (Figure 3.5.3). The

increase in the values of PDI reflected the increase in randomness of polymer chain scission. In other words irregular chain breakages lead to the formation of macromolecules of varying molecular masses. It was also clear from GPC data that PS-TiO_2 composites underwent predominant mass loss as well as better chain breakage compared to pristine PS and PS-ZnO. Accounting these facts it could be concluded that TiO_2 acted as a good photocatalyst for the degradation of solid phase PS.
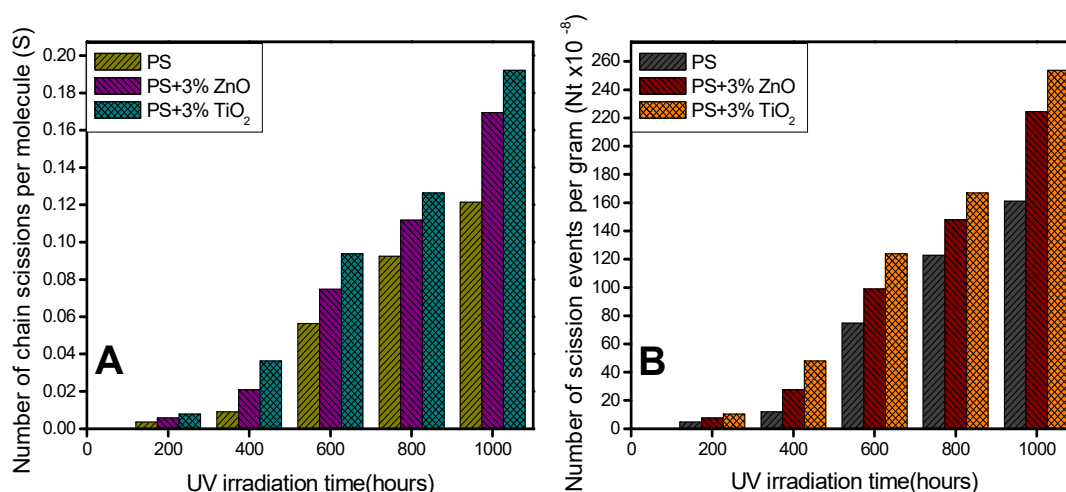
Figure 3.5.2. A): *Number of chain scissions per molecule (S) and **B):** number of scission events per gram (N_t) of PS and PS-3% TiO_2 composite under different UV irradiation time.*
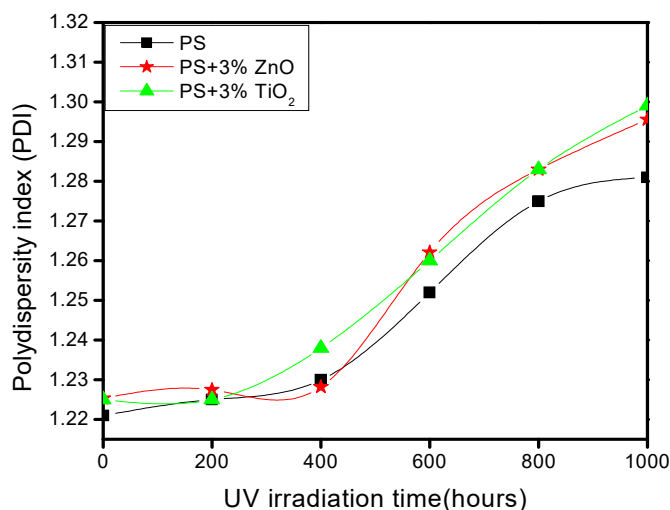
Figure 3.5.3. *Polydispersity index (PDI) of PS and PS-3%TiO_2, PS-3%ZnO composite under different UV irradiation time.*

3.4.2 FTIR Spectroscopy

Changes in chemical structures of the polymer specimens at regular intervals of UV irradiation were investigated through FTIR spectroscopy. Photodegradation of PS and PS composites were further confirmed by FTIR spectroscopy. For the PS and PS composites under study, it was found that the intensities of peaks corresponding to carbonyl (>C=O), hydroxyl (-OH)/ hydroperoxy (-OOH), carbon- carbon double bond (>C=C<), conjugated carbon-carbon double bonds etc stretching vibrations have increased with respect to UV irradiation time. It was also clear from the FTIR spectra that all the functional groups and multiple bonds formed were associated with the PS main chain and not on phenyl rings (Figure 3.6.1, 3.6.2 and 3.6.3).

From the FTIR spectra, it was found that pristine PS and PS composites before and after UV irradiation of regular intervals (200, 400, 600, 800 and 1000 hours) showed characteristic peaks of phenyl ring at around 691 cm^{-1}, 752 cm^{-1}, 905 cm^{-1} and 1027 cm^{-1} with no change in their intensities. These bands attributed to the C-H out of plane bending frequencies of the phenyl ring. The peak at 1448 cm^{-1} corresponding to aromatic carbon-carbon double bond stretch (Ar-C=C- stretch) also showed no change in peak intensity. The above observations show that phenyl rings of PS remain intact after UV irradiation.
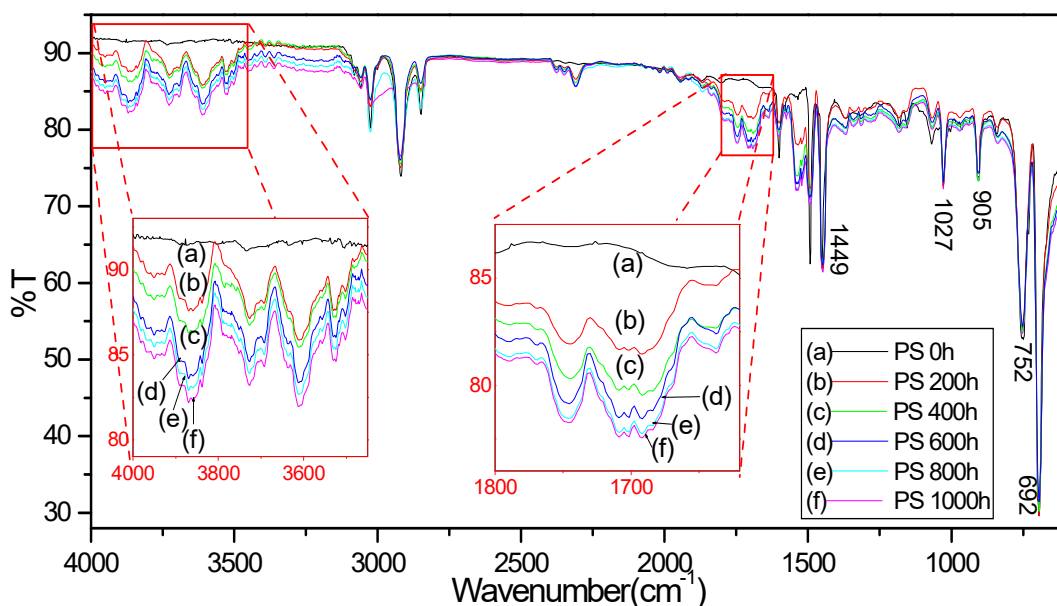
Figure 3.6.1. *FTIR spectra of PS after different UV exposure time intervals ranging from 0 h to 1000 h*
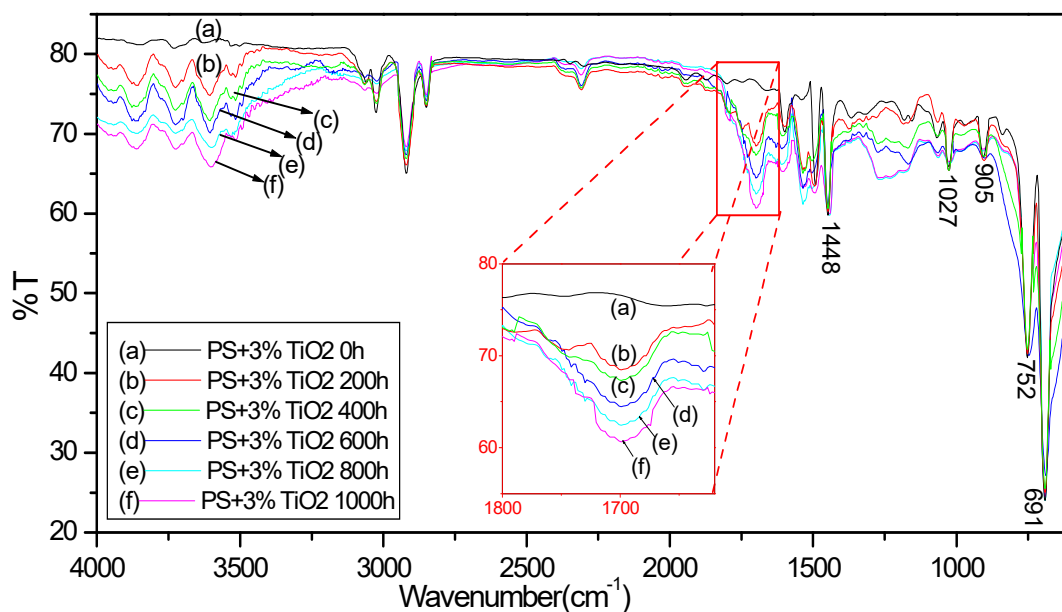
Figure 3.6.2*. FTIR spectra of PS-3%TiO$_2$ after different UV exposure time intervals ranging from 0 h to 1000 h*
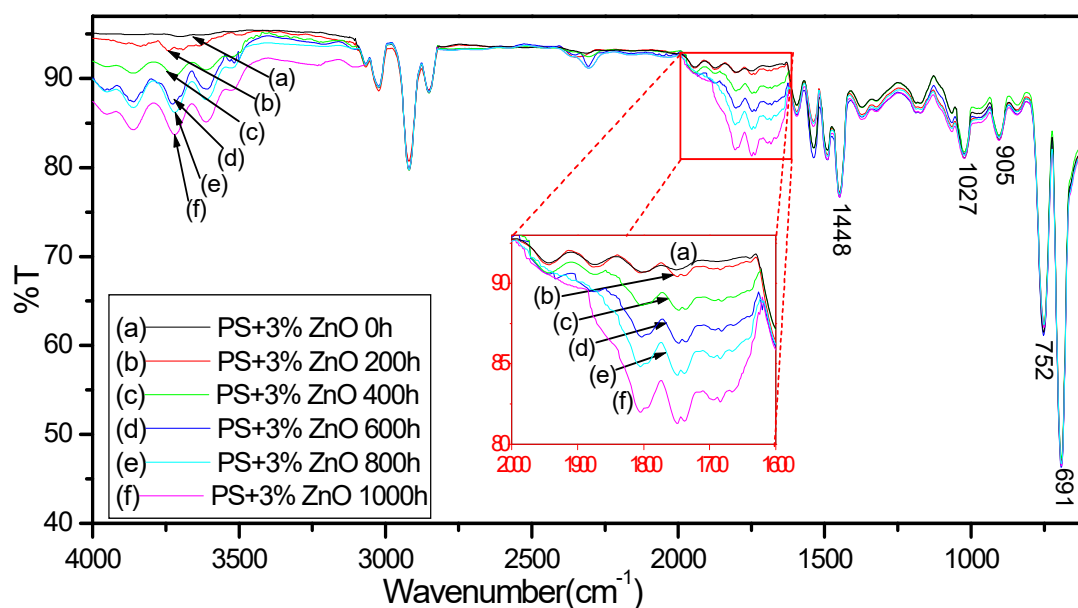
Figure 3.6.3*. FTIR spectra of PS-3%ZnO after different UV exposure time intervals ranging from 0 h to 1000 h*

An increase in the intensity of bands corresponding to carbonyl frequencies ranging between 1750 to 1650 cm^{-1} were observed upon the increase in UV irradiation time. These observations clearly revealed the fact that there was formation and increase in the intensities of carbonyl ($>C=O$) stretching bands (1740- 1700 cm^{-1}) as well as carbon- carbon double bond ($>C=C<$) stretching bands (1680-1650 cm^{-1}) upon UV irradiation. The increase in vibrational bands observed at around 1630-1600

cm^{-1} could be assigned to conjugate multiple bond formation upon UV irradiation which was further supported by UV-DRS analysis explained in section 3.4.3 below. The intensity of bands corresponding to hydroxyl and/or hydroperoxy groups (3700-3600 cm^{-1}) also showed an appreciable increase during UV irradiation. Formation of new -OH /-OOH groups upon UV irradiation was established from this observation. The two parameters affecting the increase in the intensities of oxygen containing functional groups and multiple bonds as discussed above were UV irradiation time as well as photocatalyst loading concentrations. FTIR spectra of PS loaded with varying weight percentages of nano TiO$_2$ (0%, 0.5%, 1%, 2% and 3%) were also analysed. It was concluded that as the percentage of nano TiO$_2$ loading increased, enhancement in the absorption bands corresponding to -OH, -OOH, >C=O, >C=C<, conjugated carbon-carbon double bonds etc took place for a particular UV irradiation time. Since excess TiO$_2$ loading (>3% by weight) inversely effected the mechanical properties of PS composite (discussed in section 3.4.6 below), TiO$_2$ loading was optimized to be 3% by weight, throughout the study. As the entire study is based on comparison between the efficiencies of various photocatalysts for effective photodegradation of PS, The catalytic loading percentages throughout the entire study was focused on 3 weight percentage.

The following conclusions were drawn from the observation made from FTIR spectra. The increase in intensities of >C=O, -OH, -OOH, Ph-C=O etc., functional groups suggested that photo-oxidative mechanism has taken place upon UV irradiation. Increase in the intensities of bands corresponding to >C=C< stretch, conjugated >C=C< , =C-H bend etc suggests that chain and/or bond scission (due to -C–C- or -C-H bond breakage) had taken place (as evident from GPC and supported by UV-DRS). Since there was no change in aromatic >C=C< (stretch) and aromatic -C-H (out of plane bend), it was clear that the phenyl ring remained intact upon UV irradiation. Photo-oxidative degradation of PS-TiO$_2$ and PS-ZnO composites took place in a more accelerated way compared to pristine PS upon UV irradiation highlighting the efficiency of nano TiO$_2$ and nano ZnO catalysts. PS-TiO$_2$ composite (Figure 3.6.2) exhibited predominant photo-oxidative degradation of PS compared to PS-ZnO composite (Figure 3.6.3) confirming the better efficiency of nano TiO$_2$ compared to nano ZnO.

The observations and conclusions made from FTIR spectra is tabulated below (Table 3.3)

Table 3.3. Important observations made from FTIR spectra of PS and PS-composites.

IR vibration peaks	Assigned functional groups	Change in intensity up on UV irradiation
3700-3600 cm^{-1}	Free –OH/-OOH	Intensity increased
1740-1700 cm^{-1}	>C=O stretch	Intensity increased
1680-1650 cm^{-1}	>C=C< stretch	Intensity increased
1630-1600 cm^{-1}	Conjugated >C=C< stretch	Intensity increased
1452 cm^{-1}, 1600 cm^{-1}	Aromatic >C=C< stretch	No change
1027, 905, 752, 691 cm^{-1}	Ar C-H (Out of plane bend)	No change
830 cm^{-1}	Conjugated >C=C< bend	Intensity increased
650 cm^{-1}	=C-H bend	Intensity increased

3.4.3   UV-visible Diffused Reflectance Spectroscopy (UV-DRS)

UV-visible diffused reflectance spectra (UV-DRS) of pristine PS, PS-TiO$_2$ and PS-ZnO showed notable changes in their characteristic absorption bands upon UV exposure (Figure 3.7.1 A, B & C). An appreciable decrease in the absorption peaks of the polymer specimens under study were observed in the UV region (between 230-400 nm) with respect to the increase in UV irradiation time. This observable hypochromic effect reflected degradation of polymer chain. As evident from FTIR spectra explained above the increase in >C=O (n→π*) absorption bands with UV exposure time could not be identified over this area (230-290 nm) due to their low intensity. Depletion of polymer chain lead to a decrease in the absorption bands that dominated the formation of >C=O groups which should otherwise have caused an increase in intensity (due to n→π* transition) over this area (230-290 nm). The region of UV spectra with wavelength below 230 nm showed an increase in absorption bands with respect to UV irradiation time. This hyperchromic effect could be due to the

increase in the absorption bands of -OH ($n \to \pi^*$), >C=O ($\pi \to \pi^*$) and >C=C< ($\pi \to \pi^*$) functional groups upon irradiation. Another striking trend observable from the UV-vis spectra was an increased bathochromic shift (red shift) and slight increase in absorption intensity in the visible region with respect to the irradiation time for all specimens. Formation and increase in conjugated double bonds between carbon atoms was evident from this observation. The observable trends as mentioned above of UV DRS were predominant in PS-TiO$_2$ composites. UV DRS hence supports the fact that TiO$_2$ is a better catalyst compared to ZnO for the photodegradation of PS under UV radiation.
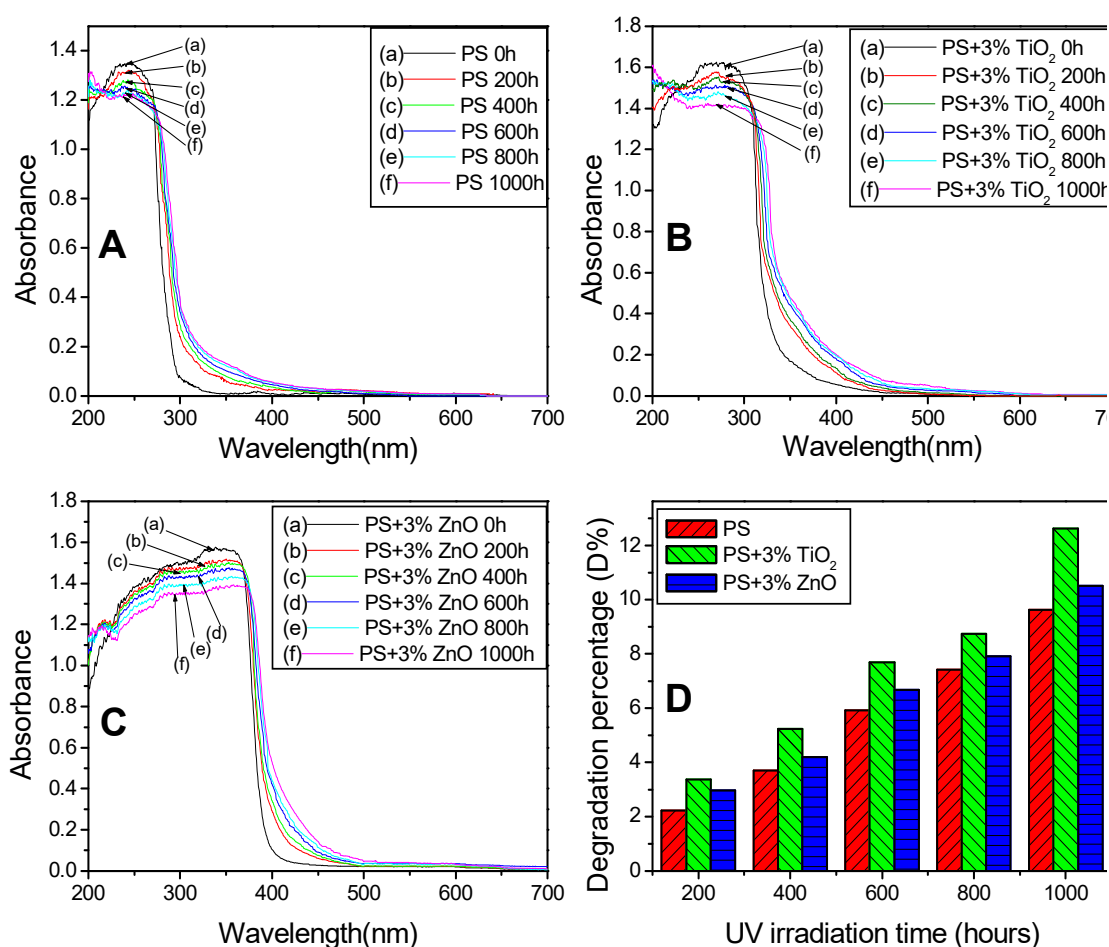
Figure 3.7.1. *UV-DRS of PS (A), PS-3%TiO$_2$ (B) and PS-3%ZnO (C) at regular UV irradiation intervals and their degradation percentages (D%).*

The percentages of photodegradation (D%) at each time interval of UV irradiation were calculated using equation 3.11 from UV-visible spectra.

$$D\% = \left(\frac{A_0 - A}{A_0}\right) X 100 \tag{3.11}$$

Where A_0 and A represents the absorption maxima of the polymer specimens before and after UV irradiation respectively.

D% was found to be higher for PS-TiO$_2$ composites compared to PS-ZnO and pristine PS (Figure 3.7.1 D). The D% of PS, PS+3%ZnO, PS+3%TiO$_2$ after 1000 hours UV exposure was 9.63, 10.56 and 12.62 % respectively. In other words the degradation efficiency of photodegradation of PS has increased upon loading it with ZnO or TiO$_2$.
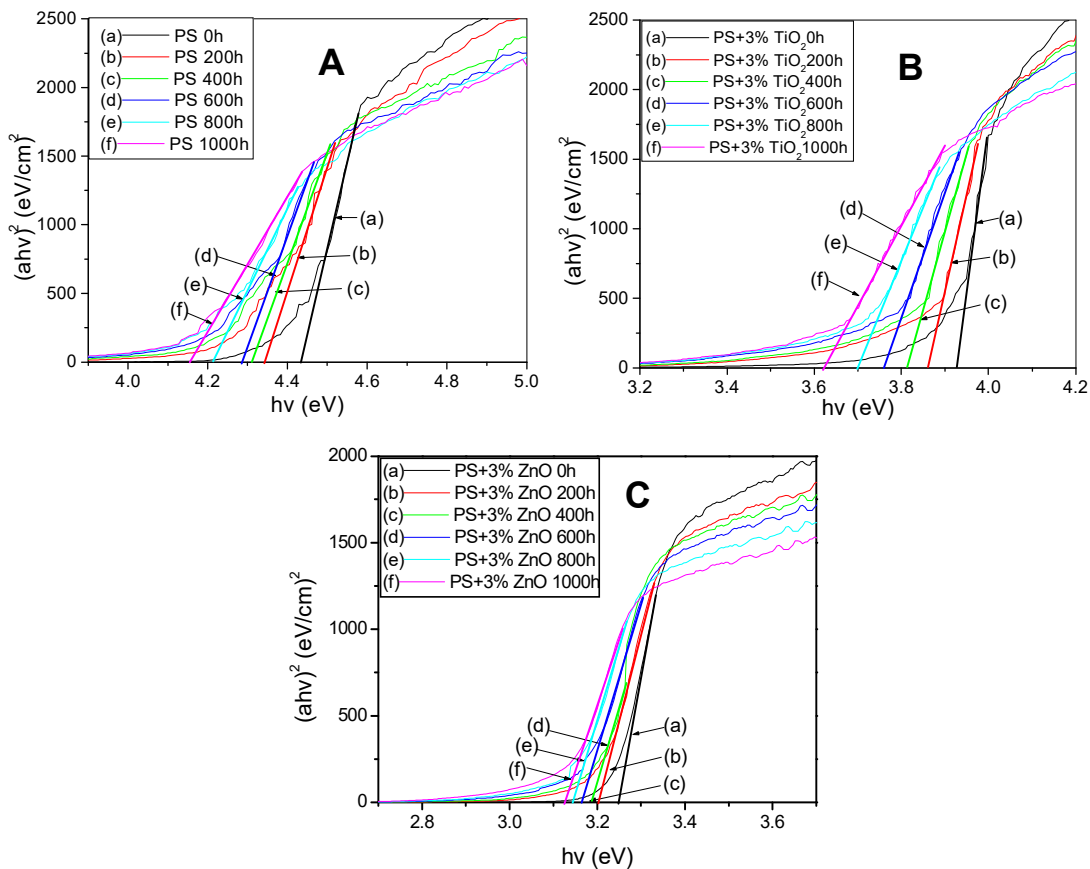
Figure 3.7.2. *Optical bandgap energy determination from the plot of $(\alpha h\upsilon)^2$ v/s h\upsilon for PS (A), PS-3%(TiO$_2$) (B) and PS-3%ZnO) (C) subjected to different UV exposure time intervals ranging from 0 h to 1000 h*

Optical bandgap energy (E_g) of PS, PS-TiO$_2$ and PS-ZnO films before and after UV irradiations of different intervals were determined using Tauc relation (Equation 3.12)[39–43].

$$\alpha h\upsilon = A(h\upsilon - E_g)^n \qquad\qquad (3.12)$$

Where α is the absorption coefficient, $h\upsilon$ is the energy of photon in eV (h= Plank's constant and υ = frequency of radiation), A is a constant (different for different transitions), E_g is the bandgap energy and the index n is assumed to have different values corresponding to different electronic transitions (n= ½ for direct allowed transition and n=2 for indirect allowed transition)

A plot of $(\alpha h\upsilon)^2$ versus $h\upsilon$ gave the direct allowed bandgap energy (E_g) of PS as well as PS composites, on extrapolating the linear portion of the curve to the X axis (where α=0) (Figure 3.7.2). The E_gs for PS as well as PS-composites showed a decrease in value upon increase in the time of UV irradiation. E_g of PS, PS-3% TiO_2 and PS-3% ZnO were determined to be 4.43, 3.93 and 4.04 eV respectively. The decrease in E_g of PS-TiO_2 and PS-ZnO composites in comparison with pristine PS was hence clear.

3.4.4   Scanning electron microscopy (SEM)
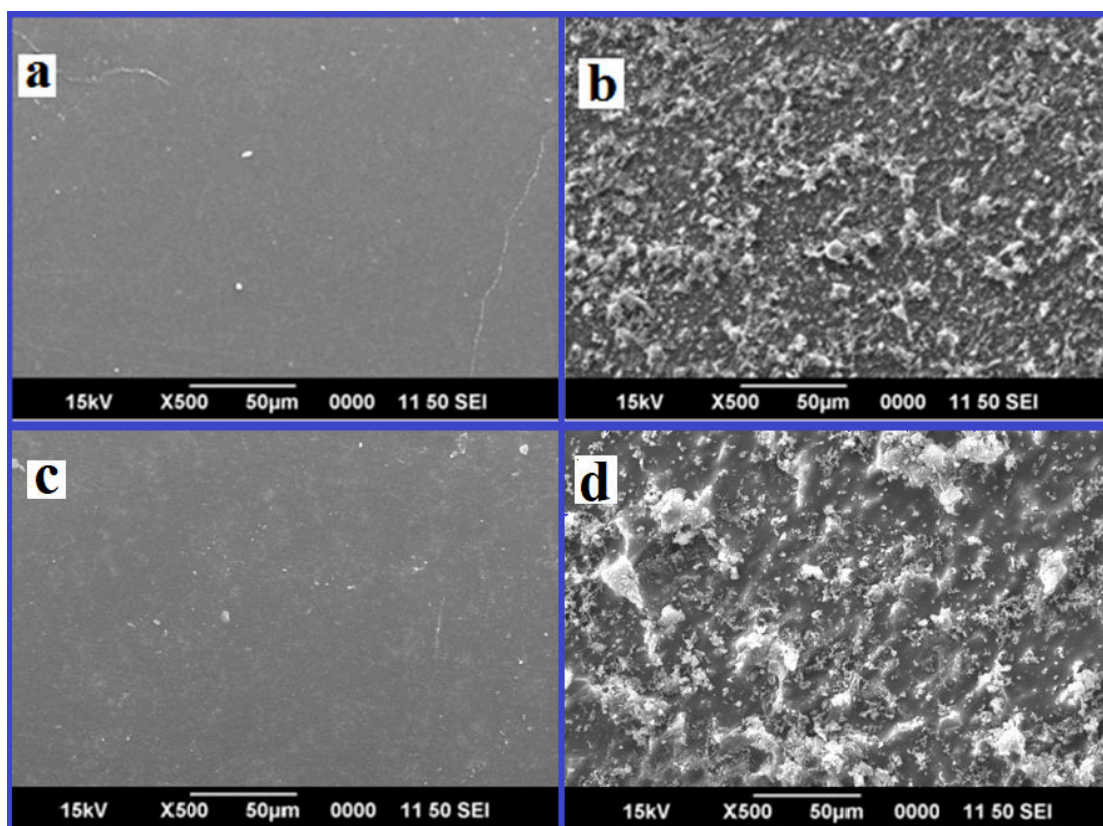
Figure 3.8. *SEM image of PS-3%TiO₂ and PS-3%ZnO respectively before (a & c) and after (b & d) UV irradiation of 1000 h*

The change in surface morphology of the UV irradiated PS composites as a consequence of photodegradation was observable from their SEM images. Figure 3.8 a & c represents the SEM images of PS-3%TiO₂ and PS-3%ZnO respectively before UV irradiation and figure 3.8 b & d show these composites after 1000 hours of UV exposure. The increase in the surface roughness upon UV irradiation as a result of photodegradation could be clearly identified from figure 3.8 b &d when compared with figure 3.8 a and c.

3.4.5   Thermogravimetric Analysis (TGA)
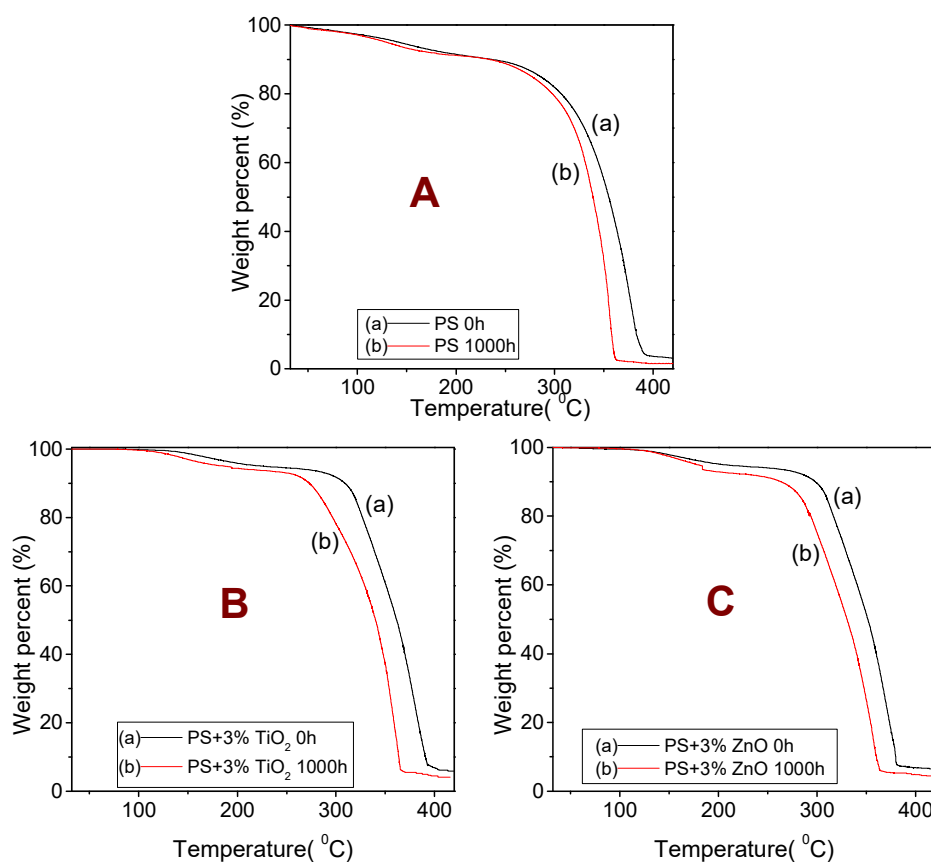
Figure 3.9. *TGA thermogram of PS, PS-3%TiO₂, PS-3%ZnO before and after UV irradiation of 1000 h*

TG analysis was conducted in an inert atmosphere by circulating nitrogen gas continuously through the sample holding crucible. From the TGA thermogram it was observed that the decomposition temperature of PS-ZnO and PS-TiO₂ composites were higher compared to that of pristine PS (Figure 3.9).

The first stage of weight loss for PS and PS-composites observed at a temperature around 118°C may attribute to the desorption of water molecules. The decomposition temperature of PS observed at 252-394°C increased for the PS composites (269-380°C for PS+3% ZnO composite and 272-407°C for PS+3% TiO$_2$ composite). The increase in decomposition temperature of PS composites highlighted the fact that the thermal stability of PS has increased upon nano ZnO and nano TiO$_2$ loading. It was also observed that decomposition temperature of UV irradiated PS and PS composites decreased appreciably compared to their unirradiated counterparts. UV irradiation of PS and PS-composites lead to the breakage or weakening of polymer chains, resulting to a decrease of decomposition temperature. PS loaded with ZnO and TiO$_2$ catalysts exhibited higher thermal decomposition compared to pristine PS under UV irradiation. Higher thermal decomposition rate under UV irradiation was observed in PS-TiO$_2$ composite highlighting the fact that nano TiO$_2$ has caused better photodegradation over the PS matrix compared to nano ZnO.

3.4.6   Mechanical Properties of PS, PS-TiO$_2$ and PS-ZnO composites

Flexural and tensile properties of PS and PS composites were determined using a universal testing machine (UTM) before and after UV irradiation of certain intervals.

The stress-strain graph (Figure 3.10.1) of PS, PS-TiO$_2$ and PS-ZnO looked similar with no visible area under the curve. This observation could lead us to the conclusion that PS and PS composites under study were strong but not very tough. If the polymer specimens were tough and elastic, a smooth curve of higher surface area would have been observed instead of steep slope with sudden break. PS composites of nano TiO$_2$ and ZnO showed enhanced tensile property compared to pristine PS. The value of tensile strength of pristine PS observed at 52.92 MPa was found to have increased with the increasing percentage of nano TiO$_2$ loaded up to 3% by weight (tensile strength=53.23 MPa). At 5% by weight of nano TiO$_2$ loading the value of tensile strength showed a decrease in value (52.95 MPa) instead of increasing (Figure 3.10.2 A). Due to this reason, 3% nano TiO$_2$ loading in PS was considered to be the optimum catalytic concentration and throughout the study 3% catalyst loading was considered for various other investigations regarding photodegradation studies. A comparison of tensile properties of PS, PS-3% ZnO and PS-3%TiO$_2$ was made and it was found that the value of tensile strength found to be 52.92 MPa in PS increased up to 53.12 MPa

in PS-3% ZnO and 53.23 MPa in PS-3%TiO$_2$ composite. The enhancement in the tensile property suggested strong binding between nano TiO$_2$ /nano ZnO particles and PS chains preventing an easy break. PS loaded with nano TiO$_2$ or nano ZnO could enhance the strength of PS but could not enhance its toughness as evident from the steep stress-strain plot with almost no area under the curve. The superior mechanical properties demonstrated by PS nano composites over pristine PS promises the scope of their wide applications in various sectors where strength of the polymer material remains primary concern. The tensile strengths of PS, PS-TiO$_2$ and PS-ZnO decreased as the time of UV irradiation increased (Figure 3.10.3 A). The decrease in tensile strength attributed to the weakening or cleavage of bonds in polymer chain as a consequence of photodegradation upon UV light exposure. Nano TiO$_2$ and nano ZnO loaded PS composites underwent better decrease in tensile values under UV irradiation. Maximum decrease in the tensile strength upon UV irradiation was observed in PS-TiO$_2$ composites compared to pristine PS and PS-ZnO composites under study.

Flexural properties of PS and PS composites displayed similar trend as that of their tensile properties. Here too an enhancement in the flexural strength of PS was observed as the percentage of nano TiO$_2$ loading increased (Figure 3.10.2 B). The flexural strength observed for PS at 82.98 MPa increased drastically to 86.96 MPa in PS-3% ZnO and to 87.24 MPa in PS-3%TiO$_2$ (Figure 3.10.3 B). UV exposure resulted in a decrease in the values of flexural strengths as observed in the case of tensile strengths of the specimens. Maximum decrease in flexural strength upon UV irradiation was observed in PS-TiO$_2$ composites compared to other specimens under study, as observed in the case of tensile strength.

Depletion of mechanical property as a consequence of chain degradation was clearly understood from the above observation. The fact that nano TiO$_2$ and nano ZnO acted as good photocatalysts leading to photodegradation of PS was further supported by the study of mechanical properties of the composites. Nano TiO$_2$ proved to be more efficient compared to nano ZnO for the degradation of PS photochemically. Deterioration of mechanical properties of PS composites upon UV irradiation leads to their easy destructions in an accelerated way.
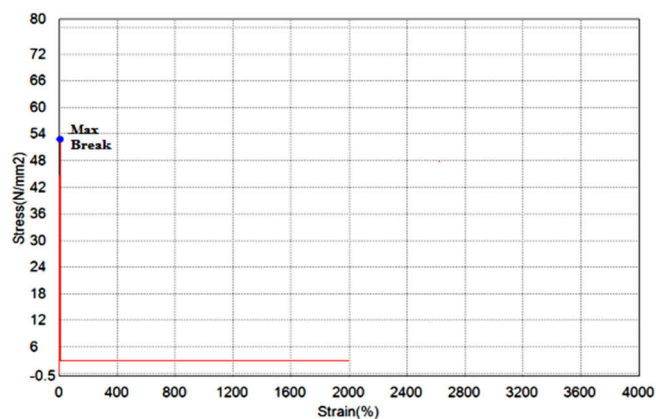
Figure 3.10.1. Stress-strain plot of pristine PS
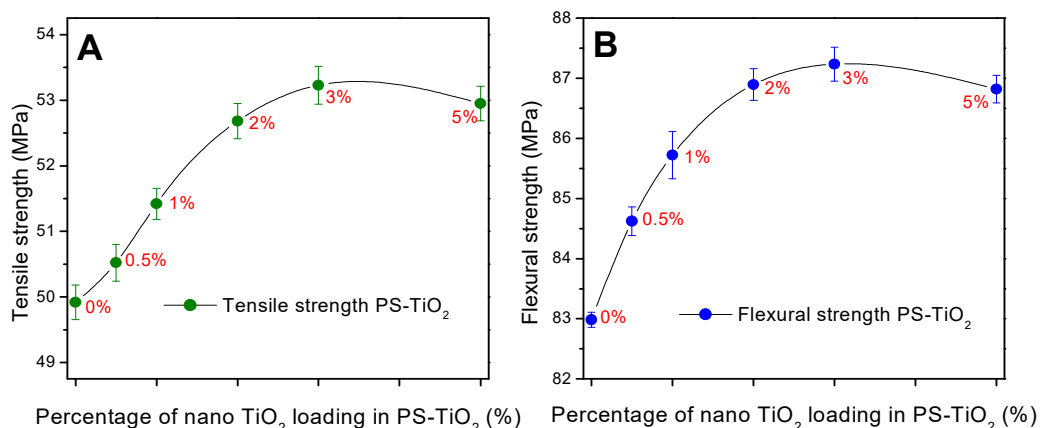
Figure 3.10.2. Tensile (A) and flexural (B) strengths of PS with different weight percentages of TiO$_2$
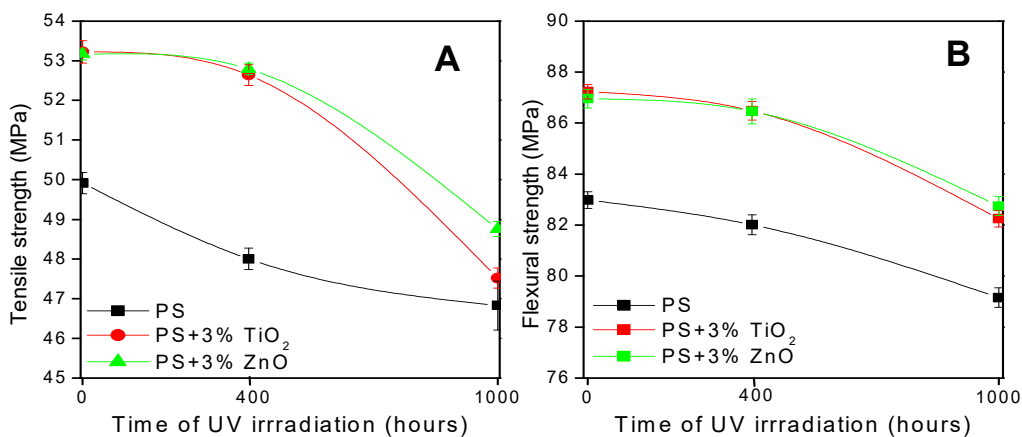
Figure 3.10.3. Tensile (A) and flexural (B) strengths of PS, PS-TiO$_2$ and PS-ZnO composites exposed to UV radiation for 0, 400 and 1000 h

3.4.7 Electrical Properties of PS, PS-TiO$_2$ and PS-ZnO composites

Dielectric breakdown or Breakdown voltage (BDV) and dielectric permittivity of the polymer specimens were measured. BDV of the polymer samples measured in

alternating current of frequency 50Hz is as illustrated in Figure 3.11.1. The BDV of PS before UV irradiation was determined to be 25.17 kV/mm. The BDV of PS-TiO$_2$ and PS-ZnO composites showed an increased value having 30.03 and 29.11 kV/mm respectively. The increased value of BDV of PS-TiO$_2$ and PS-ZnO composites indicated the existence of electron trapping and scattering interfaces between the polystyrene matrix and nano TiO$_2$/ZnO particles[44]. The dielectric breakdown of all the specimens decreased upon UV irradiation. The decrease in BDV with respect to UV irradiation time could be attributed to the formation of charge centers due to photodegradation. As evident from FTIR spectra, UV- DRS and GPC, the PS chain underwent chain scissions and photo-oxidation upon UV irradiation which had taken place through various ions/radical intermediates leading to the accumulation of charge centers over the polymer matrix. The charge centers formed along the polymer chain as a consequence of photodegradation lead to the flow of electric current much easier through the polymer matrix resulting in the breakdown of the specimens at comparatively lower voltage applied (lower BDV)[44]. Decrease in the BDV upon UV irradiation was predominant in PS-TiO$_2$ composite compared to PS and PS-ZnO composites.
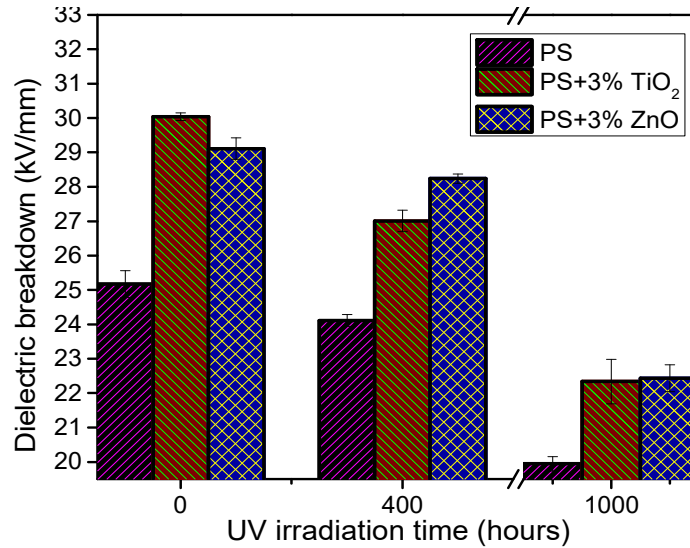
Figure 3.11.1*. Dielectric breakdown (breakdown voltage) of PS, PS-3%TiO$_2$ and PS-3%ZnO at varying UV irradiation time*

Dielectric permittivity (ε_r) of the polymer specimens were calculated from their determined capacitance value using equation 3.13[45,46].

$$C = \varepsilon_r \, \varepsilon_0 \left({A}/{t} \right) \tag{3.13}$$

Where, C is the capacitance; ε_r is the dielectric permittivity; ε_o is the dielectric permittivity of free space (8.854×10^{-12} F/m); A is the area and t is the thickness of the polymer specimens.

The composites (PS-TiO_2 and PS-ZnO) exhibited better dielectric permittivity (ε_r) compared to that of pristine PS (Figure 3.11.2). The ε_r of PS as well as PS composites increased upon UV irradiation. The formation of charge centers/dipoles as a result of photodegradation of PS resulted to an increase in ε_r which could most predominantly be seen in PS-TiO_2 composite compared to the other specimens.
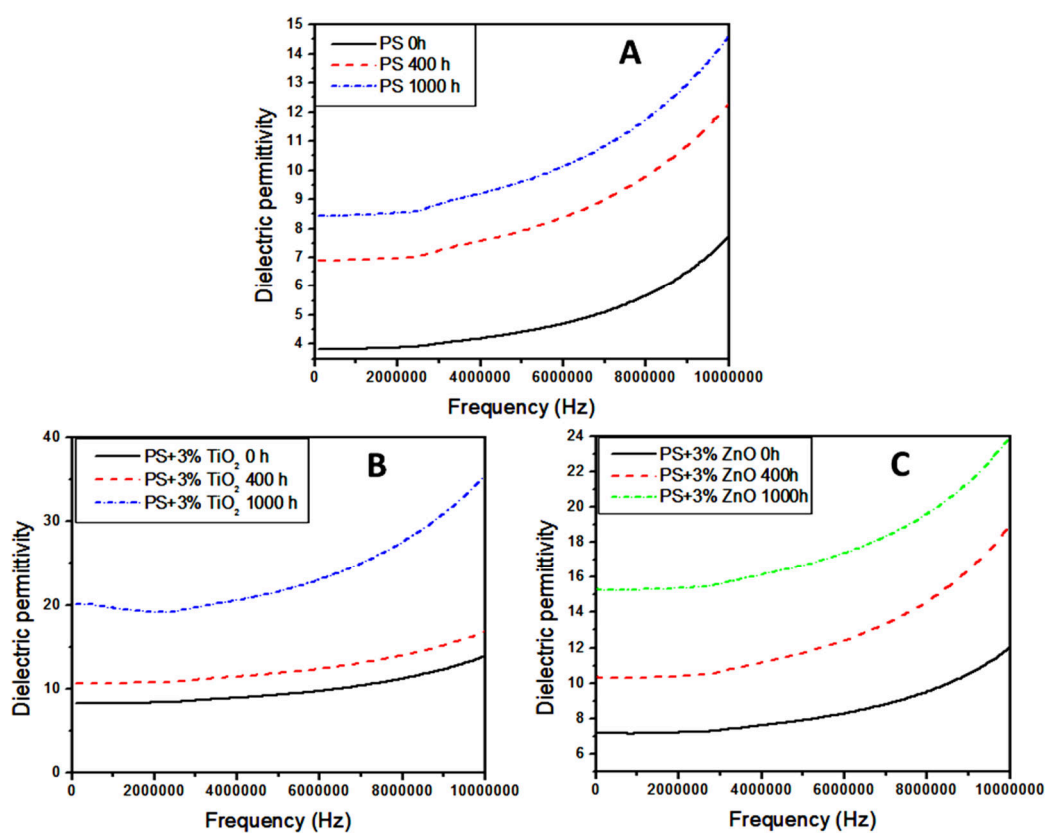
Figure 3.11.2. *Dielectric permittivity of PS, PS-3%TiO$_2$ and PS-3%ZnO at UV irradiation intervals of 0 h,400 h and 1000 h.*

3.4.8 Weight loss measurement

Weight loss of pristine PS as well as PS-composites was measured regularly after 200 hours of UV exposure time under same conditions. A considerable weight loss was observed in the samples with increase in the time of exposure. It was also found that the weight loss of TiO_2 loaded PS was found to be higher compared to that of PS-ZnO and pristine PS as shown in Figure 3.12. The observed weight loss may be due to

the escape of volatile species during the photodegradation process. Diffusion of H•, O_2•, OH• and OH_2• radical species created upon UV light exposure of the composites (as discussed in the forthcoming section 3.5) could diffuse through the polymer matrix leading to the formation of carbon centered radicals[47]. Successive radical interactions result in polymer chain cleavage with oxygen getting incorporated to the carbon center causing evolution of gases like CO_2, CO etc[48]. The interaction of H• and O_2• could also lead to the formation and evolution of H_2O molecules.
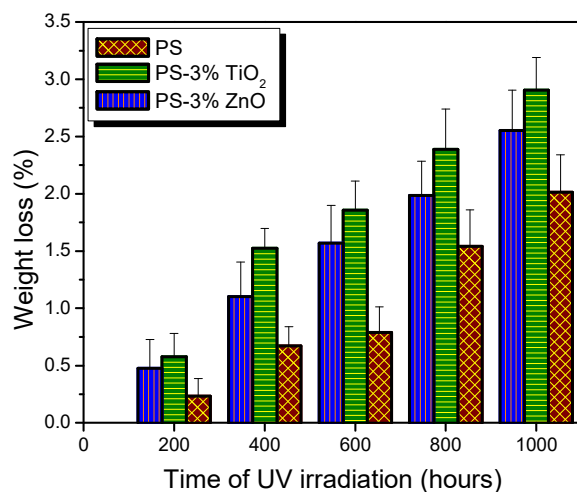
Figure 3.12. *Weight loss percentages of PS, PS-TiO$_2$ and PS-ZnO Composites at regular intervals of UV irradiation*

3.4.9 Visual observations
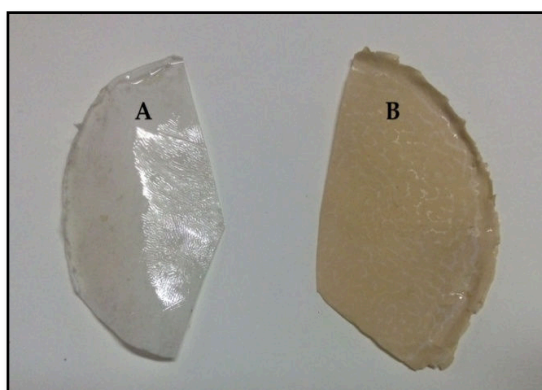
Figure 3.13. *PS-TiO$_2$ composite before UV irradiation (A) and after UV irradiation of 1000 h (B)*

A slight yellowing and loss of transparency was observed in UV exposed PS and PS-composite sheets. UV exposure of the specimens also resulted in increased

brittleness. Increased surface roughness and accumulation of yellow powders of depleted polymer layers could also be observed over the surface. These physically observed facts suggested that a change in optical and mechanical properties of PS as well as PS composites had occurred as a consequence of UV irradiation (Figure 3.13).

3.5 Mechanism of Photodegradation of PS under UV radiation

Table 3.4 highlights the important observations and conclusions drawn from various monitoring techniques of PS, PS-TiO$_2$ and PS-ZnO photodegradation explained above based on which the mechanism of photodegradation was proposed. In general, we could conclude that photo-oxidation mechanism has taken place as revealed by FTIR spectra.

Table 3.4. *Observations and conclusions made from GPC, FTIR spectroscopy, UV-DRS, electrical studies, weight loss measurements and SEM.*

Observations (with the increase in UV exposure time)	Conclusions
GPC • Decrease in $\overline{M}_w$ and $\overline{M}_n$ • Increase in no: of chain scission per macro molecule (S) • Increase in scission events per gram (N$_t$) • Decrease in mechanical properties of PS (Tensile & Flexural strengths)	• -C-C- or -C-H bond of the polymer chain has ruptured upon UV exposure • Scission of polymer chains was random
Electrical Studies • Dielectric strength (BDV) has decreased • Dielectric constant has increased	• Formation of charge centers • Decrease in the capacitance property
FTIR • Increase in the intensity of peaks corresponding to >C=O, -OH, -OOH, >C=C<, conjugated >C=C< etc • No change in the intensity of peaks corresponding to phenolic stretch or bend.	• Formation of new >C=C< linkages • Formation of new >C=O groups • Formation of new –OH, -OOH etc. groups • Formation of new >C=C-C=C-C=C< (conjugation) • Phenolic ring remains intact
UV-DRS • Decrease in characteristic absorption peaks of PS.	• Loss of characteristic absorption of PS due to photodegradation.

• Peaks have shifted towards higher wavelength.	• Red shift (Which could also be observed as slight yellowing of PS after irradiation)
Bandgap energy (E$_g$) calculations	
• Reduces to lower energy	• The ability of polymer specimens to absorb UV radiation has decreased.
Thermal studies (TGA)	
• Decrease in decomposition temperature	• Thermal stability has decreased due to chain scission within PS
Weight loss measurements	
• Weight loss was observed	• Loss of volatile species/gases formed as a consequence of photodegradation of PS
SEM	• Change in surface morphology of PS
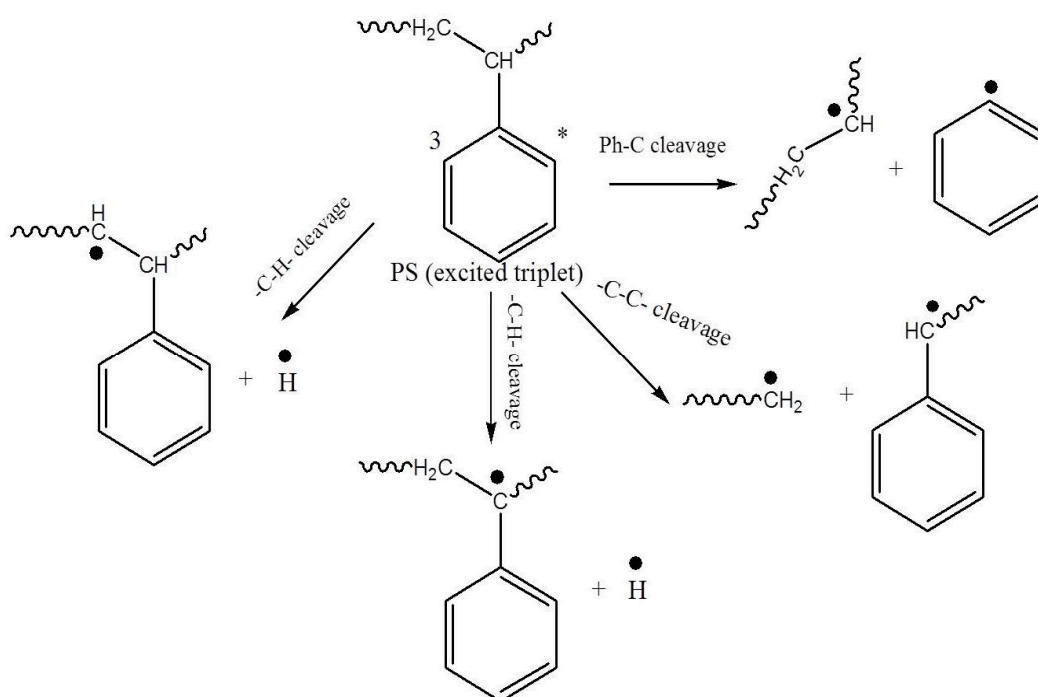
Figure 3.14.1. Possible -C-C- and/or -C-H- bond scissions at various sites of PS.

Mechanism of photodegradation of PS followed random pathways due to the multiple possibility of bond breakage, bond recombination, addition or elimination of various atoms. Based on all the above observations summarised in Table 3.4 the following mechanism could be considered.

Photodegradation starts with the phenolic rings of PS absorbing UV radiation and getting excited into singlet states and then undergoing an inter system crossing (ISC) into excited triplet states. Various photochemical reactions originate from excited

triplet state of benzene rings in PS. As evident from GPC data, -C-C- and/or -C-H-bond scissions at various sites could be initiated (Figure 3.14.1). FTIR spectra shows the evidence of formation of alkenic >C=C< double bonds and conjugated double bonds. This could be possible when cleavage of -C-H bonds belonging to adjacent carbons occur as represented in Figure 3.14.2.
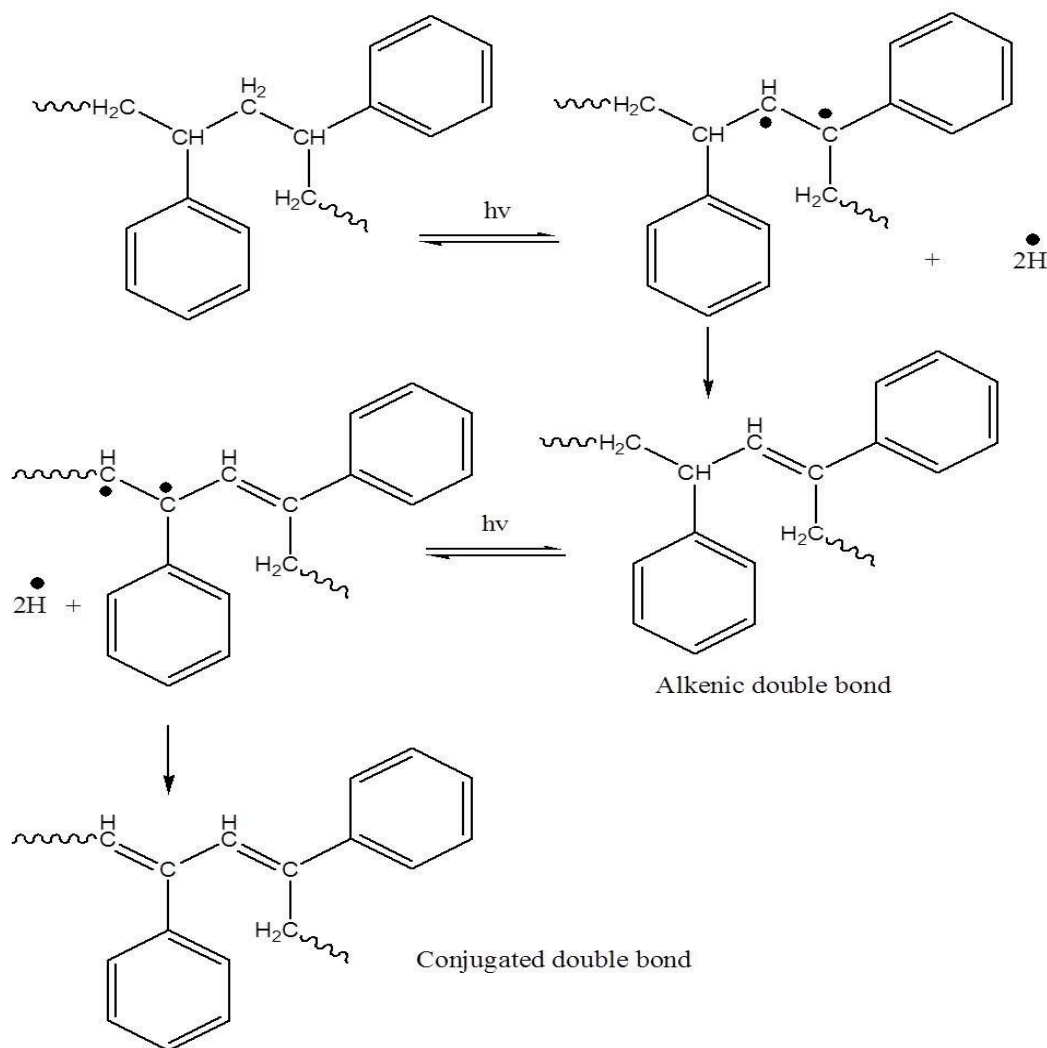
Figure 3.14.2. Formation of C=C double bond and conjugated double bonds.

Formation of >C=O, -OOH, -OH etc., groups were also evident from FTIR spectra. This could only be possible due to the adsorption of H_2O and O_2 molecules on the surface of PS. H_2O and O_2 could also be trapped on PS as impurities during the time of its manufacture. These molecules form reactive radicals or ions when interacted with incoming UV radiations. The radicals or ions could further interact

with PS chain forming macromolecular radicals or ions. The possible mechanism is as illustrated in Figure 3.14.3.
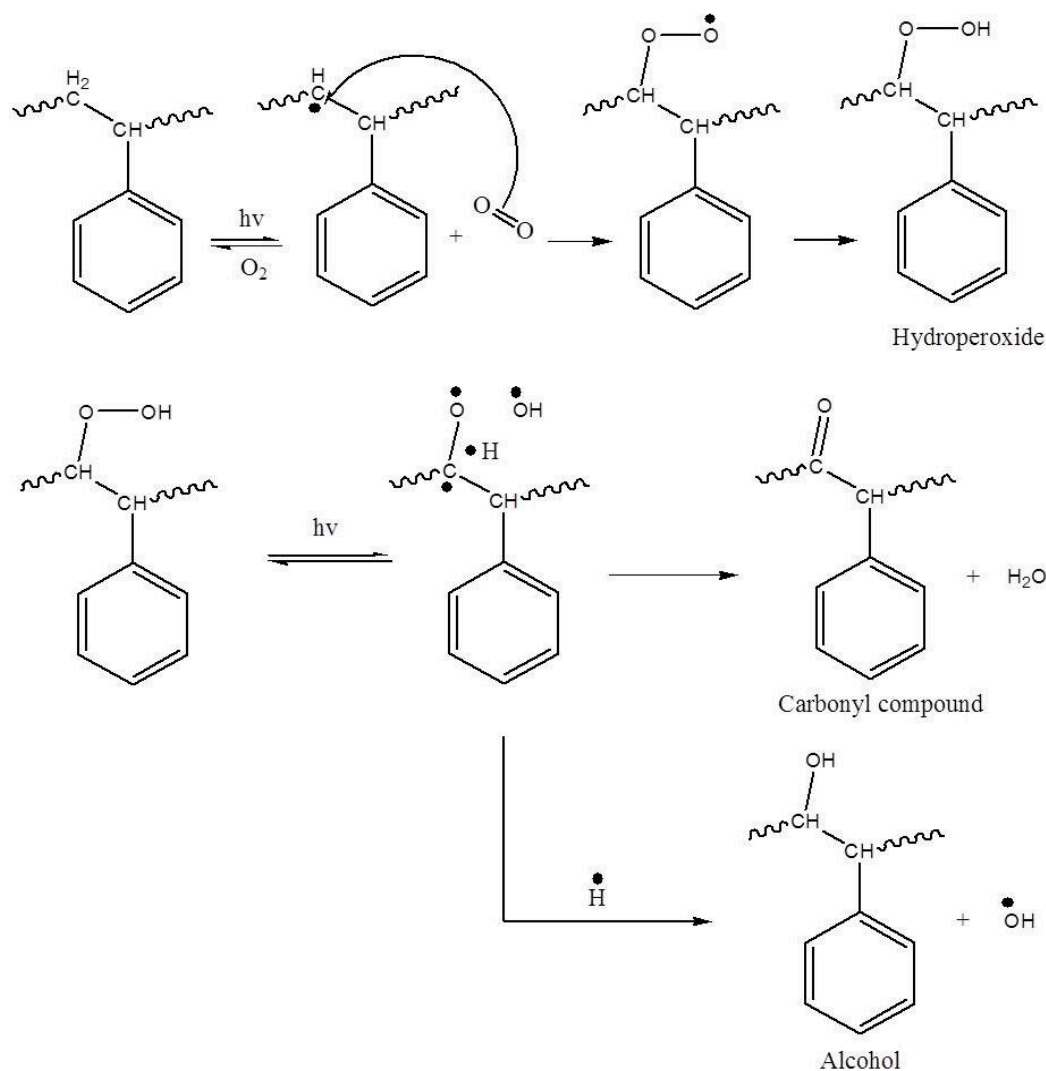
Figure 3.14.3. Formation of –OOH, >C=O and –OH.

Results of various analyses discussed above supported the fact that the rate of photodegradation of PS increased in the presence of nano TiO_2 as well as nano ZnO photocatalyst. It was also found that increase in the percentage of catalyst loaded to PS matrix showed no observable shift (red or blue shift) in the characteristic IR bands of PS. This observation made it clear that there existed no chemical bond between PS and TiO_2. The interaction between PS and TiO_2 was just physical. The mechanism of photodegradation of PS-TiO_2 and PS-ZnO composite occurs not only by PS absorbing UV radiations to get excited but also by nano TiO_2 and nano ZnO particles absorbing UV radiations creating electron-hole pair[49]. Electrons get excited from valence band

to conduction band leaving behind holes in valence band. Photocatalysis is possible only when the newly created electron-hole pair interacts with external atoms or molecules before recombining. Adsorbed O_2 molecules over the surface of ZnO or TiO_2 interact with the excited electrons in conduction band to form ions such as O^-, $O_2^{\bullet-}$ etc. H_2O or OH^- ions adsorbed on the surface of ZnO and TiO_2 results in the formation of H^+, $OH^\bullet$, OH^- etc species[50]. These newly created ions and radicals further interacts with PS chain forming hydroxides, hydroperoxides, carbonyl compounds etc. and the degradation process get propagated as illustrated through figure 3.14.1, 3.14.2 and 3.14.3.

3.6. Conclusion

Nano TiO_2 and ZnO particles were successfully synthesised and characterized. Sonication assisted sol-gel technique resulted in nano TiO_2 particles of spherical morphology. ZnO synthesised through sonication assisted precipitation results in nano ZnO particles resembling spheres with irregular edges. ZnO synthesis via hydrothermal method (controlled hydrolysis) resulted in spherical nano ZnO particles while that synthesised through hydrothermal method (uncontrolled hydrolysis) resulted in hexagonal ZnO rods of length reaching up to micro scale. Crystal growth occurred due to excess water resulted in larger size of these ZnO rods. XRD patterns of TiO_2 confirmed that anatase phase predominated over rutile phase. The synthesised nano TiO_2 and nano ZnO particles were successfully loaded into PS matrix whose photodegradation was studied in comparison with that of pristine PS. Photodegradation had taken place in solid phase PS sheets when subjected to UV irradiation (253 nm) under normal condition. Photodegradation of PS was proportional to UV irradiation time. The rate of photodegradation was higher in PS-TiO_2 and PS-ZnO composites and the rate of degradation increased with the increase in the percentage of photocatalysts loaded into PS matrix. The degradation of PS and PS-TiO_2 composite had taken place through photo-oxidative mechanism as evident from the increase in vibrational peaks corresponding to >C=O, -OH, -OOH, >C=C< and conjugated double bonds observed in FTIR spectroscopy upon UV irradiation. Through UV-DRS, changes in regular absorption bands in the UV region were also observed for PS, PS-TiO_2 and PS-ZnO composites upon irradiation. Weight loss of PS-composites was more compared to pristine PS films upon increase in UV

irradiation time. Tensile and flexural properties of PS as well as PS- composites decreased with the increase in the time of irradiation. Dielectric strength of the specimens increased with UV exposure time. The decrease in dielectric breakdown values measured in AC at a frequency of 50 Hz suggested the formation of charged centers upon UV irradiation. These results highlighted the fact that depletion in mechanical, electrical and chemical properties has taken place as a result of UV irradiation of PS, PS-TiO_2 and PS-ZnO composites. Better photocatalytic efficiency for the degradation of PS was exhibited by nano TiO_2 in comparison with nano ZnO particles.

References

1. Yousif, E. & Haddad, R. Photodegradation and photostabilization of polymers, especially polystyrene: review. *Springerplus* **2**, 398 (2013).
2. Ali, G. Q. *et al.* Photostability and Performance of Polystyrene Films Containing 1,2,4-Triazole-3-thiol Ring System Schiff Bases. *Molecules* **21**, (2016).
3. Grassie, N. & Weir, N. A. The photooxidation of polymers. IV. A note on the coloration of polystyrene. *J. Appl. Polym. Sci.* **9**, 999–1003 (1965).
4. Rabek, J. & Ranby, B. Studied on the photooxidation mechanism of polymers, photolysis and photooxidation of polystyrene. *J. Polym. Sci.* **12**, (1974).
5. Lucki, J. & Rånby, B. Photo-oxidation of polystyrene—Part I. Formation of hydroperoxide groups in photo-oxidised polystyrene and 2-phenyl butane. *Polym. Degrad. Stab.* **1**, 1–16 (1979).
6. Al Safi, S. A., Al Mouamin, T. M., Al Sieadi, W. N. & Al Ani, K. E. Irradiation Effect on Photodegradation of Pure and Plasticized Poly (4-Methylstyrene) in Solid Films. *Mater. Sci. Appl.* **5**, 300 (2014).
7. Jane, M., Tryon, M. & Achhammer, B. G. Study of degradation of polystyrene, using ultraviolet spectrophotometry. *J. Res. Natl. Bur. Stand. (1934).* **51**, (1953).
8. Timóteo, G. A. V, Fechine, G. J. M. & Rabello, M. S. Stress Cracking and Photodegradation: The Combination of Two Major Causes of HIPS Failure. *Macromol. Symp.* **258**, 162–169 (2007).
9. Ani, K. E. Al & Ramadhan, A. E. Photodegradation kinetics of poly(para-substituted styrene) in solution. *Polym. Degrad. Stab.* **93**, 1590–1596 (2008).
10. Rincón G., A. Photodegradation of chain halogenated polystyrene: Poly (c-chloro and c-bromostyrene)s. *Polym. Bull.* **38**, 191–196 (1997).
11. Gewert, B., Plassmann, M., Sandblom, O. & MacLeod, M. Identification of Chain Scission Products Released to Water by Plastic Exposed to Ultraviolet Light. *Environ. Sci. Technol. Lett.* **5**, 272–276 (2018).
12. Lei, Y., Lei, H. & Huo, J. Innovative controllable photocatalytic degradation of polystyrene with hindered amine modified aromatic polyamide dendrimer/ polystyrene-grafted-TiO2 photocatalyst under solar light irradiation. *Polym. Degrad. Stab.* **118**, 1–9 (2015).
13. Retamoso, C. *et al.* Effect of particle size on the photocatalytic activity of modified rutile sand (TiO2) for the discoloration of methylene blue in water. *J. Photochem. Photobiol. A Chem.* **378**, 136–141 (2019).
14. Dodd, A. C., McKinley, A. J., Saunders, M. & Tsuzuki, T. Effect of Particle Size on the Photocatalytic Activity of Nanoparticulate Zinc Oxide. *J. Nanoparticle Res.* **8**, 43 (2006).
15. Adhikari, S. & Lachgar, A. Effect of particle size on the photocatalytic activity of

BiNbO4 under visible light irradiation. in *Journal of Physics: Conference Series* vol. 758 (2016).

16. Khan, M. M., Adil, S. F. & Al-Mayouf, A. Metal oxides as photocatalysts. *J. Saudi Chem. Soc.* **19**, 462–464 (2015).

17. Riente, P. & Noël, T. Application of metal oxide semiconductors in light-driven organic transformations. *Catal. Sci. Technol.* **9**, 5186–5232 (2019).

18. Kiriakidis, G. & Binas, V. Metal oxide semiconductors as visible light photocatalysts. *J. Korean Phys. Soc.* **65**, 297–302 (2014).

19. Pelizzetti, E. & Minero, C. Metal Oxides as Photocatalysts for Environmental Detoxification. *Comments Inorg. Chem.* **15**, 297–337 (1994).

20. Kamat, P. V & Meisel, D. Nanoscience opportunities in environmental remediation. *Comptes Rendus Chime* **6**, 999–1007 (2003).

21. Kumar, S. G. & Rao, K. S. R. K. Comparison of modification strategies towards enhanced charge carrier separation and photocatalytic degradation activity of metal oxide semiconductors (TiO2, WO3 and ZnO). *Appl. Surf. Sci.* **31517**–**3**, S0169-4332 (2016).

22. Chen, D. & Ray, A. K. Removal of toxic metal ions from wastewater by semiconductor photocatalysis. *Chem. Eng. Sci.* **56**, 1561–1570 (2001).

23. He, J.-A., Mosurkal, R., Samuelson, L. A., Li, L. & Kumar, J. Dye-sensitized Solar Cell Fabricated by Electrostatic Layer-by-Layer Assembly of Amphoteric TiO2 Nanoparticles. *Langmuir* **19**, 2169–2174 (2003).

24. Chen, X. & Mao, S. S. Titanium Dioxide Nanomaterials: Synthesis, Properties, Modifications, and Applications. *Chem. Rev.* **107**, 2891–2959 (2007).

25. Vijayalakshmi, R. & Rajendran, V. Synthesis and characterization of nano-TiO 2 via different methods. **4**, 1183–1190 (2012).

26. Thomas, R. T., Nair, V. & Sandhyarani, N. TiO2 nanoparticle assisted solid phase photocatalytic degradation of polythene film: A mechanistic investigation. *Colloids Surfaces A Physicochem. Eng. Asp.* **422**, 1–9 (2013).

27. Kavitha, T; Rajendran, A. D. A. Synthesis and Characterization of Nanosized TiO2 Powder Derived From a Sol-Gel Process an Acidic Condition. *Int. J. Eng. Sci. Emerg. Technol.* **4**, 90–95 (2013).

28. Kavitha, T., Rajendran, A. & Durairajan, A. Synthesis, characterization of TiO2 nano powder and water based nanofluids using two step method. *Eur. J. Appl. Eng. Sci. Res.* **1**, 235–240 (2012).

29. Baruwati, B., Kumar, D. K. & Manorama, S. V. Hydrothermal synthesis of highly crystalline ZnO nanoparticles : A competitive sensor for LPG and EtOH. *Sensors Actuators B* **119**, 676–682 (2006).

30. Arami, H., Mazloumi, M., Khalifehzadeh, R. & Sadrnezhaad, S. K. Sonochemical preparation of TiO2 nanoparticles. *Mater. Lett.* **61**, 4559–4561 (2007).

31. Thamaphat, K., Limsuwan, P., Ngotawornchai, B. & others. Phase characterization of TiO2 powder by XRD and TEM. *Kasetsart J.(Nat. Sci.)* **42**, 357–361 (2008).

32. Hassanjani-Roshan, A., Kazemzadeh, S. M., Vaezi, M. R. & Shokuhfar, A. Effect of sonication power on the sonochemical synthesis of titania nanoparticles. *J. Ceram. Process. Res.* **12**, 299–303 (2011).

33. Byrne, C., Fagan, R., Hinder, S., McCormack, D. E. & Pillai, S. C. New approach of modifying the anatase to rutile transition temperature in TiO2 photocatalysts. *RSC Adv.* **6**, 95232–95238 (2016).

34. Lee, H. Y. & Kale, G. M. Hydrothermal Synthesis and Characterization of Nano-TiO2. *Int. J. Appl. Ceram. Technol.* **665**, 657–665 (2008).

35. Tian, J. *et al.* Photocatalyst of TiO2/ZnO nano composite film: Preparation, characterization, and photodegradation activity of methyl orange. *Surf. Coatings Technol.* **204**, 205–214 (2009).

36. López, R. & Gómez, R. Band-gap energy estimation from diffuse reflectance measurements on sol-gel and commercial TiO2: a comparative study. *J. Sol-Gel Sci. Technol.* **61**, 1–7 (2012).

37. Reddy, K. M., Manorama, S. V & Reddy, A. R. Bandgap studies on anatase titanium dioxide nanoparticles. *Mater. Chem. Phys.* **78**, 239–245 (2003).
38. Chandran, A., Francis, N., Jose, T. & George, K. Synthesis, structural characterization and optical bandgap determination of ZnS nanoparticles. *SB Acad. Rev.* **17**, 17–21 (2010).
39. Jaleh, B. *et al.* UV-degradation effect on optical and surface properties of polystyrene-TiO2 nanocomposite film. *J. Iran. Chem. Soc.* **8**, S161--S168 (2011).
40. Abdelghany, A. M., Abdelrazek, E. M., Badr, S. I. & Morsi, M. A. Effect of gamma-irradiation on (PEO/PVP)/Au nanocomposite: Materials for electrochemical and optical applications. *Mater. Des.* **97**, 532–543 (2016).
41. Sangawar, V. & Golchha, M. Evolution of the optical properties of Polystyrene thin films filled with Zinc Oxide nanoparticles. *Int J Sci Eng Res* **4**, 2700–2705 (2013).
42. Alwan, T. J. Refractive index dispersion and optical properties of dye doped Polystyrene films. *Malaysian Polym. J.* **5**, 204–213 (2010).
43. Sirohi, S. & Sharma, T. P. Bandgaps of cadmium telluride sintered film. *Opt. Mater. (Amst).* **13**, 267–269 (1999).
44. Wang, D., Huang, M., Zha, J., Zhao, J. & Dang, Z. Dielectric Properties of Polystyrene Based Composites Filled with Core-Shell BaTiO 3 / Polystyrene Hybrid Nanoparticles. *IEEE Trans. Dielectr. Electr. Insul.* **21**, 1438–1445 (2014).
45. Rao, Y., Qu, J., Marinis, T. & Wong, C. P. A precise numerical prediction of effective dielectric constant for polymer-ceramic composite based on effective-medium theory. *IEEE Trans. Components Packag. Technol.* **23**, 680–683 (2000).
46. Grove, T. T., Masters, M. F. & Miers, R. E. Determining dielectric constants using a parallel plate capacitor. *Am. J. Phys.* **73**, 52–56 (2005).
47. Hwang, D., Shul, Y. & Chu, Y. Photodegradation behavior of the polycarbonate/TiO2 composite films under the UV irradiation in ambient air condition. *Polym. Compos.* **36**, 1462–1468 (2014).
48. Cho, S. & Choi, W. Solid-phase photocatalytic degradation of PVC–TiO2 polymer composites. *J. Photochem. Photobiol. A Chem.* **143**, 221–228 (2001).
49. Shang, J., Chai, M. & Zhu, Y. Solid-phase photocatalytic degradation of polystyrene plastic with TiO2 as photocatalyst. *J. Solid State Chem.* **174**, 104–110 (2003).
50. Nagaveni, K., Hegde, M. S., Ravishankar, N. & Subbanna, G. N. Synthesis and Structure of Nanocrystalline TiO 2 with Lower Band Gap Showing High Photocatalytic Activity. *Langmuir* **9**, 2900–2907 (2004).

Chapter 4

Accelerated Photodegradation of Polystyrene Using Nano TiO$_2$ and ZnO Surface Modified with Polyaniline

Abstract

Polyaniline (PANI) was synthesised using chemical oxidation method by the polymerisation of aniline in the presence of ammonium peroxodisulphate (APS), in HCl medium. Composites of TiO$_2$-PANI and ZnO-PANI were also developed using the same method where aniline was polymerised over the surface of dispersed TiO$_2$ or ZnO. TiO$_2$-PANI/ZnO-PANI composites with 3, 10 and 30 mol percentages of PANI with respect to TiO$_2$/ZnO were prepared. XRD analysis proved that the crystal morphology of TiO$_2$ as well as ZnO was retained in the composites. Strong molecular interactions existed between PANI and TiO$_2$/ZnO as evident from FTIR spectroscopy, supported by UV-DRS. TiO$_2$-PANI existed as dispersed particles having crystal nature. ZnO-PANI composites however showed some aggregations. All the TiO$_2$-PANI and ZnO-PANI photocatalyst composites were loaded into PS matrix whose photodegradation was studied in the presence of UV radiation. PS-TiO$_2$-PANI and well as PS-ZnO-PANI was mechanically stronger and thermally more stable compared to PS-TiO$_2$ and PS-ZnO. PS-composites underwent photo-oxidative degradation on UV irradiation. The mechanical, electrical and thermal properties of the PS-composites showed variations upon UV irradiation. It was evident that the photocatalytic efficiency of TiO$_2$ and ZnO was enhanced considerably on coupling them with PANI. PS-TiO$_2$-PANI underwent better photodegradation compared to PS-ZnO-PANI.

4.1. Introduction

One of the effective methods that could be employed for the enhancement of photocatalytic activity of semiconductor metal oxide is coupling them with a suitable conjugated system[1,2]. Inorganic semiconductors blended with conducting polymers have gained much attention due to their widespread applications which include photocatalysis[3,4]. Conjugated polymers like polyaniline (PANI) have been of quite interest to the researchers due to its astonishing chemistry and physics[5]. The advantages of PANI include high stability in environment (due to conjugation), high efficiency in carrying charges, low cost, ease for preparation etc. Due to these reasons PANI has been adopted in various fields of applications including photochemistry, electrochemistry, optics, biosensing etc[6–9]. The photochemistry of semiconductor metal oxides which are limited to UV region could be extended to visible region also upon blending them with PANI. The extended π-conjugation of PANI which can exchange charge carriers with semiconductor metal oxides to which they are blended is the primary reason for this. TiO_2 and ZnO are n-type semiconductors[10] and PANI is considered as p-type semiconducting polymer[11]. The combination of p-type PANI semiconductor with n-type TiO_2 or ZnO semiconductors hence open up the path for developing new hybrid composite with good capacitance property and stability[12]. TiO_2-PANI and ZnO-PANI blends exhibit enhanced photocatalytic behaviour[13–16]. PANI acts as photosensitizer that can enhance the photocatalytic efficiency of TiO_2 and ZnO to which it is associated. As PANI could absorb in the UV as well as visible region of the spectra, incorporation of PANI into TiO_2 and ZnO particles could reduce their band gap energies[17]. Surface modified TiO_2 and ZnO using PANI could hence bring about better quantum yield.

This chapter presents the photodegradation studies of PS using organo-inorganic photocatalysts TiO_2-PANI and ZnO-PANI under UV radiation. Different combination of TiO_2-PANI and ZnO-PANI has been synthesized. Chemical oxidative polymerization has been employed for the polymerization of aniline over dispersed nano particles (TiO_2 or ZnO). This method is quite simple and allows the polymerization of polyaniline over the surface of nano particles.

Section I

Synthesis and characterisation of TiO₂-PANI and ZnO-PANI composites

4.2. Methods

4.2.1. Synthesis of PANI

Polyaniline (PANI) was synthesized by chemical oxidative polymerization method. 1.25ml of aniline was dissolved in 125 ml HCl (1M) solution in a beaker (beaker A) and stirred for 15 minutes using a magnetic stirrer. 3.125 g of ammonium peroxodisulphate (APS) was dissolved in 125 ml HCl (1M) in another beaker (beaker B) and stirred for 15 minutes. Beaker 'A' was now taken into an ice bath. Contents in beaker 'B' was now added drop wise into beaker 'A' with vigorous stirring. The beaker was then kept under stirring for 12 hours. The contents in the beaker turned dark blue after 10 minutes of stirring. The colour of solution was then transformed into dark green after another half an hour. The dark green colour remained unchanged thereafter. The green colour indicated the possibility of PANI existing as emeraldine salt. The green coloured solid mass was filtered out from solution. This was then washed using acetone followed by distilled water several times. The dark green solid mass hence obtained was dried at 60°C for 12 hours and ground into fine powder[18–21].

4.2.2. Synthesis of nano TiO₂-PANI composites

Insitu polymerisation of aniline (via chemical oxidative polymerization) over dispersed TiO₂ was followed for the development of TiO₂-PANI nano composite. The number of moles of nano TiO₂ and aniline taken were varied in order to get composites with varying mole percentages. In order to prepare TiO₂-3% PANI composite (3 mol % of PANI with respect to TiO₂), the following procedure was adopted. Typically, 0.034 ml of aniline was dissolved in 35 ml (1M) HCl in beaker 'A' and stirred for 15 minutes. 0.966 g of nano TiO₂ was added into the beaker slowly and by vigorous stirring. The mixture was now sonicated using probe sonicator for 30 minutes. Simultaneously 0.086 g of APS was dissolved in 35 ml (1M) HCl and stirred for 15 minutes in another beaker (B). Beaker 'A' was now

immediately transferred into an ice bath with vigorous stirring and the contents of beaker 'B' was added drop wise into beaker 'A'. The mixture was now stirred vigorously for 12 hours. The green solid mass was filtered out from the solution, washed with acetone followed by distilled water and dried for 12 hours at 60°C[22].

Similar procedure was used for the synthesis of TiO_2-10% PANI and TiO_2-30% PANI composites. The mole percentages of the components taken were varied in each case.

The table 4.1.1 below represents the weights of various components added for the TiO_2-PANI composite preparation.

Table 4.1.1. Mole percentages and weights of the components in TiO_2-PANI composites

Composite	TiO₂ Mole %	PANI Mole %	Weight of nano TiO₂ (g)	Volume of aniline (ml)	Weight of APS in (g)
TiO_2+3%PANI	97	3	0.966	0.034	0.086
TiO_2+10%PANI	90	10	0.886	0.114	0.286
TiO_2+30%PANI	70	30	0.657	0.343	0.857

4.2.3. Synthesis of nano ZnO-PANI composites

ZnO-PANI Composites were also developed adopting the same technique as that used for the preparation of TiO_2-PANI composites[23]. Nano TiO_2 has been replaced by nano ZnO here. The table 4.1.2 below represents the weight of the components taken along with their composition in ZnO-PANI composites.

Table 4.1.2. Mole percentages and weights of the components in ZnO-PANI composites

Composite	ZnO Mole %	PANI Mole %	Weight of nano ZnO (g)	Volume of aniline (ml)	Weight of APS in (g)
ZnO+3%PANI	97	3	0.966	0.034	0.084
ZnO+10%PANI	90	10	0.888	0.112	0.280
ZnO+30%PANI	70	30	0.663	0.337	0.841

4.3. Results and Discussion

4.3.1. Powdered XRD
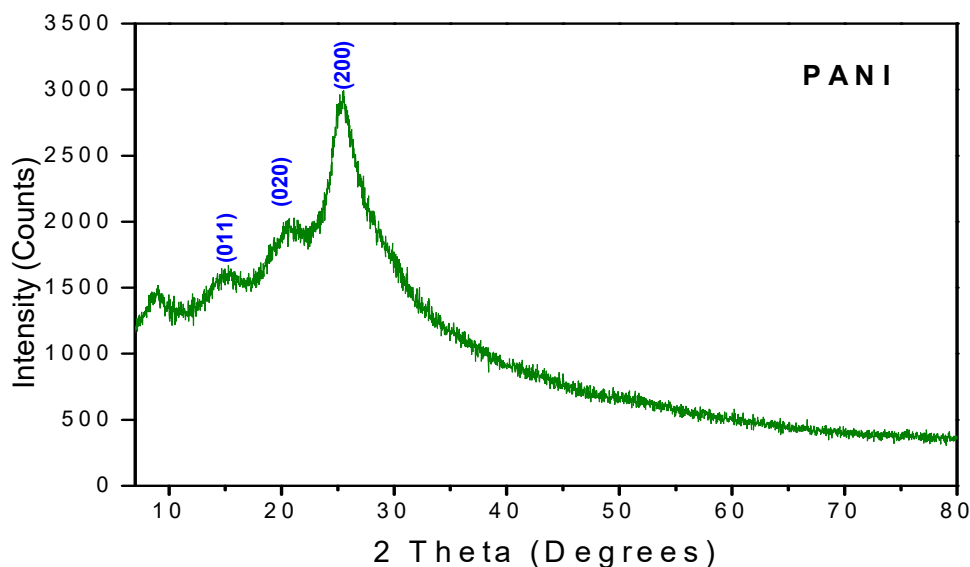
Figure 4.1.1*. XRD pattern of PANI*

The X-ray diffractogram of the synthesized PANI observed at 2θ angles 15.16°, 21.11° and 25.59° correspond to the characteristic crystal planes (011), (020) and (200) of PANI respectively (Figure.4.1.1)[24]. These three broad peaks suggest that PANI matrix exist as semi crystalline structures of very short termed orders[25]. The scattering of PANI chains along the inter planar spacing is the reason behind broadening of the observed peaks mentioned above[26]. The XRD pattern of synthesized PANI also matches with the pattern of PANI-HCl salt available in the literature[27]. The peak at 2θ =21.11° could be ascribed to the PANI chains arranged parallel to each other (the characteristic distance between the two chains holding benzene ring parallel to each other is highlighted through this peak) while 2θ =25.59° represents the perpendicular arrangement of the polymer chain[28]. The relative higher intensity of the 2θ =25.59° peak in comparison with that of 2θ =21.11° proves the existence of PANI as emeraldine salt (doped with HCl)[29]. In addition to these three peaks, another lesser intense broad peak observed at 2θ = 9.03° signifies the highly ordered structure (crystalline nature) of PANI where the d spacing is high[27]. The penetration of dopants into the PANI matrix results in such an increased crystallinity due to the increase in the d spacing[30]. Crystallinity also arises as a consequence of

repeated benzenoid and quinoid rings in the chain[31]. The coexistence of amorphous domain with crystal domains could hence be assigned for the synthesized PANI matrix. The XRD patterns as well as visually observed dark green colour of PANI suggested its existence as emeraldine salt (HCl doped)[32].
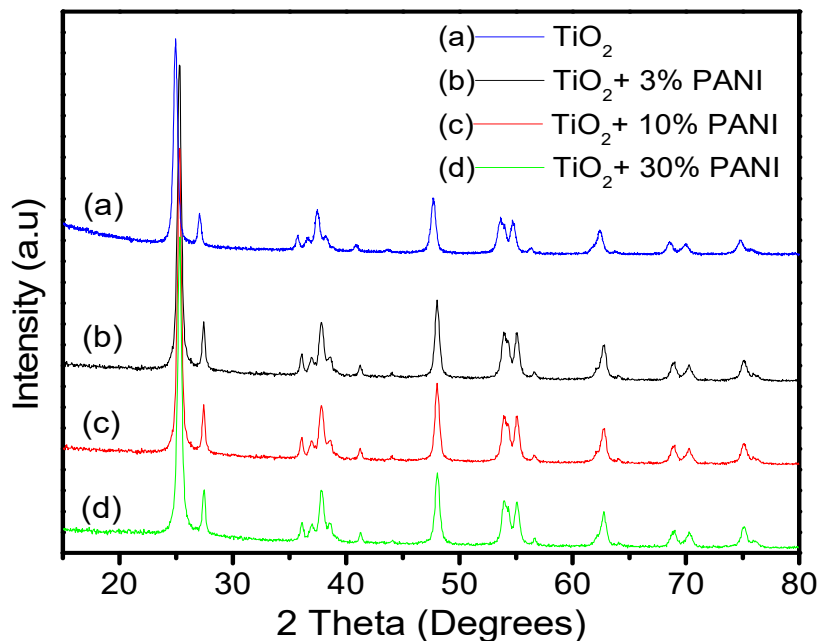
Figure 4.1.2*. XRD pattern of nano TiO₂-PANI composites*

The XRD patterns of TiO₂-PANI composites (Figure 4.1.2 b, c & d) on the other hand could not be easily differentiated from that of pristine TiO₂ (Figure 4.1.2 a). All the peaks corresponding to the TiO₂ with predominant anatase phase and a few rutile phase particles were observed. The presence of PANI however could not be identified through XRD. The crystal peaks of PANI have been suppressed by TiO₂. The hampering of crystal growth of PANI by TiO₂ is the reason for this[16]. The growth of PANI polymer chain in a solution of dispersed TiO₂ is influenced by TiO₂ particles. TiO₂ particles hamper the free chain growth of PANI by adsorbing them over TiO₂ surface and tethering their chains leading to a decrease in the degree of crystallinity[33,34]. The crystal patterns of PANI would be decreased to an appreciable extent and in some cases they may even disappear as in Figure 4.1.2 above. There was no observable shift or absence of any characteristic peaks corresponding to TiO₂ in TiO₂-PANI composites. The fact that associated PANI had no significant effect in altering the crystallinity of TiO₂ was hence concluded. From the XRD patterns of TiO₂-PANI composites it could be concluded that PANI matrix have been well adsorbed by nano TiO₂ particles nullifying their aggregation (if PANI has aggregated

with high degree of polymerization, peaks corresponding to PANI would have been observed).
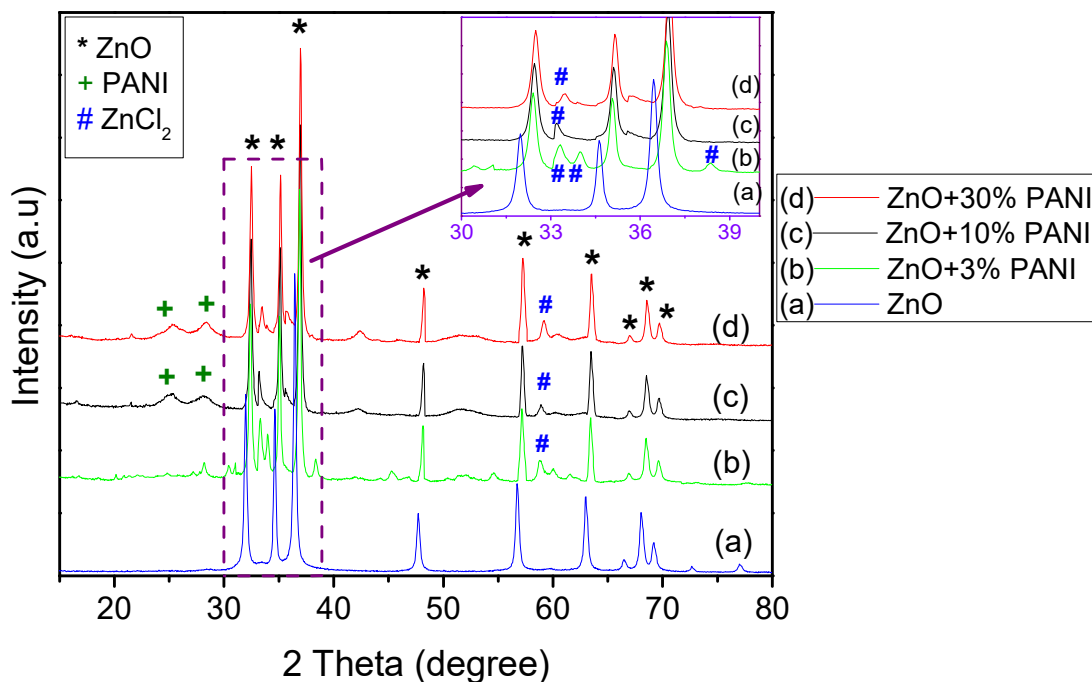
Figure 4.1.3. XRD pattern of nano ZnO-PANI composites

XRD patterns of ZnO-PANI composites exhibited all the characteristic peaks of ZnO corresponding to wurtzite hexagonal structure (Figure 4.1.3). The peak positions of ZnO had only negligibly shifted in all the ZnO-PANI composites revealing the fact that the associated PANI had no much influence on the crystal structure of ZnO. The composites too existed in wurtzite structure. In addition to the characteristic peaks of ZnO, peaks corresponding to $ZnCl_2$ were also observed at $2\theta = 32°$, $33°$ and $55°$ for the composites. ZnO-PANI composites were developed by insitu growth of PANI over the surface of dispersed ZnO particles in aqueous media containing HCl. ZnO particles can interact with the HCl molecules to form $ZnCl_2$ salt as per the following equation[35].

$$ZnO + 2\,HCl \rightarrow \; ZnCl_2 + H_2O \tag{4.1}$$

The formation of $ZnCl_2$ as per equation (4.1) is however far less, as the strength of HCl in the solution is just 1M and also the developing PANI polymer chains utilizes the H^+ and Cl^- ions from the solution leading to further decrease in the concentration of these ions in the solution. The presence of PANI associated with ZnO was

observed as very low intense peaks. The peaks observed at 2θ angles 15.16°, 21.11° and 25.59° for synthesized PANI were shifted to new peaks observed at higher 2θ angles for ZnO-10% PANI and ZnO-30% PANI composites. The composite ZnO-3% PANI exhibited no peaks corresponding to PANI. This could be explained on the basis of tethering of PANI chains and hampering of crystal growth by ZnO as discussed in the case of TiO_2-PANI composites.

The crystallite sizes of the composite particles were calculated using Debye Scherrer's formula and the values obtained are as tabulated below (Table 4.2.1).

Table 4.2.1. *Values of crystallite sizes of TiO_2-PANI and ZnO-PANI composites*

TiO_2-PANI	Crystallite size (nm)	ZnO-PANI	Crystallite size (nm)
TiO_2+0% PANI	18.9	ZnO+0% PANI	30.7
TiO_2+3% PANI	20.5	ZnO +3% PANI	31.0
TiO_2+10% PANI	20.7	ZnO +10% PANI	31.1
TiO_2+30% PANI	20.8	ZnO +30% PANI	31.5

The crystallite size of both TiO_2-PANI and ZnO-PANI composites increased compared to pristine TiO_2 and pristine ZnO respectively. We could also observe a negligible increase in the crystallite sizes of the TiO_2-PANI and ZnO-PANI composites with the increase in the percentage of PANI.

The interplanar distance (d) calculated for TiO_2-PANI (Table 4.2.2) as well as ZnO-PANI (Table 4.2.3) show only a negligible decrease compared to that of pristine TiO_2 and ZnO respectively. It could be assumed that the crystal morphology of TiO_2 is not much affected on PANI incorporation.

Table 4.2.2. *Interplanar distance (d) corresponding to each 2θ angles of TiO_2-PANI composites in comparison to pristine TiO_2*

TiO_2		TiO_2 +3% PANI		TiO_2 +10% PANI		TiO_2 +30% PANI	
2 θ°	d (Å)	2 θ°	d (Å)	2 θ°	d (Å)	2 θ°	d (Å)
24.94	3.57	25.29	3.52	25.29	3.52	25.32	3.51
27.07	3.29	27.41	3.25	27.41	3.25	27.49	3.24
35.71	2.51	36.09	2.49	36.09	2.49	36.12	2.48

37.44	2.4	37.81	2.38	37.81	2.38	37.89	2.37
40.89	2.21	41.21	2.19	41.23	2.19	41.26	2.19
47.7	1.91	48.02	1.89	48.02	1.89	48.04	1.89
53.64	1.71	53.92	1.70	53.92	1.70	53.97	1.70
54.73	1.68	55.05	1.67	55.09	1.67	55.1	1.67
62.4	1.49	62.74	1.48	62.79	1.48	62.74	1.48
68.5	1.37	69.01	1.36	69.03	1.36	69.01	1.36
69.95	1.34	70.26	1.34	70.29	1.34	70.26	1.34
74.8	1.27	75.13	1.26	75.15	1.26	75.13	1.26

Table 4.2.3. *Interplanar distance (d) corresponding to each 2θ angles of ZnO-PANI composites in comparison to pristine ZnO*

ZnO		ZnO +3% PANI		ZnO +10% PANI		ZnO +30% PANI	
2 θ°	d (Ǎ)	2 θ°	d (Ǎ)	2 θ°	d (Ǎ)	2 θ°	d (Ǎ)
31.97	2.80	32.41	2.76	32.45	2.76	32.50	2.75
34.62	2.59	35.06	2.56	35.11	2.55	35.13	2.55
36.45	2.46	36.88	2.44	36.93	2.43	36.97	2.43
47.71	1.90	48.14	1.89	48.19	1.89	48.24	1.88
56.75	1.62	57.19	1.61	57.24	1.61	57.26	1.61
63.01	1.47	63.43	1.47	63.48	1.46	63.53	1.46
66.48	1.41	66.89	1.40	66.95	1.40	67.00	1.40
68.05	1.38	68.47	1.37	68.52	1.37	68.57	1.37
69.18	1.36	69.6	1.35	69.65	1.35	69.70	1.35
72.70	1.30						
77.00	1.24						

4.3.2. FESEM, EDX, HRTEM and SAED

The SEM image of TiO_2-10% PANI composite revealed its crystalline spherical morphology (Figure 4.2.1 A). Particle size determined through SEM ranged between 20 nm and 50 nm. The EDX pattern (Figure 4.2.1 B) showed that the composite was pure without any other impurities. The EDX patterns observed at 4.5, 4.93 and 0.45 keV represent the Kα1, Kβ1 and Lα1 peaks of titanium respectively. The EDX peaks corresponding to oxygen and carbon were also observed at 0.53 (Kα1) and 0.277 (Kα1) keV respectively. The EDX peak for nitrogen which was supposed to appear at 0.392 (Kα1) was not visible due to the overlap of carbon and titanium peaks with the

less intense peak of nitrogen. The presence of nitrogen was however confirmed through FTIR spectra of the composites by the appearance of absorption peaks corresponding to C-N, C-N$^+\bullet$ and N-H vibration modes respectively (discussed in section 4.3.3).
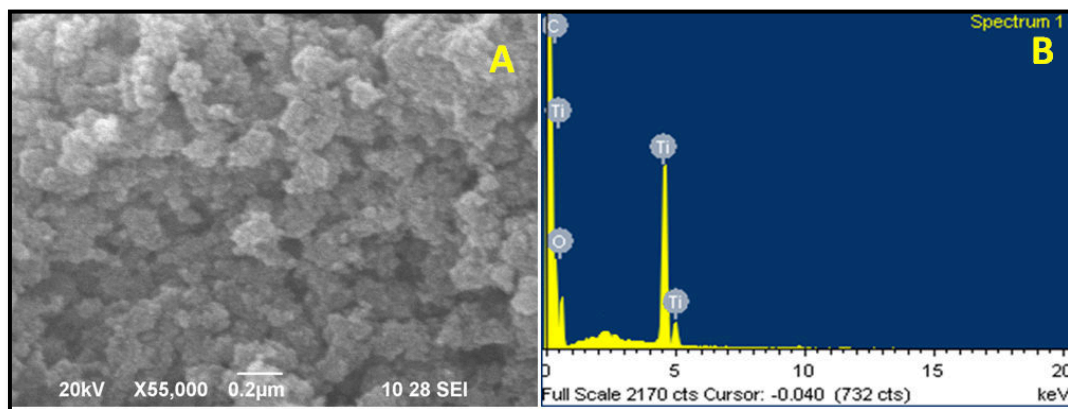
Figure 4.2.1. *SEM image (A) and EDX pattern (B) of nano TiO$_2$-10% PANI composite*
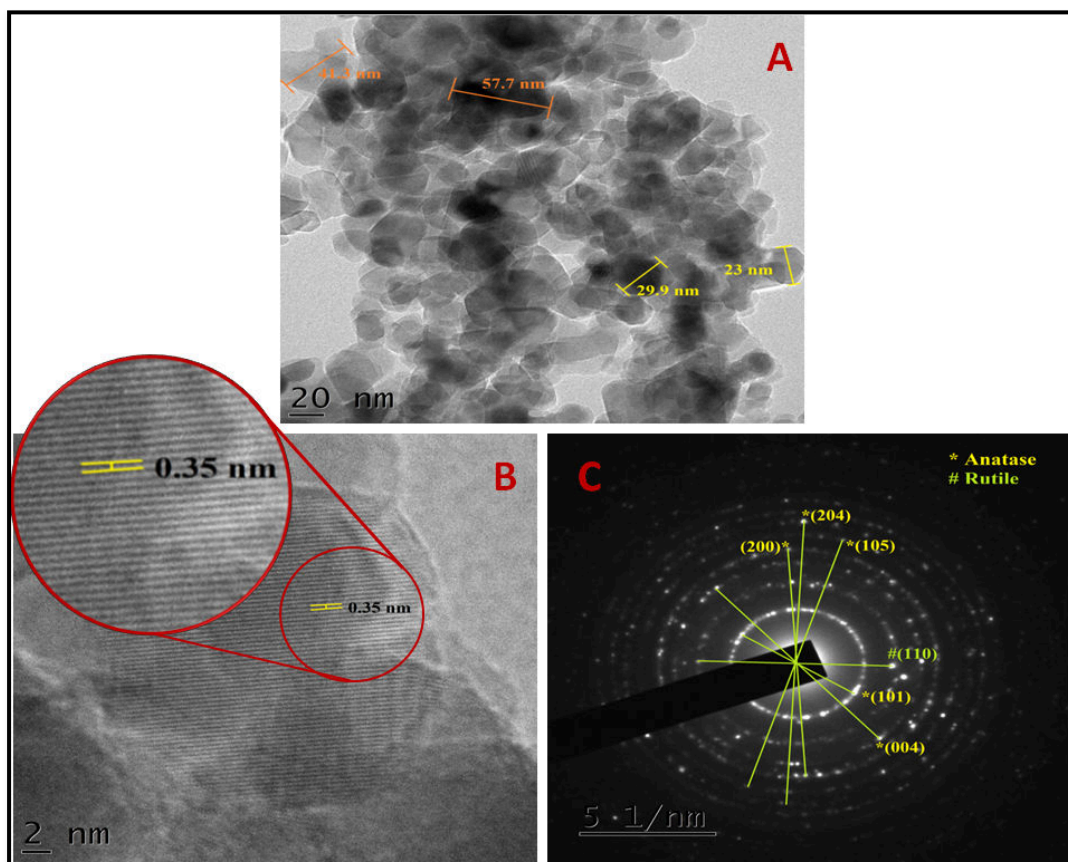
Figure 4.2.2. *TEM images (A & B) and SAED pattern (C) of nano TiO$_2$-10% PANI composite*

HRTEM image of TiO_2-10% PANI composite revealed its crystalline nature existing as distinguished individual particles (Figure 4.2.2 A). The particle size ranged between 20 nm to 60 nm without much aggregation. The fact that PANI was well dispersed in the presence of nano TiO_2 without much aggregation was hence clear. At higher resolution, lattice fringes with 0.35 nm spacing were visible (Figure 4.2.2 B). These patterns represented the interplanar distance (d) of (101) crystal planes of nano TiO_2 particles (plane observed at $2\theta=24.9°$ in XRD). The selected area electron diffraction (SAED) pattern of the composite (Figure 4.2.2 C) further confirms its crystalline nature through the clear ring patterns with distinguishable spots. Crystal planes corresponding to some of the spots were identified by comparing them with XRD patterns as marked in Figure 4.2.2 C.
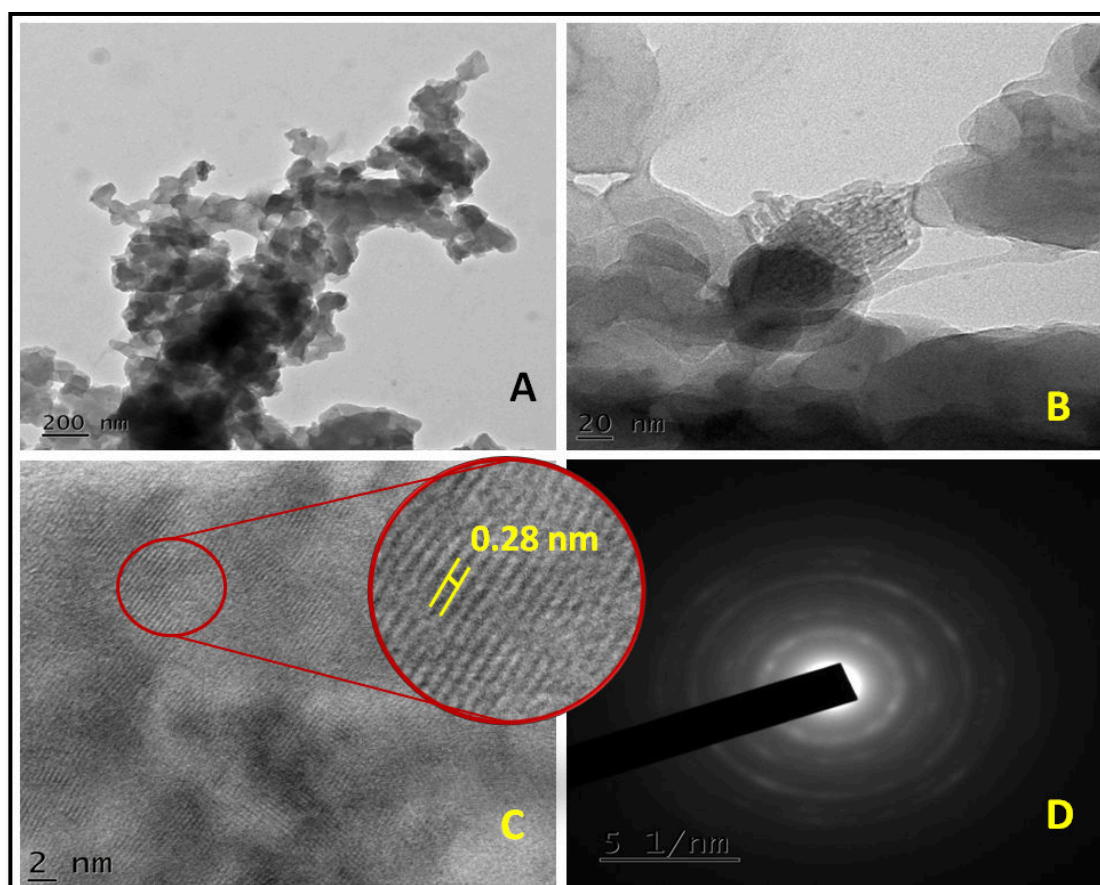
Figure 4.2.3. *TEM images (A, B & C) and SAED pattern (D) of nano ZnO-PANI composite*

From the TEM image of ZnO-PANI composite the particles looked much more aggregated compared to that of TiO_2-PANI composite (Figure 4.2.3 A). Some amorphous regions could be observed in TEM image of the composite (Figure 4.2.3 B). Crystal planes with inter planar distance (d=0.28 nm) was observed as lattice fringes in high resolution images which represent the (100) plane of ZnO wurtzite structure (Figure 4.2.3 C). SAED patterns of the composites appeared as halo like rings (Figure 4.2.3 D). The spots in SAED pattern were more spread out compared to sharp spots of TiO_2-PANI composite. The fact that ZnO-PANI composite consists of amorphous regions in addition to crystalline regions was hence clear.

4.3.3. FTIR Spectroscopy
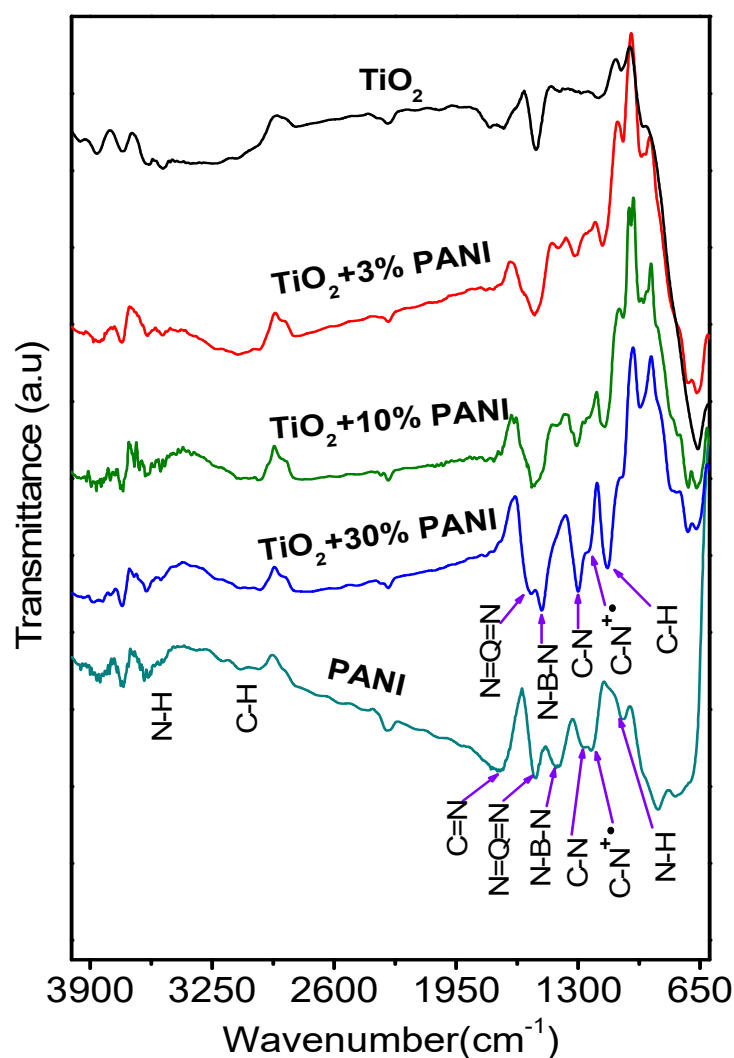
Figure 4.3.1. *FTIR spectra of TiO_2, PANI and TiO_2-PANI composites*

FTIR spectra of PANI showed peaks at 1527 and 1409 cm^{-1} corresponding to N=Q=N and N-B-N stretching frequencies respectively ['Q' represents quinoid and 'B' represents benzenoid structures of benzene ring] (Figure 4.3.1). The coexistence of quinoid and benzenoid structures in PANI was hence clear. Peaks at 1265, 1226 and 1069 cm^{-1} correspond to secondary aromatic amine C-N stretching, C-N$^{+\bullet}$ polaron stretching and N-H stretching vibrations in charged polaron units respectively. Broad peak between 881-690 cm^{-1} originated from the C-H in plane bending of 1,4-disubstituted benzene ring. The peak observed at 1710 cm^{-1} corresponds to C=N stretching vibration of imine group (due to the presence of quinoid units) in PANI. The peaks around 3617 and 3000 cm^{-1} arose from N-H and C-H stretching vibrations respectively. The predominance of quinoid structure over benzenoid structure in PANI was clear from the observed more intense peak belonging to N=Q=N stretching frequency compared to that of N-B-N. This observation further revealed the presence of HCl doped PANI[36–38]. IR spectra of TiO$_2$-PANI composite exhibited all the peaks corresponding to synthesized pristine PANI. Some of the striking observations made from FTIR spectra of TiO$_2$-PANI composites are as pointed out below:

➢ The intensity of absorption peak belonging to N=Q=N was weaker than that of N-B-N for TiO$_2$-PANI composites.

➢ As we move from TiO$_2$-3% PANI to TiO$_2$-30% PANI (lower to higher concentration of PANI), peak intensity corresponding to N=Q=N increased gradually. As we again move on to pristine PANI (0% TiO$_2$), the intensity of N=Q=N vibrations were higher than that of N-B-N.

➢ The absorption intensities corresponding to C-N stretching, C-N$^{+\bullet}$ polaron stretching also were weakened in the case of TiO$_2$-3% PANI and increased gradually as we move towards pristine PANI.

➢ The absorption intensity corresponding to imine C=N stretching vibration also followed the same trend as above ie., increased with respect to PANI concentration.

A very important conclusion regarding the interaction between TiO$_2$ and PANI were revealed from the above observations. The chance of existence of coordination bond between titanium and nitrogen were possible here[16]. The structure of PANI and

the possible interaction between TiO$_2$ and ZnO with PANI are represented diagrammatically in the section 4.3.5.
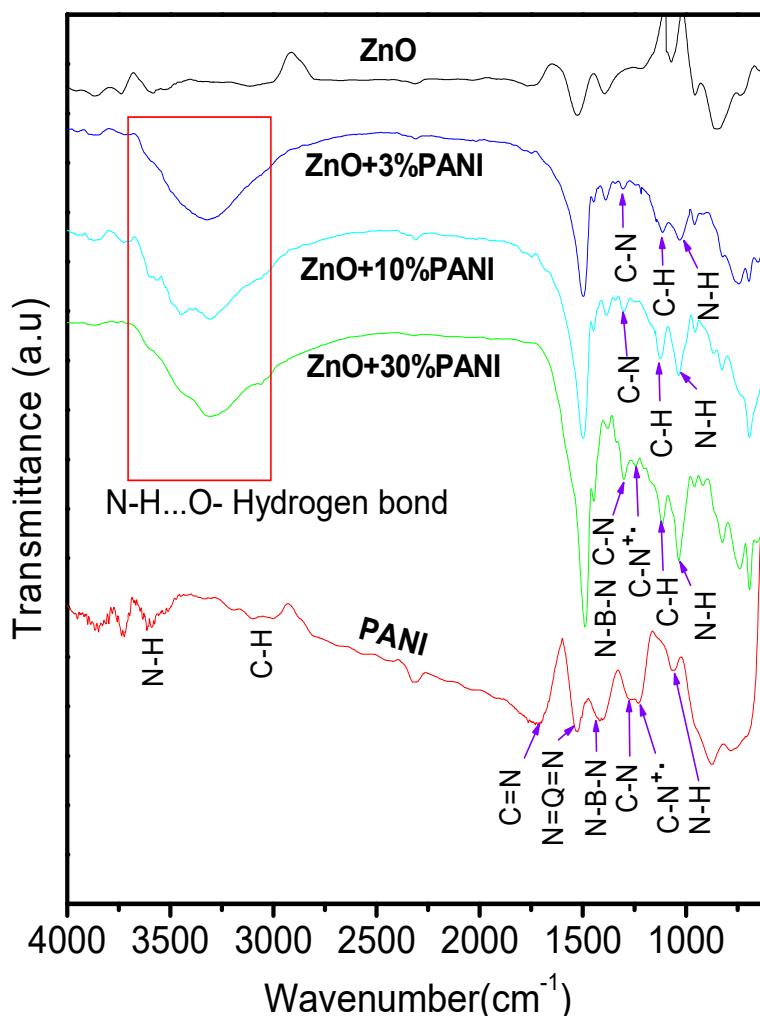
Figure 4.3.2. FTIR spectra of ZnO, PANI and ZnO-PANI composites

The observations made from the FTIR spectra of ZnO-PANI composites (Figure 4.3.2) were similar to that of TiO$_2$-PANI composites as discussed above. The intensities of N=Q=N stretching vibration was weaker than that of N-B-N and almost difficult to be distinguished in the composites. The intensities of C-N, C-N$^{+•}$ (polaron) and C=N (imine) stretching vibrations too were weaker in the composites and their intensities decreased as the percentage of ZnO in the composites increased from ZnO-30% PANI to ZnO-3% PANI. The intensity of N-H bending was also weakened. In addition to these observations which were similar to that observed in TiO$_2$-PANI composites, another observation was that there appeared a broad band between 3100 and 3600 cm^{-1} engulfing the NH stretching vibrations. These broad

bands could be attributed to the hydrogen bond existing between the -NH group of PANI and oxygen of ZnO[31,39–41].

4.3.4. UV-visible Diffused reflectance spectroscopy (UV-DRS)

The UV-visible spectra of PANI, nano TiO$_2$ and TiO$_2$-PANI composites obtained through UV-DRS analysis (Figure 4.4.1A) showed that nano TiO$_2$ absorbed only in the UV region while pristine PANI absorbed in UV as well as visible region of the spectra with major absorption bands in visible region. The TiO$_2$-PANI composites as expected absorbed in both UV and visible region of the spectra which highlighted the fact that coupling of PANI with nano TiO$_2$ extended the possibility of the composite to act as a photocatalyst or as a photosensitizer in the UV-visible region.
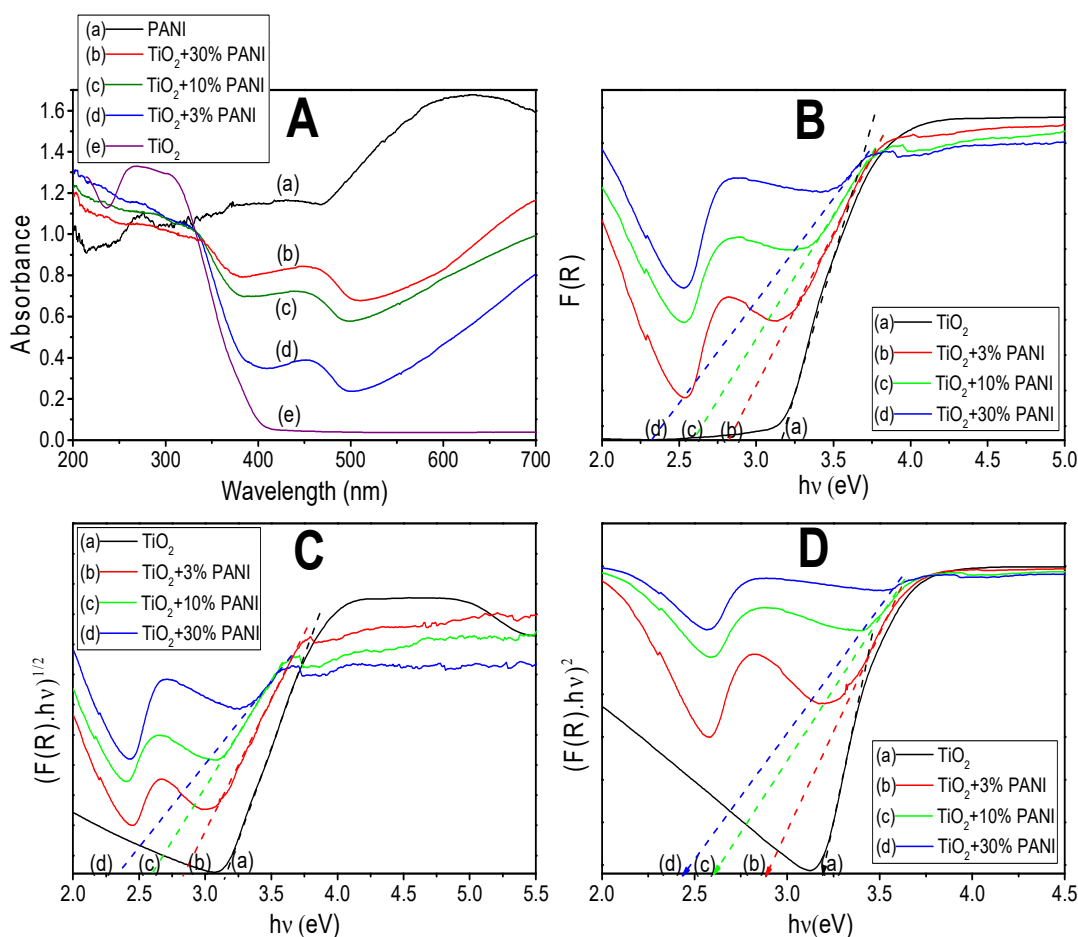
***Figure 4.4.1*.A)** *UV-visible spectra,* **B)** *Plot of F(R) versus hν,* **C)** *(F(R)hν)$^{1/2}$ versus hν and* **D)** *(F(R)hν)^2 versus hν of TiO$_2$, PANI and TiO$_2$-PANI composites*

The UV-visible spectra of PANI obtained through UV-DRS analysis gave three major characteristic absorption bands (Figure 4.4.1A). The band observed in the UV

region with maximum absorption at 276 nm could be attributed to the transition of electron from π (HOMO) to π* (LUMO) orbitals of benzenoid rings (also called exciton transition). Another broad band with absorption maxima 418 nm arose due to polaron to π* electron transition. This absorption band confirms the presence of polarons (C-N$^{+\bullet}$) in the PANI chain as a result of HCl doping. Another broad band with absorption maximum observed at 632 nm attributed to the π to polaron transfer within PANI. This band also represents localized electrons in PANI[42,43].

The absorption spectra of TiO$_2$-PANI composites exhibited the bands corresponding to TiO$_2$ as well as PANI with slight peak shifts. The peak observed at 276 nm for pristine PANI was completely masked by the bands of TiO$_2$ in the same region. The peak around 418 nm observed in PANI was slightly red shifted. This reveals the fact that the polaron to π* transfer in PANI was interrupted by the association of PANI with TiO$_2$. Another striking observation was that the absorption band around 632 nm in PANI was completely reconstructed in TiO$_2$-PANI composite with an endless long tail peak starting from around 480 nm. The "free-carrier-tail"[28] attributes to the extended delocalization of electrons arising due to the expansion of PANI chain in association with TiO$_2$. In other words, the compact conformation of PANI chain due to strong interactions within the chain which gave a band at around 632 nm for PANI, was modified in the presence of TiO$_2$ into an expanded conformation. This expanded conformation resulted in better delocalization of charge carriers and interaction with isolated polarons leading to a "tail band" extending up to near IR region of the spectra in TiO$_2$-PANI composites. It should also be noted from the UV-visible spectra that the band intensities corresponding to polaron was decreased in TiO$_2$-PANI composites. Even though the presence of TiO$_2$ extended the chain conformation of PANI, the intensities of peaks arising due to polaron structure decreased as the percentage of TiO$_2$ in the composites increased (i.e. from TiO$_2$-30% PANI to TiO$_2$-3% PANI). This observation was in support to the observations made from FTIR spectra that the polarons decreased in the composites as percentage of TiO$_2$ increased (as discussed in section 4.3.5).

Optical bandgap energies (E$_g$) were determined from the reflectance spectra of TiO$_2$-PANI composites by the application of Kubelka-Munk function (F(R)) in Tauc plot and it was found that the values of E$_g$ decreased in TiO$_2$-PANI composites as the

percentage of PANI increased (figure 4.4.1 B,C and D). The values of E_g are as tabulated below (Table 4.2.4)

Table 4.2.4. Values of optical bandgap energies of TiO₂-PANI composites

Method	Bandgap Energy in eV			
	TiO₂	TiO₂ +3% PANI	TiO₂ +10% PANI	TiO₂ +30% PANI
F(R) vs hυ	3.16	2.78	2.58	2.32
(F(R)hυ)² vs hυ	3.22	2.80	2.60	2.40
(F(R)hυ)^{1/2} vs hυ	3.18	2.80	2.59	2.36

Figure 4.4.2.A) UV-visible spectra, B) Plot of F(R) versus hυ, C) (F(R)hυ)² versus hυ and D) (F(R)hυ)^{1/2} versus hυ of ZnO, PANI and ZnO-PANI composites

The UV-visible absorption patterns of ZnO-PANI composites (Figure 4.4.2) too followed the similar trend as seen in the case of TiO₂-PANI composites. Here too the absorption bands which were supposed to be present at around 276 nm ($\pi \rightarrow \pi^*$ transition) could not be identified due to the overlap of bands in the UV region of

ZnO. The ZnO-PANI composites too gave absorption bands in the UV as well as visible region of the spectra. The intensity of absorption band observed at around 418 nm for PANI (polaron $\rightarrow \pi^*$ transition) due to quinoid ring was lower for ZnO-3% PANI composite (ie highest percentage (70%) ZnO). In ZnO-PANI composites too, the band observed at around 632 nm ($\pi \rightarrow$ polaron transfer) for PANI due to localized electrons were reconstructed into "tail band" as observed in TiO_2-PANI composites. Here the intensity of the "tail band" was appreciably lowered in the composites with highest percentages of ZnO (i.e. ZnO-10% PANI and ZnO-30% PANI). In addition to the existence of expanded conformation of PANI chain in the presence of ZnO, the decrease in the polarons were also evident from these observations[44].

Optical bandgap energies (E_g) were determined from the reflectance spectra of ZnO-PANI composites found to have decreased as the percentage of PANI in the composites increased (figure 4.4.2 B,C and D). The values of E_g are as tabulated below (Table 4.2.5)

Table 4.2.5. *Values of optical bandgap energies of ZnO- PANI composites*

Method	Bang gap Energy in eV			
	ZnO	ZnO +3% PANI	ZnO +10% PANI	ZnO +30% PANI
F(R) vs hυ	3.2	2.78	2.47	2.40
(F(R)hυ)^2 vs hυ	3.25	2.80	2.57	2.42
(F(R)hυ)$^{1/2}$ vs hυ	3.27	2.84	2.62	2.43

4.3.5. Structure and interaction within TiO$_2$-PANI or ZnO-PANI composites

Based on the results obtained from various characterization techniques of PANI and composites of PANI with TiO_2 and ZnO, the structure of PANI and interactions between TiO_2 and ZnO with PANI would be as represented in Figure 4.5. The co-existence of benzenoid and quinoid segments in PANI was evident from FTIR spectra and UV-DRS. FTIR also showed the presence of C-N, C-N$^{+\bullet}$ polaron, imine C=N and N-H functional groups in PANI. It was also observed from the spectra that the intensity of stretching vibrations corresponding to quinoid segments were comparatively higher than benzenoid segments.
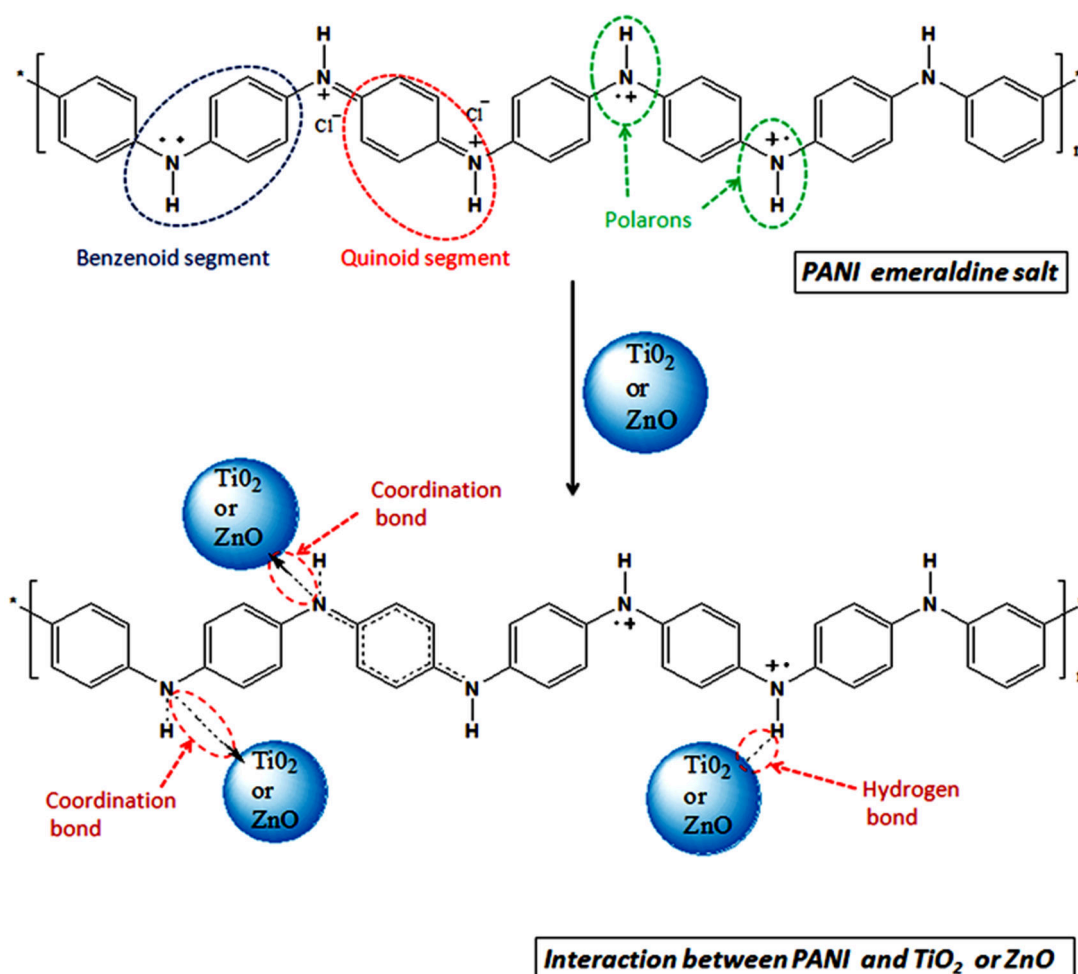
Figure 4.5. *Structure of PANI and interaction between TiO₂/ZnO and PANI*

In the composites of PANI with TiO_2 and ZnO slight shift in the IR peak positions were observed for various functional groups of PANI. Decrease in IR band intensities of C-N$^{+\bullet}$ polaron, imine C=N and N-H functional groups were observed here. In addition to this, the band intensities corresponding to quinoid decreased with respect to the increase in the percentage of TiO_2/ZnO in the composites. TiO_2/ZnO-PANI also showed the existence of hydrogen bonds in the composites. The possibility of existence of coordination bonds and hydrogen bonds between PANI and TiO_2 or ZnO was assumed based on all these observations (Figure 4.5). There are possibilities that the quinoid structures either get converted into benzenoid structure or the C=N stretching vibrations get weakened if coordination bond exists between Ti or Zn metal and nitrogen of PANI. Interactions of PANI with nano particles could also weaken the stretching vibrational intensities of N-H group which are adjacent to these interaction sites.

Section II

Photodegradation of polystyrene using TiO₂-PANI and ZnO-PANI catalysts

PS-TiO$_2$-PANI and PS-ZnO-PANI photocatalysts were loaded into PS matrix whose photodegradation was studied under UV radiation.

4.4. Results and Discussion

4.4.1. Gel permeation chromatography (GPC) analysis

The average molecular weights ($\overline{M}_w$ and $\overline{M}_n$) measured for PS-TiO$_2$-PANI as well as PS-ZnO-PANI composites, using gel permeation chromatography, decreased as the time of UV irradiation is increased.

The decrease in the average molecular weights of PS-TiO$_2$-PANI was in the order PS-(TiO$_2$-10% PANI) > PS-(TiO$_2$-30% PANI) > PS-(TiO$_2$-3% PANI) (Figure 4.6.1). This revealed that for PS-TiO$_2$-PANI composites, the average molecular weight decreased first on UV irradiation as the percentage of PANI incorporation increases from 3% to 10% PANI and then increased as the percentage of PANI increases to 30%. Similar trend was observed in PS-ZnO-PANI composites also with the order of weight loss as PS-(ZnO-10% PANI) > PS-(ZnO-30% PANI) > PS-(ZnO-3% PANI) (Figure 4.6.2). Here too the optimum percentage of PANI loading versus ZnO was found to be 10% for maximum weight loss.
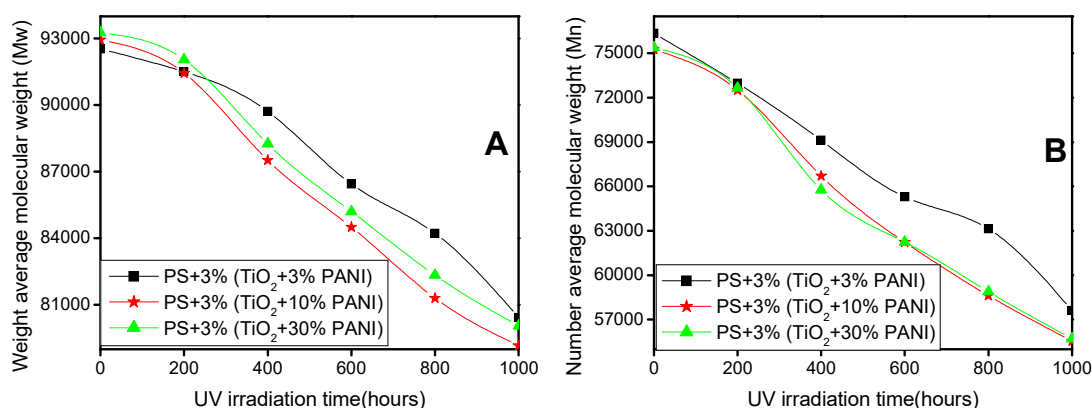
Figure 4.6.1. A) *Weight average ($\overline{M}_w$) and* ***B)*** *number average ($\overline{M}_n$) molecular weights of PS-TiO$_2$-PANI composite under different UV irradiation time*
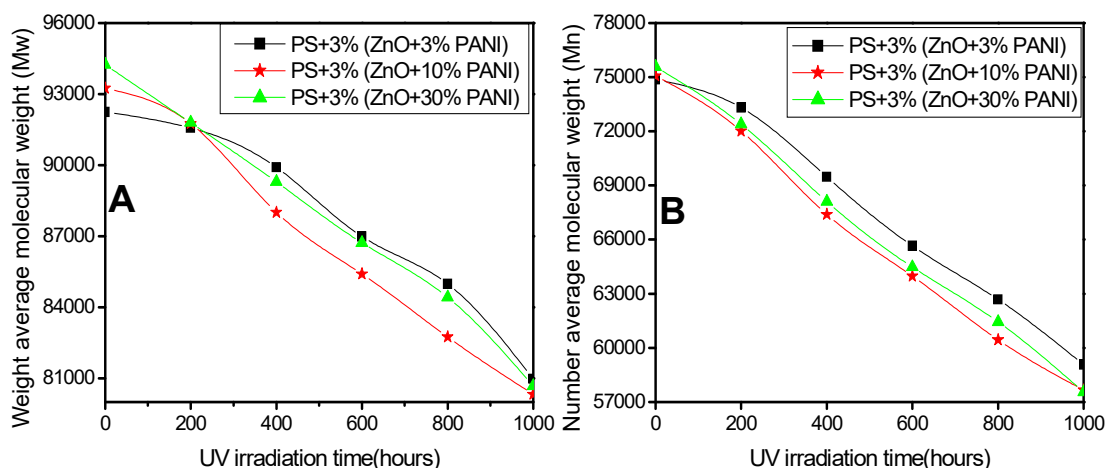
Figure 4.6.2. A) *Weight average ($\bar{M}_w$) and* **B)** *number average ($\bar{M}_n$) molecular weights of PS-ZnO-PANI composite under different UV irradiation time*

The number of chain scissions per molecules (S) and the number of scission events per gram of (N_t) increased upon UV irradiation in PS-TiO$_2$-PANI (Figure 4.6.3) as well as PS-ZnO-PANI (Figure 4.6.4) composites. Maximum increase in chain scissions were observed in the composites containing 10% PANI.

Polydispersity index (PDI) too increased as the time of UV irradiation increased (Figure 4.6.5). The increase in PDI was found to be maximum for PS-(TiO$_2$-30%PANI) and PS-(ZnO-30% PANI) composites. This shows that the maximum randomness in PS chain scission increases as the percentage of PANI in the polymer composites increased.
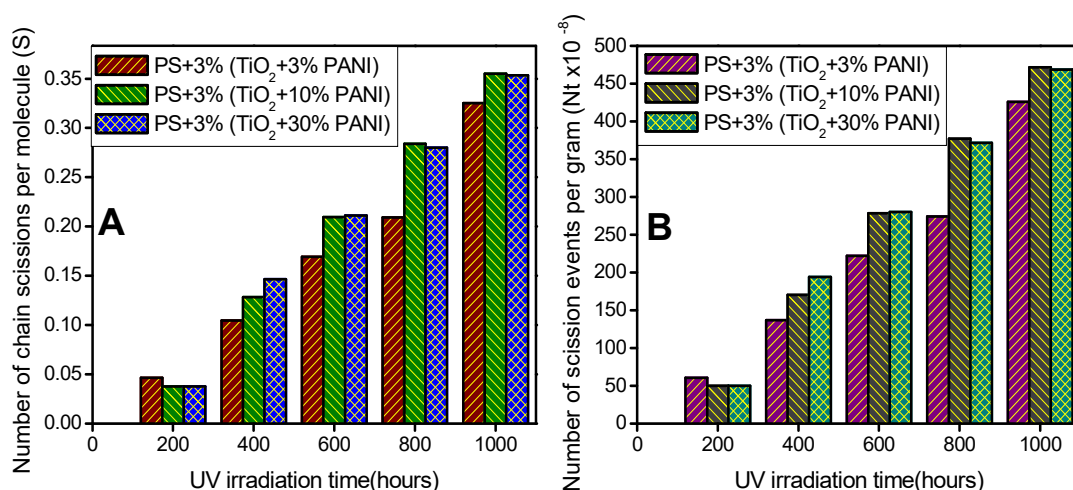
Figure 4.6.3. (A) *Number of chain scissions per molecule (S) and* **(B)** *number of scission events per gram (N_t) of PS-TiO$_2$-PANI composite under different UV irradiation time.*
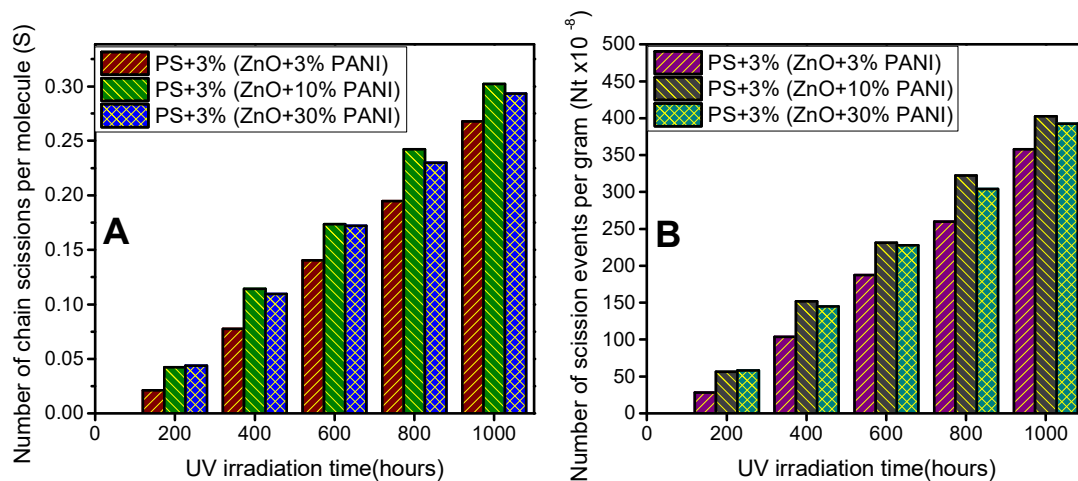
Figure 4.6.4. A) *Number of chain scissions per molecule (S) and **B)** number of scission events per gram (N_t) of PS-ZnO-PANI composite under different UV irradiation time.*
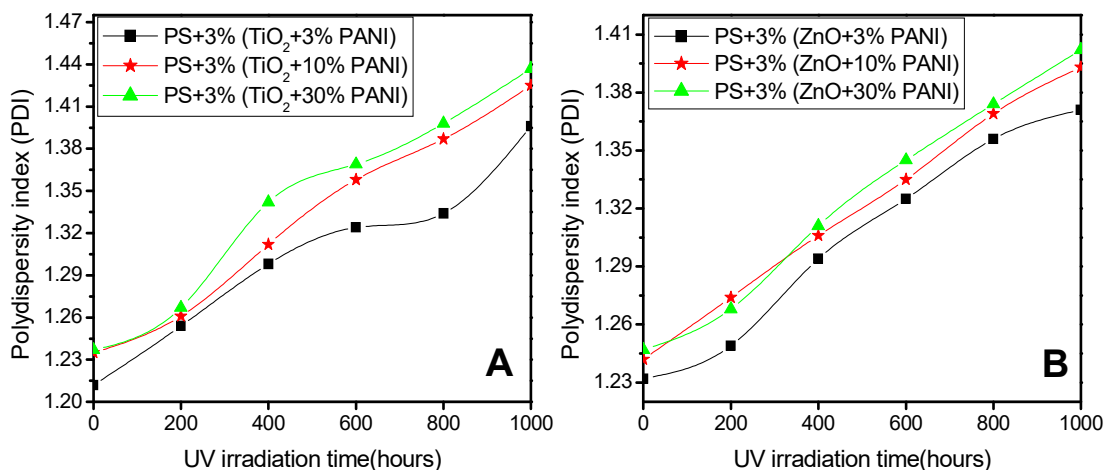
Figure 4.6.5. *Polydispersity index (PDI) of PS -TiO_2-PANI and PS-ZnO –PANI composite under different UV irradiation time.*

From the GPC value it could be concluded that the chain scission of PS-TiO_2 and PS-ZnO composites upon UV irradiation were increased on incorporating them with PANI. This result highlighted the fact that nano TiO_2 and nano ZnO coupled with PANI served as an efficient photocatalyst in the photodegradation of PS upon UV irradiation. Increase in mole percentage of PANI associated with TiO_2 and ZnO further increased the rate of chain scission of PS-TiO_2-PANI and PS-ZnO-PANI composites however excess percentage of PANI decelerated chain scission rate. The deceleration in photodegradation of the polymer composites in the presence of excess PANI could be due to the fact that excess PANI hinders the availability of UV radiation to nano TiO_2 and ZnO particles. However optimum percentage of PANI

coupled with these nano particles could act as a new modified catalyst for effective degradation of PANI photochemically. The mechanism of photodegradation of the composites is discussed in section 4.5.

4.4.2. FTIR spectroscopy

PS-PANI, PS-TiO$_2$-PANI and PS-ZnO-PANI composites were monitored using FTIR spectrometer at regular intervals of UV irradiation. The spectra of all these composites were almost identical to that of pristine PS and other PS-composites discussed in the previous chapter. The photodegradation of the composites via photo-oxidation under study, was identified through the variation in intensities of the peaks corresponding to the stretching vibrations of >C=O, -OH/-OOH, isolated >C=C<, conjugated carbon-carbon double bonds etc. PS-PANI composites exhibited only a slight increase in the peak intensities of these functional groups. The photo-oxidation here was not much accelerated using PANI which confirms that PANI alone is not a good photocatalyst. In addition to this, at higher UV irradiation time the FTIR spectrum was quiet confusing. The absorption intensities of functional groups failed to show regular increase with respect to UV irradiation time. The photodegradation of PANI itself under UV irradiation might be the reason. A slight increase in the rate of photodegradation was however observed in PS-PANI composites compared to pristine PS. This may be due to the fact that PANI existing as emeraldine salt could easily conduct the charge carriers created in the composite matrix on UV light interaction.

PS-TiO$_2$-PANI composites exhibited enhanced photo-oxidation in presence of UV radiation compared to PS-TiO$_2$ composites. The photocatalytic activity of the composites followed the same trend as observed in GPC analysis. The photo-oxidation upon UV irradiation of the composites followed the order PS-(TiO$_2$-10% PANI) > PS-(TiO$_2$-30% PANI) > PS-(TiO$_2$-3% PANI). In other words, the rate of photo-oxidation increased as the percentage of PANI in the composite increased from 3% to 10% and at higher percentage of PANI (30%), the rate of photo-oxidation decreased. Figure 4.7.1 and 4.7.2 represent the FTIR spectra of PS-(TiO$_2$-10% PANI) and PS-(TiO$_2$-30% PANI) composites respectively. The increase in >C=O (1740-1700 cm^{-1}) and >C=C< (1680-1650 cm^{-1}) stretching bands were clearly visible upon UV irradiation for the composites. Increase in the stretching frequencies

corresponding to conjugated carbon bonds (1630-1600 cm^{-1}) and -OH/-OOH (3700-3600 cm^{-1}) were also observed. The characteristic peaks of phenyl ring due to -C-H out of plane bending of the rings were observed at 691 cm^{-1}, 752 cm^{-1}, 905 cm^{-1} and 1027 cm^{-1} without any change upon UV irradiation. Aromatic >C=C< stretching observed at 1448 cm^{-1} was also not altered upon UV irradiation. It could be hence assumed that the phenyl ring remained intact upon UV irradiation.
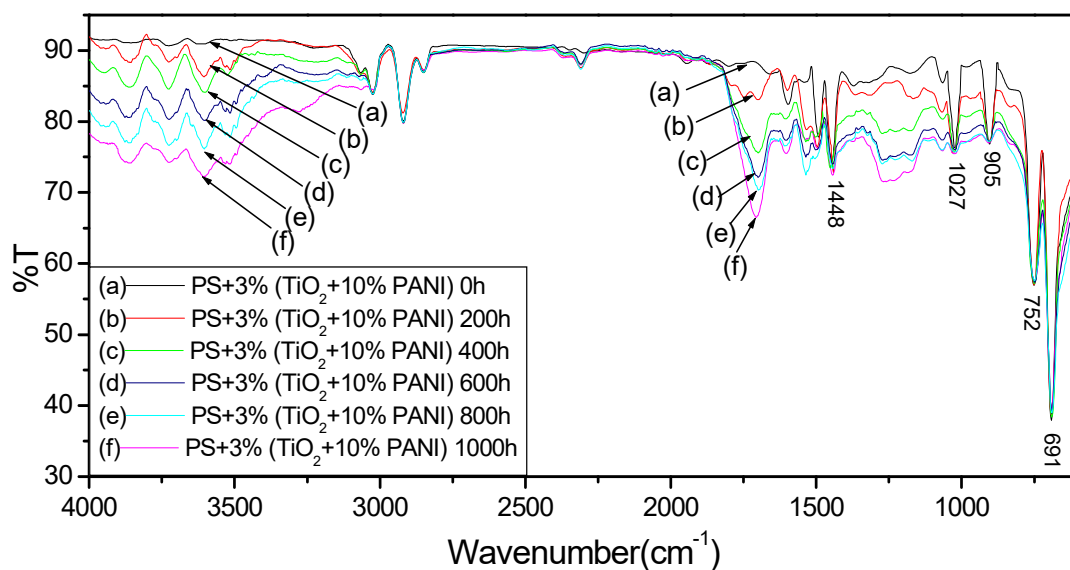
Figure 4.7.1. FTIR spectra of PS-(TiO$_2$-10% PANI) composite after different UV exposure time intervals ranging from 0 h to 1000 h.
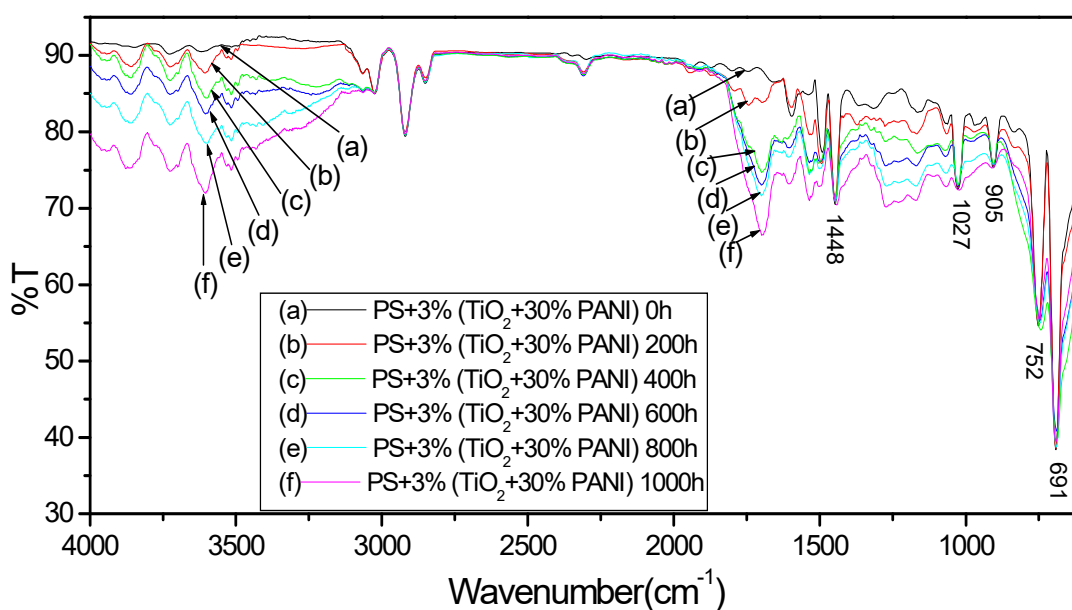
Figure 4.7.2. FTIR spectra of PS-(TiO$_2$-30% PANI) composite after different UV exposure time intervals ranging from 0 h to 1000 h.
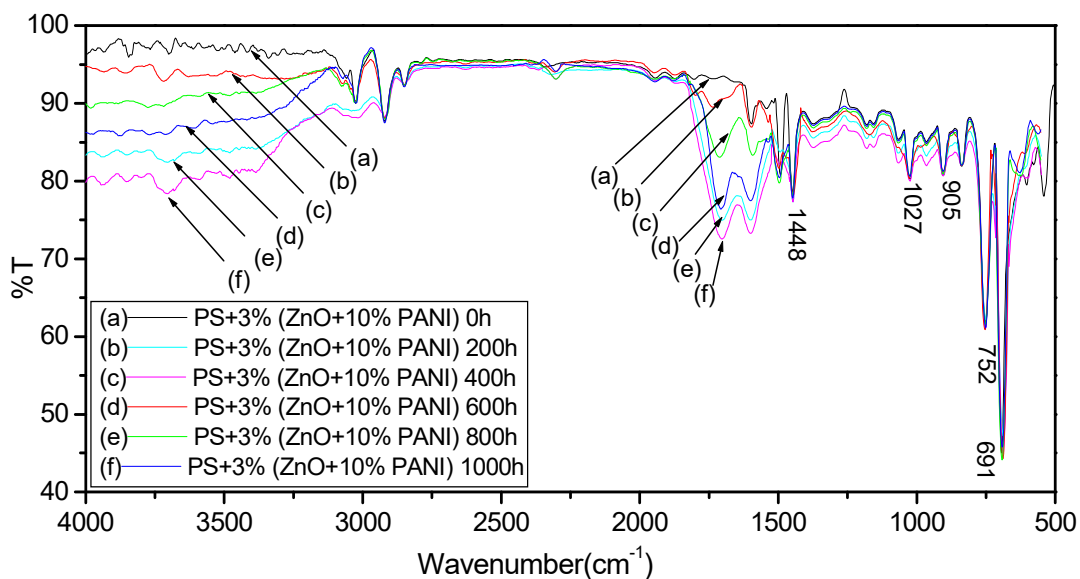
Figure 4.7.3*. FTIR spectra of PS-(ZnO-10% PANI) composite after different UV exposure time intervals ranging from 0 h to 1000 h.*
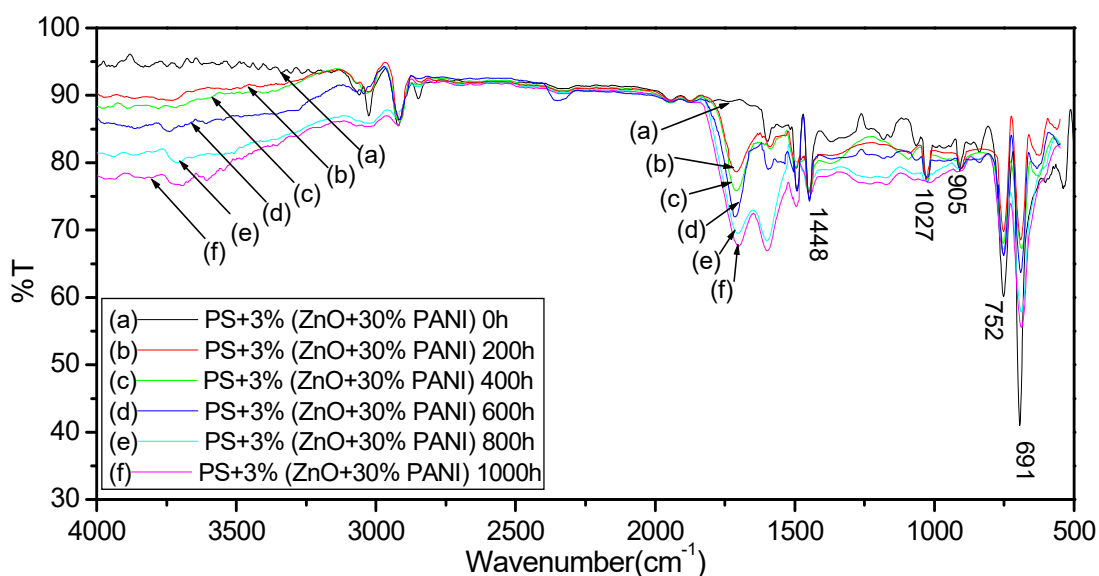
Figure 4.7.4*. FTIR spectra of PS-(ZnO-30% PANI) composite after different UV exposure time intervals ranging from 0 h to 1000 h.*

Similar trend in the IR spectra were also observed in the case of PS-ZnO-PANI composites. Here too the maximum photo-oxidation was observed in PS-(ZnO-10% PANI) (Figure 4.7.3) composites compared to PS-(ZnO-3% PANI) and PS-(ZnO-30% PANI) (Figure 4.7.4). PS-ZnO-PANI composites underwent enhanced photo-oxidation compared to PS-ZnO composite. ZnO coupled with PANI hence proved to be better photocatalyst which could enhance the photocatalytic activity of ZnO. Excess PANI however adversely affected the photocatalytic activity of ZnO.

4.4.3. UV- visible Diffused Reflectance Spectroscopy (UV-DRS)

UV-DRS of PS-PANI, PS-TiO_2-PANI and PS-ZnO-PANI composites showed absorption bands in the UV as well as visible region of the spectra. Even very low percentage of PANI could influence the optical property of the entire PS composite.
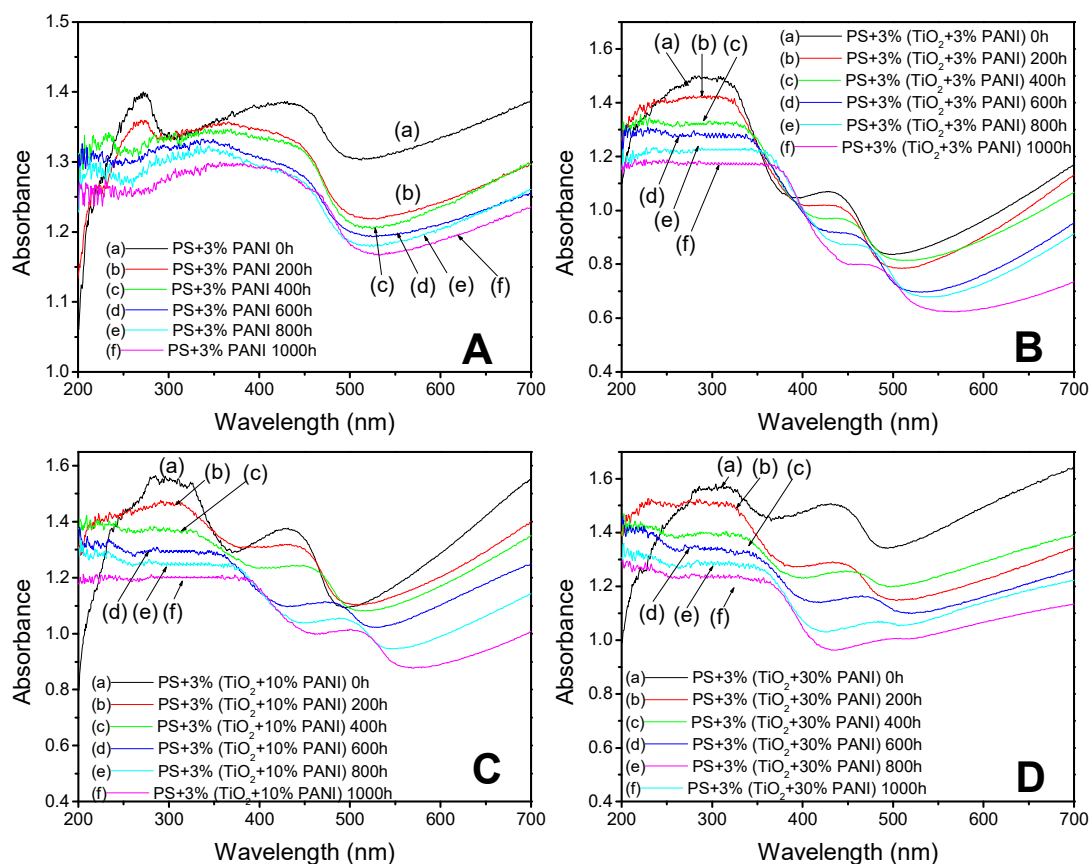
Figure 4.8.1. UV-DRS of (A) PS-3% PANI, (B) PS-3% (TiO2+3% PANI), (C) PS-3% (TiO2+10% PANI) and (D) PS-3% (TiO2+30% PANI) at regular UV irradiation intervals

The UV visible spectra of PS-PANI as well as PS-TiO_2-PANI composites (Figure 4.8.1) showed absorption bands with two absorption maxima between wavelengths 230-350 nm (UV region) and 400- 500 nm (visible region) and a "tail band" starting from around 500 nm and extending to far-red region. The band observed at 230-350 nm is contributed by combined bands of PS, nano TiO_2 and PANI absorption. In the case of PS, the absorption bands observed in this region arises due to the combined absorption of phenyl rings. The absorption band of TiO_2 in this region is due to the absorption of UV light by the electrons in the valence band. The bands observed in

this region for PANI corresponds to $\pi \rightarrow \pi^*$ transition of benzenoid ring. PANI alone is responsible for the bands observed in the visible region of the spectra. The "tail band" observed for PS-PANI composite (Figure 4.8.1 A) indicates the interaction between PS and PANI by which the confirmation of PANI has been modified into expanded conformation which allows better delocalization of electrons ($\pi \rightarrow$polaron transfer). As the time of UV irradiation increases, decrease in the absorption intensities were noticed for PS-PANI as well as PS-TiO$_2$-PANI composites. In addition to this, slight red shift in the absorption bands was also noticed. The decrease in the absorption bands of the composites supports photodegradation of the composites. UV-visible spectra also support the fact that photodegradation of PS-TiO$_2$-PANI was much more efficient compared to that of PS-TiO$_2$ composite. In addition to this it was also found that the photodegradation of PS-(TiO$_2$-10% PANI) was predominant.
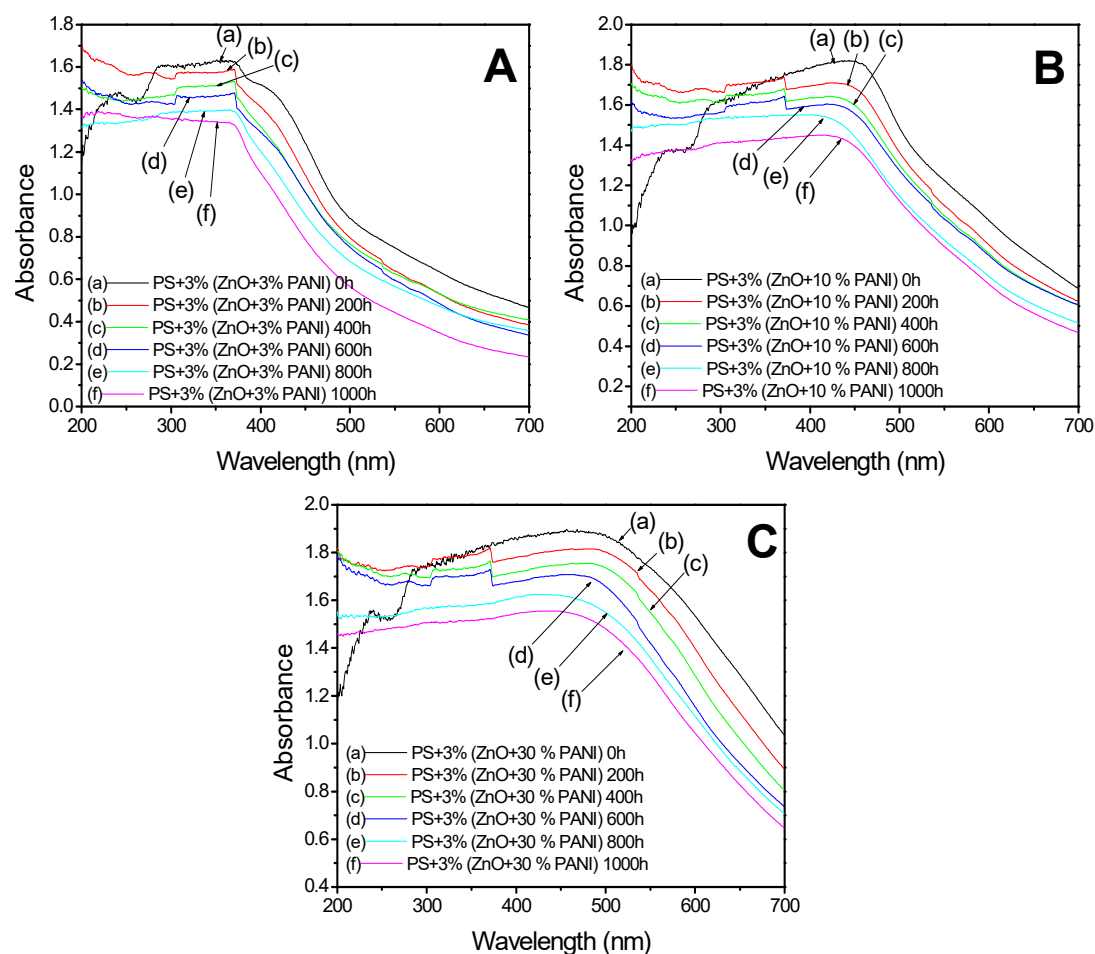
Figure 4.8.2. *UV-DRS of (A) PS-3% (ZnO+3% PANI), (B) PS-3% (ZnO +10% PANI) and (C) PS-3%(ZnO+30% PANI) at regular UV irradiation intervals*

UV-visible spectra of PS-ZnO-PANI composites looked different from that of PS-TiO$_2$-PANI composites (Figure 4.8.2). The bands in the UV region were completely overlapped by the bands between 400-500 nm wavelengths in the visible region. Intensity of absorption bands after 500 nm wavelength decreased so that tail like band was invisible.

Degradation percentage (D%) of the composites determined from the UV-visible spectra are as shown below (Figure 4.8.3). Maximum D% among the PS-TiO$_2$-PANI composites was observed for PS-(TiO$_2$-10% PANI) and that among PS-ZnO-PANI composites were for PS-(ZnO-10% PANI). The D% of PS-TiO$_2$-PANI composites was higher compared to that of PS-ZnO-PANI composites. The Degradation efficiency of PS-(TiO$_2$-3% PANI), PS-(TiO$_2$-10% PANI) and PS-(TiO$_2$-30% PANI) increased by 11.7, 13.88 and 13.2 % and that of PS-(ZnO-3% PANI), PS-(ZnO-10% PANI) and PS-(ZnO-30% PANI) increased by 7.78, 9.71 and 8 % respectively with respect to pristine PS.
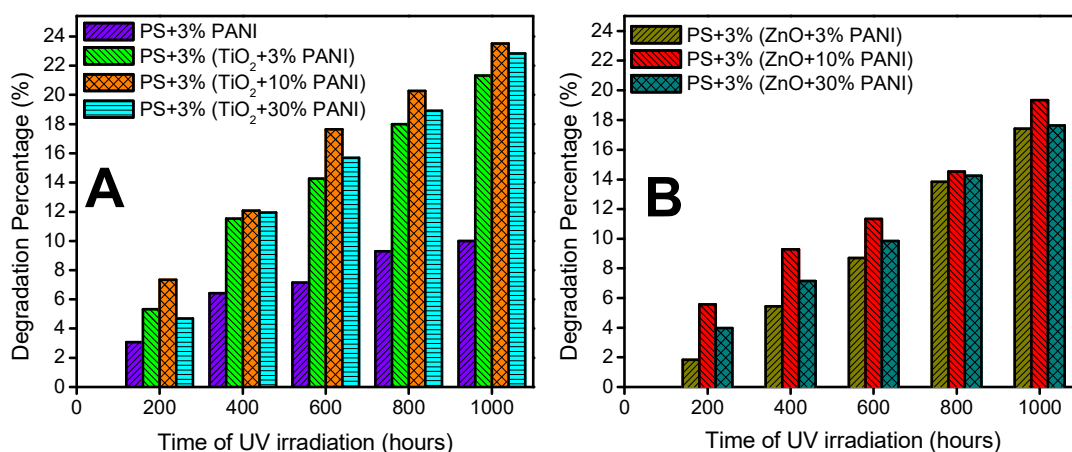
Figure 4.8.3. Degradation percentages (D%) of PS-TiO$_2$-PANI (A) and PS-ZnO-PANI composites (B)

4.4.4. Scanning electron microscopy (SEM)

The SEM image of PS-3% PANI composite showed some aggregations over the matrix (Figure 4.9 a). The aggregation could be due to the PANI macro molecules loaded into the matrix. Dispersion of TiO$_2$-30% PANI within PS matrix was found to be much better compared to PANI alone (Figure 4.9 b). The surface morphology of

the PS-3%(TiO_2-30% PANI) composite has changed with increased roughness after 1000 hours of UV irradiation due to photodegradation (Figure 4.9 c).
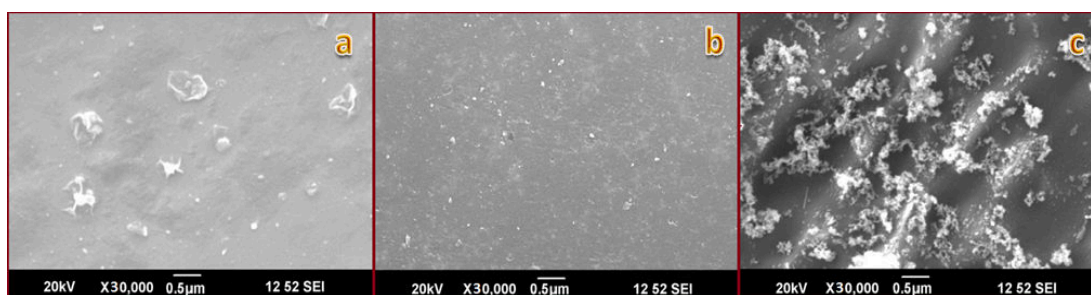
Figure 4.9. SEM image of PS-3% PANI (a) and PS-3%(TiO_2-30% PANI) (b) before UV irradiation and PS-3%(TiO_2-30% PANI) (c) after UV irradiation of 1000 h

4.4.5. Thermogravimetric Analysis (TGA)

TGA was conducted in nitrogen atmosphere for the composites. TGA thermogram of PS-3%(TiO_2-10% PANI) and PS-3%(ZnO-10% PANI) (Figure 4.10) showed two stages of weight loss attributing to the water desorption and decomposition of the composites. At a temperature ≈ 290°C, PS-3%(TiO_2-10% PANI) started to decompose. The decomposition temperature of PS-3%(ZnO-10% PANI) started at 278°C. The decomposition temperature of the composites shifted to lower values after 1000 hours of UV irradiation. Decreased thermal stability of the composites due to photodegradation in the presence of UV radiation leads to this observable shift.
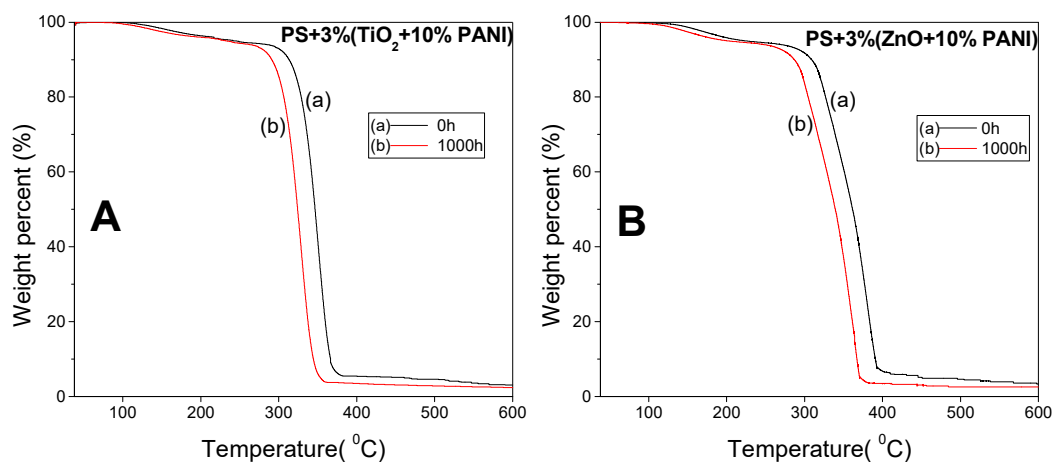
Figure 4.10. TGA thermogram of PS-3%(TiO_2-10% PANI) (A) and PS-3%(ZnO-10% PANI) (B) composites before and after UV irradiation of 1000 h

4.4.6. Mechanical Properties

The mechanical properties of PS-PANI composites were not so appreciable as compared to PS-TiO$_2$-PANI or PS-ZnO-PANI composites (Figure 4.11.1 & 4.11.2). The decrease in mechanical strengths of PS-PANI composites could be due to small aggregations of PANI which prevented uniform dispersion along the PS matrix (as evident from Figure 4.9). The tensile and flexural strengths of PS-PANI were however better compared to pristine PS.
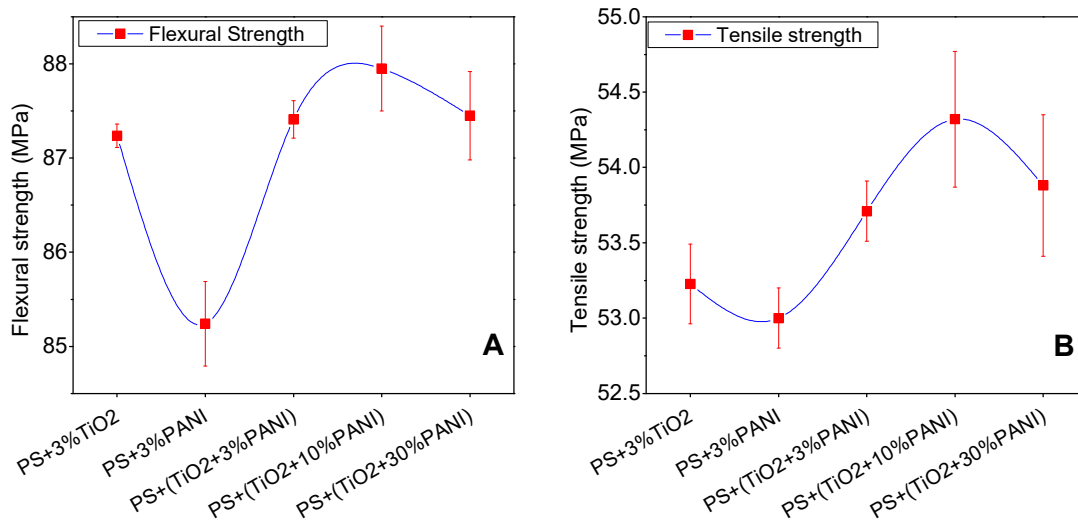
Figure 4.11.1. *Flexural (A) and tensile (B) strengths of PS-TiO$_2$, PS-PANI and PS-TiO$_2$-PANI composites- a comparison*
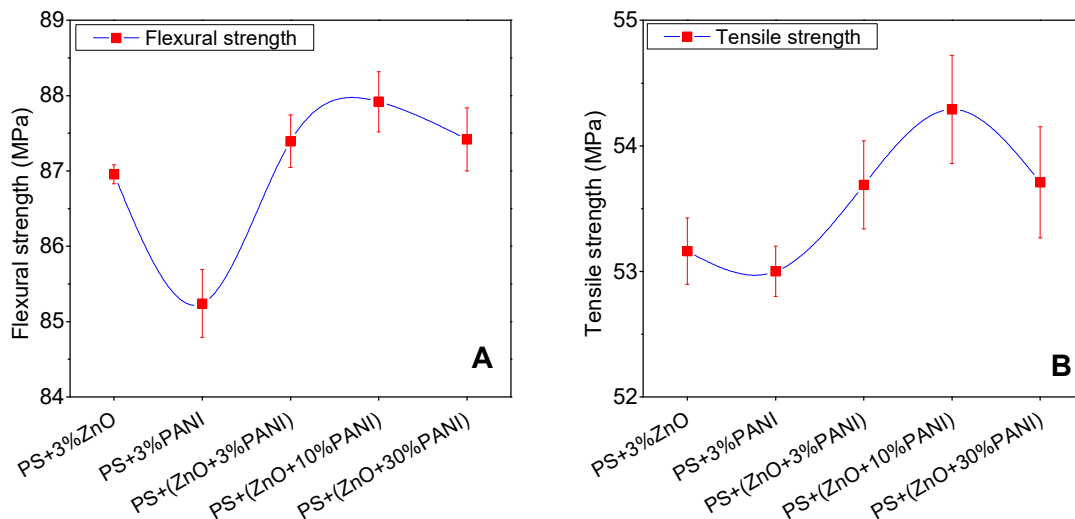
Figure 4.11.2. *Flexural (A) and tensile (B) strengths of PS-ZnO, PS-PANI and PS-ZnO-PANI composites - a comparison*

Figure 4.11.1 shows that the tensile and flexural properties of PS-TiO$_2$-PANI composites were slightly enhanced compared to PS-TiO$_2$ composites. We could also observe that the maximum mechanical strengths were observed in PS-(TiO$_2$-10% PANI) composite. As the percentage of PANI associated with TiO$_2$ in the composites increased, the mechanical strength further decreased. This phenomenon could be explained based on the extent of dispersion of TiO$_2$-PANI composite within PS matrix. At higher percentage of PANI much larger aggregates of TiO$_2$-PANI resulted. The interaction of PANI with adjacent PANI molecules might have caused this aggregation. The extent of dispersion of TiO$_2$-PANI composites with higher percentage of PANI (30% PANI) was not much appreciable. The non-uniform dispersion may result in defective voids within the polymer matrix which decrease its mechanical properties.

Similar is the case with PS-ZnO-PANI composites (Figure 4.11.2). A little enhancement in the mechanical properties was observed for the composites compared to that of PS-ZnO composites. Decrease in mechanical properties was however observed in composites with higher percentage of PANI (30%) as discussed above.
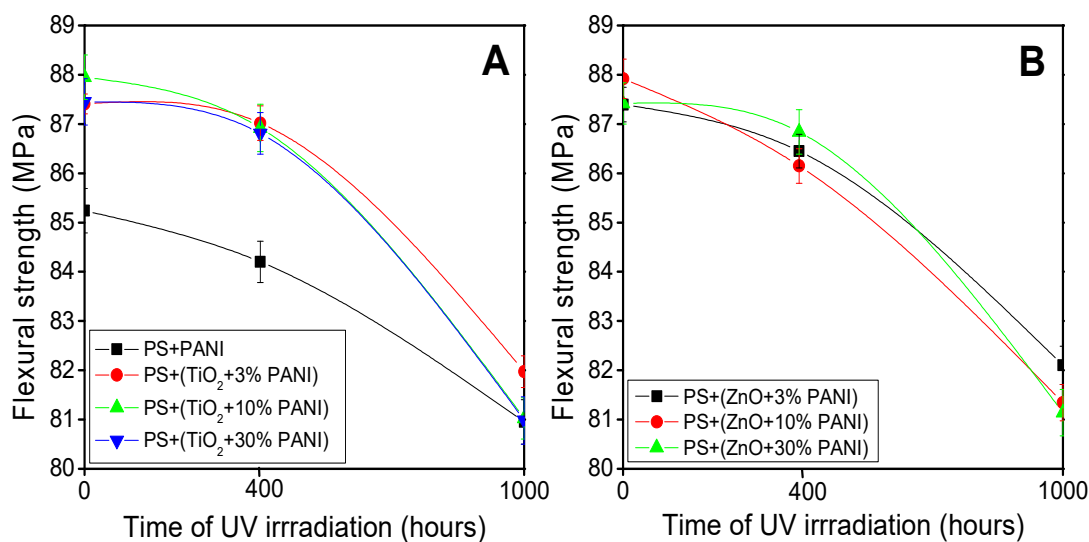
Figure 4.11.3. *Flexural strengths of PS-TiO$_2$-PANI (A) and PS-ZnO-PANI (B) composites exposed to UV radiation for 0, 400 and 1000 h*
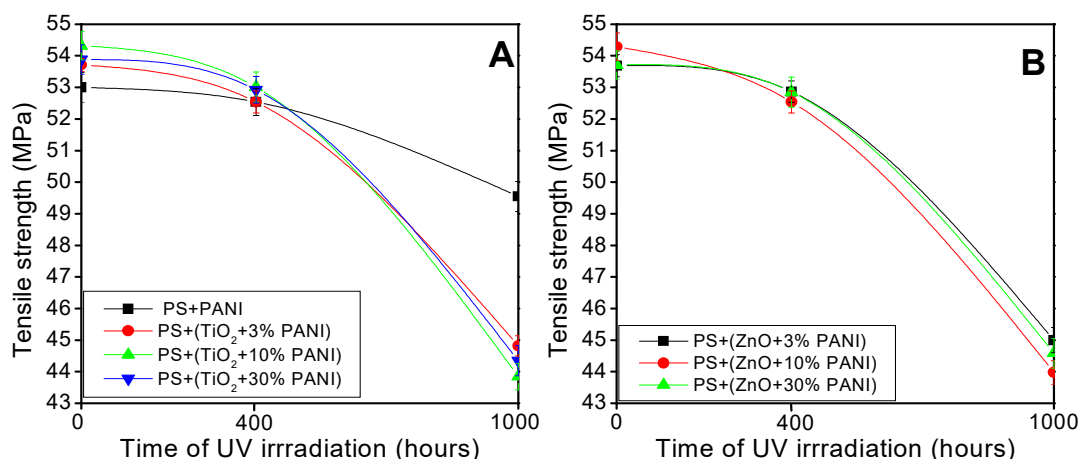
Figure 4.11.4. *Tensile strengths of PS-TiO$_2$-PANI (A) and PS-ZnO-PANI (B) composites exposed to UV radiation for 0, 400 and 1000 h*

The flexural (Figure 4.11.3) and tensile (Figure 4.11.4) properties of PS-TiO$_2$-PANI as well as PS-ZnO-PANI composites decreased as the time of UV irradiation increased. The deterioration in the mechanical properties of the composites was evident through this observation. These composites underwent better mechanical degradation compared to PS-TiO$_2$ and PS-ZnO composites. This was due to the better conduction of charge carriers from the polymer surface to their inner matrix. As the percentage of PANI associated with TiO$_2$ and ZnO increased from 3% to 10% in the polymer composites, the rate of mechanical degradation upon UV irradiation increased. As the percentage of PANI further increased to 30%, the degradation rate decreased.

4.4.7. Electrical Properties

The BDV of the PS-TiO$_2$-PANI and PS-ZnO-PANI composites measured in alternating current of frequency 50Hz (Figure 4.12.1) were found to have much lower values compared to PS, PS-TiO$_2$ and PS-ZnO composites (refer chapter 3). The decreased value of BDV in these composites supports the fact that PANI associated with TiO$_2$ and ZnO is conducting. Even 3% of TiO$_2$-3% PANI or ZnO-3% PANI could decrease the BDV of the PS composites. The value of BDV decreased as the percentage of PANI in the composites increased. The values of BDV of PS-TiO$_2$-PANI composites were 21.3 kV/mm (PS-3%(TiO$_2$-3% PANI), 18.78 kV/mm (PS-3%(TiO$_2$-10% PANI) and 14.85 kV/mm (PS-3%(TiO$_2$-30% PANI) and that for PS-

ZnO-PANI composites were 20.62 kV/mm (PS-3%(ZnO-3% PANI), 18.24 kV/mm (PS-3%(ZnO-10% PANI) and 15.32 kV/mm for (PS-3%(ZnO-30% PANI).
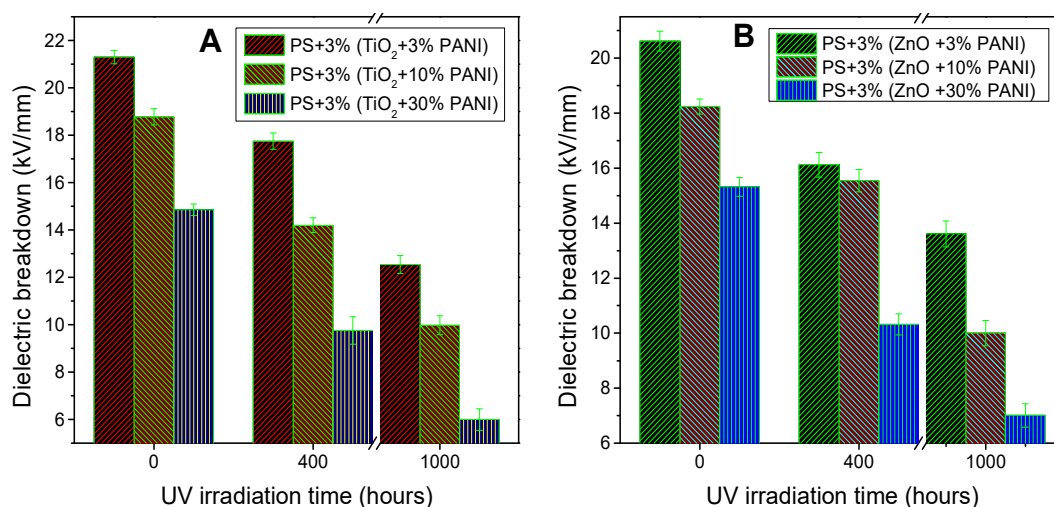
Figure 4.12.1*. Dielectric breakdown (breakdown voltage) of PS-TiO₂-PANI and PS-ZnO-PANI composites at varying UV irradiation time*

The value of BDVs of all these composites further decreased as the time of UV irradiation increased (Figure 4.12.1). The decrease in BDV values supported the formation of charge centres due to photodegradation of the composites. Higher decrease in the values of BDV was found in PS-TiO₂-PANI composites compared to that of PS-ZnO-PANI composites. In both the composites, the one containing 10 % PANI with respect to TiO₂ or ZnO exhibited better decrease in the BDV values upon UV irradiation compared to the other composites under study.
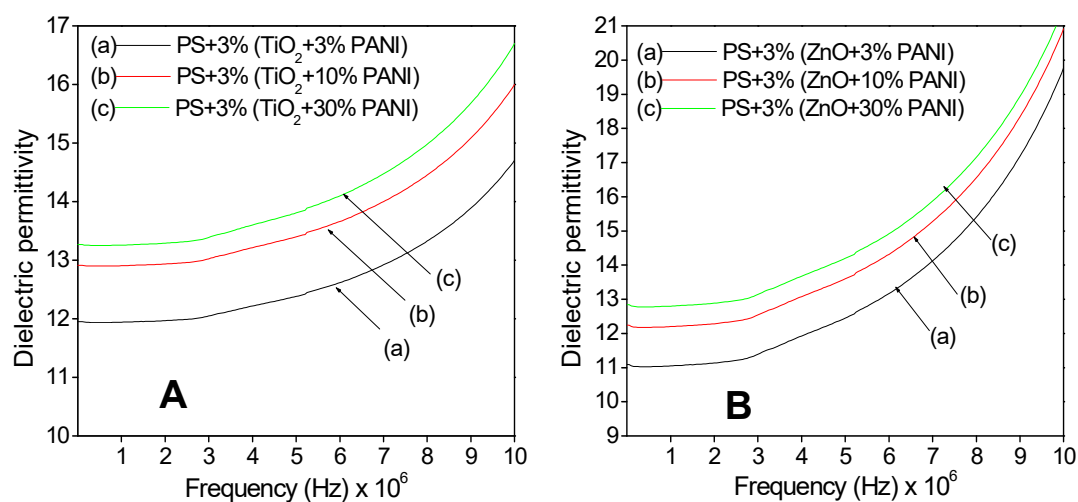
Figure 4.12.2*. Dielectric constants of PS-TiO₂-PANI and PS-ZnO-PANI composites*
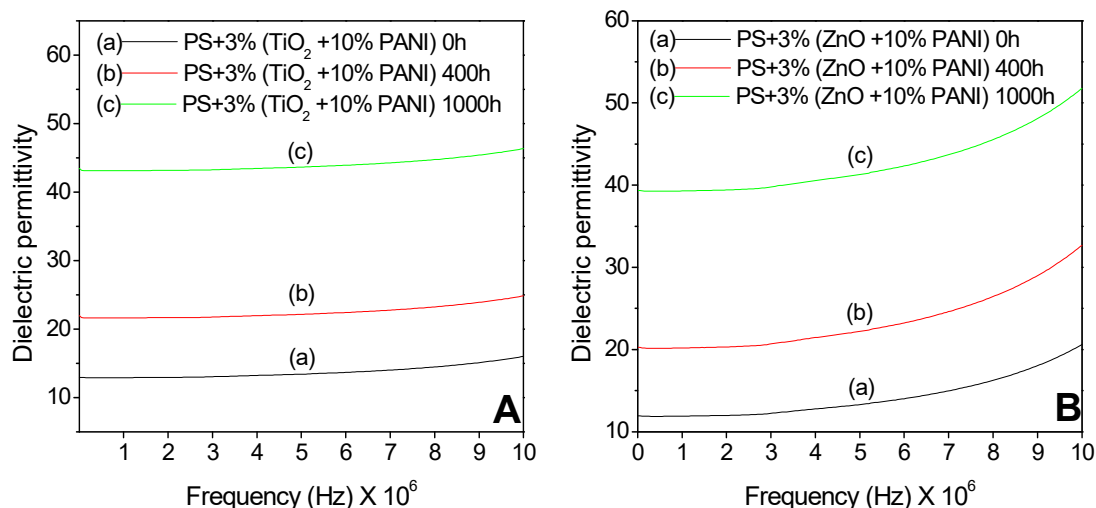
Figure 4.12.3*. Dielectric constants of PS-TiO₂-PANI and PS-ZnO-PANI composites at UV irradiation intervals of 0 h, 400 h and 1000 h.*

The dielectric permittivity (ε_r) calculated from capacitance measurements of the composites was found to increase as the percentage of PANI increased (Figure 4.12.2). This shows that PS-TiO₂-PANI and PS-ZnO-PANI composites could be developed for capacitance applications. The ε_r of the composites further increased upon UV irradiation due to the formation of polarisable species on photodegradation (Figure 4.12.3). PS-TiO₂-PANI composites showed better increase in the values of ε_r compared to PS-ZnO-PANI

4.4.8. Weight loss
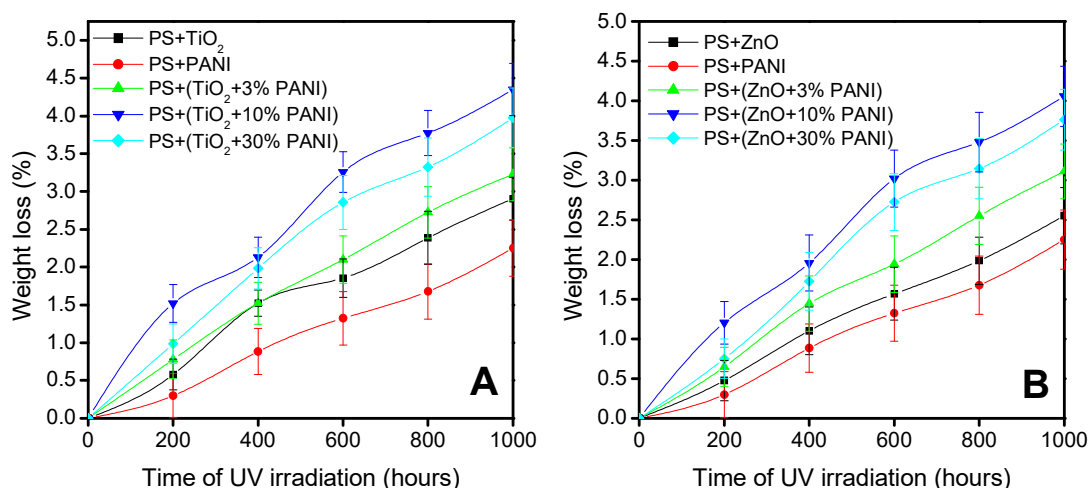
Figure 4.13*. Comparison of weight loss percentages of PS-TiO₂ and PS-PANI composites with PS-TiO₂-PANI (A) and PS-ZnO-PANI (B) composites at regular intervals of UV irradiation*

The weight loss percentage of PS composite loaded with TiO_2-10% PANI (Figure 4.13A) and ZnO-10% PANI (Figure 4.13B) was found to be higher compared to the other specimens under study. Weight loss observed in the PS composites was due to the evolution of gases like CO, CO_2, H_2O, H_2 etc as the side products during the UV degradation process. Weight loss observed in the composites was in accordance with the order of photodegradation. All these observations pointed out the fact that the photocatalytic efficiency of nano TiO_2 and ZnO were enhanced by coupling them with PANI up to an optimum percentage.

4.5. Mechanism of Photocatalysis of TiO_2-PANI and ZnO-PANI composites
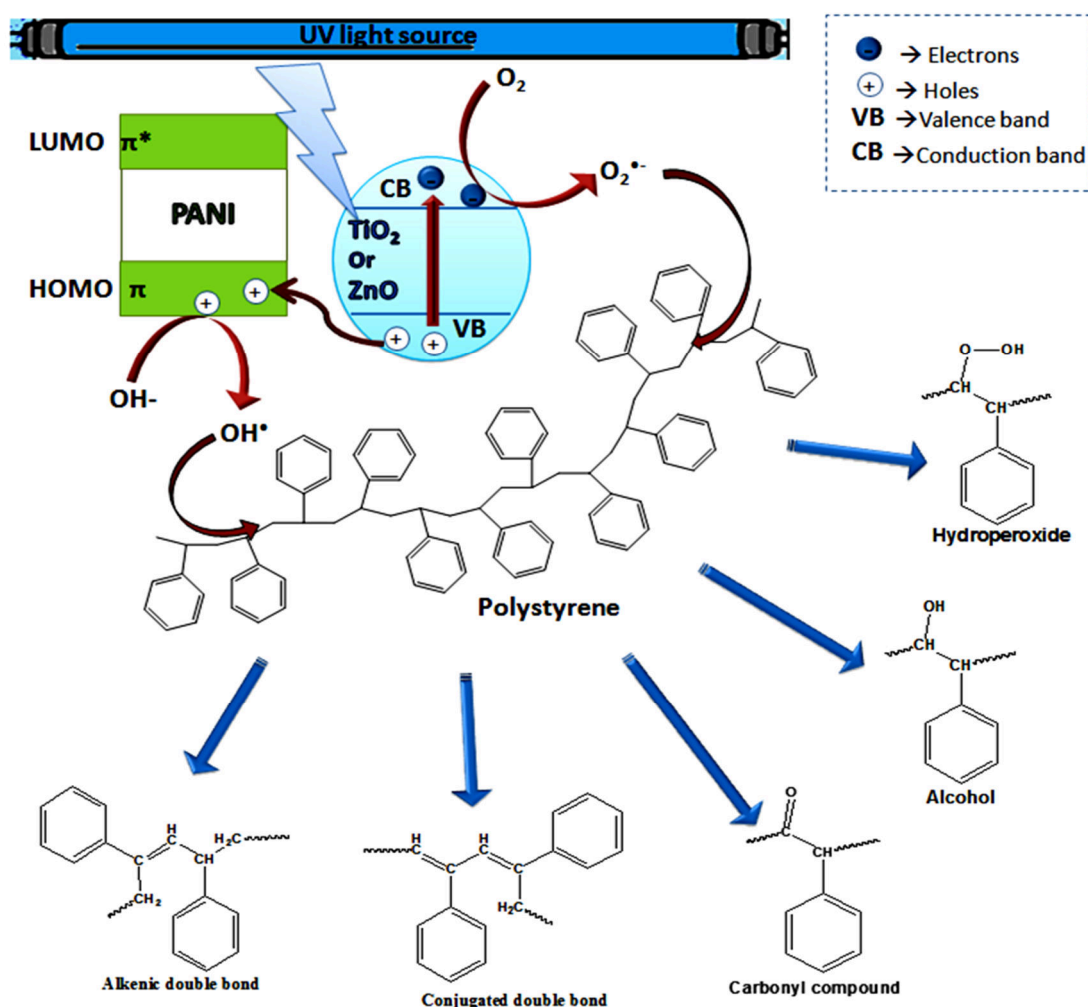
Figure 4.14. *Mechanism of photodegradation of PS using TiO_2-PANI or ZnO-PANI composites.*

Photocatalytic activity of nano TiO_2 and nano ZnO were appreciably enhanced when coupled with PANI. Accelerated photodegradation exhibited by PS-TiO_2-PANI and PS-ZnO-PANI composites compared to that of pristine PS-TiO_2 and PS-ZnO composites is an evidence to this fact. Enhancement in photocatalytic activity could be explained on the basis of enhanced charge separation accomplished on the interfaces of PANI and TiO_2 or ZnO. When UV radiations are absorbed by TiO_2 or ZnO particles, electrons get excited from their valence bands (VB) to conduction band (CB). The energies of the highest occupied molecular orbital (HOMO) of PANI lie between the VB and CB of TiO_2 or ZnO. The holes left behind in the VB of TiO_2 or ZnO are transferred to the HOMO of PANI. Chance for recombination of the photogenerated electrons and holes is therefore minimized[46–49]. These electrons now interact with the O_2 molecules creating superoxide radicals ($O_2\bullet^-$) which interacts with PS matrix initiating photodegradation. In addition to this, the holes transferred to the HOMO of the PANI can interact with the adsorbed water or OH^- ions to produce species like $OH^\bullet$ which interacts with the PS chain and the photodegradation is enhanced (Figure 4.14).

4.6. Conclusion

PANI has been successfully prepared by chemical oxidative polymerization from aniline monomer. Green coloured HCl doped emeraldine salt of PANI have been obtained. TiO_2-PANI and ZnO-PANI composites have been developed by insitu polymerization of aniline over nano TiO_2 and ZnO. Powder XRD confirms that TiO_2-PANI composites were crystalline while ZnO-PANI existed in semicrystalline structure which was further confirmed through HRTEM. The free chain growth of PANI was hampered by nano TiO_2 and ZnO particles which made its (PANI's) X-ray diffraction patterns only partially visible in ZnO-PANI composites and invisible in TiO_2-PANI composites. FTIR spectra of the composites confirmed strong interaction between TiO_2 and ZnO with PANI. Through UV-DRS, charge delocalization due to extended conformation of PANI over the nano particles was observed.

An appreciable acceleration in the photodegradation of PS was confirmed using TiO_2-PANI as well as ZnO-PANI compared to nano TiO_2 and ZnO upon UV irradiation. GPC, FTIR spectroscopy, UV DRS, electrical, mechanical, thermal,

weight loss and SEM analysis were the monitoring tools employed for photodegradation studies. The rate of photodegradation increased as the percentage of PANI coupled with nano TiO_2 and nano ZnO increased. Excess percentage of PANI however inversely affected the rate. Photodegradation efficiency of PS-TiO_2-PANI followed the order PS-(TiO_2-10% PANI) > PS-(TiO_2-30% PANI) > PS-(TiO_2-3% PANI) and that of PS-ZnO-PANI followed the order PS-(ZnO-10% PANI)> PS-(ZnO-30% PANI)> PS-(ZnO-3% PANI). It was also observed that PS-TiO_2-PANI composites underwent better photodegradation compared to PS-ZnO-PANI.

References

1. Riaz, U., Ashraf, S. M. & Kashyap, J. Enhancement of photocatalytic properties of transitional metal oxides using conducting polymers: A mini review. *Mater. Res. Bull.* **71**, 75–90 (2015).
2. Chen, F., An, W., Li, Y., Liang, Y. & Cui, W. Fabricating 3D porous PANI/TiO2–graphene hydrogel for the enhanced UV-light photocatalytic degradation of BPA. *Appl. Surf. Sci.* **427**, 123–132 (2018).
3. Ansari, M. O., Khan, M. M., Ansari, S. A. & Cho, M. H. Polythiophene nanocomposites for photodegradation applications: Past, present and future. *J. Saudi Chem. Soc.* **19**, 494–504 (2015).
4. Ansari, M. O. *et al.* Enhanced Thermal Stability under DC Electrical Conductivity Retention and Visible Light Activity of Ag/TiO2@Polyaniline Nanocomposite Film. *ACS Appl. Mater. Interfaces* **6**, 8124–8133 (2014).
5. Olad, A. li, Behboudi, S. & Entezami, A. li A. Preparation, characterization and photocatalytic activity of TiO2/polyaniline core-shell nanocomposite. *Bull. Mater. Sci.* **35**, 801–809 (2012).
6. Wang, F. & Min, S. X. TiO2/polyaniline composites: An efficient photocatalyst for the degradation of methylene blue under natural light. *Chinese Chem. Lett.* **18**, 1273–1277 (2007).
7. Olad, A. & Naseri, B. Preparation, characterization and anticorrosive properties of a novel polyaniline/clinoptilolite nanocomposite. *Prog. Org. Coatings* **67**, 233–238 (2010).
8. Olad, A. & Rashidzadeh, A. Preparation and anticorrosive properties of PANI/Na-MMT and PANI/O-MMT nanocomposites. *Prog. Org. Coatings* **62**, 293–298 (2008).
9. Boeva, Z. & Sergeyev, V. Polyaniline: Synthesis, Properties, and Application. *Polym. Sci. Ser. C* **56**, 153–164 (2014).
10. Anitha, V. C., Banerjee, A. N. & Joo, S. W. Recent developments in TiO2 as n- and p-type transparent semiconductors: synthesis, modification, properties, and energy-related applications. *J. Mater. Sci.* **50**, 7495–7536 (2015).
11. Yakuphanoglu, F. & Şenkal, B. F. Electronic and Thermoelectric Properties of Polyaniline Organic Semiconductor and Electrical Characterization of Al/PANI MIS Diode. *J. Phys. Chem. C* **111**, 1840–1846 (2007).
12. Ganesan, R. & Gedanken, A. Organic-organic hybrid materials based on polyaniline/TiO2 nanocomposites for ascorbic acid fuel cell systems. *Nanotechnology* **19**, 435709 (2008).
13. Gilja, V. *et al.* Stability and synergistic effect of polyaniline/TiO2 photocatalysts in degradation of azo dye in wastewater. *Nanomaterials* **7**, 412 (2017).
14. Gilja, V., Vrban, I., Mandić, V., Žic, M. & Hrnjak-Murgić, Z. Preparation of a PANI/ZnO composite for efficient photocatalytic degradation of acid blue. *Polymers (Basel).* **10**, 940 (2018).
15. Saravanan, R. *et al.* Conducting PANI stimulated ZnO system for visible light

photocatalytic degradation of coloured dyes. *J. Mol. Liq.* **221**, 1029–1033 (2016).

16. Min, S., Wang, F. & Han, Y. An investigation on synthesis and photocatalytic activity of polyaniline sensitized nanocrystalline TiO2 composites. *J. Mater. Sci.* **42**, 9966–9972 (2007).

17. Senadeera, G. K. R., Kitamura, T., Wada, Y. & Yanagida, S. Deposition of polyaniline via molecular self-assembly on TiO2 and its uses as a sensitiser in solid-state solar cells. *J. Photochem. Photobiol. A Chem.* **164**, 61–66 (2004).

18. Tang, S.-J. *et al.* Polymerization of aniline under various concentrations of APS and HCl. *Polym. J.* **43**, 667–675 (2011).

19. Abu-Thabit, N. Y. Chemical Oxidative Polymerization of Polyaniline: A Practical Approach for Preparation of Smart Conductive Textiles. *J. Chem. Educ.* **93**, 1606–1611 (2016).

20. Bu, Y. & Chen, Z. Role of Polyaniline on the Photocatalytic Degradation and Stability Performance of the Polyaniline/Silver/Silver Phosphate Composite under Visible Light. *ACS Appl. Mater. Interfaces* **6**, 17589–17598 (2014).

21. Olad, A., Asadi, N., Mohammadi, S. & Rahimeh, A. The use of adsorption method to preparation of polyaniline / ZnO nanocomposite varistor. *J. Mater. Sci. Mater. Electron.* **29**, 9692–9699 (2018).

22. Raghava, K., Karthik, K. V, Prasad, S. B. B., Soni, S. K. & Jeong, H. M. Enhanced photocatalytic activity of nanostructured titanium dioxide / polyaniline hybrid photocatalysts Enhanced photocatalytic activity of nanostructured titanium dioxide / polyaniline hybrid photocatalysts. *Polyhedron* **120**, 169–174 (2016).

23. Khan, J. S., Radhakrishnan, A. & Beena, B. Polyaniline/Zinc oxide nanocomposite as a remarkable antimicrobial agent in contrast with PANI and ZnO. *Indian J. Adv. Chem. Sci* **6**, 71–76 (2018).

24. Eskizeybek, V., Gülce, H., Gülce, A., Avc\i, A. & Akgül, E. Preparation of polyaniline/ZnO nanocomposites by using arc-discharge synthesized ZnO nanoparticles and photocatalytic applications. *J. Fac.Eng.Arch. Selcuk Univ* **27**, (2012).

25. Mostafaei, A. & Zolriasatein, A. Synthesis and characterization of conducting polyaniline nanocomposites containing ZnO nanorods. *Prog. Nat. Sci. Mater. Int.* **22**, 273–280 (2012).

26. Li, X., Wang, G., Li, X. & Lu, D. Surface properties of polyaniline/nano-TiO2 composites. *Appl. Surf. Sci.* **229**, 395–401 (2004).

27. Singu, B. S., Srinivasan, P. & Pabba, S. Benzoyl Peroxide Oxidation Route to Nano Form Polyaniline Salt Containing Dual Dopants for Pseudocapacitor. *J. Electrochem. Soc.* **159**, A6--A13 (2011).

28. Pouget, J. P., Hsu, C.-H., Diarmid, A. G. Mac & Epstein, A. J. Structural investigation of metallic PAN-CSA and some of its derivatives. *Synth. Met.* **69**, 119–120 (1995).

29. Singla, M. L., Awasthi, S., Srivastava, A. & Jain, D. V. S. Effect of doping of organic and inorganic acids on polyaniline/Mn3O4 composite for NTC and conductivity behaviour. *Sensors Actuators A Phys.* **136**, 604–612 (2007).

30. Anilkumar, P. & Jayakannan, M. New Renewable Resource Amphiphilic Molecular Design for Size-Controlled and Highly Ordered Polyaniline Nanofibers. *Langmuir* **22**, 5952–5957 (2006).

31. Patil, S. L. *et al.* Structural, Morphological, Optical, and Electrical Properties of PANi-ZnO Nanocomposites. *Int. J. Polym. Mater. Polym. Biomater.* **61**, 809–820 (2012).

32. Sapurina, I. & Stejskal, J. The mechanism of the oxidative polymerization of aniline and the formation of supramolecular polyaniline structures. *Polym. Int.* **57**, 1295–1325 (2008).

33. Feng, W. *et al.* Synthesis and Characterization of Photoconducting Polyaniline-TiO2 Nanocomposite. *Bull. Chem. Soc. Jpn.* **73**, 2627–2633 (2000).

34. Xia, H. & Wang, Q. Ultrasonic Irradiation: A Novel Approach To Prepare Conductive Polyaniline/Nanocrystalline Titanium Oxide Composites. *Chem. Mater.* **14**, 2158–2165 (2002).

35. Daikh, S., Zeggai, F. Z., Bellil, A. & Benyoucef, A. Chemical polymerization, characterization and electrochemical studies of PANI/ZnO doped with hydrochloric acid and/or zinc chloride: Differences between the synthesized nanocomposites. *J. Phys. Chem. Solids* **121**, 78–84 (2018).

36. Khan, A. A. & Khalid, M. Synthesis of Nano-Sized ZnO and Polyaniline-Zinc Oxide Composite : Characterization , Stability in Terms of DC Electrical Conductivity Retention and Application in Ammonia Vapor Detection. (2010). doi:10.1002/app

37. Talwar, V., Singh, O. & Singh, R. C. ZnO assisted polyaniline nanofibers and its application as ammonia gas sensor. *Sensors Actuators B Chem.* **191**, 276–282 (2014).

38. Sawarkar, M., Pande, S. A. & Agrawal, P. S. Synthesis and characterization of polyaniline doped metal oxide nanocomposites. (2015).

39. Sharma, B. K., Gupta, A. K., Khare, N., Dhawan, S. K. & Gupta, H. C. Synthesis and characterization of polyaniline – ZnO composite and its dielectric behavior. **159**, 391–395 (2009).

40. Dhingra, M., Shrivastava, S., Kumar], P. [Senthil & Annapoorni, S. Polyaniline mediated enhancement in band gap emission of Zinc Oxide. *Compos. Part B Eng.* **45**, 1515–1520 (2013).

41. Zhu, S., Wei, W., Chen, X., Jiang, M. & Zhou, Z. Hybrid structure of polyaniline/ZnO nanograss and its application in dye-sensitized solar cell with performance improvement. *J. Solid State Chem.* **190**, 174–179 (2012).

42. Chauhan, S. M., Jayveer, M. & Chakarabarty, B. S. Dielectric property and conductivity study of polyaniline--CaF2 nanocomposites. *J Nano Adv Mat* **4**, 9–17 (2016).

43. Wang, Y. *et al.* Electropolymerized polyaniline/manganese iron oxide hybrids with an enhanced color switching response and electrochemical energy storage. *J. Mater. Chem. A* **3**, 20778–20790 (2015).

44. Ameen, S., Akhtar, M. S. & Kim, Y. S. An effective nanocomposite of polyaniline and ZnO : preparation , characterizations , and its photocatalytic activity. *Colloid Polym Sci* **289**, 415–421 (2011).

45. Ansari, R. & Keivani, M. B. Polyaniline Conducting Electroactive Polymers Thermal and Environmental Stability Studies. *E-Journal Chem.* **3**, 395391 (2006).

46. Asgari, E. *et al.* The comparison of ZnO/polyaniline nanocomposite under UV and visible radiations for decomposition of metronidazole: Degradation rate, mechanism and mineralization. *Process Saf. Environ. Prot.* **128**, 65–76 (2019).

47. Anand, A., Rani, N., Saxena, P., Bhandari, H. & Dhawan, S. K. Development of polyaniline/zinc oxide nanocomposite impregnated fabric as an electrostatic charge dissipative material. *Polym. Int.* **64**, 1096–1103 (2015).

48. Zhang, H., Zong, R., Zhao, J. & Zhu, Y. Dramatic Visible Photocatalytic Degradation Performances Due to Synergetic Effect of TiO2 with PANI. *Environ. Sci. Technol.* **42**, 3803–3807 (2008).

49. Zhang, H., Zong, R. & Zhu, Y. Photocorrosion Inhibition and Photoactivity Enhancement for Zinc Oxide via Hybridization with Monolayer Polyaniline. *J. Phys. Chem.* **113**, 4605–4611 (2009).

Chapter 5

Accelerated Photodegradation of Polystyrene using TiO$_2$ and ZnO Surface Modified with Graphene oxide

Abstract

Graphene oxide (GO) was prepared from graphite using modified Hummer's method. TiO$_2$-GO and ZnO-GO composites were developed using sonication assisted hydrothermal method. Composites of TiO$_2$-GO and ZnO-GO with 3, 10 and 30 percentages of GO were prepared. The crystal morphology of TiO$_2$ and ZnO remained unaltered upon GO coupling as evident through XRD analysis. XRD, Raman spectroscopy and XPS analysis confirmed partial reduction of GO, when coupled with TiO$_2$ or ZnO. XPS further confirmed the formation of Ti-O-C and Ti-C bridge bonds between TiO$_2$ and GO. TiO$_2$-GO existed as dispersed particles having crystal morphology. ZnO-GO showed slight amorphous nature. PS-TiO$_2$-GO and PS-ZnO-GO composites were mechanically stronger and thermally more stable compared to PS-TiO$_2$ and PS-ZnO. TiO$_2$-GO and ZnO-GO composites exhibited enhanced photocatalytic efficiency compared to TiO$_2$ and ZnO respectively for the UV degradation of PS. It was also observed that TiO$_2$-GO was more efficient compared to ZnO-GO for PS degradation.

5.1. Introduction

Studies worldwide have shown that the photocatalytic property of inorganic metal oxide semiconductors has appreciably enhanced in the presence of carbon based materials like carbon nano tube[1,2], fullerene[3,4] and graphene[5,6]. The photocatalytic activities of TiO_2 and ZnO coupled with such carbon allotropes have been extensively investigated with amazing results. Out of the carbon structures, graphene has an advantage of 2D planar structure with higher surface area for better interaction with other materials and can be prepared easily in the laboratory from graphite. Graphene has some marked unique properties including enhanced electrical[7], mechanical[8], thermal[9] and optical properties[10]. Better chemical stability is also observed in this transparent and flexible material[11]. Composites of graphene find application in electronics[7], composite materials[12,13], solar cells[14], ultra capacitors[15], medicine[16,17] molecular sensors[18] and so on.

Graphene oxide (GO) could be considered as a derivative of graphene with oxygen atoms bonded covalently to some of its carbon atoms leading to hydroxyl or epoxy bonds[19–23]. Carboxylic acid functional groups may also be attached to the periphery of hexagonal two dimensional planes of GO[24]. Even though GO shows slight variations in some of the properties compared to graphene, like conductivity[25], GO resembles graphene in many other aspects. Graphene could be replaced by GO where improved hydrophilicity is demanded. The functional groups >C=O, -COOH and epoxy, covalently bonded to some of the carbon atoms in GO provides better interaction with polar solvents especially water. GO is hence highly dispersible in water[26,27]. Graphene, on the other hand, is not dispersible in aqueous media. The existence of strong molecular interaction between GO and metal oxides in composites have been reported[28]. The interaction between GO and metal oxides are possible in a number of ways including the formation of hydrogen bonds, M-C[29] and M-O-C[30–33] bonds where M refers to the metal atoms in metal oxides, C for carbon and O for oxygen. These bonds act as bridges, facilitating easy charge transport between the metal oxides and GO. The properties of GO and metal oxides are entirely altered into new properties related to the composite. One of the most important properties of metal oxide-GO composite materials is related to its bandgap energy[34]. The bandgap energy of metal oxide–GO composites is lower compared to that of metal oxides. The

relevance of such bandgap shift comes into picture when the metal oxides like TiO_2 and ZnO with high bandgap energies that absorb only in the UV region, are shifted into modified materials with lower bandgap energies upon surface modification with GO. The lowering of bandgap energy allows the material to absorb in the UV as well as in the visible region extending its application to broad areas.

Decreased rate of recombination of photogenerated electrons and holes of metal oxides are observed in metal oxide-GO composites. The electrons in the conduction band of metal oxides are transferred into the carbon atoms of GO. These electrons are resonance stabilized in GO and their recombination with the holes in metal oxides are hence minimized[35]. Interfacial charge transfer of TiO_2-GO and ZnO-GO has been reported with heterojunctions of enhanced photocatalytic activity[36,37].

Photodegradation of PS in the presence of TiO_2 as well as ZnO coupled with Graphene oxide (GO) is discussed in this chapter. GO has been selected instead of graphene for surface modification of TiO_2 and ZnO keeping the following aspects in mind: (i) GO bears similar properties as graphene. (ii) GO could stabilize ZnO or TiO_2 much easier than graphene by various interactions. (iii) The oxygen containing functional groups present in GO can interact with electrons from ZnO or TiO_2 forming a bridge between them facilitating easier charge transfer. (iv) The functional groups present in GO can produce radicals when exposed to UV radiation for the initiation of photochemical reaction. (v) Preparation of GO is easier compared to graphene (vi) GO can be dispersed much easily in a wide variety of polar solvents compared to graphene so that TiO_2-GO or ZnO-GO composite preparation becomes easier.

Out of numerous methods of preparation of GO, the most widely adopted one is the oxidation of graphite developed by Hummers and Offeman in 1958[38]. Modified Hummers methods are commonly used nowadays. In this strategy, oxidizing agents are penetrated between the layers of graphite resulting in the separation of GO layers and finally the oxidation reaction is terminated with the aid of H_2O_2 and water[39,40]. The mechanism of GO formation through three stages involves the formation of H_2SO_4-graphite intercalation compound followed by its oxidation and reaction with water as reported by A.M. Dimiev and J.M. Tour in 2014[41]. The advantages of GO

preparation by Hummers or modified Hummers method are the elimination of evolution of explosive gases and decrease of reaction time[42].

Section I

Synthesis and characterisation of TiO$_2$-GO and ZnO-GO composites

5.2. Experimental

5.2.1. Synthesis of Graphene oxide (GO)

GO was prepared from graphite (150 mesh) through modified Hummers method. Typically 23 ml of sulphuric acid was cooled to 0°C in a flask to which 1g of graphite and 0.5 g NaNO$_3$ were added slowly with stirring over an ice bath. Vigorous stirring was continued for 40 minutes. 3g KMnO$_4$ was then added to this mixture while stirring was in progress, very slowly and in a controlled way, maintaining the temperature of the system below 20°C. A dark green viscous solution was obtained. Vigorous stirring was continued for another 12 hours at room temperature. To the viscous paste like reaction mixture, 40 ml distilled water was added. The dark brown mixture hence obtained was subjected to stir for another 24 hours followed by the slow addition of 10 ml 30% H$_2$O$_2$. The mixture turned yellowish brown in colour. Stirring was continued for another 6 hours. The solution hence obtained was washed 20 times thoroughly using 1M HCl followed by distilled water using a laboratory centrifuge until the pH of the solution reached 6. pH 7 could not be reached by washing the solid GO residue obtained using water practically. So the solid GO hence obtained was dried at 80°C for 12 hours in a hot air oven and finally a brownish black thin film of GO was obtained[28,43].

5.2.2. Synthesis of TiO$_2$-GO composite

TiO$_2$-GO composites were prepared by ultrasonication assisted hydrothermal process. TiO$_2$-GO composites with 1, 3, 10 and 30 weight percentages of GO namely TiO$_2$-1% GO, TiO$_2$-3% GO, TiO$_2$-10% GO and TiO$_2$-30% GO were prepared respectively. In order to prepare TiO$_2$-1% GO, 8 mg of GO was dispersed in 80 ml

water and 40 ml ethanol by vigorous sonication using an ultrasonic probe sonicator (750 W) for two hours in a flask. 800 mg of nano TiO_2 was added to the flask and the sonication was continued for another two hours. The temperature of the flask was maintained using an ice bath in order to prevent evaporation of solvents due to excess heating. The contents of the flask were transferred into a Teflon lined hydrothermal autoclave which was kept in a hot air oven at a temperature 130°C for 6 hours. The bluish grey solid residue hence obtained was filtered out from the solution and dried at 70°C for 12 hours in a hot air oven. TiO_2-3% GO, TiO_2-10% GO and TiO_2-30% GO composites were prepared by the same route varying the weight percentages of GO taken[44–46].

5.2.3. Synthesis of ZnO-GO

ZnO-GO composites were also prepared by ultrasonication assisted hydrothermal process. ZnO-GO composites with 3, 10 and 30 weight percentages of GO namely ZnO-3% GO, ZnO-10% GO and ZnO-30% GO were prepared. For the preparation of ZnO-3% GO, 30 mg of GO was dispersed in 40 ml water and sonicated for 2 hours. 1.55 g of zinc nitrate hexahydrate ($Zn(NO_3)_2.6H_2O$) was added to the dispersion. Liquid ammonia was added dropwise with vigorous stirring until a white precipitate of $Zn(OH)_2$ was formed. The entire mixture was then transferred into a Teflon lined hydrothermal autoclave which was kept in a hot air oven at a temperature 130°C for 6 hours. The solid residue hence obtained was filtered, washed with distilled water and dried at 70°C for 12 hours in a hot air oven. ZnO-10% GO and ZnO-30% GO were also prepared in similar way by changing the weight percentage of GO[47,48].

5.3. Results and Discussion

5.3.1. Powder XRD

Powder XRD pattern of prepared GO exhibits its characteristic intense peak at an angle $2\theta=10.7°$ corresponding to the (001) plane of GO. In addition to this, a broader peak of very low intensity was also observed at an angle $2\theta=26°$ corresponding to the unoxidized graphite and/or reduced GO present in traces (Figure 5.1.1).

XRD patterns of TiO_2-GO composites exhibited all the peaks corresponding to TiO_2 (Figure 5.1.1). The peak corresponding to GO was hampered and invisible in

TiO$_2$-GO composites. The dispersion of nano sized GO layers and their association with TiO$_2$ without any aggregation made the presence of GO undetectable through XRD. The absence of the characteristic peak corresponding to GO ($2\theta=10.7°$) also suggests the possibility of partial reduction of GO in TiO$_2$ composites upon hydrothermal treatment (as confirmed through Raman spectroscopy and XPS analysis discussed below). Peak sharpening were also observed in TiO$_2$-GO composites compared to pristine TiO$_2$ probably due to the increase in size of the composite particles with the incorporation of GO. The inter planar distance (d) calculated using Bragg's equation showed a slight decrease for the TiO$_2$-GO composites compared to that of pristine TiO$_2$ (Table 5.1.1). Crystallite sizes calculated from Debye Scherrer's formula was greater for TiO$_2$-GO composites as compared to pristine TiO$_2$ (Table 5.1.3)[49,50].
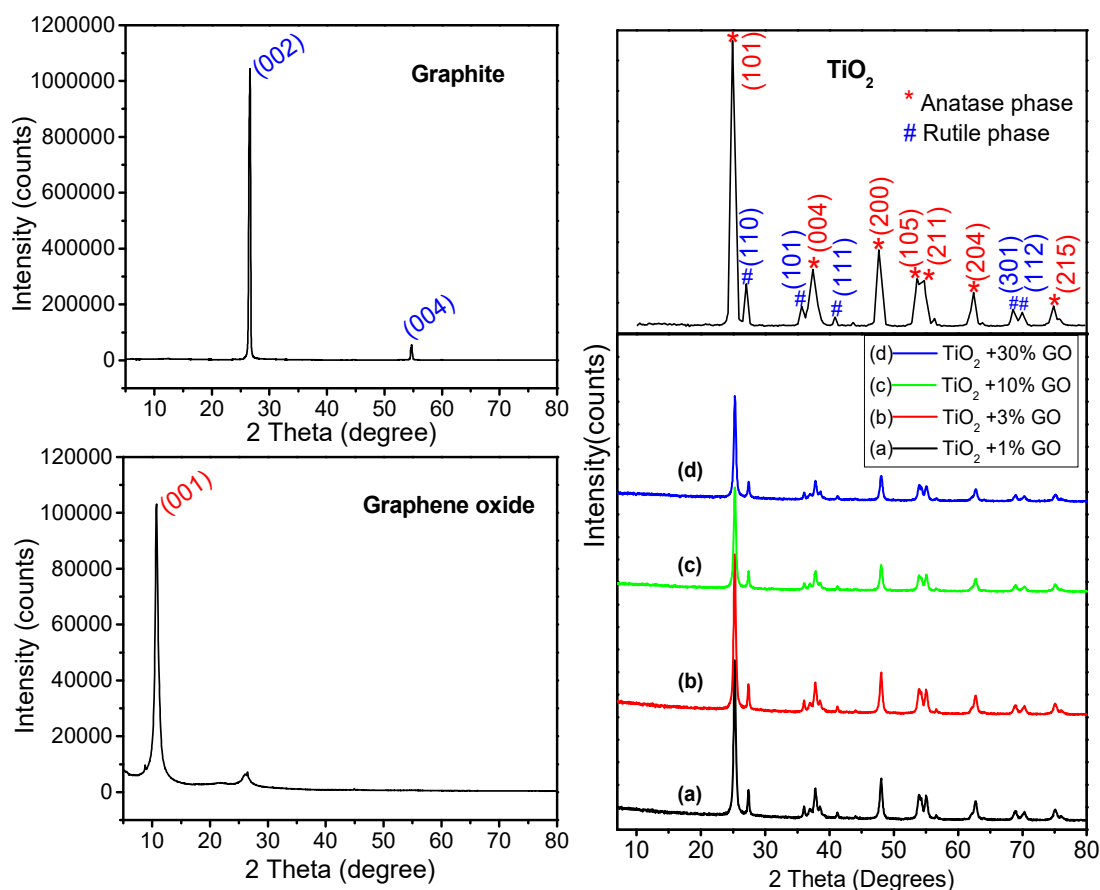
Figure 5.1.1. XRD patterns of graphite, GO, TiO$_2$ and TiO$_2$-GO composites.

XRD patterns of all the ZnO-GO composites exhibited the characteristic peaks of ZnO (Figure 5.1.2). XRD patterns of ZnO-3% GO resembled that of ZnO. For ZnO-10% GO composite new broad patterns between $2\theta=20$ to $28°$ corresponding to

reduced GO was observed. In addition to this, broad peaks at $2\theta=12.8°$, 33° and 59.6° corresponding to $Zn(OH)_2$ were also observed. The intensity of the peaks corresponding to reduced GO as well as $Zn(OH)_2$ increased in ZnO-30%GO composite. Inter planar distance (d) of the composites were calculated from Bragg's equation (Table 5.1.2) and crystallite sizes were calculated using Debye Scherrer's equation (Table 5.1.3). Crystallite sizes of the composites were slightly higher compared to that of pristine ZnO.
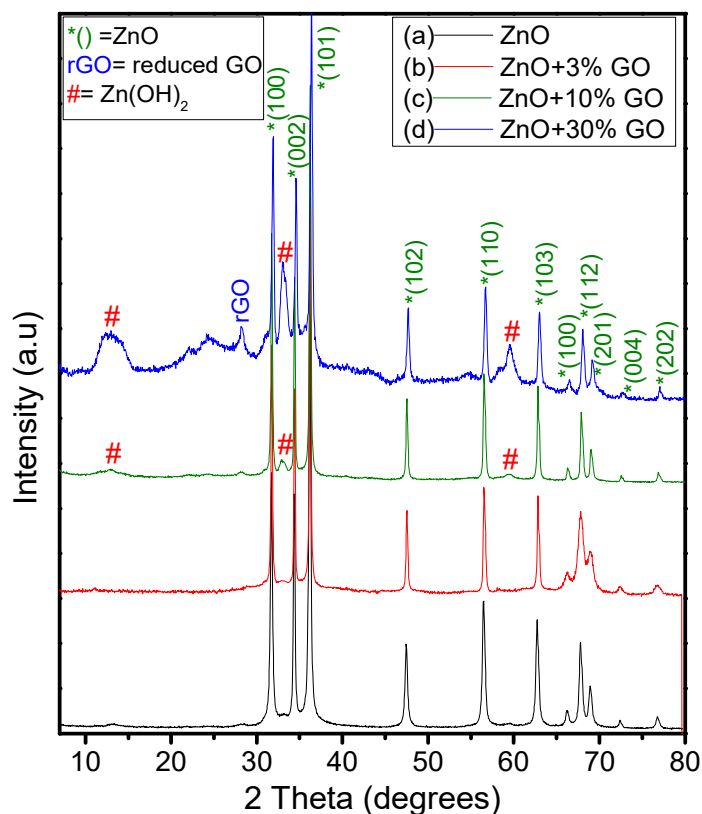
Figure 5.1.2. XRD patterns of ZnO and ZnO-GO composites.

Table 5.1.1. *Inter planar distances (d) corresponding to 2θ peaks of TiO₂ and TiO₂-GO composites*

	TiO₂		TiO₂-1%GO		TiO₂- 3% GO		TiO₂- 10%GO		TiO₂- 30%GO	
	$2\theta°$	d (Å)	$2\theta°$	d (Å)	$2\theta°$	d (Å)	$2\theta°$	d (Å)	$2\theta°$	d (Å)
Anatase phase	24.9	3.573	25.2	3.531	25.3	3.517	25.3	3.517	25.3	3.517
	37.4	2.403	37.8	2.378	37.8	2.378	37.8	2.378	37.8	2.378
	47.7	1.905	48.1	1.89	48.1	1.89	48.1	1.89	48.1	1.89
	53.6	1.708	53.8	1.703	53.8	1.703	53.8	1.703	53.8	1.703
	54.7	1.677	54.9	1.671	55	1.668	55	1.668	55	1.668
	62.4	1.487	62.7	1.481	62.7	1.481	62.7	1.481	62.7	1.481
	74.8	1.268	75.1	1.264	75.1	1.264	75.1	1.264	75.1	1.264

	2θ°	d	2θ°	d	2θ°	d	2θ°	d	2θ°	d
Rutile phase	27.1	3.288	27.4	3.252	27.4	3.252	27.4	3.252	27.4	3.252
	35.7	2.513	36	2.493	36.1	2.486	36.1	2.486	36.1	2.486
	40.8	2.21	41.2	2.189	41.2	2.189	41.2	2.189	41.2	2.189
	68.6	1.367	69.9	1.345	70	1.343	70	1.343	70	1.343
	70	1.343	70.3	1.338	70.3	1.338	70.3	1.338	70.3	1.338

Table 5.1.2. *Inter planar distances (d) corresponding to 2θ peaks of ZnO and TiO₂-GO composites*

ZnO		ZnO-3%GO		ZnO-10% GO		ZnO-30%GO	
2 θ°	d (Ǎ)	2 θ°	d (Ǎ)	2 θ°	d (Ǎ)	2 θ°	d (Ǎ)
31.97	2.80	31.98	2.79	31.98	2.79	31.98	2.79
34.62	2.59	34.65	2.59	34.65	2.59	34.65	2.59
36.45	2.46	36.47	2.46	36.47	2.46	36.47	2.46
47.71	1.90	47.73	1.9	47.73	1.9	47.73	1.9
56.75	1.62	56.77	1.6	56.77	1.6	56.77	1.6
63.01	1.47	63.05	1.47	63.05	1.47	63.05	1.47
66.48	1.41	66.5	1.4	66.5	1.4	66.5	1.4
68.05	1.38	68.07	1.38	68.07	1.38	68.07	1.38
69.18	1.36	69.2	1.36	69.2	1.36	69.2	1.36
72.70	1.30	72.73	1.3	72.73	1.3	72.73	1.3
77.00	1.24	77.03	1.24	77.03	1.24	77.03	1.24

Table 5.1.3 *Crystallite size of TiO₂-GO and ZnO-GO composites calculated using Debye- Scherrer equation.*

	Crystallite size (nm)		Crystallite size (nm)
TiO₂	17.57	ZnO	30.7
TiO₂-1%GO	20.12	ZnO - 3% GO	38.65
TiO₂- 3% GO	20.27	ZnO -10%GO	38.83
TiO₂-10%GO	20.32	ZnO -30%GO	38.99
TiO₂-30%GO	20.38		

5.3.2. FTIR Spectroscopy

FTIR spectra of GO exhibited its characteristic peaks which included $>C=O$ (1719 cm^{-1}), $>C=C<$ (1622 cm^{-1} and 1519 cm^{-1}), -C-O- (1065 cm^{-1} and 963 cm^{-1}), -OH stretching (3600-3000 cm^{-1}), -C-O-H bending (1377 cm^{-1}) and -C-H out of plane bending vibrations (673 cm^{-1}) (Figure 5.2). The presence of carboxylic acid and hydroxyl functional groups in GO were hence quite evident. FTIR spectra of TiO₂-GO composites exhibited characteristic vibration peaks corresponding to TiO₂ as well

as GO (Figure 5.2 A). A striking observation made from the IR spectra was that a considerable shift towards lower wavenumber in the peak positions occurred in TiO_2-GO composites when compared to uncoupled GO. With the increase in percentage incorporation of GO among the composites, peaks corresponding to >C=O and -C-O-H functional groups exhibited an observable shift. This observation suggested the existence of a strong interaction between TiO_2 and the oxygen atom of acid or alcoholic functional groups of GO. Increase in the intensities of IR absorption peaks of GO were also observed in the composites as the percentage of GO incorporation increased. Tabulated FTIR data of TiO_2-GO composites in comparison to GO is given in table 5.2.1.
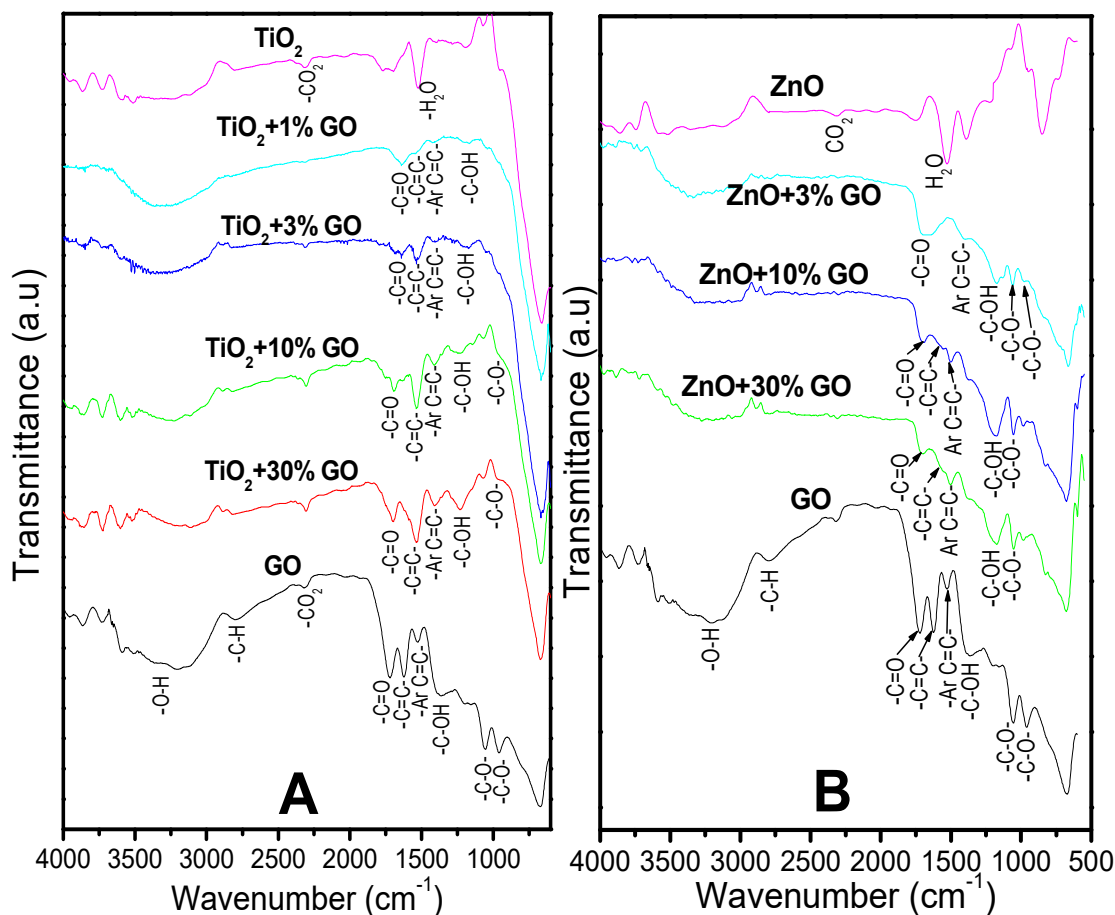
Figure 5.2. *FTIR spectra of TiO_2-GO composites (A) and ZnO-GO composites (B) in comparison with that of GO, TiO_2 and ZnO.*

Similar observations were made from FTIR spectra of ZnO-GO composites (Figure 5.2 B). The characteristic vibration bands of GO shifted towards lower wavenumber positions in ZnO-GO composites due to the interaction between ZnO

and GO. The shift in peak positions of >C=O and -C-O-H functional groups among ZnO-GO composites as the percentage of GO increased, suggested a strong interaction between ZnO and the oxygen atom of the acid or the alcoholic functional groups of GO. The tabulated FTIR data of ZnO-GO composites in comparison to GO is given in table 5.2.2.

Table 5.2.1. Highlighted peaks from FTIR spectra of GO and TiO₂-GO composites

	GO	TiO₂+30%GO	TiO₂+10%GO	TiO₂+3%GO	TiO₂+1%GO
>C=O (stretch)	1719 cm⁻¹	1699 cm⁻¹	1695 cm⁻¹	1645 cm⁻¹	1640 cm⁻¹
>C=C< (Stretch)	1622 cm⁻¹	1536 cm⁻¹	1536 cm⁻¹	1536 cm⁻¹	1536 cm⁻¹
Ar-C=C (Stretch)	1519 cm⁻¹	1412 cm⁻¹	1410 cm⁻¹	1408 cm⁻¹	1408 cm⁻¹
-C-O-H (bend)	1377 cm⁻¹	1232 cm⁻¹	1224 cm⁻¹	1176 cm⁻¹	1165 cm⁻¹
-C-O- (Stretch)	1065 cm⁻¹	Overlapped by Ti-O stretching vibrational peaks			
-C-O- (Stretch)	963 cm⁻¹	962 cm⁻¹	Overlapped by Ti-O stretching vibrational peaks.		

Table 5.2.2. Highlighted peaks from FTIR spectra of GO and ZnO-GO composites

	GO	ZnO+30%GO	ZnO+10%GO	ZnO +3%GO
>C=O (stretch)	1719 cm⁻¹	1704 cm⁻¹	1695 cm⁻¹	1690 cm⁻¹
>C=C< (Stretch)	1622 cm⁻¹	1558 cm⁻¹	1556 cm⁻¹	Overlapped by Ar-C=C band
Ar-C=C (Stretch)	1519 cm⁻¹	1505 cm⁻¹	1501 cm⁻¹	1403 cm⁻¹
-C-O-H (bend)	1377 cm⁻¹	1178 cm⁻¹	1175 cm⁻¹	1170 cm⁻¹
-C-O- (Stretch)	1065 cm⁻¹	1054 cm⁻¹.	Overlapped by Zn-O stretching vibrational peaks	
-C-O- (Stretch)	963 cm⁻¹	Overlapped by Zn-O stretching vibrational peaks.		

5.3.3. Raman Spectroscopy

GO and TiO₂-GO was analysed through Raman spectroscopy in order to study the structure and bonding within TiO₂-GO composite in detail. Raman spectra of GO presented in Figure 5.3a displays two bands at 1355 cm⁻¹ (D band) and 1587 cm⁻¹ (G band). The D band represents the disorder of sp³ carbon atom (having A₁g symmetry)

whereas G band could be attributed to the in-plane sp^2 carbon (E_{2g} symmetry) vibrational mode of graphene skeleton. Raman spectra of TiO_2-30% GO (Figure 5.3b) also shows D and G bands of graphene moiety. Bands observed at 154 cm^{-1}, 394 cm^{-1}, 511 cm^{-1} and 634 cm^{-1} could be attributed to $E_{g(1)}$, $B_{1g(1)}$, $A_{1g}+ B_{1g(2)}$ and $E_{g(2)}$ respectively of anatase phase TiO_2. A band at 2695 cm^{-1} was also observed in TiO_2-30% GO composite that attributes the characteristic 2D band of sp^2 carbon of graphene. This band was however not observed in the spectra of GO. The appearance of 2D band reveals the presence of reduced GO associated with TiO_2 in the composite. The ratio of intensities of D and G bands (I_D/I_G) calculated to be 0.93 in GO decreased to 0.62 in TiO_2-30% GO. The decrease in the I_D/I_G value shows that some of the sp^3 bonds have been converted in to sp^2 (or decrease in structural defects within sp^2 carbon) as a consequence of partial reduction of GO in TiO_2-GO composite.
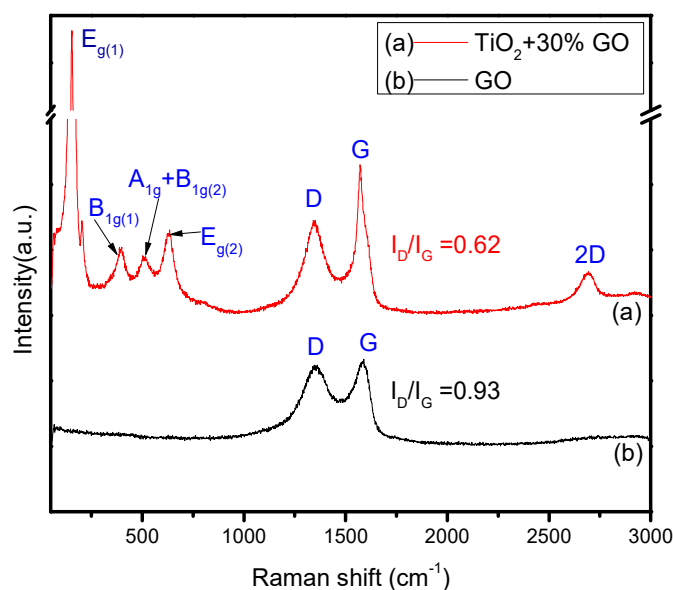
Figure 5.3. *Raman spectra of GO (a) and TiO$_2$-30% GO (b) composite*

5.3.4. X-ray photoelectron spectroscopy (XPS)

The interaction between TiO_2 and GO in TiO_2-GO composites was further clear from XPS analysis of GO and TiO_2-30%GO (Figure 5.4). XPS revealed the fact that partial reduction of GO took place in TiO_2-30%GO composites with the formation of Ti-C and Ti-O-C bonds, between TiO_2 and GO. Bands corresponding to C 1s and O 1s were observed in the XPS of GO and the bands corresponding to Ti 2p, C 1s and O 1s were observed in the XPS of TiO_2-30%GO (Figure 5.4 A).
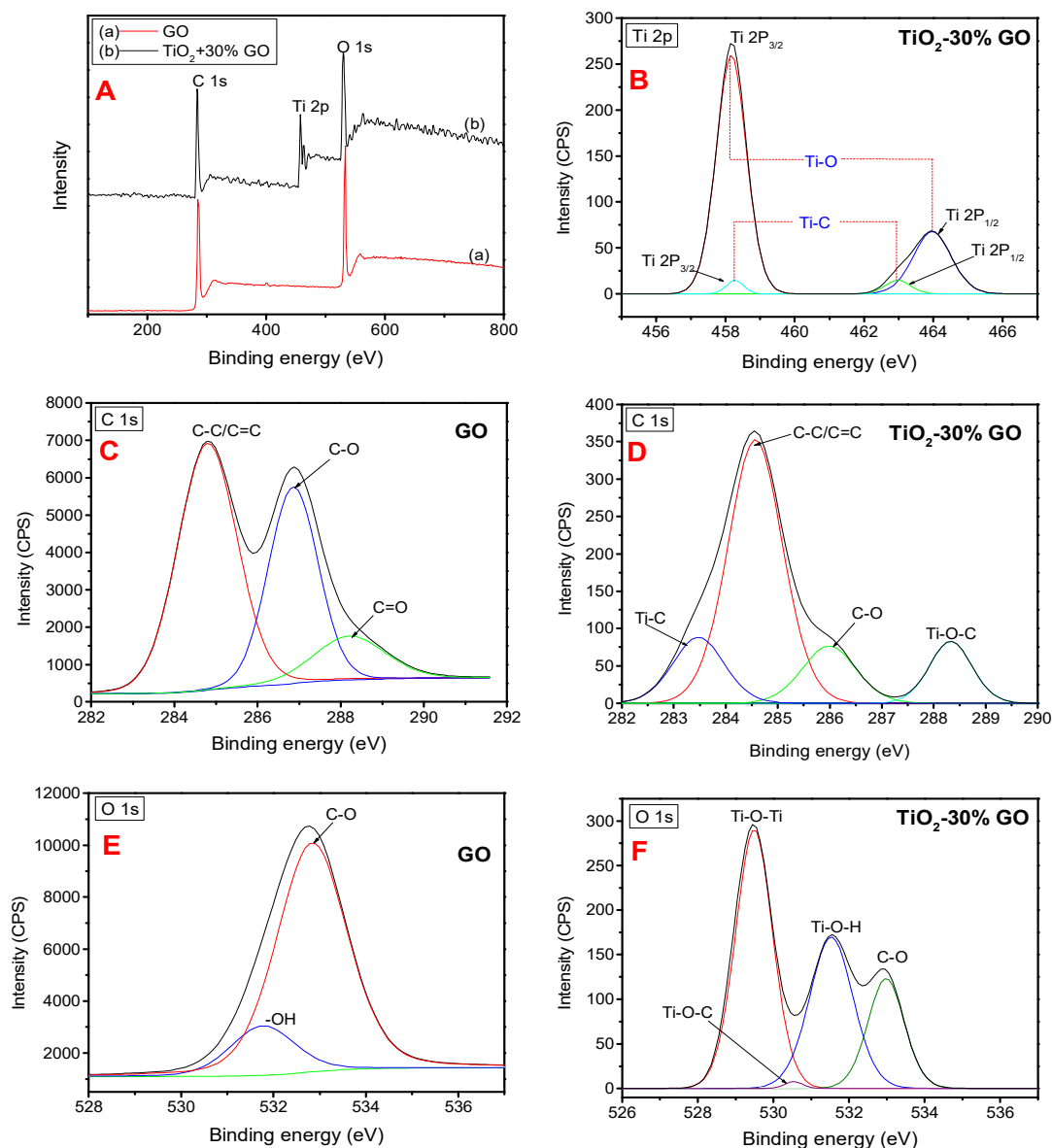
Figure 5.4. *XPS of GO and TiO₂-30%GO (A). Deconvoluted XPS of Ti 2p, C 1s and O 1s regions of GO and TiO₂-30% GO composite (B to F).*

The deconvoluted spectra of C 1s region of GO exhibited three peaks corresponding to the binding energies 284.7 eV, 286.8 eV and 288.1 eV that could be assigned to C-C/C=C, C-O and C=O bonds respectively (Figure 5.4 B). C 1s region of TiO₂-30% GO composite (Figure 5.4 E) showed that the intensity of C-O binding energy peak decreased considerably compared to the C-O peak in C 1s region of GO. This is a clear evidence of partial reduction of GO. The C=O bond observed in GO was shifted to higher binding energy (288.5 eV) in TiO₂-30% GO composite due to the formation of Ti-O-C bond between TiO₂ and GO. A new peak centered at 283.4 eV represents Ti-C bond formed between TiO₂ and GO. The O 1s region of GO showed a peak

centered at 532.9 eV representing -OH bond and a less intense peak at 531.8 representing C-O bond (Figure 5.4 C). O 1s region of TiO_2-30% GO composite displayed peaks centered at 529.4 eV, 530.5 eV, 531.5 eV and 532.95 eV representing Ti-O-Ti, Ti-O-C, Ti-O-H and C-O bonds respectively (Figure 5.4 F). The deconvoluted spectra of Ti 2p region of TiO_2-30%GO composite gave four peaks (Figure 5.4 D). The peaks at 458.1 eV ($2p_{3/2}$) and 463.9 eV ($2p_{1/2}$) originated from the Ti-O bond existing in the composite. Low intense peaks centered at 458.3 eV ($2p_{3/2}$) and 462.9 eV ($2p_{1/2}$) on the other hand originated from Ti-C bond in the composite. The existence of strong interaction between TiO_2 and GO that could facilitate easy transport of photo generated charges between the composites was evident through XPS.

5.3.5. UV-visible Diffused reflectance spectroscopy (UV-DRS)
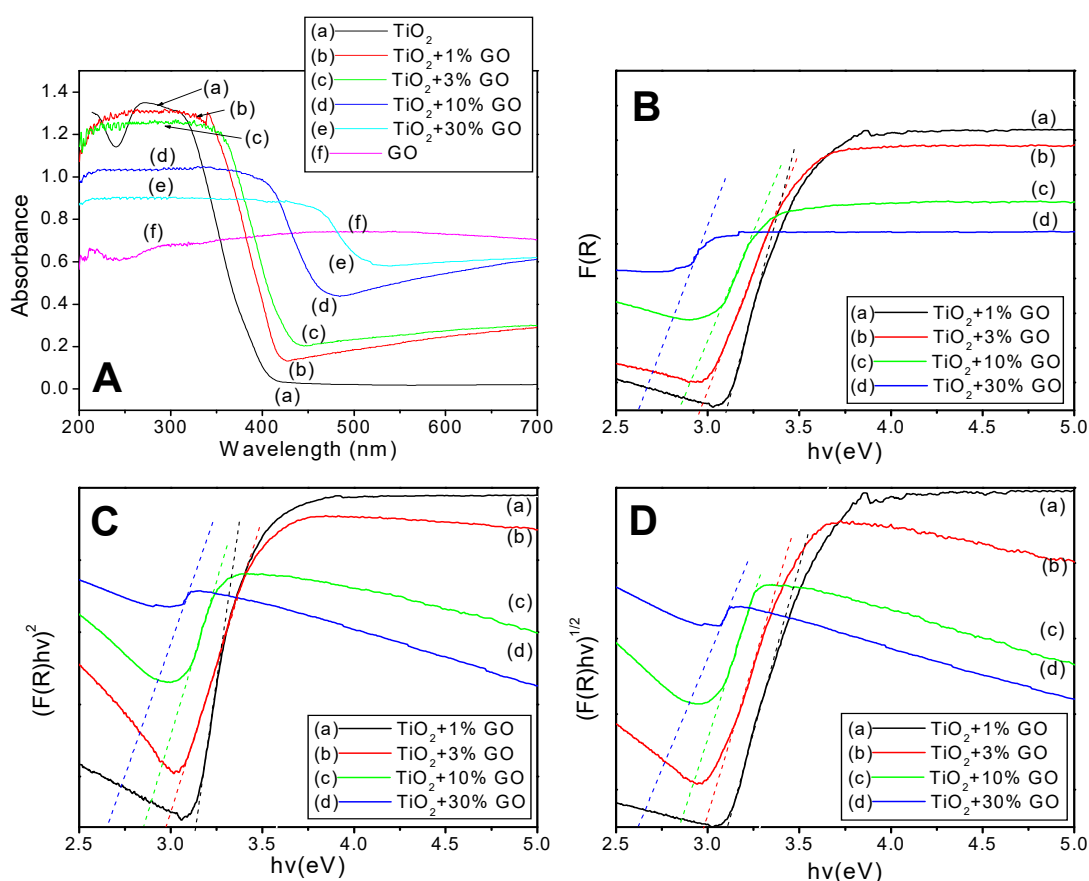
Figure 5.5.1. *UV-DRS of TiO₂, GO & TiO₂-GO composites (A). Optical bandgap energy (Eg) determination of TiO₂ and TiO₂-GO composites (B,C & D)*

UV-visible spectra obtained from UV-DRS technique showed a decrease in the characteristic absorption band in the UV region of nano TiO_2 upon GO incorporation.

A decrease in the UV absorption bands contradicted by the increase in the visible region absorption bands were observed as a consequence of increasing weight percentage of GO in TiO$_2$-GO composites (Figure 5.5.1 A). The ability of TiO$_2$-GO composites by which they can absorb in the UV as well as visible region is evident here. The visually observed bluish grey colouration of the TiO$_2$-GO composites could be seen due to the absorption in the visible region. The origin of the bluish colour may be due to the reduction of some of the Ti^{4+} ions into Ti^{3+} ions during the process of GO incorporation. Interaction of TiO$_2$ with the π bonds of reduced graphene oxide might have resulted in this reduction[51]. Determination of optical bandgap energies (E$_g$) from the plots of F(R) v/s hυ (irrespective of transitions), (F(R) hυ)^2 v/s hυ (direct E$_g$) and (F(R) hυ)$^{1/2}$ v/s hυ (indirect E$_g$) was done (Figure 5.5.1 B,C &D). The E$_g$ of the TiO$_2$-GO composites were lower than that of TiO$_2$. The E$_g$ of the composites decreased as the percentage of GO increased. The values of E$_g$ of the composites are given in table 5.3.
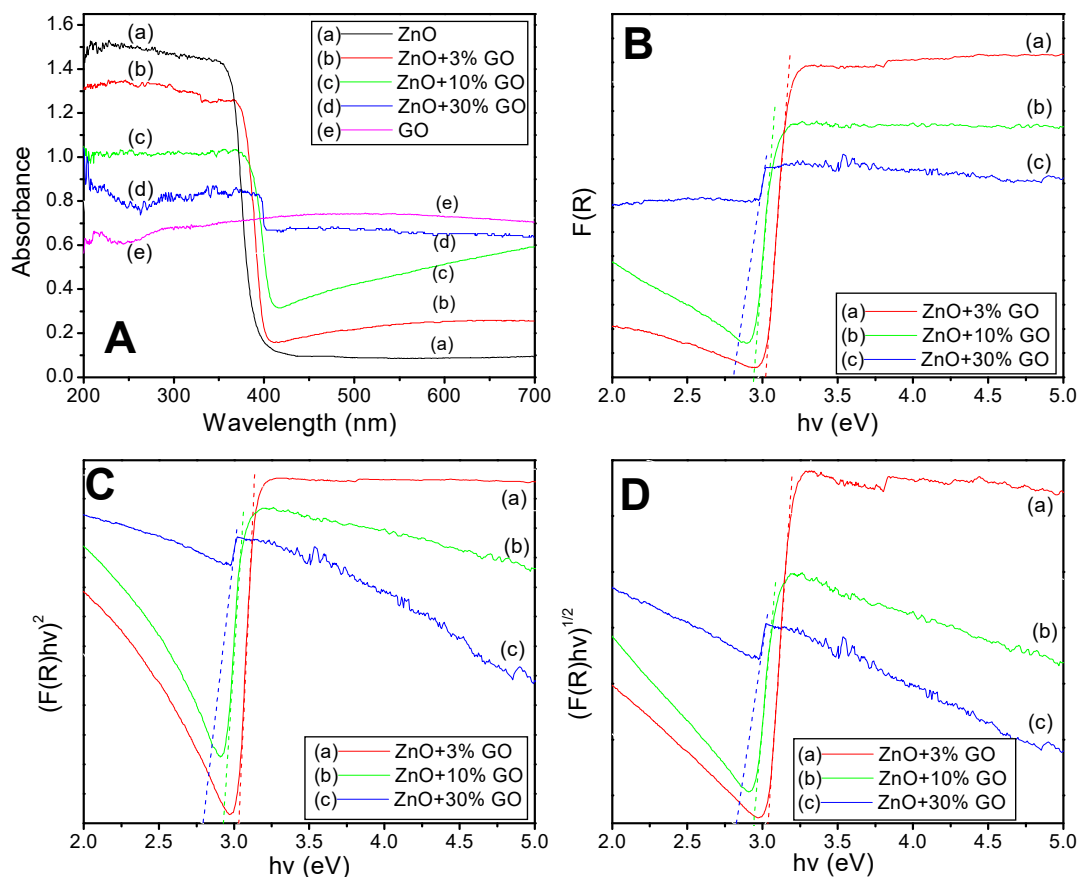
Figure 5.5.2. *UV-DRS of ZnO, GO and ZnO-GO composites (A). Optical bandgap energy (Eg) determination of ZnO and ZnO-GO composites (B, C & D)*

The UV-DRS of ZnO-GO composites followed the same trend as observed in the case of TiO_2-GO (Figure 5.5.2). The characteristic absorption bands in UV region of the spectra decreased as the percentage of GO increased. The absorption bands in visible region of the spectra on the other hand increased as the percentage of GO increased. Coupling of GO with ZnO, modified their light absorption property extending from UV region to visible region. The values of E_g of the composites (ie., E_g irrespective of transitions, direct E_g and indirect E_g) were lower than that of ZnO. A decrease in E_g among the ZnO-GO composites was noticed as the percentage of GO increased. Figure 5.5.2 B, C & D represent the plots F(R) v/s hυ, $(F(R)\,hυ)^2$ v/s hυ and $(F(R)\,hυ)^{1/2}$ v/s hυ of ZnO-GO composites. The values of E_g are given in table 5.3.

Table 5.3. Values of optical bandgap energies of TiO₂- GO and ZnO-GO.

Method	Band gap Energy in eV				
	TiO_2	TiO_2 +1%GO	TiO_2 +3%GO	TiO_2 +10%GO	TiO_2 +30%GO
F(R) vs hυ	3.16	3.10	2.96	2.84	2.62
$(F(R)hυ)^2$ vs hυ	3.22	3.13	2.97	2.85	2.65
$(F(R)hυ)^{1/2}$ vs hυ	3.18	3.11	2.98	2.84	2.62
Method	Band gap Energy in eV				
	ZnO	ZnO +3%GO	ZnO +10%GO	ZnO +30%GO	
F(R) vs hυ	3.2	3.02	2.93	2.80	
$(F(R)hυ)^2$ vs hυ	3.25	3.03	2.94	2.80	
$(F(R)hυ)^{1/2}$ vs hυ	3.27	3.03	2.94	2.80	

5.3.6. SEM-EDX, HRTEM and SAED

SEM image revealed that the prepared TiO_2-GO composites existed as nanoparticles (Figure 5.6.1 A). Atomic percentages of titanium, oxygen and carbon were 15.92, 50.93 and 33.15 respectively as detected through EDX technique for TiO_2-3% GO composite (Figure 5.6.1 B). The Kα1, Kβ1 and Lα1 peaks of titanium were observed at 4.5, 4.93 and 0.45 keV respectively. Kα1 peak of oxygen was seen at 0.53 keV and that of carbon at 0.277 keV
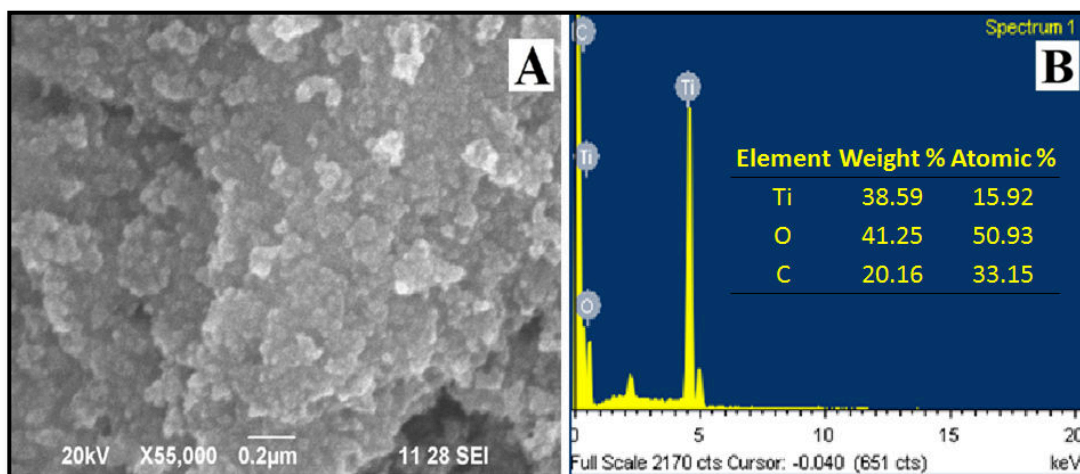
Figure 5.6.1. SEM image (A) and EDX (B) of TiO₂-30% GO composite.
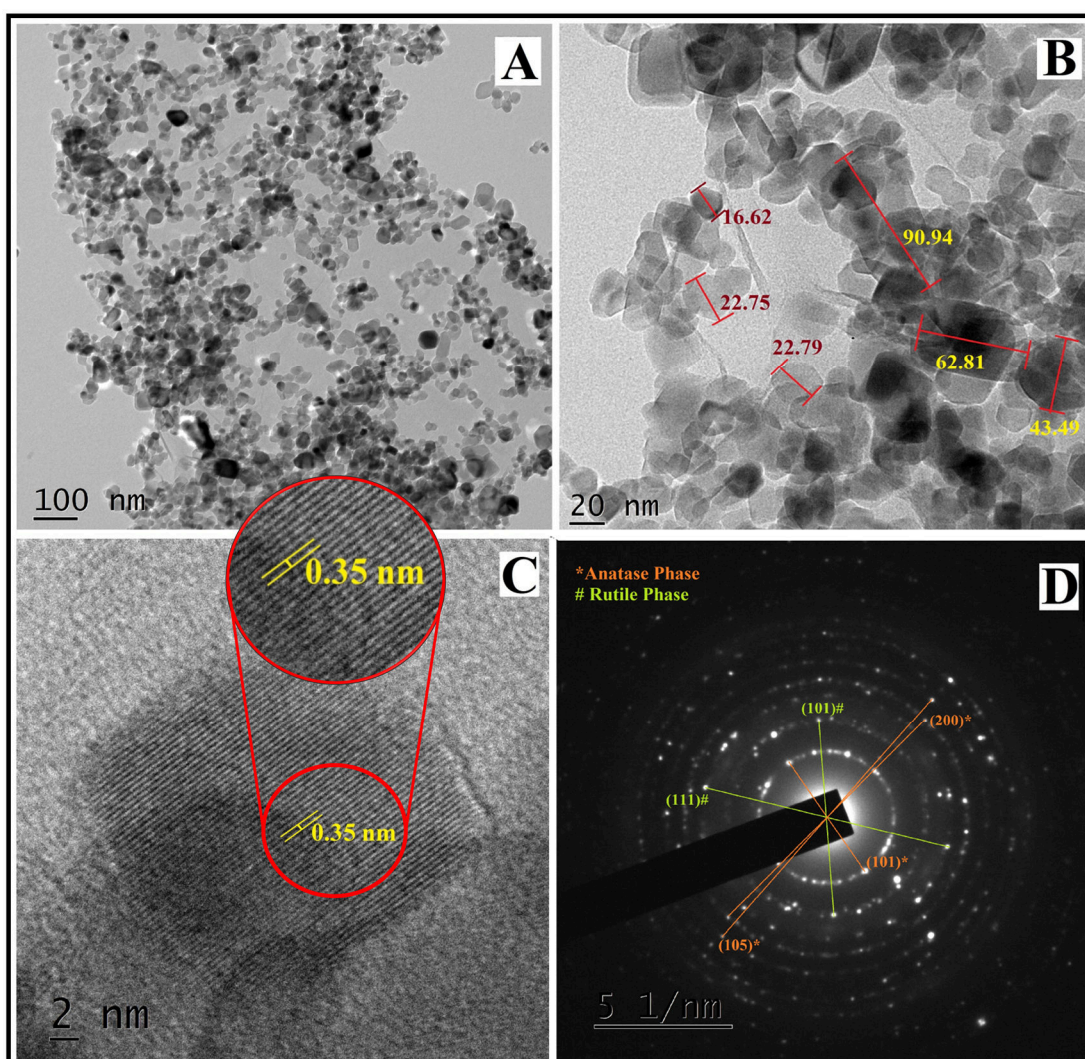
Figure 5.6.2. HRTEM image (A, B & C), SAED pattern (D) of TiO₂-3% GO

HRTEM image revealed that TiO₂-GO composite existed as separated particles. GO sheet seemed to have broken down into thin sheets of nano dimensions associated

with TiO$_2$ (Figure 5.6.2 A & B). Ultrasonication followed by hydrothermal process might have caused the sheets to break up into such nano dimensions. Lattice fringes with a spacing of 0.35 nm assigned to TiO$_2$ anatase (101) planes could be visualised through HRTEM image (Figure 5.6.2 C). Selected area electron diffraction (SAED) pattern revealed the crystalline nature of the composite with distinguished spots (Figure 5.6.2 D). Points corresponding to (101), (200) and (105) planes of anatase phase and (101), (111) planes of rutile phase TiO$_2$ were spotted from SAED patterns. The results were in well agreement with powdere XRD patterns. Average particle size was determined to be ≈ 44 nm from the HRTEM image using *image j* software.
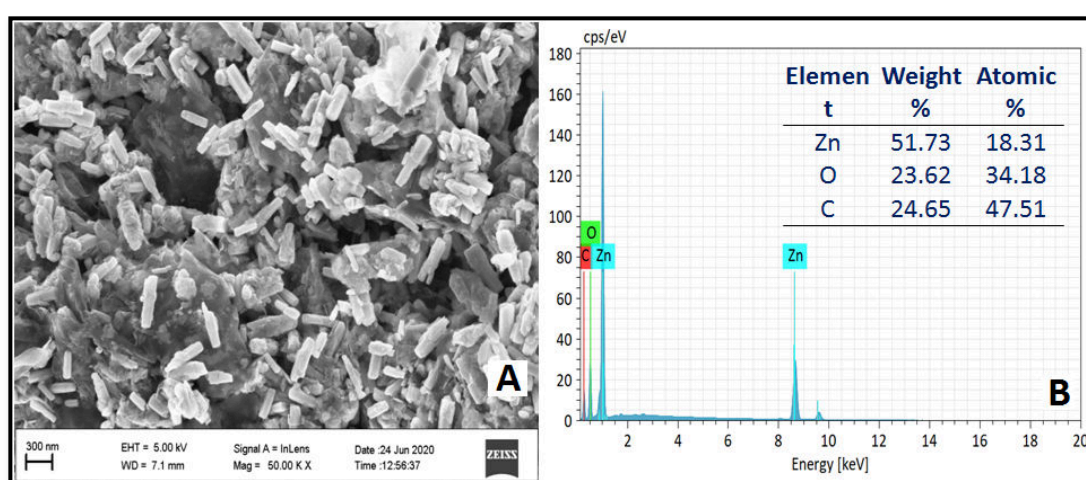
Figure 5.6.3. *FESEM image (A) and EDX (B) of ZnO-30% GO composite.*

The FESEM image of ZnO-30% GO composite showed that ZnO existed as hexagonal rods associated with GO layers (Figure 5.6.3 A). The length of the rods ranges from 90 nm to 700 nm. ZnO crystals however were bonded together by GO sheets. EDX peaks (Figure 5.6.3 B) corresponding to zinc were observed at 1.02 (Lα1, Lβ1 and Lβ3 overlap), 8.62 (overlap of Kα1 and Kα2 overlap) and 9.58 (Kβ1 and Kβ2 overlap) keV. Peak corresponding to oxygen was observed at 0.53 (Kα1) keV and that of carbon was observed at 0.277 (Kα1) keV respectively.

HRTEM of ZnO-30% GO revealed that the composites were more aggregated as compared to TiO$_2$-GO (Figure 5.6.4 A and B). The existence of ZnO particles as rods of non-uniform dimensions, observed in FESEM image were further supported by HRTEM of ZnO-30% GO composite. The GO layers existed as microsized sheets holding ZnO rods together. Some GO layers were wound around ZnO rods. The

length of the ZnO rods ranges from around 90 nm to 700 nm as observed through FESEM. Lattice fringes with a spacing of 0.28 nm assigned to (100) plane of ZnO could also be observed in the HRTEM image (Figure 5.6.4 C). SAED pattern of ZnO-30% GO composite revealed its predominant amorphous nature with halo rings (faded edges) (Figure 5.6.4 D). The spots corresponding to the plane of reduced GO (rGO), (102) and (110) planes of ZnO were however distinguished from SAED pattern of the composite.
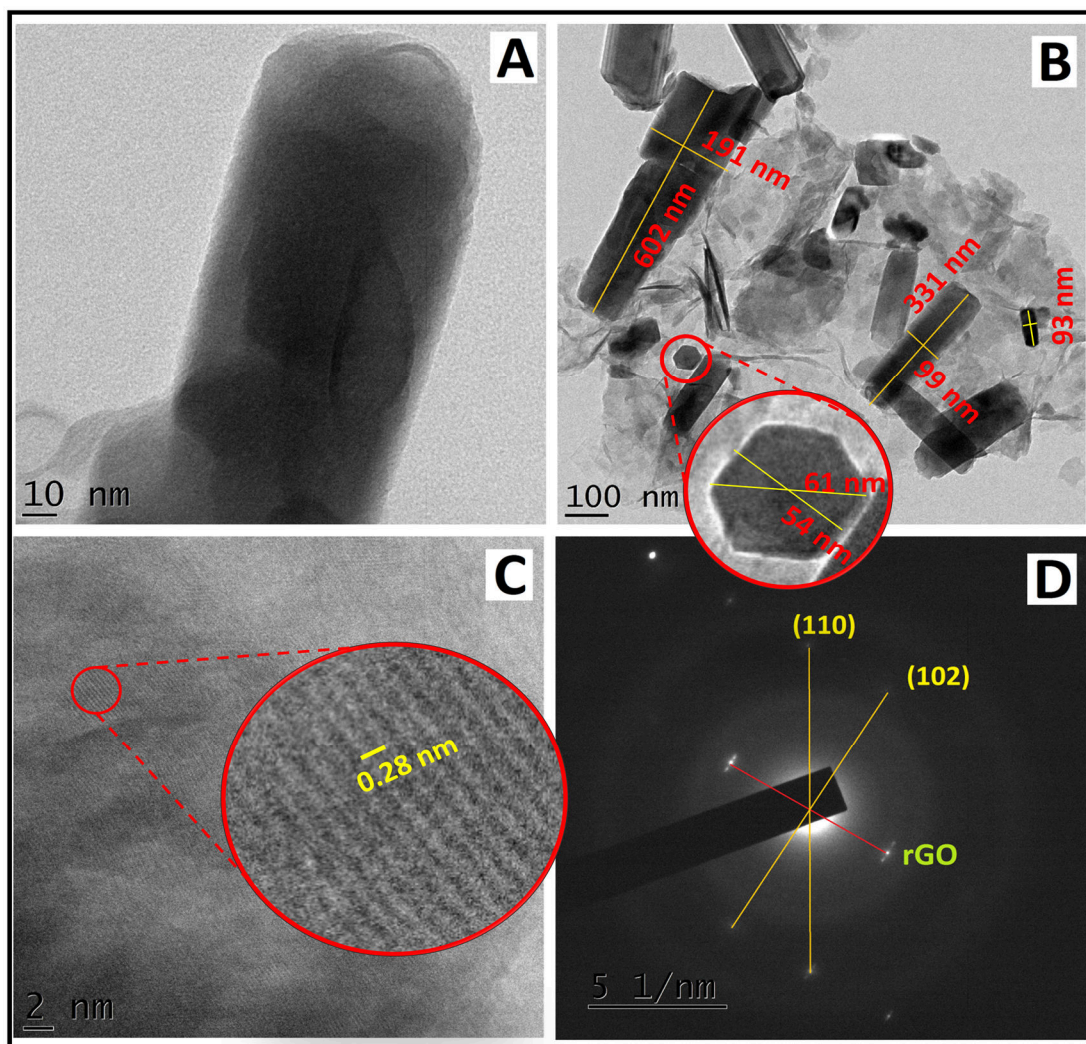
Figure 5.6.4. *HRTEM image (A,B & C), SAED pattern (D) of ZnO-30% GO*

5.3.7. Interactions of TiO$_2$/ZnO with GO in the composites

The existence of broad bands of -OH could be seen on the FTIR spectra of TiO$_2$ and ZnO as discussed in chapter 3. These broad bands of -OH vibrations arise from the OH$^-$ ions adsorbed by the surface of TiO$_2$/ZnO from the atmosphere. These -OH

groups can interact with the oxygen atoms on the >C=O or -COOH groups of GO to form hydrogen bonds as represented schematically in Figure 5.7[31]. The possibility of such hydrogen bond linkages between TiO$_2$/ZnO and GO cannot be ruled out as broad bands between 3500 cm^{-1} and 3000 cm^{-1} were present in FTIR spectra of TiO$_2$-GO as well as ZnO-GO composites.
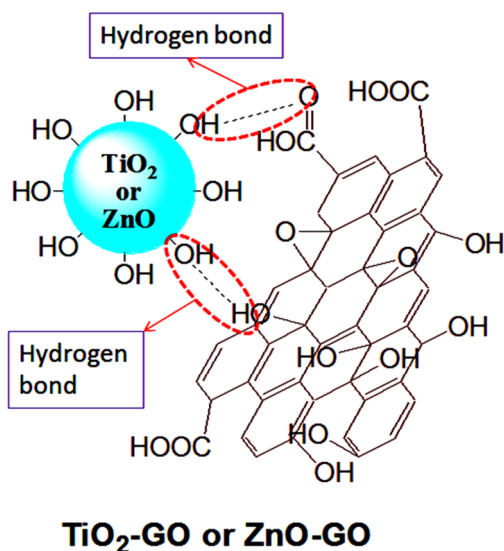
Figure 5.7. *Interaction between TiO$_2$-GO or ZnO-GO through hydrogen bond formation*

A considerable shift in the >C=O and >C=C< stretching bands of GO towards lower wavenumber along with the decrease in their intensities were observed in the FTIR spectra of TiO$_2$-GO and ZnO-GO compared to that of uncoupled GO (Figure 5.2). As the percentage of TiO$_2$/ZnO increased in the composites, the shift in the stretching bands increased along with the decrease in the peak intensities upto a level such that the presence of >C=C< was almost too difficult to be noticed. For the TiO$_2$-1% GO and ZnO-3% GO (where the percentage of TiO$_2$/ZnO was comparatively highest) the stretching bands of >C=O and >C=C< which were supposed to appear at the adjacent positions (1719cm^{-1} and 1622cm^{-1}) were shifted and merged almost into a single band. This shift may be explained due to the formation of Ti-O-C/Zn-O-C bond[32]. The existence of Ti-O-C bond in TiO$_2$-30%GO was confirmed through XPS discussed above. The condensation of -OH groups associated with TiO$_2$/ZnO and the functional groups present in GO leads to the formation of Ti-O-C/Zn-O-C bonds[26,52,53]. The bands corresponding to Ti-O-C bond supposed to appear at around 800-850 cm^{-1} for TiO$_2$-GO composites were however not clear due to the overlap of Ti-O-Ti stretching band. A peak at around 833 cm^{-1} was observed for ZnO-GO

composites which may be attributed to Zn-O-C stretching[34]. XPS analysis also showed the existence of Ti-C bond between TiO_2 and GO.

Ti-O-C/Zn-O-C and Ti-C bonds may shift the valence band of TiO_2/ZnO GO to lower level, thereby reducing the bandgap[54]. The lowering of bandgap energy (E_g) in TiO_2-GO and ZnO-GO composites was evident based on the above results.

In addition to the Ti-O-C/Zn-O-C bonds or hydrogen bond formation, the interfacial electron transfer between the heterojunctions (TiO_2-GO & ZnO-GO) is also favoured[36,37]. GO plays the role of electron acceptor which accepts electrons into its Fermi levels from the conduction band of TiO_2[35].

Section II

Photodegradation of polystyrene using TiO₂-GO and ZnO-GO composites as photocatalysts

The role of TiO_2-GO as well as ZnO-GO composites as photocatalysts in the photodegradation of PS under UV irradiation was studied. PS-TiO_2-GO and PS-ZnO-GO composites were prepared by solvent casting as discussed in chapter 2. The specimens for electrical and mechanical studies were also prepared. Photodegradation studies of the specimens were carried out. The results obtained through various monitoring techniques adopted for photodegradation studies are interpreted and discussed below.

5.4. Results and Discussion

5.4.1. Gel permeation chromatography (GPC)

The number average ($\overline{M}_n$) and weight average ($\overline{M}_w$) molecular weight of PS-TiO_2-GO (Figure 5.8.1) as well as PS-ZnO-GO (Figure 5.8.2) composites decreased as the time of UV irradiation increased. The decrease in the average molecular weight was predominant in PS-TiO_2-GO composites compared to that of PS-ZnO-GO. It was also observed that PS-TiO_2-GO and PS-ZnO-GO composites underwent a better decrease in the average molecular weights compared to that of PS-TiO_2 and PS-ZnO

composites. The maximum decrease in the average molecular weights among the PS-TiO$_2$-GO composites upon UV irradiation was observed in PS-(TiO$_2$-30% GO). The decrease in the average molecular weight in the case of PS-ZnO-GO on the other hand was observed in PS-(ZnO-10% GO). The decrease in $\bar{M}_w$ and $\bar{M}_n$ for PS-(ZnO-30% GO) was not as pronounced as that of PS-(ZnO-10% GO) composite.
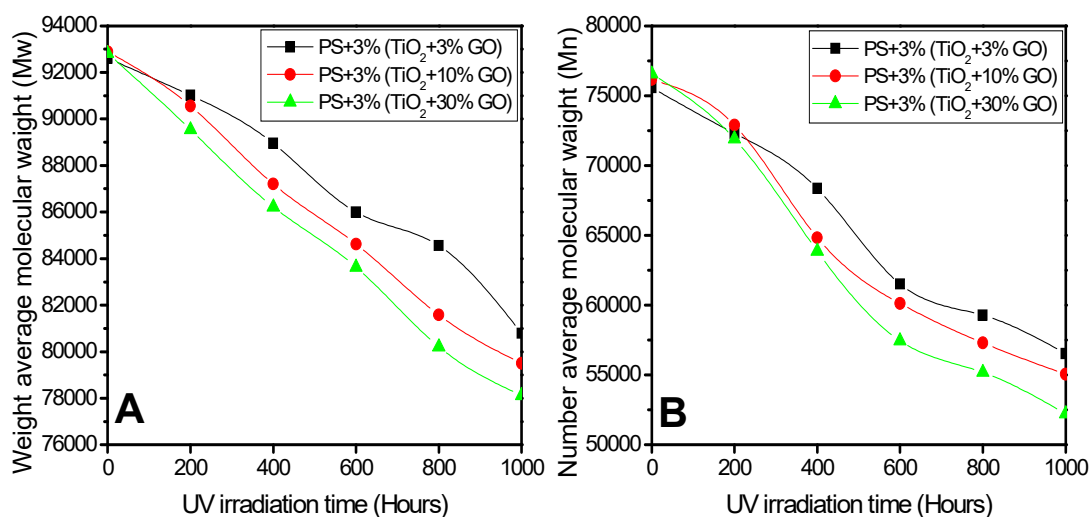
Figure 5.8.1. *A) Weight average ($\bar{M}_w$) and B) number average ($\bar{M}_n$) molecular weights of PS-TiO$_2$-GO composites under different UV irradiation time*
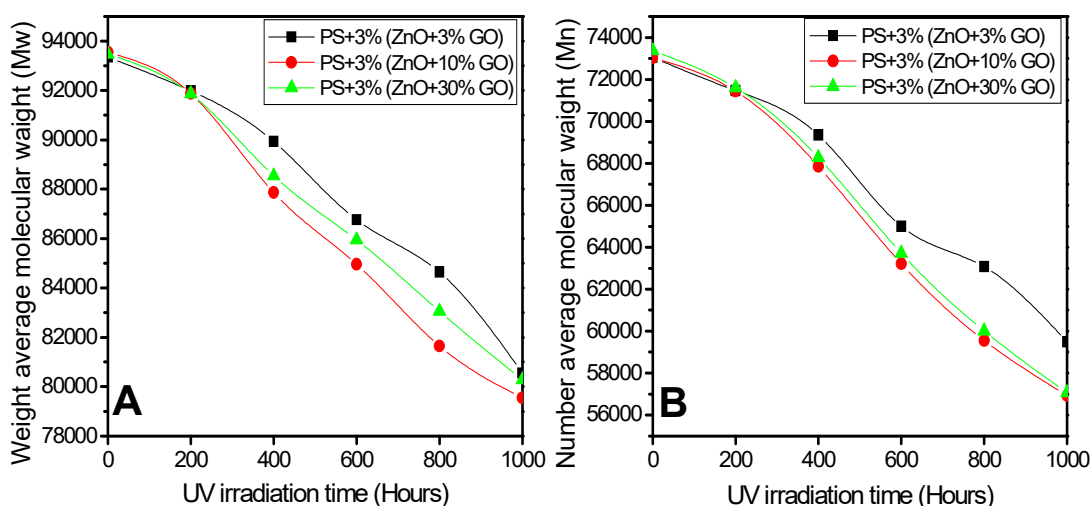
Figure 5.8.2. *A) Weight average ($\bar{M}_w$) and B) number average ($\bar{M}_n$) molecular weights of PS-ZnO-GO composites under different UV irradiation time*

The number of chain scissions per molecule (S) and the number of scission events per gram (N$_t$) of PS-TiO$_2$-GO (Figure 5.8.3) and PS-ZnO-GO (Figure 5.8.4) composites increased with respect to UV irradiation time. Maximum increase in the chain scissions on UV irradiation was observed for PS-(TiO$_2$-30% GO) among the

PS-TiO$_2$-GO composites. Among PS-TiO$_2$-GO composites, PS-(ZnO-10% GO) underwent maximum chain scission. The increased S and N_t of PS-TiO$_2$-GO composites were better, compared to that of PS-ZnO-GO composites.
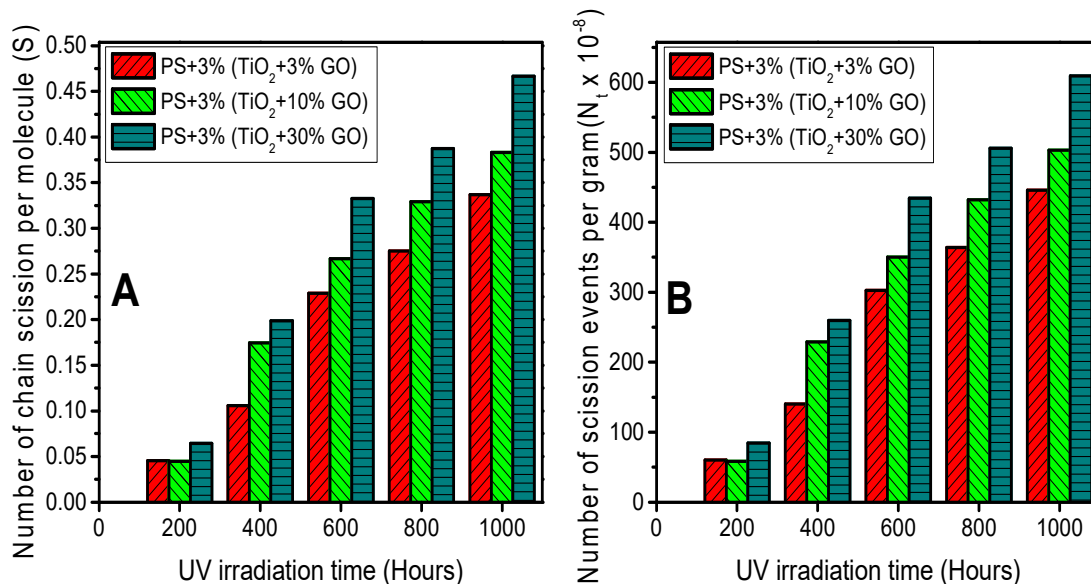
Figure 5.8.3. (A) *Number of chain scissions per molecule (S) and* ***(B)*** *number of scission events per gram (N$_t$) of PS-TiO$_2$-GO composites under different UV irradiation time intervals*
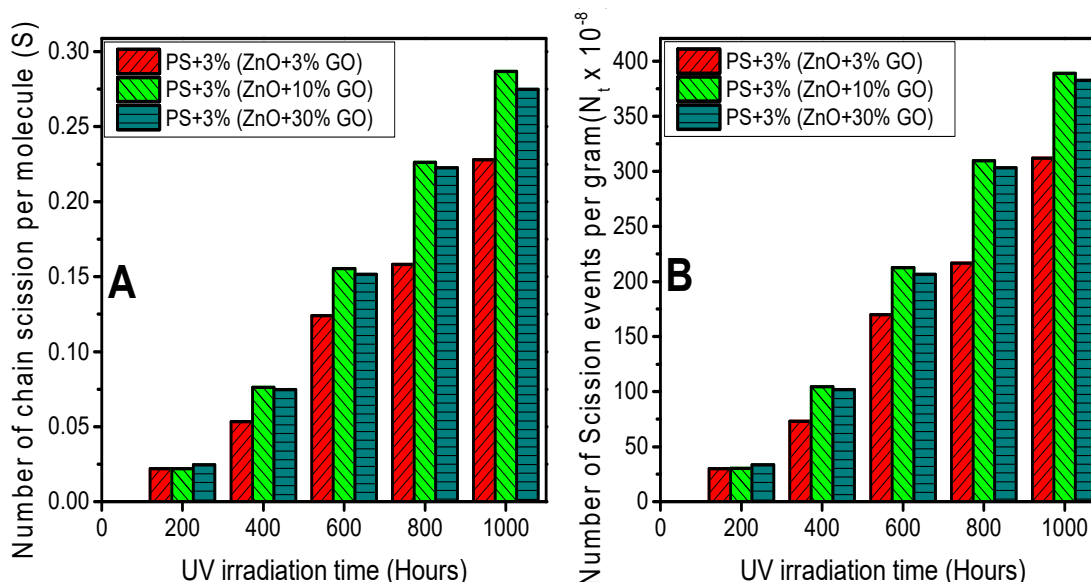
Figure 5.8.4. (A) *Number of chain scissions per molecule (S) and* ***(B)*** *number of scission events per gram (N$_t$) of PS-ZnO-GO composites under different UV irradiation time intervals*

The increase in the polydispersity index of PS-TiO$_2$-GO as well as PS-ZnO-GO composites increased as the time of UV irradiation increased (Figure 5.8.5). The increase in the randomness of chain cleavage is highlighted here.
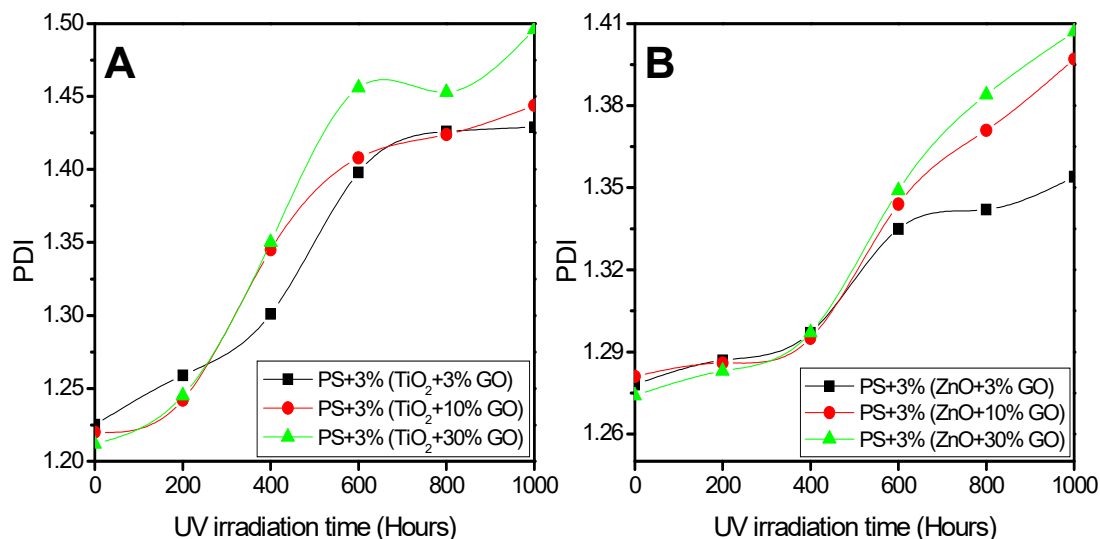
Figure 5.8.5. *Polydispersity index (PDI) of PS-TiO$_2$-GO (A) and PS-ZnO-GO (B) composites under different UV irradiation time*

5.4.2. FTIR Spectroscopy

FTIR spectra of PS-TiO$_2$-GO composites showed an increase in the intensity of stretching vibrations corresponding to >C=O (1740- 1700 cm^{-1}), -OH/ -OOH (3700-3600 cm^{-1}), >C=C< (1680-1650 cm^{-1}) etc. as the time of UV irradiation increased, suggesting photo-oxidation. We could also observe that PS-TiO$_2$-GO composites underwent better photo-oxidation compared to that of PS-TiO$_2$ composites. Enhancement in the photocatalytic efficiency of TiO$_2$ upon surface modification with GO was evident. The extent of photo-oxidation was found maximum in PS-(TiO$_2$-30% GO) composite compared to the other PS-TiO$_2$-GO composites. Photo-oxidation upon UV irradiation for PS-TiO$_2$-GO composites followed the order: PS-(TiO$_2$-30% GO) > PS-(TiO$_2$-10% GO) > PS-(TiO$_2$-3% GO) > PS-(TiO$_2$-1% GO). This trend revealed that the extent of photo-oxidation increased as the percentage of GO associated with TiO$_2$ in the composites increased. Figure 5.9.1 and 5.9.2 represents the FTIR spectra of PS-(TiO$_2$-10% GO) and PS-(TiO$_2$-30% GO) respectively.
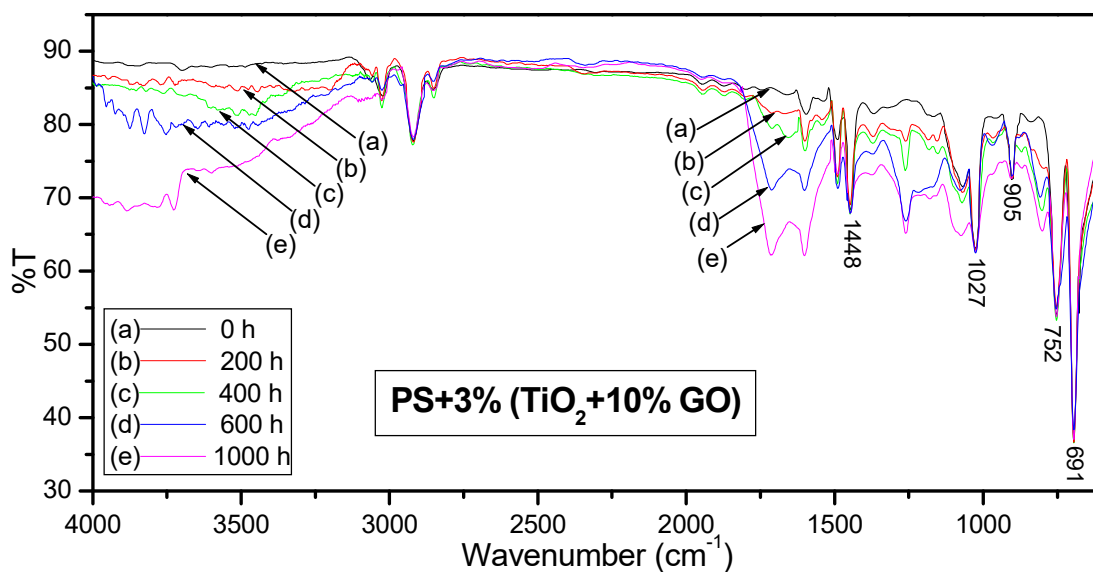
Figure 5.9.1. *FTIR spectra of PS-3%(TiO₂-10% GO) after different UV exposure time intervals ranging from 0 h to 1000 h.*
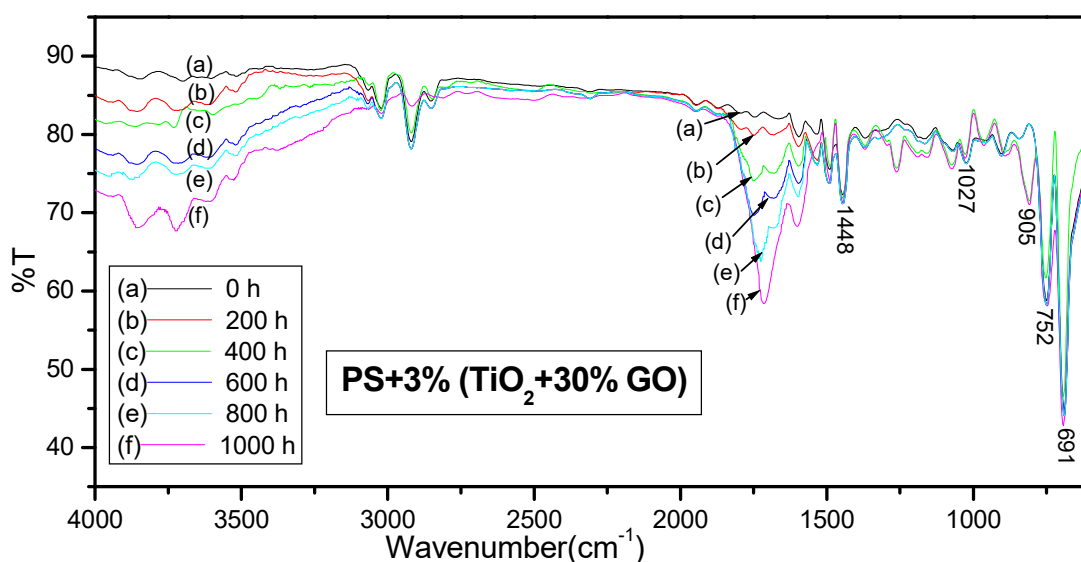
Figure 5.9.2. *FTIR spectra of PS-3%(TiO₂-30% GO) after different UV exposure time intervals ranging from 0 h to 1000 h.*

FTIR spectra of PS-ZnO-GO composites looked similar to that of PS-TiO₂-GO composites. PS-ZnO-GO composites too underwent photo-oxidation upon UV irradiation. The only difference was in the extent of photo-oxidation of the composites which was more pronounced in PS-TiO₂-GO compared to that of PS-ZnO-GO. PS-ZnO-GO underwent better photo-oxidation as compared to PS-ZnO composites. The order of photo-oxidation among PS-ZnO-GO composites was as follows: PS-(ZnO-10% GO) > PS-(ZnO-30% GO) > PS-(ZnO-3% GO). Maximum photo-oxidation

among the PS-ZnO-GO composites was exhibited by PS-(ZnO-10% GO). Excess of GO in PS-(ZnO-30% GO) composite might have hampered the rate of photo-oxidation. This irregular trend could be explained by the aggregation of ZnO-GO composites due to the uneven distribution of GO and ZnO in the composites which increased as the percentage of GO increased. Figure 5.9.3 and 5.9.4 represents the FTIR spectra of PS-(ZnO-10%GO) and PS-(ZnO-30%GO) respectively.
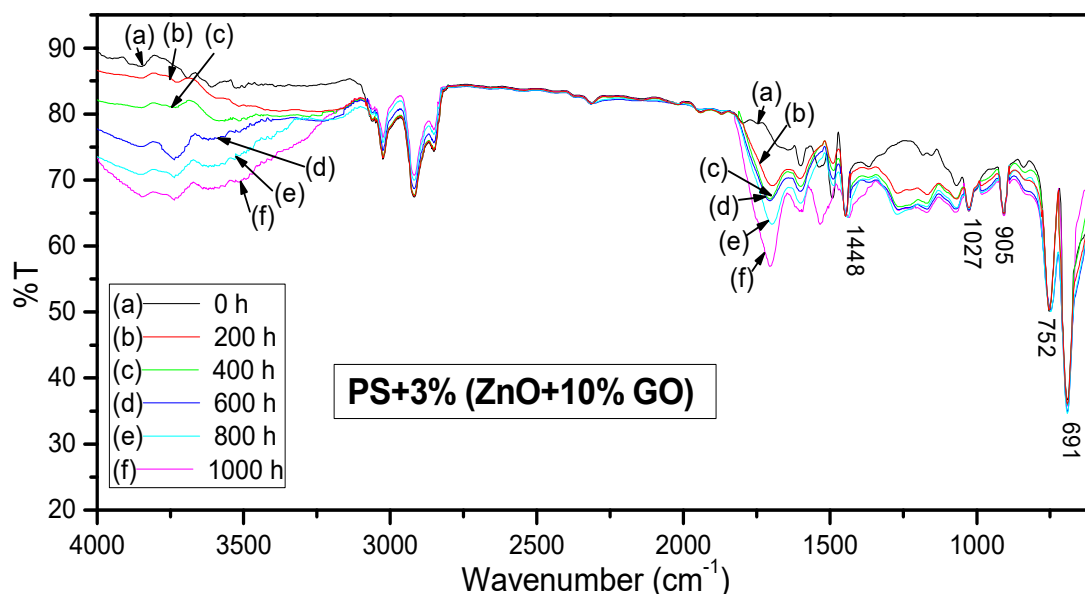
Figure 5.9.3. *FTIR spectra of PS-3%(ZnO-10% GO) after different UV exposure time intervals ranging from 0 h to 1000 h.*
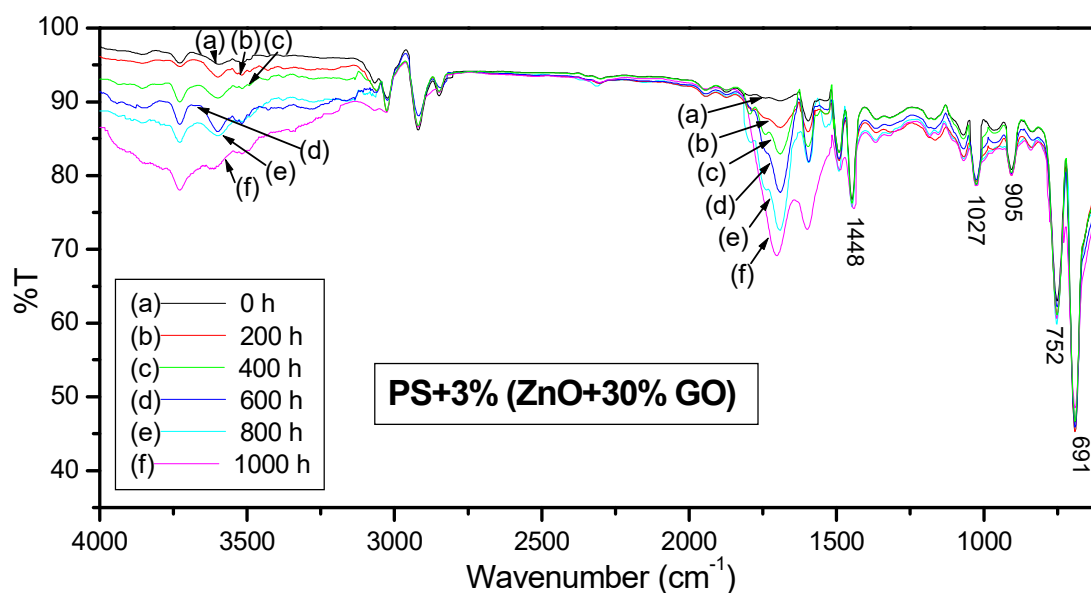
Figure 5.9.4. *FTIR spectra of PS-3%(ZnO-30% GO) after different UV exposure time intervals ranging from 0 h to 1000 h.*

The absorption bands at 691 cm⁻¹, 752 cm⁻¹, 905 cm⁻¹ and 1027 cm⁻¹ representing phenylic -C-H out of plane bending did not show changes in their intensity in both PS-TiO$_2$-GO and PS-ZnO-GO composites. The peak at 1448 cm⁻¹ corresponding to aromatic carbon-carbon double bond stretch also exhibited no change in peak intensity. This could be due to the fact that the phenyl group may have remained intact upon UV irradiation of 1000 hours.

5.4.3. UV-visible Diffused reflectance spectroscopy (UV-DRS)
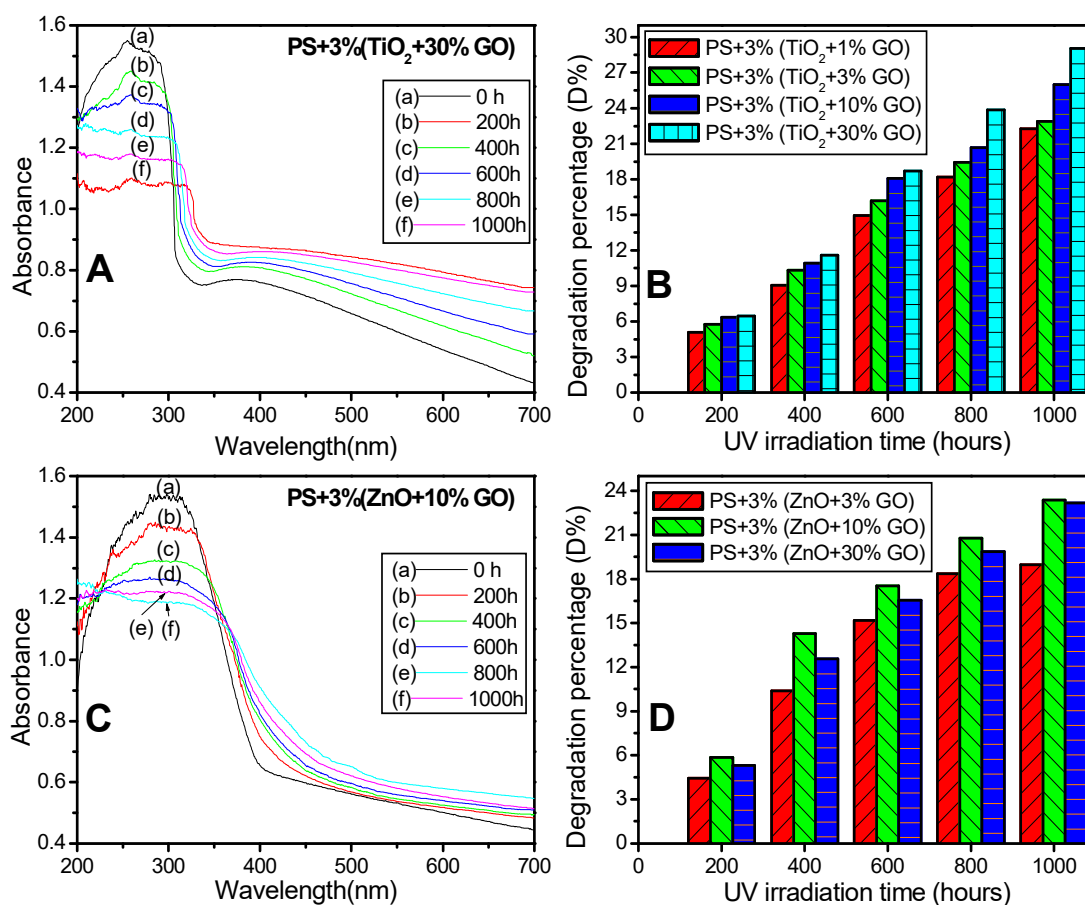
Figure 5.10.1. *UV-DRS of PS-3%(TiO$_2$-30% GO) (A), PS-3%(ZnO-10% GO) (C) and degradation percentages of PS-TiO$_2$-GO (B), PS-ZnO-GO (D) composites at different UV exposure time intervals ranging from 0 h to 1000 h*

Both PS-TiO$_2$-GO and PS-ZnO-GO absorbed in the UV as well as in the visible region of spectra as evident from their UV-DRS. Maximum absorption was observed in the UV region of the spectra for all the composites. The absorption in the UV region decreased as the time of UV irradiation increased. Maximum decrease in the UV absorption bands was observed in PS-(TiO$_2$-30%GO) among PS-TiO$_2$-GO

composites (Figure 5.10.1 A). PS-(ZnO-10%GO) underwent maximum decrease in UV absorption among the PS-ZnO-GO composites (Figure 5.10.1 D). A red shift was observed with a slight increase in the absorption bands in visible region for the composites, with an increase in UV exposure time. Degradation percentage determined from UV-DRS of PS-TiO$_2$-GO as well as PS-ZnO-GO are represented in Figure 5.10.1 B and Figure 5.10.1 D respectively. The degradation efficiency of PS-(TiO$_2$-3% GO), PS-(TiO$_2$-10% GO) and PS-(TiO$_2$-30% GO) increased by 13.24, 16.38 and 19.4 % and that of PS-(ZnO-3% GO), PS-(ZnO-10% GO) and PS-(ZnO-30% GO) increased by 9.35, 13.74 and 13.54 % respectively with respect to pristine PS.

Optical bandgap energy (E$_g$) of PS-TiO$_2$-GO and PS-ZnO-GO films before and after UV irradiations at different time intervals was determined using Tauc relation. The values of E$_g$ decreased towards lower energy with respect to UV exposure time of the composites. Figure 5.10.2 represents the direct E$_g$ determination of PS-(TiO$_2$-30% GO) and PS-(ZnO-10% GO) composites by plotting $(\alpha h\upsilon)^2$ versus hυ and extrapolating the linear portion of the curve towards energy (hυ) axis. The decrease in E$_g$ could be due to the formation of conjugated double bonds or other species that can absorb the visible light. Degradation of PS chain, leading to the decrease in characteristic UV absorption of PS composites upon UV irradiation also plays a vital role in the decrease of E$_g$ of the composites.
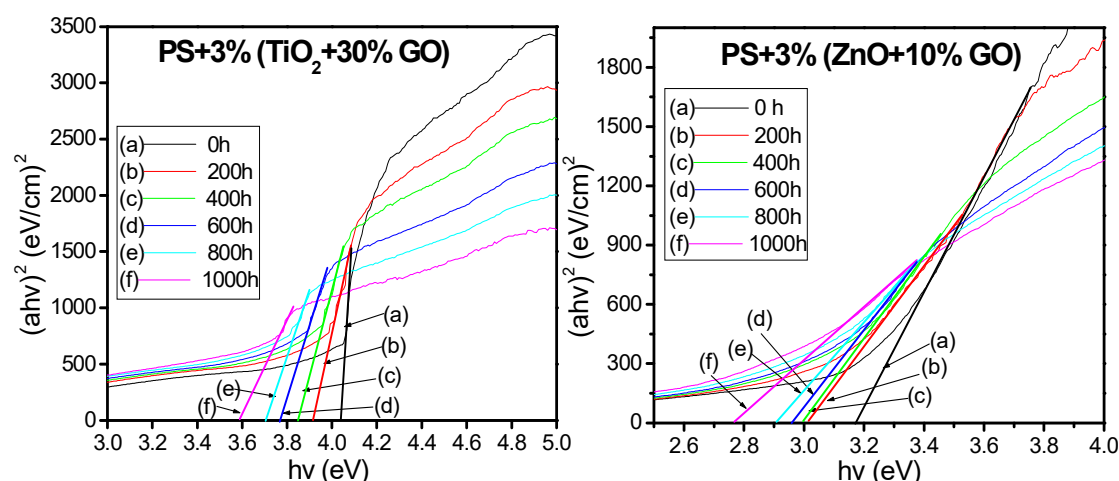
Figure 5.10.2. *Optical bandgap energy determination from the plot of $(\alpha h\upsilon)^2$ v/s hυ for PS-3%(TiO$_2$-30% GO) (A) and PS-3%(ZnO-10% GO) (C) composites subjected to different UV exposure time intervals ranging from 0 h to 1000 h*

5.4.4. Mechanical Properties
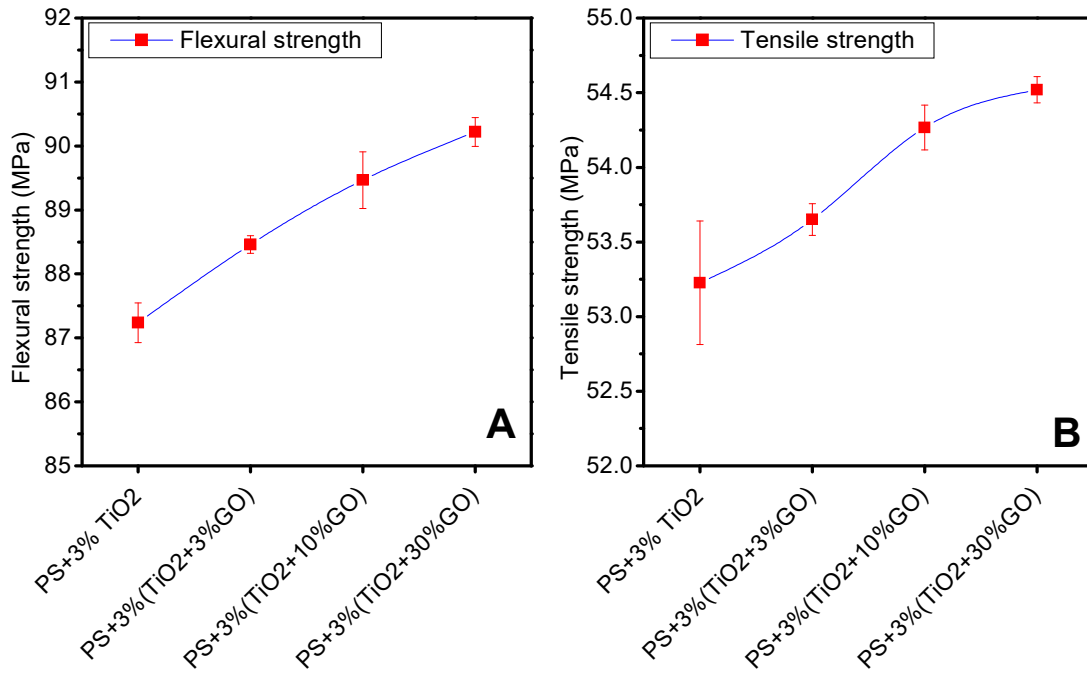
Figure 5.11.1. *Flexural (A) and tensile (B) strengths of PS-TiO$_2$-GO composites before UV irradiation- a comparison*
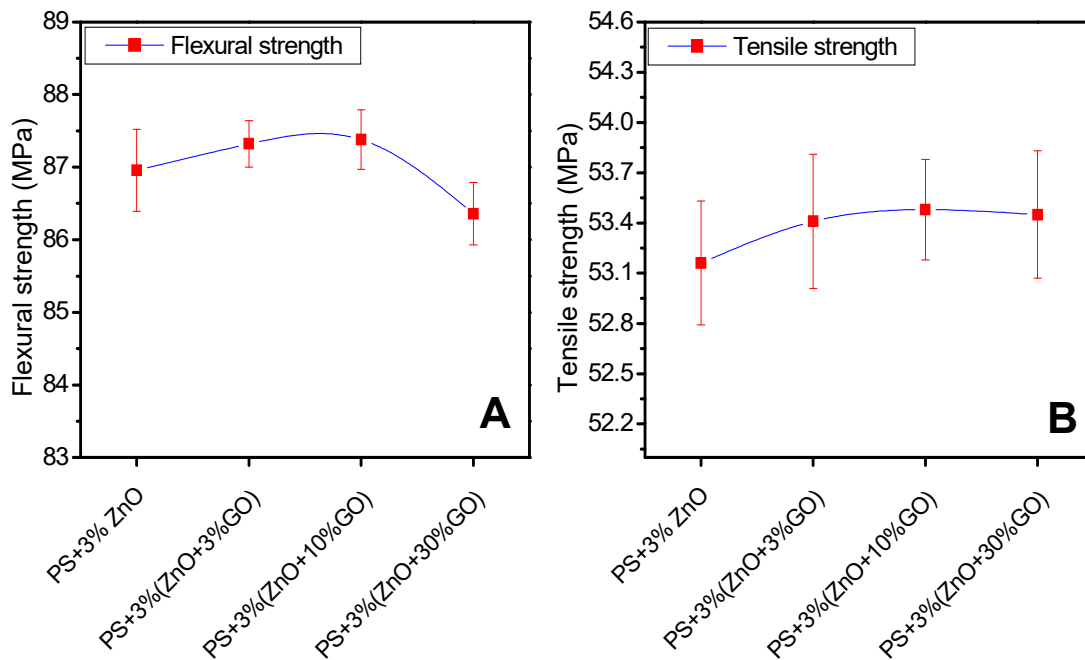
Figure 5.11.2. *Flexural (A) and tensile (B) strengths of PS-ZnO-GO composites before UV irradiation-a comparison*

The flexural and tensile strengths of non-irradiated PS-TiO$_2$-GO composites were greater than that of PS-TiO$_2$ composites (Figure 5.11.1). It was also found that the mechanical strength of the composites increased as the percentage of GO in the composites increased. Maximum flexural and tensile strengths were observed in PS-(TiO$_2$-30% GO) compared to the other PS-TiO$_2$-GO composites. This enhanced mechanical property of PS-TiO$_2$-GO composites promises their application in such devices or commodities where better mechanical strength is in demand.

The flexural and tensile strengths of PS-ZnO-GO composites were better compared to PS-ZnO composite (Figure 5.11.2). In the present study, maximum mechanical strength was observed in PS-(ZnO-10% GO) among the PS-ZnO-GO composites. The mechanical strength of PS-(ZnO-10% GO) was even greater than PS-(ZnO-30% GO).

Comparing Figures 5.11.1 and 5.11.2, it was observed that mechanical strengths of PS-TiO$_2$-GO composites were better than that of PS-ZnO-GO composites. This fact could be explained on the basis of poor distribution of ZnO-GO compared to that of TiO$_2$-GO along the PS matrix. It could be visualized from the SEM and HRTEM images discussed in previous section that ZnO-GO existed as small aggregates while TiO$_2$-GO existed as dispersed nanostructures. The existence of nano sized TiO$_2$ in TiO$_2$-GO composites provided better surface area for associating with GO, breaking them apart into nanosheets. The growth of ZnO particles to bigger rod shaped structures in ZnO-GO composites, on the other hand, provided comparatively lesser surface area for GO association. The GO which remained unassociated with ZnO existed as aggregates as observed in SEM and HRTEM images. Loading PS with ZnO-GO hence resulted in composites with comparatively lower mechanical strength compared to PS loaded with TiO$_2$-GO.

The flexural (Figure 5.11.3) and tensile (Figure 5.11.4) strengths of PS-TiO$_2$-GO and PS-ZnO-GO composites decreased as the time of UV irradiation increased. PS-TiO$_2$-GO composites underwent better decrease in the mechanical properties compared to PS-ZnO-GO composites upon UV irradiation. PS-(TiO$_2$-30% GO) composite underwent maximum decrease in mechanical properties among the PS-TiO$_2$-GO composites. PS-(ZnO-10% GO) showed maximum decrease in the mechanical properties among the PS-ZnO-GO composites.
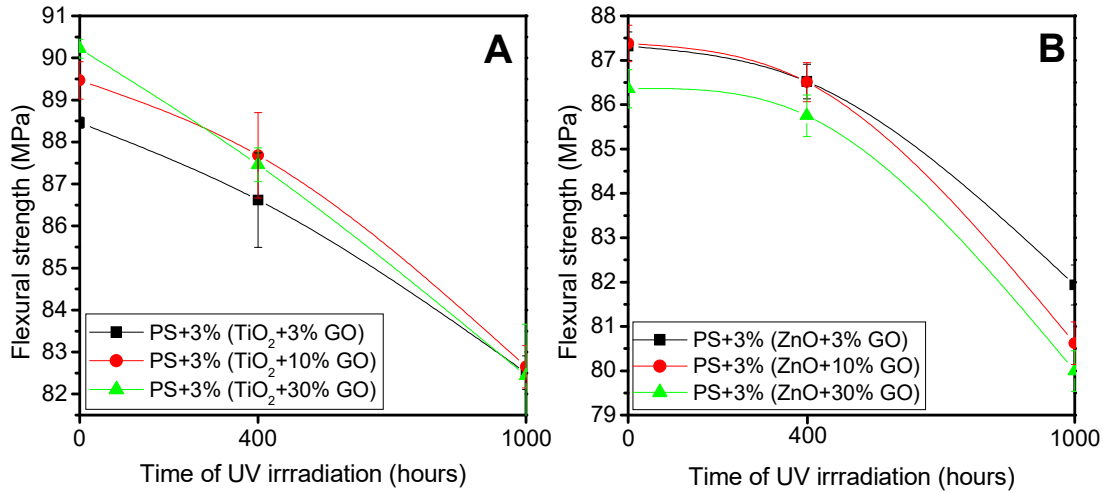
Figure 5.11.3. Flexural strength of A) PS-TiO$_2$-GO and B) PS-ZnO-GO composites exposed to UV radiation for 0, 400 and 1000 h.
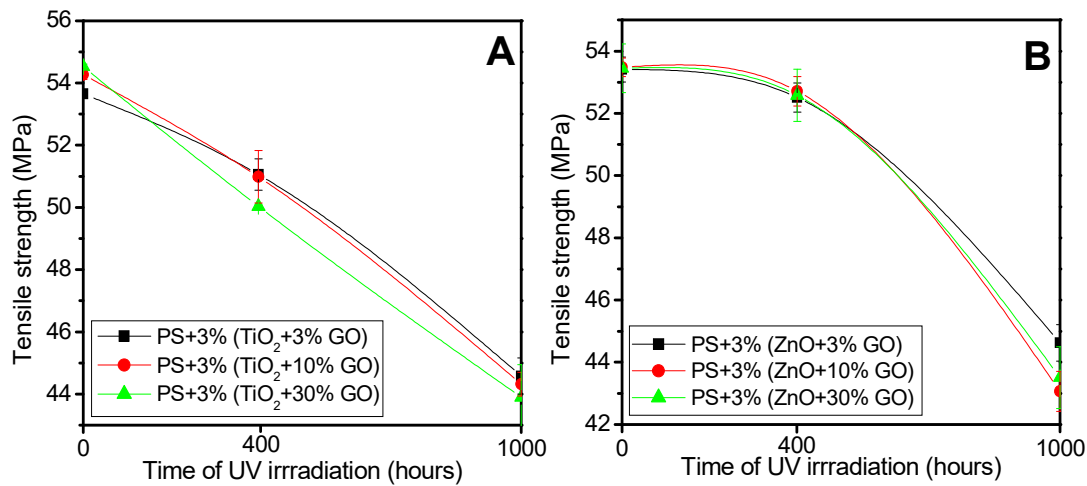
Figure 5.11.4. Tensile strengts A) PS-TiO$_2$-GO and B) PS-ZnO-GO composites exposed to UV radiation for 0, 400 and 1000 h.

5.4.5. Electrical properties

Dielectric breakdown (BDV) of PS-TiO$_2$-GO and PS-ZnO-GO composites was lower compared to PS-TiO$_2$ and PS-ZnO composites respectively. BDV of the composites decreased as the percentage of GO in the composites increased (Figure 5.12.1). The presence of conducting GO in the composites might have resulted in the easy passage of electric current leading to easier breakdown of the composites. BDV of the composites decreased with the increase in UV irradiation time (Figure 5.12.1). The formation of charged centers with better mobility through the composites on UV irradiation was hence evident. BDV of PS-(TiO$_2$-30% GO) decreased to a greater

extent among the PS-TiO₂-GO composites with the increase in UV irradiation time. PS-(ZnO-10% GO) composite showed better decrease in BDV among the PS-ZnO-GO composites upon UV irradiation.
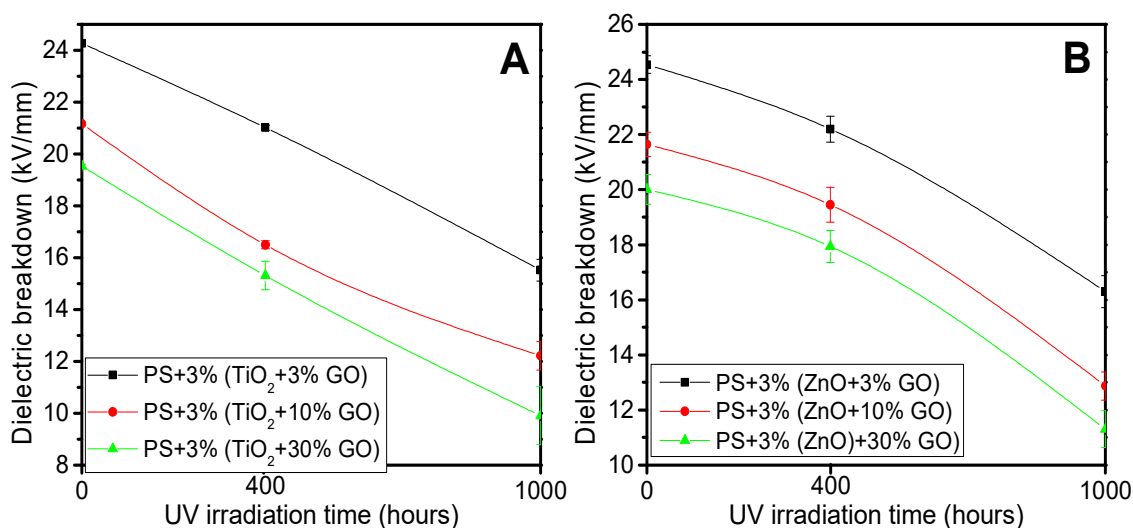
Figure 5.12.1. *Dielectric breakdown of PS-TiO₂-GO and PS-ZnO-GO composites exposed to UV radiation for 0, 400 and 1000 h.*

Dielectric permittivity (ε_r) of the composites increased as the time of UV irradiation increased. Figure 5.12.2 represents the dielectric permittivity of PS-(TiO₂-30% GO) and PS-(ZnO -30% GO) composites with UV exposure intervals of 0, 400 and 1000 hours respectively. In both the composites, ε_r increased as the time of UV irradiation increased.
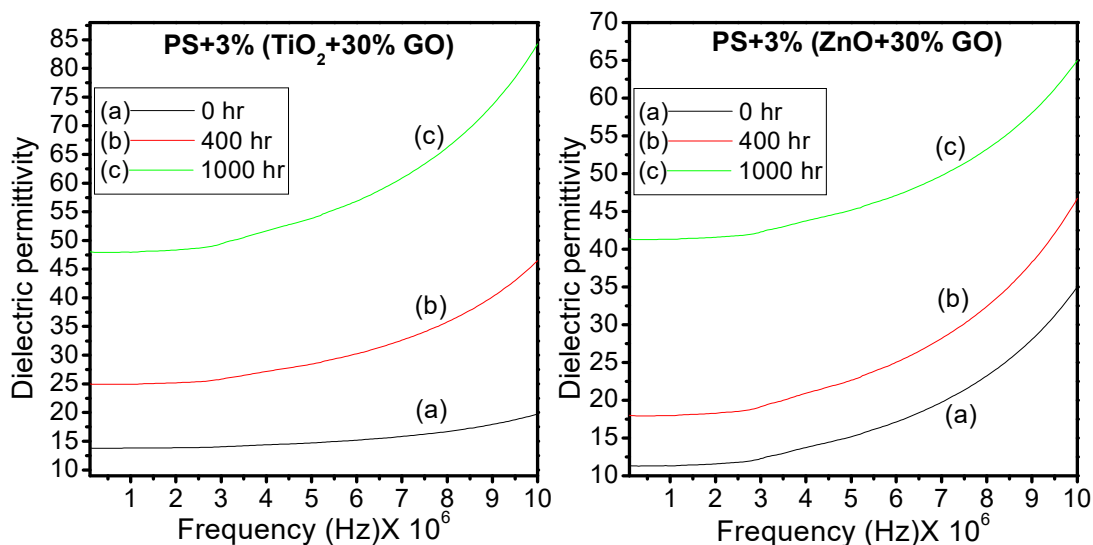
Figure 5.12.2. *Dielectric permittivity of PS-(TiO₂-30%GO) and PS-(ZnO-30%GO) composites exposed to UV radiation for 0, 400 and 1000 h.*

5.4.6. Thermogravimetric Analysis (TGA)
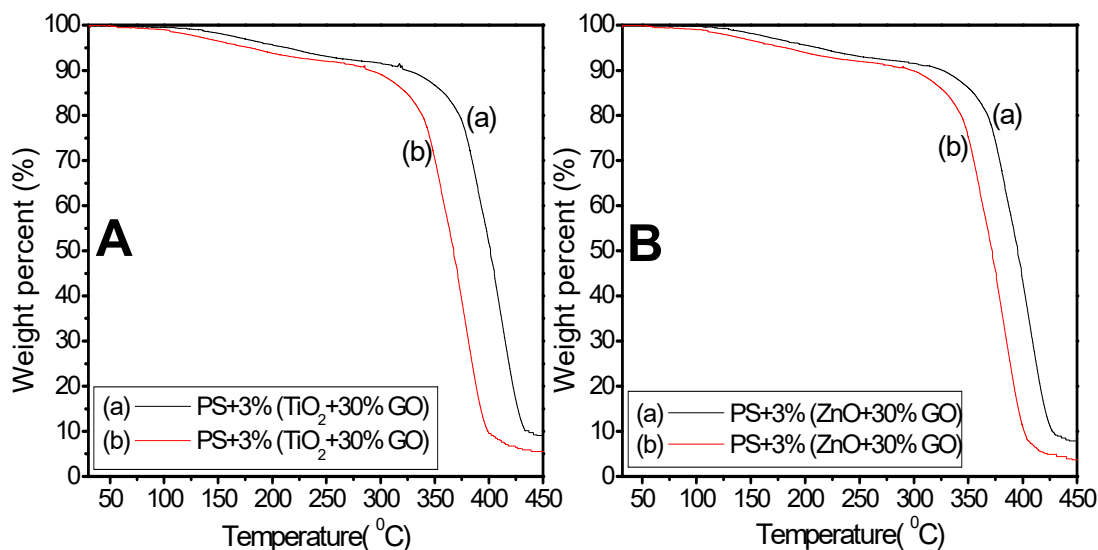
Figure 5.13. *TGA thermogram of PS-3% (TiO₂+30% GO) (A) and PS-3% (ZnO+30% GO) (B) composites before and after UV irradiation of 1000 h*

TGA thermograms of PS-(TiO$_2$-30% GO) and PS-(ZnO-30% GO) conducted under nitrogen atmosphere as represented in figure 5.13, displayed two stages of weight loss. The first stage of weight loss represents water desorption and the second stage represent decomposition of the polymer composites. The decomposition temperature of PS-(TiO$_2$-30% GO) ranged between 320-434°C before UV irradiation (Figure 5.13 A). The decomposition temperature of PS-(ZnO-30% GO) before UV irradiation was between 314-429°C respectively (Figure 5.13 B). The decomposition temperatures of the composites decreased with the increase in UV exposure time. The decomposition temperature of PS-(TiO$_2$-30% GO) decreased 872-401°C and that of PS-(ZnO-30% GO) decreased to 292-408°C respectively upon UV irradiation of 1000 hours. Decreased thermal stability of the polymer composites as a result of degradation is evident here.

5.4.7. Weight loss

Weight loss percentage of PS-TiO$_2$-GO and PS-ZnO-GO composites exposed to UV radiation of varying time intervals ranging from 0 to 1000 hours are represented below (Figure 5.14). The percentage of weight loss increased with respect to UV irradiation time. Evolution of volatile species produced during the photodegradation process is evident here. PS-(TiO$_2$-30% GO) underwent maximum weight loss among

PS-TiO$_2$-GO composites and PS-(ZnO-10% GO) underwent maximum weight loss among PS-ZnO-GO composites upon UV irradiation.
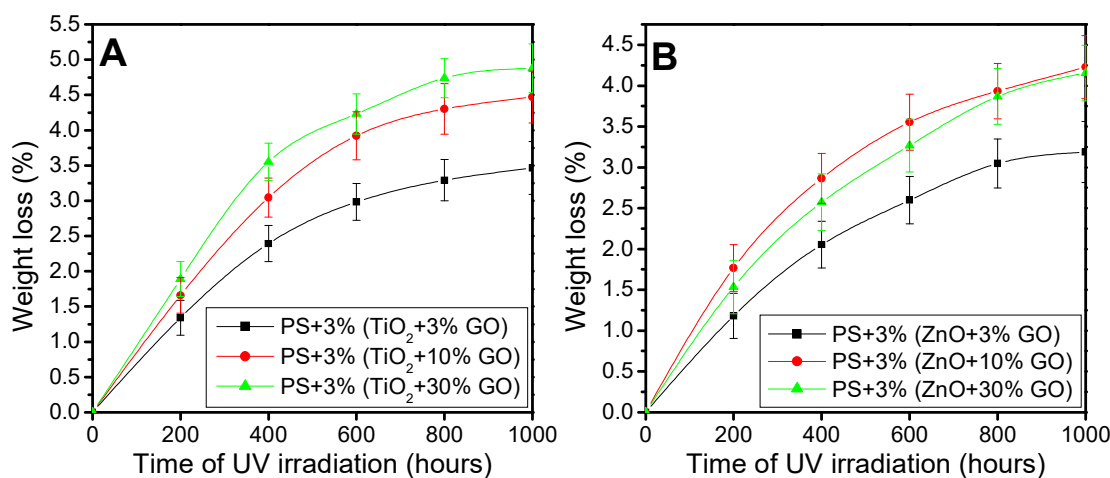
Figure 5.14. *Comparison of weight loss percentages of PS-3%(TiO$_2$- GO) (A) and PS-3%(ZnO-GO)(B) composites at regular intervals of UV irradiation*

5.5. Mechanism of Photodegradation of PS-TiO$_2$-GO/ PS-ZnO-GO composites

It was confirmed from various analytic techniques discussed above that PS-TiO$_2$-GO and PS-ZnO-GO composites underwent better photo-oxidative degradation compared to PS-TiO$_2$ and PS-ZnO composites. In other words, the photocatalytic efficiency of TiO$_2$ and ZnO has been enhanced on coupling them with GO. GO coupled with TiO$_2$ or ZnO reduces the electron–hole recombination upto an appreciable extent. Raman spectroscopy proved the partial reduction of GO (into reduced graphene oxide) in TiO$_2$-GO composites discussed above. The reduced graphene oxide acts as better electron sink. The photogenerated electrons present in the conduction band (CB) of TiO$_2$ or ZnO are transferred into the Fermi levels of carbon atoms of these reduced GO instead minimizing the chance of recombining[35]. These electrons are resonance stabilized in the GO sheet and can recombine with adsorbed oxygen producing various reactive species (like O$^-$, O$_2\bullet^-$ etc). These species interact with the PS chain initiating photo-oxidation of the chain. The holes left behind in the VB of TiO$_2$ or ZnO can now combine easily with the adsorbed water or OH$^-$ ions resulting in the formation of OH$\bullet$ which interacts with the PS chain initiating another set of reactions including –OH and –OOH substitution over the chain (Figure 5.15).
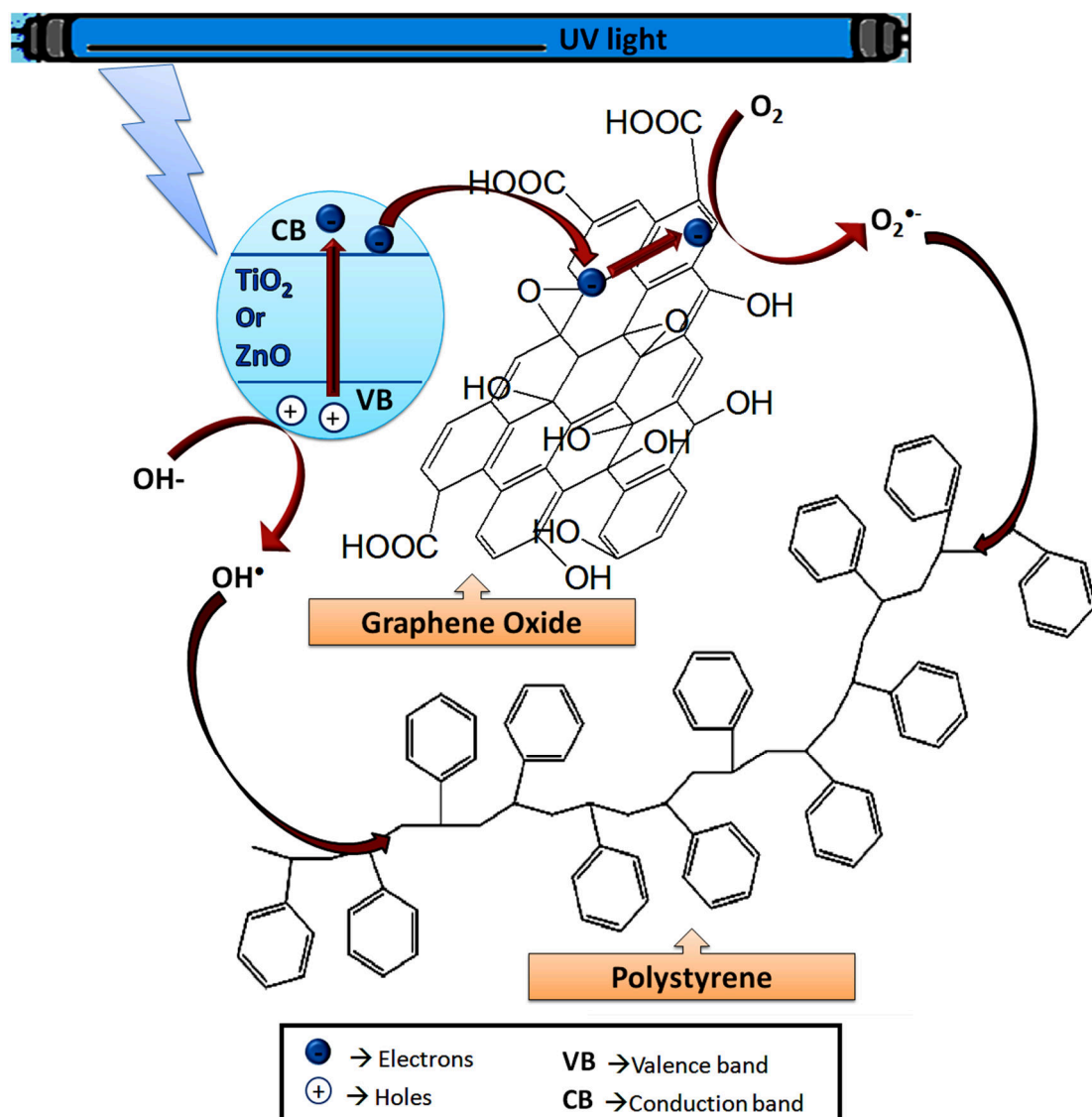
Figure 5.15. *Schematic representation of photodegradation mechanism of PS by TiO$_2$-GO/ZnO-GO catalysts through charge transfer*

Other than the interfacial charge transfer occurring in the heterojunctions of the metal oxides and GO, the formation of Ti-O-C/Zn-O-C and Ti-C bonds act as a bridge for the transport of electrons. The photogenerated electrons transported from the TiO$_2$/ZnO to the carbon atoms of GO are highly stabilized and hence the chance of recombination of the electron-hole pair is minimized.

5.6. Conclusions

GO could be successfully prepared from graphite through chemical oxidation approach following ultrasonication assisted modified Hummer's method. TiO$_2$-GO and ZnO-GO composites were prepared through ultrasonication assisted hydrothermal

method. Preparation of TiO_2-GO resulted in nano sized separated crystalline particles whereas ZnO-GO were aggregated. Photodegradation of PS in the presence of TiO_2-GO and ZnO-GO composites as photocatalysts were studied. Both PS-TiO_2-GO and PS-ZnO-GO underwent photo-oxidative degradation in the presence of UV radiation. They also underwent polymer chain scission upon UV irradiation. The composites underwent better photodegradation compared to PS-TiO_2 as well as PS-ZnO composites. Mechanical properties of the composites were enhanced in PS-TiO_2-GO and PS-ZnO-GO composites compared to PS-TiO_2 and PS-ZnO composites. Possible application of the composites, where better mechanical strength is in demand, is hence promised. The mechanical strength of the composites decreased when subjected to UV irradiation. The value of BDV of the composites was lower than that of PS-TiO_2, PS-ZnO and even PS. The possibility for the application of the composites, where better conductivity is required, can hence be assured. BDV of the composites decreased upon UV irradiation. Formation of charged species as a consequence of photodegradation was hence evident. Dielectric permittivity of the composites increased upon UV irradiation due to the formation of charged dipoles. The thermal stability of the composites too decreased as a consequence of photodegradation as evident from TGA. It can be concluded that the photocatalytic efficiency of TiO_2 and ZnO was enhanced upon coupling with GO. The possibility of various interactions including hydrogen bond and Ti-O-C/Zn-O-C bond formation between TiO_2/ZnO and GO could have assisted the intrafacial charge transfer between the heterojunctions of TiO_2/ZnO and GO. The photogenerated electrons can transfer from the conduction bands of TiO_2/ZnO into Fermi levels of GO. This appreciably decreases the electron-hole recombination possibility within TiO_2 or ZnO. The resonance stabilized electrons delocalized in the π bonds of GO can interact with oxygen atoms in the atmosphere leading to reactive species that could initiate the photodegradation of PS chain. The holes left behind in the valence band of TiO_2/ZnO could further combine with the adsorbed water molecules or OH^- ions resulting in OH• that can interact with PS chain resulting in its degradation. PS-TiO_2-GO composites underwent better photo-oxidative degradation compared to PS-ZnO-GO composites. PS-(TiO_2-30% GO) exhibits maximum photodegradation among PS-TiO_2-GO composites and PS-(ZnO-10% GO) exhibits maximum photodegradation among PS-ZnO-GO composites.

References

1. Girishkumar, G., Vinodgopal, K. & Kamat, P. V. Carbon Nanostructures in Portable Fuel Cells: Single-Walled Carbon Nanotube Electrodes for Methanol Oxidation and Oxygen Reduction. *J. Phys. Chem. B* **108**, 19960–19966 (2004).
2. Brown, P., Takechi, K. & Kamat, P. V. Single-Walled Carbon Nanotube Scaffolds for Dye-Sensitized Solar Cells. *J. Phys. Chem. C* **112**, 4776–4782 (2008).
3. Eckert, J.-F. *et al.* Fullerene−Oligophenylenevinylene Hybrids: Synthesis, Electronic Properties, and Incorporation in Photovoltaic Devices. *J. Am. Chem. Soc.* **122**, 7467–7479 (2000).
4. Thomas, K. G., George, M. V & Kamat, P. V. Photoinduced Electron-Transfer Processes in Fullerene-Based Donor–Acceptor Systems. *Helv. Chim. Acta* **88**, 1291–1308 (2005).
5. Iijima, S. Helical microtubules of graphitic carbon. *Nature* **354**, 56–58 (1991).
6. Rao, C. N. R., Sood, A. K., Voggu, R. & Subrahmanyam, K. S. Some Novel Attributes of Graphene. *J. Phys. Chem. Lett.* **1**, 572–580 (2010).
7. Novoselov, K. S. *et al.* Electric Field Effect in Atomically Thin Carbon Films. *Science (80-.).* **306**, 666–669 (2004).
8. Lee, C., Wei, X., Kysar, J. W. & Hone, J. Measurement of the elastic properties and intrinsic strength of monolayer graphene. *Science (80-.).* **321**, 385–388 (2008).
9. Balandin, A. A. *et al.* Superior Thermal Conductivity of Single-Layer Graphene. *Nano Lett.* **8**, 902–907 (2008).
10. Huang, X., Qi, X., Boey, F. & Zhang, H. Graphene-based composites. *Chem. Soc. Rev.* **41**, 666–686 (2012).
11. Singh, E. & Nalwa, H. S. Stability of graphene-based heterojunction solar cells. *RSC Adv.* **5**, 73575–73600 (2015).
12. Stankovich, S. *et al.* Graphene-based composite materials. *Nature* **442**, 282–286 (2006).
13. Jasuja, K. & Berry, V. Implantation and Growth of Dendritic Gold Nanostructures on Graphene Derivatives: Electrical Property Tailoring and Raman Enhancement. *ACS Nano* **3**, 2358–2366 (2009).
14. Wang, X., Zhi, L. & Müllen, K. Transparent, Conductive Graphene Electrodes for Dye-Sensitized Solar Cells. *Nano Lett.* **8**, 323–327 (2008).
15. Stoller, M. D., Park, S., Zhu, Y., An, J. & Ruoff, R. S. Graphene-based ultracapacitors. *Nano Lett.* **8**, 3498–3502 (2008).
16. Liu, Z., Robinson, J. T., Sun, X. & Dai, H. PEGylated Nanographene Oxide for Delivery of Water-Insoluble Cancer Drugs. *J. Am. Chem. Soc.* **130**, 10876–10877 (2008).
17. Liu, Z., Tabakman, S., Welsher, K. & Dai, H. Carbon nanotubes in biology and medicine: in vitro and in vivo detection, imaging and drug delivery. *Nano Res.* **2**, 85–120 (2009).
18. Robinson, J. T., Perkins, F. K., Snow, E. S., Wei, Z. & Sheehan, P. E. Reduced graphene oxide molecular sensors. *Nano Lett.* **8**, 3137–3140 (2008).
19. Park, S. & Ruoff, R. S. Chemical methods for the production of graphenes. *Nat. Nanotechnol.* **4**, 217–224 (2009).
20. He, H., Riedl, T., Lerf, A. & Klinowski, J. Solid-State NMR Studies of the Structure of Graphite Oxide. *J. Phys. Chem.* **100**, 19954–19958 (1996).
21. He, H., Klinowski, J., Forster, M. & Lerf, A. A new structural model for graphite oxide. *Chem. Phys. Lett.* **287**, 53–56 (1998).
22. Lerf, A., He, H., Forster, M. & Klinowski, J. Structure of Graphite Oxide Revisited. *J. Phys. Chem. B* **102**, 4477–4482 (1998).
23. Cai, W. *et al.* Synthesis and Solid-State NMR Structural Characterization of 13C-Labeled Graphite Oxide. *Science (80-.).* **321**, 1815–1817 (2008).
24. Dreyer, D. R., Park, S., Bielawski, C. W. & Ruoff, R. S. The chemistry of graphene oxide. *Chem. Soc. Rev.* **39**, 228–240 (2010).
25. Kamat, P. V. Graphene-Based Nanoarchitectures. Anchoring Semiconductor and Metal Nanoparticles on a Two-Dimensional Carbon Support. 520–527 (2010). doi:10.1021/jz900265j
26. Naknikham, U. *et al.* Mutual-stabilization in chemically bonded graphene oxide–TiO2

heterostructures synthesized by a sol–gel approach. *RSC Adv.* **7**, 41217–41227 (2017).

27. Williams, G., Seger, B. & Kamat, P. V. TiO2-Graphene Nanocomposites. UV-Assisted Photocatalytic Reduction of Graphene Oxide. *ACS Nano* **2**, 1487–1491 (2008).

28. Kumar, A., Bansal, A., Behera, B., Jain, S. L. & Ray, S. S. Ternary hybrid polymeric nanocomposites through grafting of polystyrene on graphene oxide-TiO2 by surface initiated atom transfer radical polymerization (SI-ATRP). *Mater. Chem. Phys.* **172**, 189–196 (2016).

29. Huang, Q. *et al.* Enhanced Photocatalytic Activity of Chemically Bonded TiO2/Graphene Composites Based on the Effective Interfacial Charge Transfer through the C–Ti Bond. *ACS Catal.* **3**, 1477–1485 (2013).

30. He, D., Li, Y., Wang, J., Yang, Y. & An, and Q. Tunable Nanostructure of TiO$_2$/Reduced Graphene Oxide Composite for High Photocatalysis. *Appl. Microsc.* **46**, 37–44 (2016).

31. Gillespie, P. N. O. & Martsinovich, N. Origin of Charge Trapping in TiO2/Reduced Graphene Oxide Photocatalytic Composites: Insights from Theory. *ACS Appl. Mater. Interfaces* **11**, 31909–31922 (2019).

32. Benjwal, P., Kumar, M., Chamoli, P. & Kar, K. Enhanced photocatalytic degradation of methylene blue and adsorption of arsenic(III) by reduced graphene oxide (rGO)–metal oxide (TiO2/Fe3O4) based nanocomposites. *RSC Adv.* **5**, 73249–73260 (2015).

33. Umrao, S. *et al.* A possible mechanism for the emergence of an additional bandgap due to a Ti–O–C bond in the TiO2–graphene hybrid system for enhanced photodegradation of methylene blue under visible light. *RSC Adv.* **4**, 59890–59901 (2014).

34. Djellabi, R., Yang, B., Wang, Y., Cui, X. & Zhao, X. Carbonaceous biomass-titania composites with TiOC bonding bridge for efficient photocatalytic reduction of Cr(VI) under narrow visible light. *Chem. Eng. J.* **366**, 172–180 (2019).

35. Tang, B., Chen, H., Peng, H., Wang, Z. & Huang, W. Graphene Modified TiO$_2$ Composite Photocatalysts: Mechanism, Progress and Perspective. *Nanomater. (Basel, Switzerland)* **8**, (2018).

36. Rakkesh, R. A., Durgalakshmi, D. & Balakumar, S. Efficient sunlight-driven photocatalytic activity of chemically bonded GNS–TiO2 and GNS–ZnO heterostructures. *J. Mater. Chem. C* **2**, 6827–6834 (2014).

37. Liang, Y., Wang, H., Sanchez Casalongue, H., Chen, Z. & Dai, H. TiO2 nanocrystals grown on graphene as advanced photocatalytic hybrid materials. *Nano Res.* **3**, 701–705 (2010).

38. Hummers, W. S. & Offeman, R. E. Preparation of Graphitic Oxide. *J. Am. Chem. Soc.* **80**, 1339 (1958).

39. Sreekanth, T. V. M., Jung, M.-J. & Eom, I.-Y. Green synthesis of silver nanoparticles, decorated on graphene oxide nanosheets and their catalytic activity. *Appl. Surf. Sci.* **361**, 102–106 (2016).

40. Marcano, D. C. *et al.* Improved Synthesis of Graphene Oxide. *ACS Nano* **4**, 4806–4814 (2010).

41. Dimiev, A. M. & Tour, J. M. Mechanism of Graphene Oxide Formation. *ACS Nano* **8**, 3060–3068 (2014).

42. Lowe, S. & Zhong, Y. L. Challenges of Industrial-Scale Graphene Oxide Production: Fundamentals and Applications. in *Graphene Oxide: Fundamentals and Applications* 410–431 (2016). doi:10.1002/9781119069447.ch13

43. Paulchamy, B., Arthi, G. & Lignesh, B. D. A simple approach to stepwise synthesis of graphene oxide nanomaterial. *J Nanomed Nanotechnol* **6**, 1 (2015).

44. Gao, P., Li, A., Sun, D. D. & Ng, W. J. Effects of various TiO2 nanostructures and graphene oxide on photocatalytic activity of TiO2. *J. Hazard. Mater.* **279**, 96–104 (2014).

45. Rong, X. *et al.* Preparation , characterization and photocatalytic application of TiO 2 – graphene photocatalyst under visible light irradiation. *Ceram. Int.* 1–10 (2014). doi:10.1016/j.ceramint.2014.10.072

46. Perera, S. D. *et al.* Hydrothermal Synthesis of Graphene-TiO2 Nanotube Composites with Enhanced Photocatalytic Activity. *ACS Catal.* **2**, 949–956 (2012).

47. Ameen, S., Akhtar], M. [Shaheer, Seo, H.-K. & Shin], H. [Shik. Advanced ZnO–graphene oxide nanohybrid and its photocatalytic Applications. *Mater. Lett.* **100**, 261–265 (2013).
48. Lee, K. S., Park, C. W., Lee, S. J. & Kim, J.-D. Hierarchical zinc oxide/graphene oxide composites for energy storage devices. *J. Alloys Compd.* **739**, 522–528 (2018).
49. Arami, H., Mazloumi, M., Khalifehzadeh, R. & Sadrnezhaad, S. K. Sonochemical preparation of TiO2 nanoparticles. *Mater. Lett.* **61**, 4559–4561 (2007).
50. Zhang, Y., Tang, Z.-R., Fu, X. & Xu, Y.-J. Engineering the Unique 2D Mat of Graphene to Achieve Graphene-TiO2 Nanocomposite for Photocatalytic Selective Transformation: What Advantage does Graphene Have over Its Forebear Carbon Nanotube? *ACS Nano* **5**, 7426–7435 (2011).
51. Štengl, V., Bakardjieva, S., Grygar, T. M., Bludská, J. & Kormunda, M. TiO 2-graphene oxide nanocomposite as advanced photocatalytic materials. *Chem. Cent. J.* **7**, 41 (2013).
52. Zhang, H., Lv, X., Li, Y., Wang, Y. & Li, J. P25-graphene composite as a high performance photocatalyst. *ACS Nano* **4**, 380–386 (2009).
53. Liu, H. *et al.* A green and direct synthesis of graphene oxide encapsulated TiO2 core/shell structures with enhanced photoactivity. *Chem. Eng. J.* **230**, 279–285 (2013).
54. Khannam, M., Sharma, S., Dolui, S. & Dolui, S. K. A graphene oxide incorporated TiO2 photoanode for high efficiency quasi solid state dye sensitized solar cells based on a poly-vinyl alcohol gel electrolyte. *RSC Adv.* **6**, 55406–55414 (2016).

Chapter 6

UV Degradation of Polystyrene using Organic Photosensitizers Coupled and Uncoupled with Nano TiO₂

Abstract

Photodegradation of PS was studied in the presence of a few benzophenone derivatives and triphenylmethane dyes as photosensitizers. The benzophenone derivatives acted as effective photosensitizers for the UV degradation of PS. Triphenylmethane dyes on the other hand were not appreciable photosensitizers for the photodegradation of PS. Photocatalytic activity of TiO₂ enhanced considerably in the presence of benzophenone derivatives and triphenylmethane dyes. Photocatalytic activity of benzophenones, under of UV light could be explained on the basis of diradicaloid formation. The difficulty in diradicaloid formation of 2-hydroxy-4-methoxybenzophenone (2HO4MOBP) due to photoenolization made it a weaker photosensitizer, compared to the other benzophenone derivatives under study. It was evident from the FTIR spectra that formation of alkenic double bonds dominated over other oxygen containing functional groups when PS-benzophenone based photosensitizer composites were subjected to UV irradiation.

6.1. Introduction

The effect of various substituted benzophenone and triphenylmethane dyes which acts as photosensitizers for the photodegradation of polystyrene (PS) is studied in this chapter. The photocatalytic efficiency of nano TiO_2 in the presence of these photosensitizers is also studied. Benzophenone (BP) is a renowned photosensitizer used in various photochemical reactions including photodegradation of polymers[1,2]. The photodegradation of PS by BP has been extensively studied[3–7]. BP absorbs UV radiation leading to homolytic cleavage of the π bond belonging to its >C=O group producing radicals. The photochemistry of BP is based on the reaction of these radicals with another species before recombination. The two phenyl rings directly connected to the carbonyl carbon are in conjugation with it. This ensures the stability of the radicals formed, minimizing the chance of recombination up to an extent. The radicals can be transferred to the neighbouring molecules initiating different types of photochemical reactions according to the nature of molecules. These reactions are named as *triplet-triplet energy transfer (T-TET)*, *type I electron transfer*, *type I H-abstraction and type II singlet oxygen* process[8]. In T-TET process, the spin and the energy are transferred between excited triplet state of benzophenone ($^3BP^*$) and the neighbouring molecule as elucidated in figure 6.1.
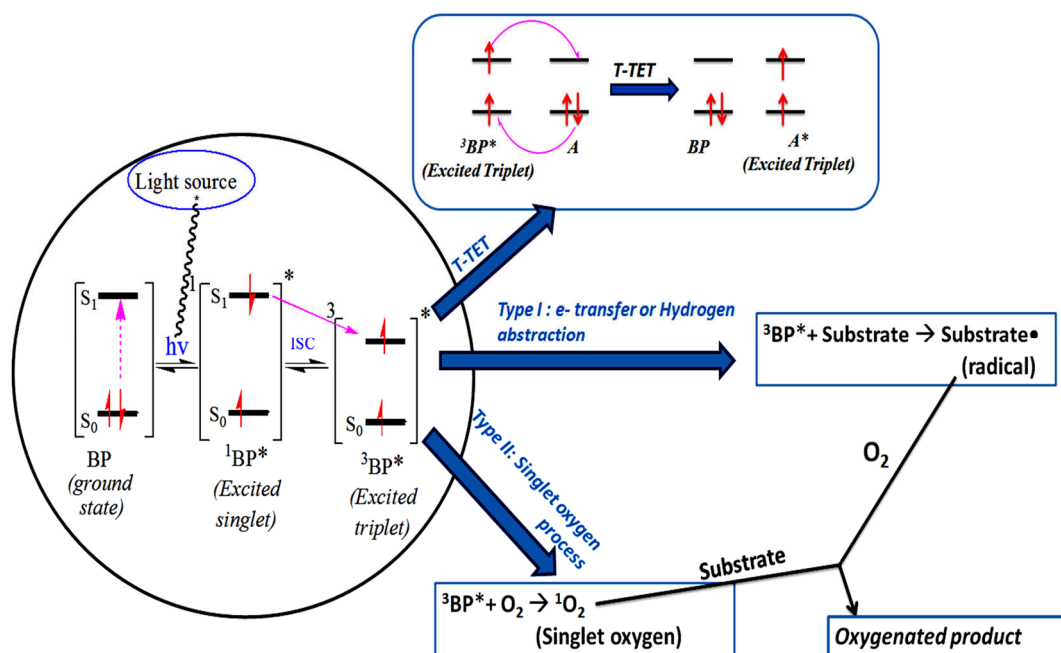
***Figure 6.1**. Photoreactions of benzophenone*

T-TET in BP-naphthalene[9,10] and BP-fluorine-naphthalene[11] systems have been reported. *Type I* processes take place when $^3BP^*$ reacts with neighbouring substrate or solvent. Electron transfer or hydrogen abstraction takes place during *type I* process. The result of this reaction is formation of radicals in the solvent or substrate molecules triggering radical initiated photochemical reactions in most cases. *Type II singlet oxygen* process take place when $^3BP^*$ reacts with oxygen. Singlet oxygen is produced as a consequence of these reactions by energy transfer which are reactive and can interact with another substrate to initiate photochemical reactions[12].

The stability of the radicals in $^3BP^*$ is the key factor that determines all types of energy transfer or processes discussed above. The stability of the radicals in $^3BP^*$ can be increased by increasing the aromaticity of the phenyl rings in the system. Substitution of electron donating groups on the phenyl ring can increase their aromaticity. Substituted benzophenones containing electron releasing as well as withdrawing groups have been chosen in this study and their photocatalytic efficiency have been compared with that of unsubstituted benzophenone for the photodegradation of PS under UV radiation.

The absorption of benzophenone is limited to the UV region of the spectrum. The use of selective organic dyes in the place of BP comes into picture in this point of view. Organic dyes can absorb in the UV as well as visible region. Organic dyes have been extensively used in various applications especially in the fields of dye sensitized solar cells (DSSC)[13,14], organic light emitting diodes (OLED)[15,16], liquid crystals (LC)[17,18], sensors for photoconductivity[19] and so on. Dye photosensitized photodegradation of polymers has also been studied[20,21]. Triphenylmethane dyes (methyl blue and malachite green) have been adopted as photosensitizer for PS photodegradation in this study. Triphenylmethane dyes are cheap with an attractive property of their brilliant colours[22]. Dyes also exhibit amazing properties in association with other substances. For example, proteins bonded to triphenylmethane dyes exhibit enhanced quantum yield, photo reactivity, intersystem crossing and fluorescence. The interaction of these dyes with proteins through type I electron or hydrogen transfer process as explained above resulted in these enhanced properties[23]. Polymers incorporated with triphenylmethane dyes are widely used in various fields

including medicines, waste water treatments, gas separation, painting industry, dyeing process etc[24].

TiO$_2$ coupled with BP photosensitizers as well as with triphenylmethane dyes promises an effective photocatalyst with enhanced properties. TiO$_2$-BP blend has proven to be an efficient photocatalyst for the photo-oxidative degradation of polyethylene. The interaction of BP with the hydroxy (OH•) and hydroperoxy (OOH•) radicals (which are produced by interaction of the electrons and holes produced in TiO$_2$ with water and oxygen) leading to further radical formation on exposure to sunlight have been discussed here. The radical products react with the polyethylene chain resulting to its photodegradation[25]. When triphenylmethane dyes are coupled with TiO$_2$, the mechanism is rather different. The dye absorbs light radiation in the visible and UV region leading to charge separation at the interface of TiO$_2$ and dye. The process termed as photo induced electron injection leads to the charge transport from excited dyes into the conduction band of TiO$_2$[26].

Section:I

UV degradation of polystyrene using benzophenone derivatives and organic dyes as photosensitizers

Photodegradation of PS using benzophenone derivatives and triphenylmethane dyes has been discussed in this section. The benzophenone derivatives are hereafter termed as '*benzophenone based photosensitizers*' and the triphenyl methyl dyes are termed as '*dye photosensitizers*'. The benzophenone based photosensitizers included in this study are benzophenone (BP), 2-hydroxy-4-methoxybenzophenone (2HO4MOBP), 4-methoxybenzophenone (4MOBP), 2-chlorobenzophenone (2ClBP) and 4-nitrobenzophenone (4NBP). The dye photosensitizers included in this study are malachite green (MG) and methyl blue (MB).

Structure and properties of the benzophenone based photosensitizers and dye photosensitizers included in this work are as tabulated in tables 6.1.1 and 6.1.2.

Table 6.1.1. List of benzophenone based photosensitizers
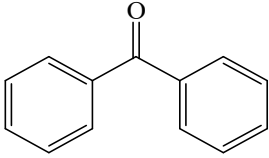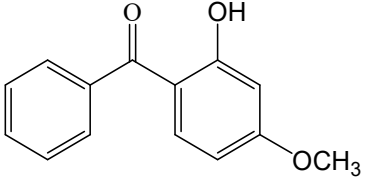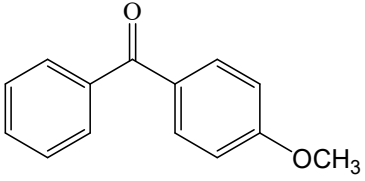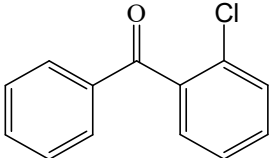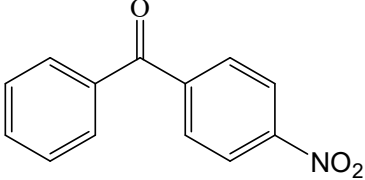
Benzophenone based photosensitizers				
Structure	Name	Abbreviation	Boiling point (°C)	Melting point (°C)
	Benzophenone	BP	305.4	48.5
	2-hydroxy-4-methoxybenzophenone	2HO4MOBP	150-160	62-64
	4-methoxybenzophenone	4MOBP	354-356	60-63
	2-chlorobenzophenone	2ClBP	330	44-47
	4-nitrobenzophenone	4NBP	390±25	136-138

Table 6.1.2. List of dye photosensitizers

Dye photosensitizers				
Structure	Name	Abbreviation	Boiling point (°C)	Melting point (°C)
	Malachite green	MG	520.91	158-160
	Methyl blue	MB	-	-

The preparation of PS-dye and PS-benzophenone based photosensitizer composites were as explained in chapter 2. The required weight percentage of the photosensitizers was incorporated into the PS. Specimens for electrical and mechanical measurements were also prepared.

6.2. Results and Discussion

6.2.1. Gel permeation chromatography (GPC)

The $\overline{M}_w$ and $\overline{M}_n$ of PS loaded with benzophenone based photosensitizers (Figure 6.2.1) as well as dye photosensitizers (Figure 6.2.2) decreased with respect to UV irradiation time. Comparative decrease in the average molecular weights upon UV irradiation showed only slight variation among the composites. The decrease in $\overline{M}_w$

and $\overline{M}_n$ among PS-benzophenone based photosensitizer composites was found to be maximum in PS-4MOBP and minimum in PS-2HO4MOBP compared to their other counterparts under study (Figure 6.2.1). Among the PS-dye composites, the extent of decrease in the average molecular weights of PS-MG and PS-MB were almost similar upon UV irradiation. PS-MB however exhibited slightly enhanced reduction in the average molecular weights compared to that of PS-MG composite (Figure 6.2.2).
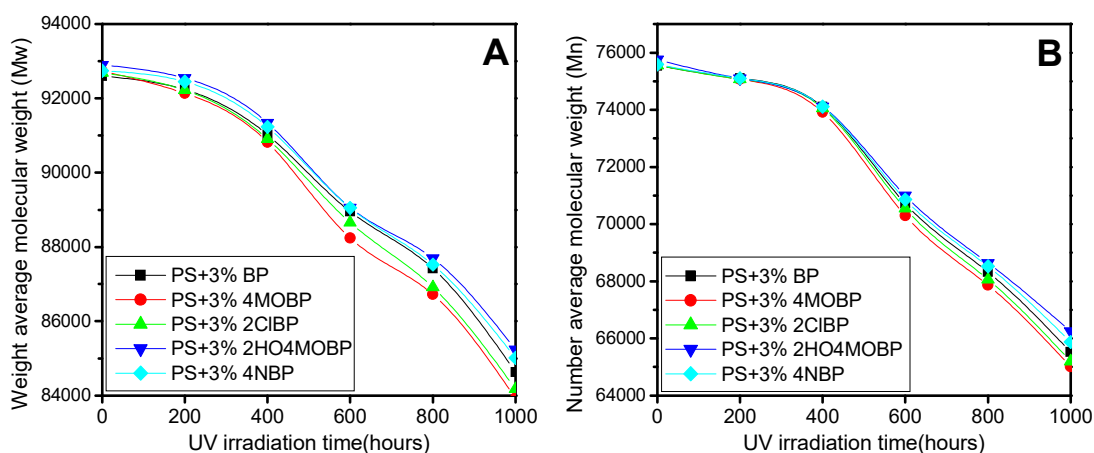
Figure 6.2.1. A) *Weight average ($\overline{M}_w$) and **B)** number average ($\overline{M}_n$) molecular weights of PS-benzophenone based photosensitizer composites under different UV irradiation time*
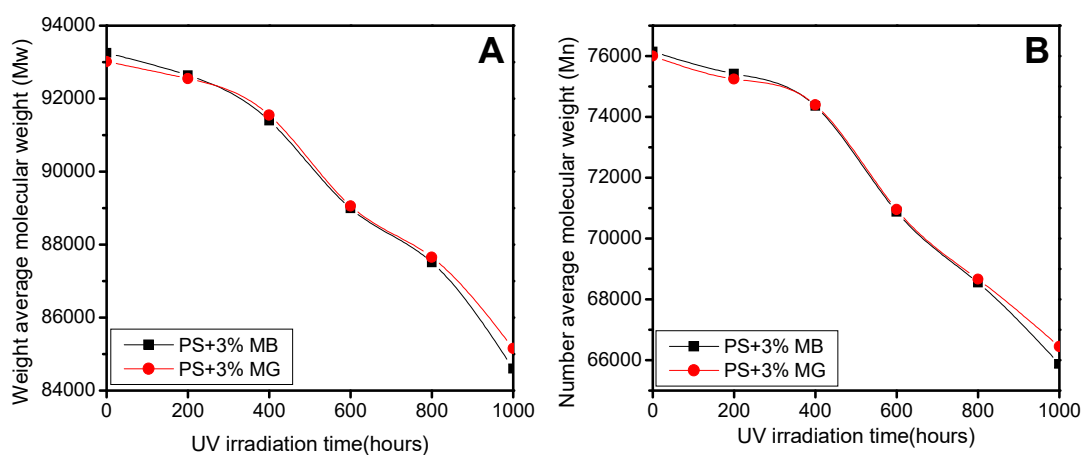
Figure 6.2.2. A) *Weight average ($\overline{M}_w$) and **B)** number average ($\overline{M}_n$) molecular weights of PS-dye composites under different UV irradiation time*

The number of chain scission per molecule (S) and number of scission events per gram (N_t) determined from $\overline{M}_n$ for the PS-benzophenone based photosensitizer composites were found to be maximum for PS-4MOBP and minimum for PS-2HO4MOBP upon UV irradiation (Figure 6.2.3). The values of S and N_t of PS-MB

were slightly higher than that of PS-MG among PS-dye photosensitizers composites upon UV irradiation (Figure 6.2.4).
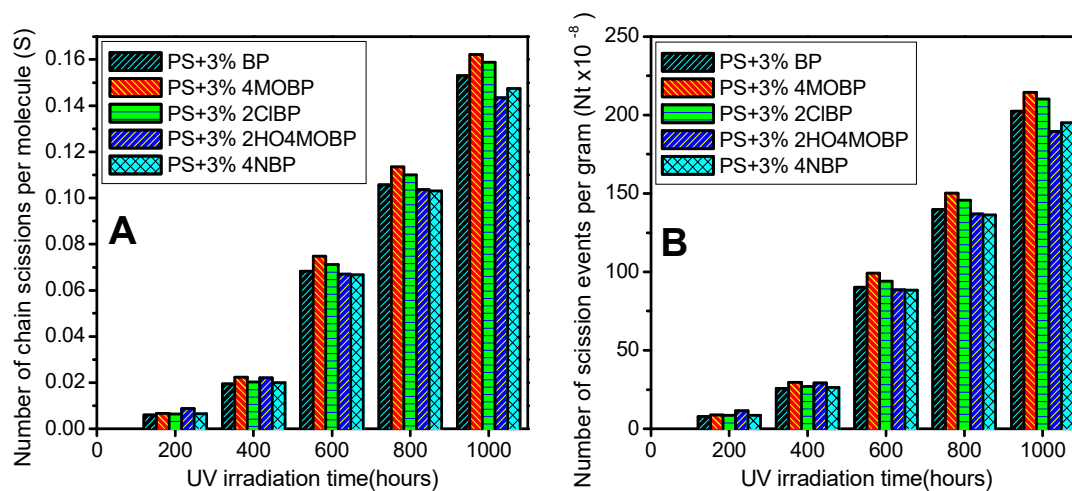
Figure 6.2.3. A) *Number of chain scissions per molecule (S) and **B)** number of scission events per gram (N_t) of PS-benzophenone based photosensitizer composites under different UV irradiation time intervals*
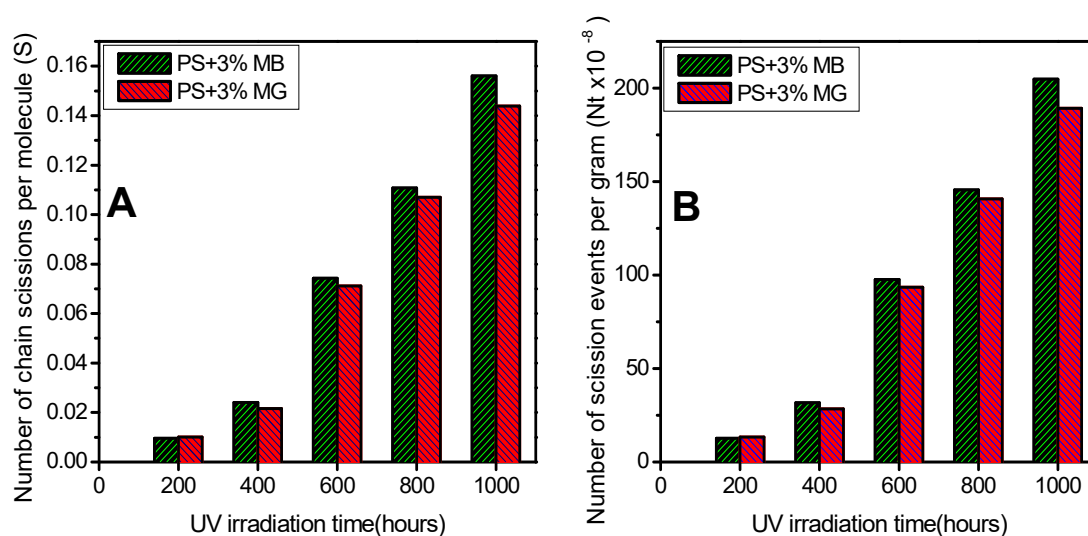
Figure 6.2.4. A) *Number of chain scissions per molecule (S) and **B)** number of scission events per gram (N_t) of PS- dye photosensitizer composites under different UV irradiation time intervals*

Polydispersity index (PDI) of all the PS composites increased as the time of UV irradiation increased (Figure 6.2.5). The increase in chain scission in random manner due to photodegradation was evident here.

From the GPC data, maximum chain scission, as well as maximum decrease in the average molecular mass was observed in PS-4MOBP composite among the PS-

benzophenone based composites. It was also noted that various substituents on benzophenone altered the rate of chain scission of the PS matrix to which they are loaded. Among the PS-dye composites, PS-MB exhibited maximum chain cleavage and decrease in average molecular mass compared to PS-MG.
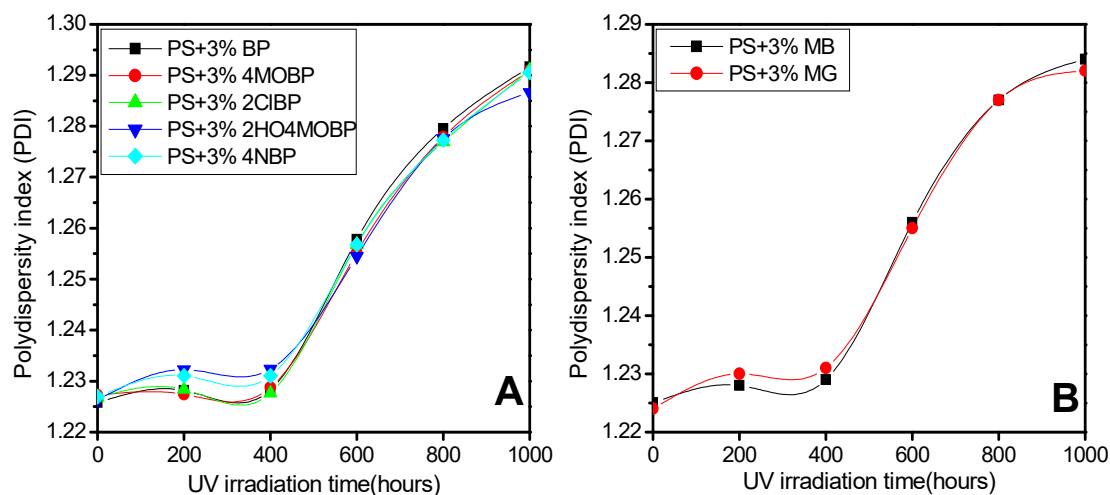
Figure 6.2.5. Polydispersity index (PDI) of PS–benzophenone based and PS-dye photosensitizer composites, under different UV irradiation time.

6.2.2. FTIR Spectroscopy

The FTIR spectra of the PS composites displayed all the bands corresponding to the stretching vibrations of PS as well as the photosensitizers loaded into it (Figure 6.3). The bands at 1740-1700 cm^{-1} observed in all the PS-benzophenone based photosensitizer composites before UV irradiation attributed to >C=O stretching vibrations of benzophenone moiety. Even though only 2HO4MOBP contains -OH group, the spectra of all PS-benzophenone based photosensitizer composites exhibited bands corresponding to -OH (3700- 3600 cm^{-1}) before UV irradiation. This could be due to the enolic form of benzophenone moiety existing in the composites or could be due to the adsorbed water from the atmosphere. As the time of UV irradiation increased, an increase in the bands corresponding to >C=O and -OH or -OOH was observed suggesting photo-oxidation of PS chain. A striking observation for all PS-benzophenone based photosensitizer composites was that increase in the intensity of the bands between 1700 and 1650 cm^{-1} (>C=C< stretching) was a little more than that of the bands between 1740 and 1700 cm^{-1}(>C=O stretching). This observation supports the fact that the formation of alkenic double bonds over the PS chain took place much effectively than the formation of carbonyl bonds for PS-benzophenone

based photosensitizer composites upon UV irradiation. In the coming section (section 6.5), the possible reason for this observation is explained through suitable mechanism. An increase in the band intensities corresponding to conjugated carbon-carbon double bonds were also observed at around 1600 cm^{-1}. The yellowing of the composites upon UV exposure was a visual support to the conjugated double bond formation which is further supported by the UV-visible spectroscopy to be discussed shortly.
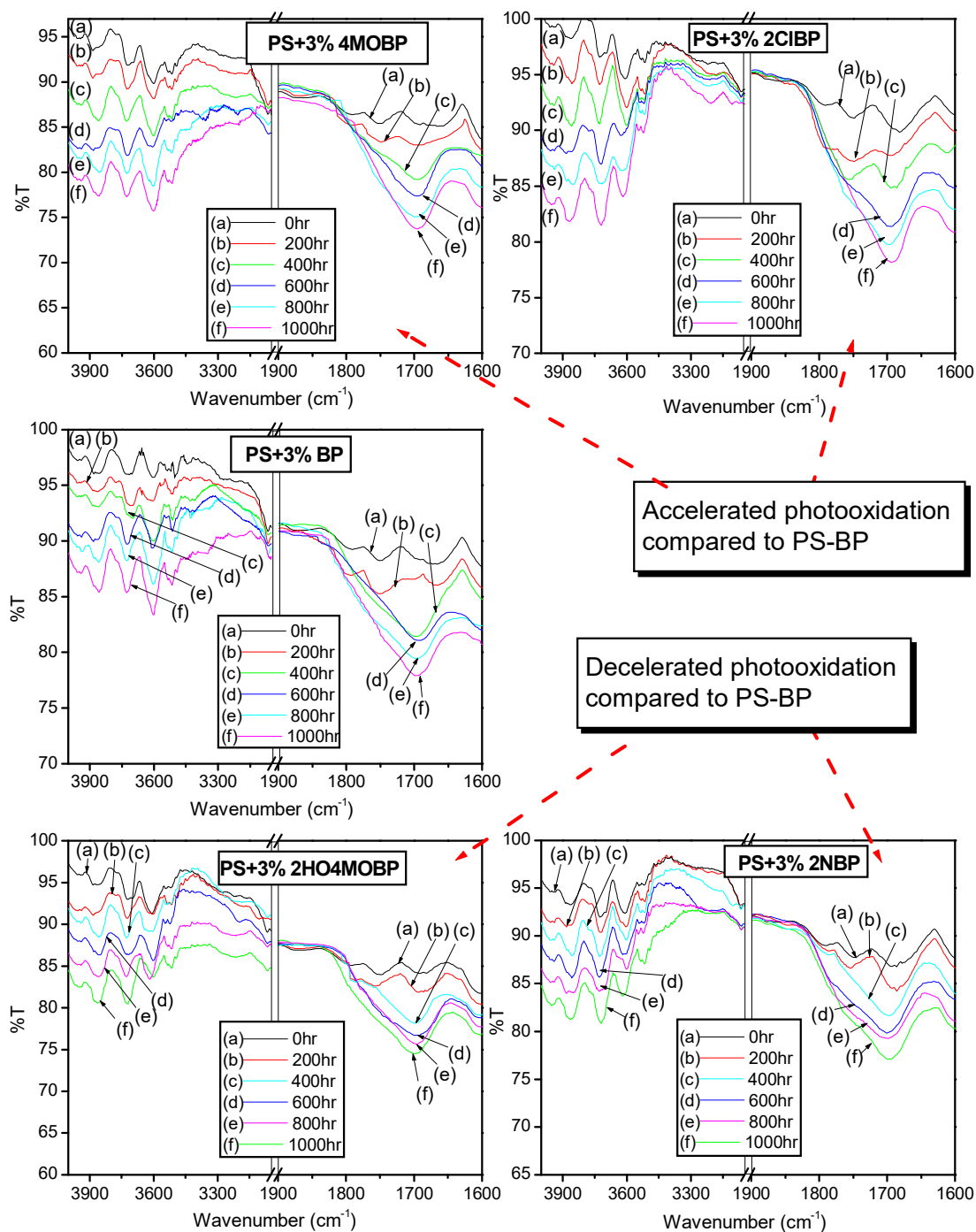
Figure 6.3. *FTIR spectra of PS-benzophenone based photosensitizer composites at different UV exposure time intervals ranging from 0 h to 1000 h.*

Bands observed at around 690, 750, 905 and 1025 cm^{-1} attributing -C-H out of plane bending of the phenyl rings. The peaks at around 1448 cm^{-1} was unaltered upon UV irradiation. This observation supports the fact that the phenyl rings of PS matrix remained unaltered upon UV irradiation of 1000 hours. In addition to this we could also arrive into a possible conclusion that the phenyl rings of benzophenone derivatives used as photosensitizers too remained without much degradation.

Maximum photo-oxidation was observed in PS-4MOBP followed by PS-2ClBP composites and minimum photo-oxidation was observed in PS-2HO4MOBP among the PS-benzophenone based photosensitizer composites. The extent of photo-oxidation of the PS-photosensitizer composites was however lower compared to PS-TiO$_2$ composite.

Observations made from the FTIR spectra after UV irradiation of the PS-dye photosensitizer composites were entirely different from that of PS-benzophenone based photosensitizer composites. Much acceleration in the photodegradation was not observed in PS-MB and PS-MG composites under UV radiation. The increase in the absorption band intensities corresponding to >C=O, -OH, >C=C< etc was not in accordance with UV irradiation time. The random increase in the bands of these functional groups upon UV irradiation suggested the possibility of degradation/ reactions occurring on the organic dyes themselves. Randomness in the FTIR spectra upon UV irradiation made it difficult to draw a conclusion regarding the photo-oxidation on PS chains.

6.2.3. UV- visible diffused reflectance spectroscopy (UV-DRS)

UV-DRS of PS-benzophenone based photosensitizer composites showed that their prominent absorption is in the UV region (Figure 6.4.1). Since PS as well as benzophenone derivatives had their absorption maxima in the UV region, their composites gave rise to broad band between 200-400 nm. The absorptions in the visible region were almost absent. The intensity of absorption bands between 200-400 nm in all the PS-benzophenone based photosensitizers decreased as the time of UV irradiation increased. This observed trend supported photodegradation. In addition to the decrease in the intensity of absorption bands between 200-400 nm, bathochromic shifts were also observed in the composites upon UV irradiation. Maximum decrease

in the band intensity was observed in the PS-4MOBP composites followed by PS-2ClBP and the minimum decrease was observed in PS-2HO4MOBP among PS-benzophenone based composites.
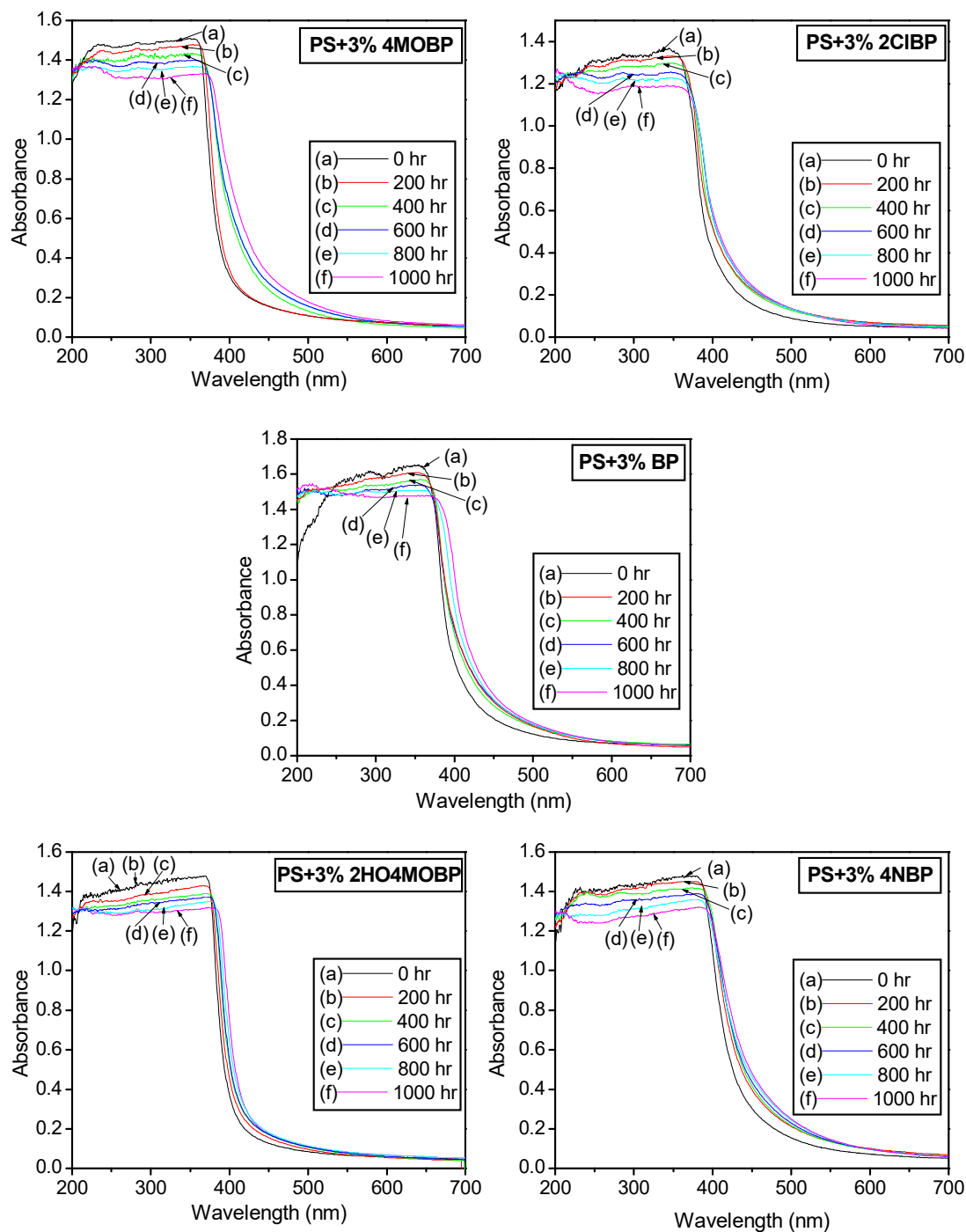
Figure 6.4.1. *UV-DRS of PS-benzophenone based photosensitizer composites at regular UV irradiation time intervals*

UV-DRS of PS-dye photosensitizer composites displayed absorption bands in the UV as well as visible region of the spectra (Figure 6.4.2). PS-MB composites

exhibited absorption band with λ_{max} at 273 nm ($\pi\rightarrow\pi^*$). A shoulder peak was observed at around 322 nm. Another less intense broad band was observed between 368 nm and 442 nm ($n\rightarrow\pi^*$). A broad absorption band starting from 457 nm with λ_{max} at around 600 nm was also observed in the visible region ($n\rightarrow\pi^*$). A sudden change in the shape of absorption bands were noticed even after 200 hours of UV irradiation of PS-MB composite. The shoulder peak observed at around 300 nm was completely masked by a new band between 200 to 350 nm in the UV irradiated composites. Upon UV exposure for 200 hours, the intensity of broad band observed in the visible region with λ_{max} at around 600 nm had decreased considerably. On further UV exposure, the intensity of absorption bands in the UV region decreased with a red shift. The intensity of the broad bands in visible region observed, decreases gradually up to the measured region. The decrease in intensity of bands observed in the visible region could be due to the change in chemical structure or degradation of MB itself. The quinonoid part of the dye might have transformed into benzenoid structure as a result of UV irradiation leading to its decolouration. The decrease in the intensity of bands observed in the UV region could be due to the degradation of PS as well as MB.
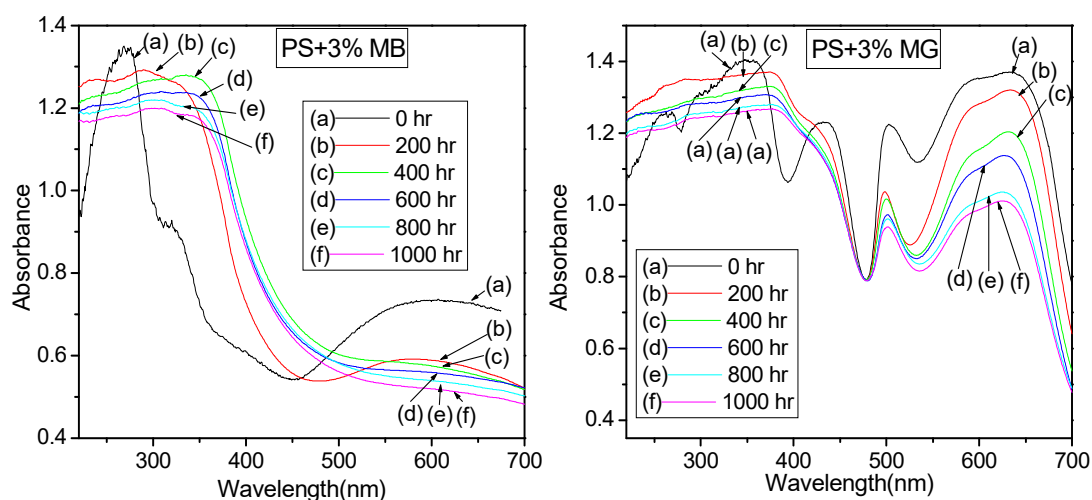
Figure 6.4.2. UV-DRS of PS- dye composites at regular UV irradiation time intervals

The absorption bands of PS-MG composites (Figure 6.4.2) were observed at 263 nm and 348 nm (highest intensity) with a shoulder peak at 303 nm ($\pi\rightarrow\pi^*$) in the UV region. Another band extended from UV region to visible region having λ_{max} at 433 nm ($n\rightarrow\pi^*$). The bands observed in the visible region at 502 nm and 634 nm (broad high intense band) with a shoulder peak at 594 nm were of high intensity. UV irradiation of PS-MG composites resulted in rearrangement of peak positions and

intensities. As observed in the case of PS-MB composites, the bands at the UV region of PS-MG composites too transformed into broader bands between 200-400 nm masking the peak at 263 nm upon UV irradiation. The band at 433 nm remained as shoulder of the broad band between 200-400 nm even after UV irradiation. A decrease in the intensity of absorption bands in the UV region of PS-MG composites were observed upon UV irradiation. This could be due to the degradation of PS and MG. Decrease in the intensity of the bands in the visible region was also observed upon UV irradiation. This could be due to the degradation/ structural change of MG dye on UV irradiation.

6.2.4. Mechanical properties

The mechanical (flexural and tensile) properties of non-irradiated PS-benzophenone based photosensitizer and PS-dye composites almost looked similar except for a lower value observed in PS-MG composite compared to others (Figure 6.5.1). This observed decrease in the mechanical properties could be due to small aggregation of MG formed within the PS composites affecting its uniform dispersion up to an extent.
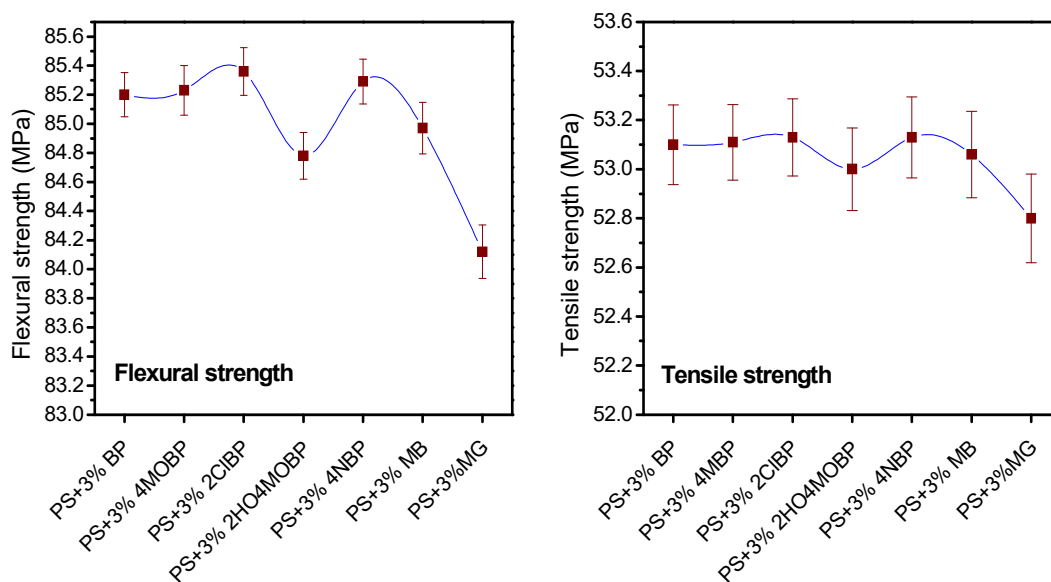
Figure 6.5.1. *Flexural (A) and tensile (B) strengths of PS-benzophenone based photosensitizer and PS-dye composites before UV irradiation-a comparison*

Plots of mechanical properties of PS-benzophenone based and PS-dye composites with respect to UV irradiation of 0, 400 and 1000 hours are presented in figure 6.5.2.

Out of the PS-benzophenone based photosensitizer composites, PS-3% 4MOBP (which exhibited maximum degradation) and PS-3% 2HO4MOBP (which exhibited minimum degradation) were chosen for mechanical testing. The mechanical properties of PS-3% MG and PS-3% MB were also tested. Figure 6.5.2 shows that the mechanical properties of all the composites decreased upon UV irradiation. PS-4MOBP composite underwent more mechanical deterioration compared to PS-2HO4MOBP as expected. The mechanical properties of PS-dye composites were not as expected. Even though we have noticed that PS-MB composite underwent better photodegradation compared to PS-MG composite, a decrease in the flexural and tensile strength of PS-MB was less compared to PS-MG. The possible reason for such an anomalous trend could be the poor dispersion of MG compared to MB in the PS matrix. The slight aggregation of MG along the PS matrix might have weakened the mechanical strengths of PS-MG composite.
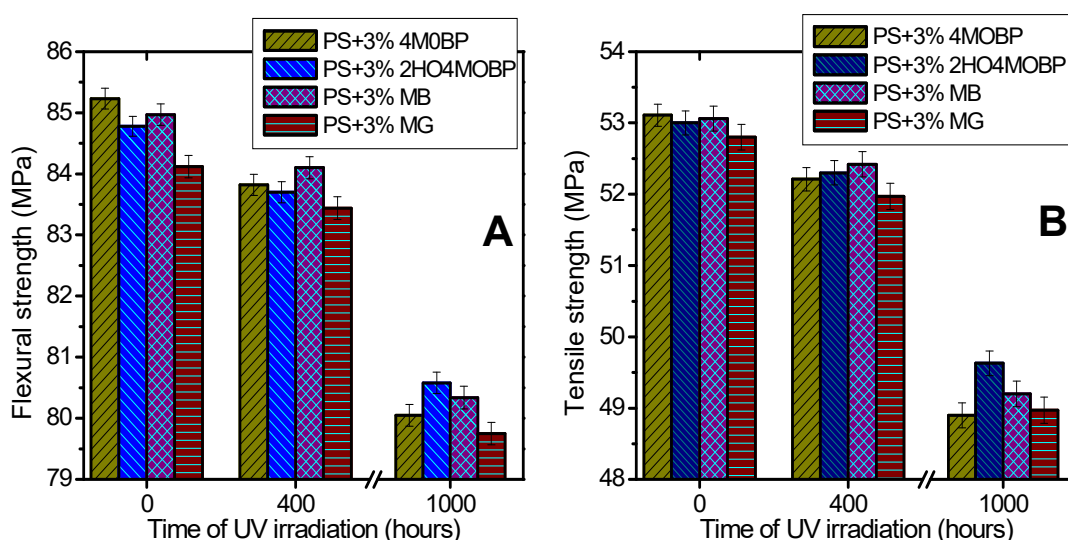
Figure 6.5.2. *Flexural (A) and tensile (B) strengths of PS-benzophenone based and PS-dye composites exposed to UV radiation for 0,400 and 1000 h*

6.2.5. Electrical properties

Breakdown voltage (BDV) of PS-3% 4MOBP and PS-3% 2ClBP which underwent better photodegradation among the PS-benzophenone based photosensitizer composites and PS-3% MB which underwent better degradation among the PS-dye composites were measured at UV irradiation time intervals 0, 400 and 1000 hours (Figure 6.6.1). A decrease in the BDV of the composites with respect to UV irradiation time was observed. The extent of decrease in the values of BDV

was found to be better for PS-3% 2ClBP compared to that of PS-3% 4MOBP composite even though the later underwent better photodegradation compared to PS-3% 2ClBP. This observed decrease in BDV upon photodegradation could be due to the formation of more current conducting charge carriers in PS-3% 2ClBP compared to PS-3% 4MOBP on UV exposure.
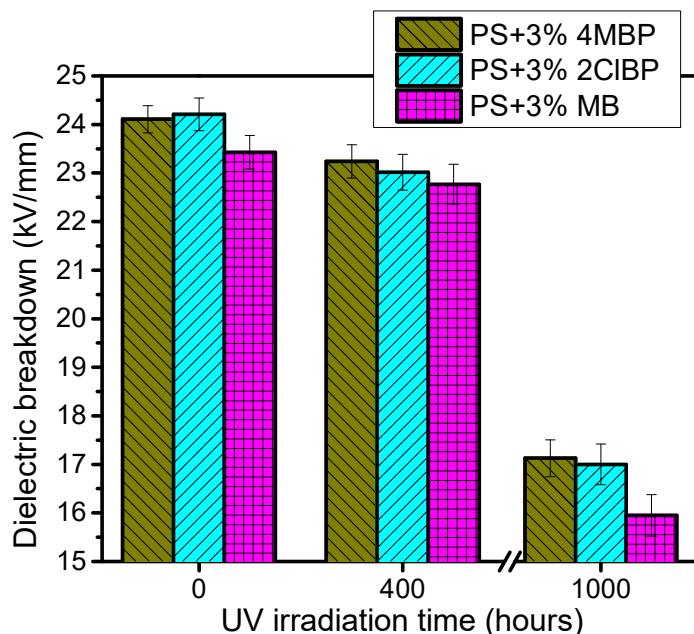
Figure 6.6.1. *Dielectric breakdown (breakdown voltage) of PS-4MOBP, PS-2ClBP and PS-MB composites with varying UV irradiation time*

Dielectric permittivity (ε_r) of PS-3% 4MOBP, PS-3% 2ClBP among the PS-photosensitizer composites (Figure 6.6.2) and PS-3% MB and PS-3% MG among PS-dye composites (Figure 6.6.3) were measured at UV irradiation time intervals of 0, 400 and 1000 hours. The ε_r of all the composites increased as the time of UV irradiation is increased. Formation of charged polar species on UV exposure of the samples as a result of photodegradation was hence evident. PS-3% 2ClBP underwent better increase in ε_r compared to PS-3% 4MOBP as the time of UV irradiation increased. This shows that better charged dipoles may be found in UV irradiated PS-3% 2ClBP compared to that of PS-3% 4MOBP. For the PS-dye system, PS-3% MB exhibited better decrease in the value of ε_r compared to PS-3% MG upon UV irradiation.
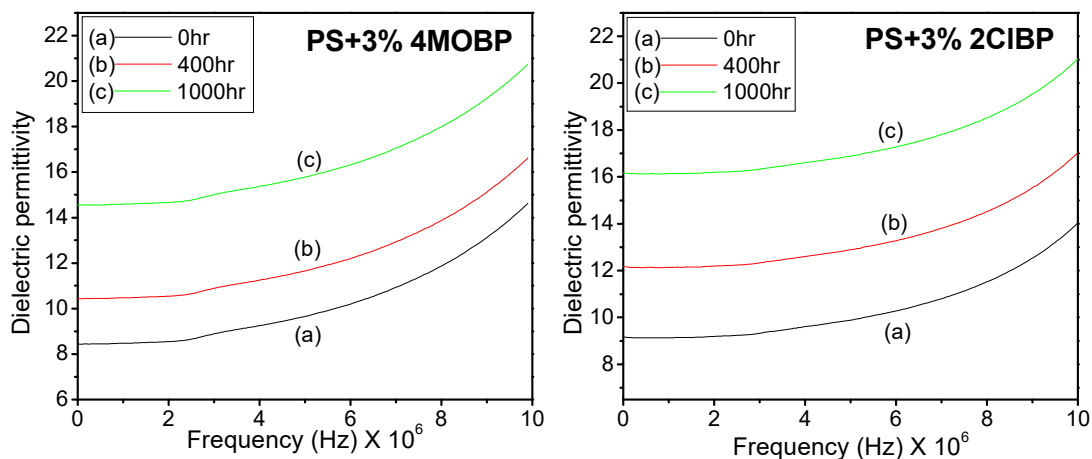
Figure 6.6.2. *Dielectric permittivity of PS-3% 4MOBP and PS-3% 2ClBP composites at UV irradiation intervals of 0 h, 400 h and 1000 h.*
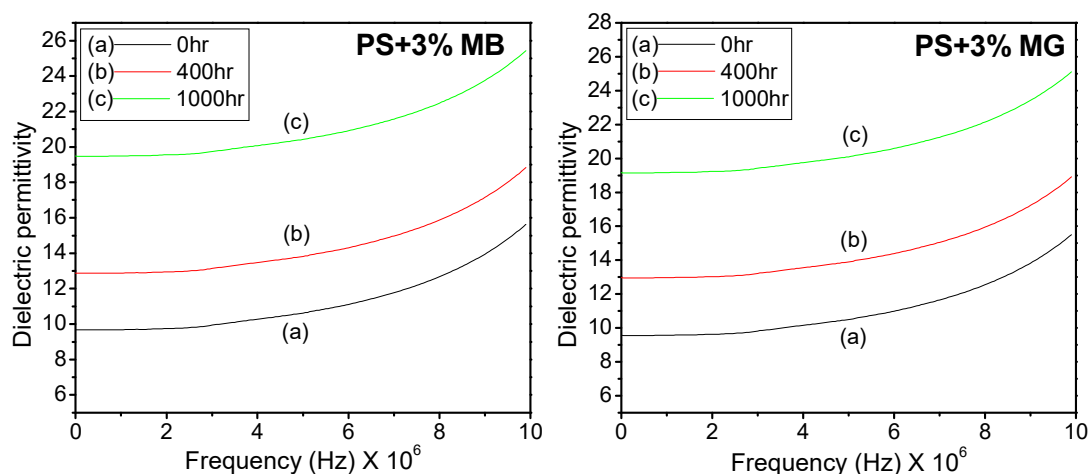
Figure 6.6.3*. Dielectric permittivity of PS-3% MB and PS-3% MG composites at UV irradiation intervals of 0 h, 400 h and 1000 h.*

6.2.6. Thermogravimetric Analysis (TGA)

The TGA of PS-3% 4MOBP (Figure 6.7 A) and PS-3% MB (Figure 6.7 B) which underwent maximum photodegradation among the PS-benzophenone based photosensitizer and PS-dye photosensitizer composites respectively were conducted under nitrogen atmosphere. The thermogram of both the composites looked alike with two stages of weight losses. The first stage of weight loss attributed to the water desorption process and the second stage of weight loss represents the decomposition of the composites. The decomposition temperature range for PS-3% 4MOBP and PS-3% MB was 264-404°C and 269-408°C respectively. In both the composites the

decomposition shifted to lower temperature range after UV irradiation. The decomposition temperature range for PS-3% 4MOBP was shifted to 252-392°C and that of PS-3% MB to 260-399°C upon UV irradiation of 1000 hours. The decrease in the thermal property of the composites as a consequence of photodegradation on UV exposure was hence concluded from this observation. Sharp decrease in the decomposition peaks terminated at around 404°C (weight percent=4.16%) for PS-3% 4MOBP beyond which the decrease in weight percentage was too slow. Similar observation was made for PS-3% MB beyond 408°C (weight percent=4.2%). The termination point of steep decomposition curve of both the composites shifted to lower values upon UV exposure of 1000 hours.
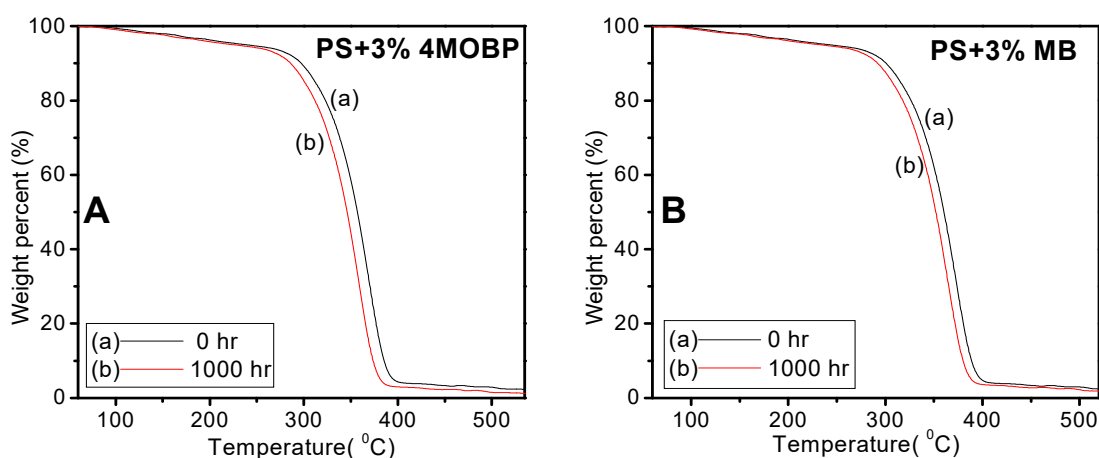
Figure 6.7. *TGA thermogram of PS-3% 4MOBP (A) and PS-3% MB (B) composites before and after UV irradiation of 1000 h*

6.2.7. Weight loss
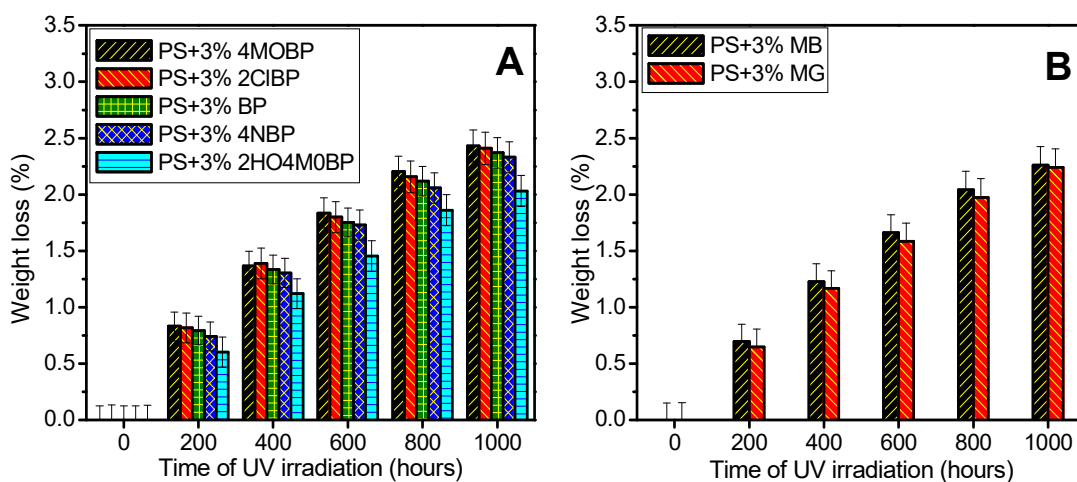
Figure 6.8. *Comparison of weight loss percentages of PS-3% benzophenone based photosensitizer (A) and PS-3% dye (B) composites at regular intervals of UV irradiation*

Weight loss was observed in all the PS-benzophenone based photosensitizer composites (Figure 6.8 A) as well as PS-dye composites (Figure 6.8 B) as the time of UV irradiation of the samples increased. The weight loss percentage of the PS-benzophenone based composites followed the order:- PS-3% 4MOBP > PS-3% 2ClBP > PS-3% BP > PS-3% 4NBP > PS-3% 2HO4MOBP. The weight loss percentage of PS-dye composites followed the following order: - PS-3% MB> PS-3% MG.

Section:II

Enhanced photocatalytic activity of nano TiO$_2$ coupled benzophenone derivatives and organic dyes for the UV degradation of polystyrene

6.3. Preparation of PS-TiO$_2$ -photosensitizer composites

Three sets of PS-TiO$_2$-benzophenone based photosensitizer composites were prepared as described in chapter 2. In the first set, the mole percentage of benzophenone based photosensitizers were 50% of nano TiO$_2$. In the second set, the mole percentage of TiO$_2$ and benzophenone based photosensitizers were of equal mole percentage. In the third set, nano TiO$_2$ was 50 mole percentage of benzophenone based photosensitizers. All these composites were 3% by weight of PS.

The prepared combinations of PS-TiO$_2$-dye photosensitizer were much different from that of PS-TiO$_2$-benzophenone based photosensitizer composites. In this case, better efficiency among the nano TiO$_2$-dye composites were observed at low mole percentage of the dye. Better degradation efficiency was observed when the mole percentage of dyes was 5% of nano TiO$_2$. This optimisation in the percentage of dyes was done by comparing the photodegradation of PS using nano TiO$_2$-dye composites where the mole percentages of the dyes were varied from 0.5% to 10% of nano TiO$_2$.

The tables below describe in detail, the composition of the PS-TiO$_2$-benzophenone based photosensitizer and PS-TiO$_2$-dye photosensitizer composites prepared in our study for the photodegradation of PS.

Table 6.2.1. *PS-TiO₂-benzophenone based photosensitizer composites*

<table>
<tr><td colspan="3">PS+3% (TiO₂+50% benzophenone based photosensitizer) composites</td></tr>
<tr><td rowspan="6">Set 1</td><td><i>Sl no:</i></td><td><i>Composites</i></td><td><i>Description</i></td></tr>
<tr><td>1</td><td>PS+3% (TiO₂+50% BP)</td><td rowspan="5">All the benzophenone based compounds are 50 mole % of nano TiO₂.
The TiO₂-50% photosensitizer composites are 3 weight % of PS</td></tr>
<tr><td>2</td><td>PS+3% (TiO₂+50% 2HO4MOBP)</td></tr>
<tr><td>3</td><td>PS+3% (TiO₂+50% 4MOBP)</td></tr>
<tr><td>4</td><td>PS+3% (TiO₂+50% 2ClBP)</td></tr>
<tr><td>5</td><td>PS+3% (TiO₂+50% 4NOBP)</td></tr>
<tr><td colspan="3">PS+3% (TiO₂+benzophenone based photosensitizer) composites</td></tr>
<tr><td rowspan="6">Set 2</td><td><i>Sl no</i></td><td><i>Composites</i></td><td><i>Description</i></td></tr>
<tr><td>1</td><td>PS+3% (TiO₂+BP)</td><td rowspan="5">All the benzophenone based compounds and nano TiO₂ are of equal mole %
The TiO₂- photosensitizer composites are 3 weight % of PS</td></tr>
<tr><td>2</td><td>PS+3% (TiO₂+2HO4MOBP)</td></tr>
<tr><td>3</td><td>PS+3% (TiO₂+4MOBP)</td></tr>
<tr><td>4</td><td>PS+3% (TiO₂+2ClBP)</td></tr>
<tr><td>5</td><td>PS+3% (TiO₂+4NOBP)</td></tr>
<tr><td colspan="3">PS+3% (Benzophenone based photosensitizer + 50% TiO₂) composites</td></tr>
<tr><td rowspan="6">Set 3</td><td><i>Sl no</i></td><td><i>Composites</i></td><td><i>Description</i></td></tr>
<tr><td>1</td><td>PS+3% (BP + 50% TiO₂)</td><td rowspan="5">Nano TiO₂ was 50 mole % of benzophenone based compounds
The photosensitizer-50% TiO₂ composites are 3 weight % of PS</td></tr>
<tr><td>2</td><td>PS+3% (2HO4MOBP+ 50% TiO₂)</td></tr>
<tr><td>3</td><td>PS+3% (4MOBP+ 50% TiO₂)</td></tr>
<tr><td>4</td><td>PS+3% (2ClBP+ 50% TiO₂)</td></tr>
<tr><td>5</td><td>PS+3% (4NOBP+ 50% TiO₂)</td></tr>
</table>

Table 6.2.2. *PS-TiO₂-dye photosensitizer compositse*

<table>
<tr><td></td><td><i>Sl no</i></td><td><i>Composites</i></td><td><i>Description</i></td></tr>
<tr><td rowspan="2">Set 1</td><td>1</td><td>PS+3% (TiO₂ + 0.5% MB)</td><td rowspan="2">The dyes are 0.5 mole % of TiO₂
The TiO₂-0.5% dye is 3 weight % of PS</td></tr>
<tr><td>2</td><td>PS+3% (TiO₂ + 0.5% MG)</td></tr>
<tr><td rowspan="2">Set 2</td><td>1</td><td>PS+3% (TiO₂ + 1% MB)</td><td rowspan="2">The dyes are 1 mole % of TiO₂
The TiO₂-1% dye is 3 weight % of PS</td></tr>
<tr><td>2</td><td>PS+3% (TiO₂ + 1% MG)</td></tr>
<tr><td rowspan="2">Set 3</td><td>1</td><td>PS+3% (TiO₂ + 2% MB)</td><td rowspan="2">The dyes are 2 mole % of TiO₂
The TiO₂-2% dye is 3 weight % of PS</td></tr>
<tr><td>2</td><td>PS+3% (TiO₂ + 2% MG)</td></tr>
<tr><td rowspan="2">Set 4</td><td>1</td><td>PS+3% (TiO₂ + 3% MB)</td><td rowspan="2">The dyes are 3 mole % of TiO₂
The TiO₂-3% dye is 3 weight % of PS</td></tr>
<tr><td>2</td><td>PS+3% (TiO₂ + 3% MG)</td></tr>
</table>

Set 5	1	PS+3% (TiO$_2$ + 5% MB)	• The dyes are 5 mole % of TiO$_2$
	2	PS+3% (TiO$_2$ + 5% MG)	• The TiO$_2$-5% dye is 3 weight % of PS
Set 6	1	PS+3% (TiO$_2$ + 7% MB)	• The dyes are 7 mole % of TiO$_2$
	2	PS+3% (TiO$_2$ + 7% MG)	• The TiO$_2$-7% dye is 3 weight % of PS
Set 7	1	PS+3% (TiO$_2$ + 10% MB)	• The dyes are 10 mole % of TiO$_2$
	2	PS+3% (TiO$_2$ + 10% MG)	• The TiO$_2$-10% dye is 3 weight % of PS

For the preparation of PS-TiO$_2$-photosensitizer composites, particular mole percentage of the photosensitizers with respect to nano TiO$_2$ was weighed. Nano TiO$_2$ and the weighed photosensitizers were mixed. 3 weight percentage of the TiO$_2$-photosensitizer mixture was loaded into PS as described in chapter 2.

6.4. Results and Discussion

Out of the three sets of PS-TiO$_2$-benzophenone based photosensitizer, those with equal percentages of TiO$_2$-benzophenone based photosensitizer combination (table 6.2.1, set 2) showed enhanced degradation as evident from various monitoring techniques used. The composites in which the percentage of TiO$_2$ was only 50% of benzophenone based photosensitizers (table 6.2.1, set 3) showed comparatively lesser degradation. In the case of TiO$_2$-dye system, entirely different observations were observed. Enhancement in the photocatalytic activity was observed in nano TiO$_2$-dye composites as expected. TiO$_2$-dye composites were efficient only at lower dye percentages for the effective photodegradation of PS. Their efficiency increased upto 5 mole % dyes coupled with TiO$_2$ (we have studied the photodegradation of PS using various TiO$_2$-dye combinations having 0.5, 1, 2, 3, 5, 7 and 10 mole % dyes coupled with nano TiO$_2$). When the percentage of the dyes coupled with nano TiO$_2$ exceeded 5%, the photocatalytic efficiency of the composites for PS degradation gets reduced. The observations and conclusions made from various analytical techniques are discussed below.

6.4.1. Gel Permeation Chromatography (GPC)

A better decrease in $\overline{M}_w$ and $\overline{M}_n$ was observed in PS-TiO$_2$-benzophenone based photosensitizer composites as well as PS-TiO$_2$-dye composites compared to the PS-benzophenone based photosensitizer and PS-dye composites upon UV irradiation. The decrease in average molecular weights was predominant in PS-(TiO$_2$-4MOBP)

composites followed by PS-(TiO$_2$-2ClBP) (Figure 6.9.1). Among the PS-TiO$_2$-organic dye systems, PS-(TiO$_2$-5% MB) showed maximum decrease in the value of $\overline{M}_w$ and $\overline{M}_n$ compared to PS-(TiO$_2$-5% MG) (Figure 6.9.2).
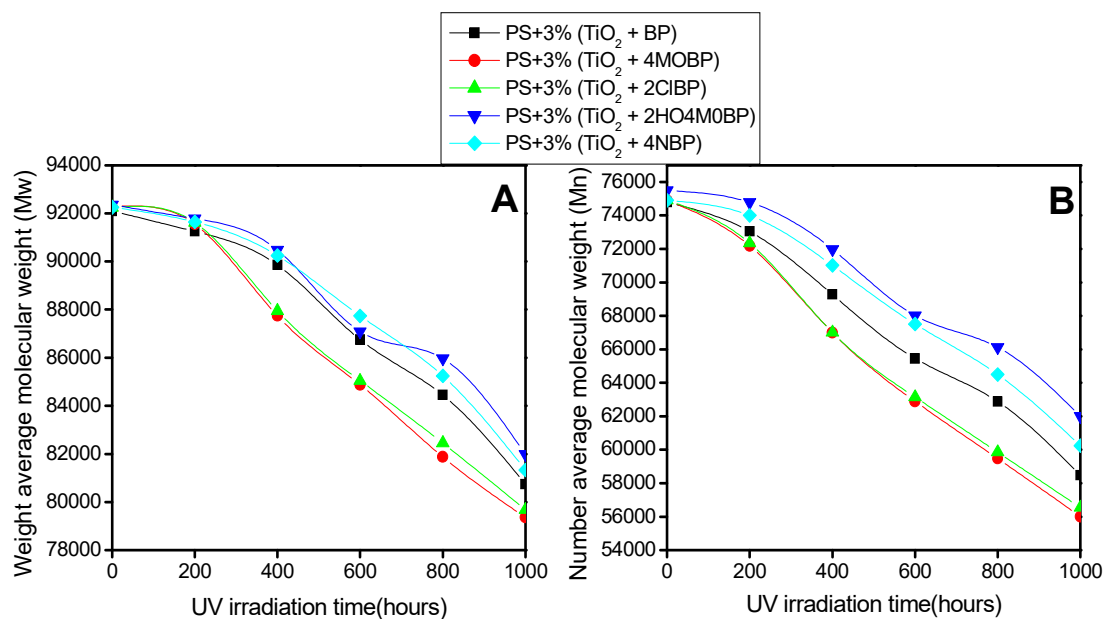
Figure 6.9.1. *A) Weight average ($\overline{M}_w$) and B) number average ($\overline{M}_n$) molecular weights of PS-TiO$_2$- benzophenone based photosensitizer composites under different UV irradiation time*
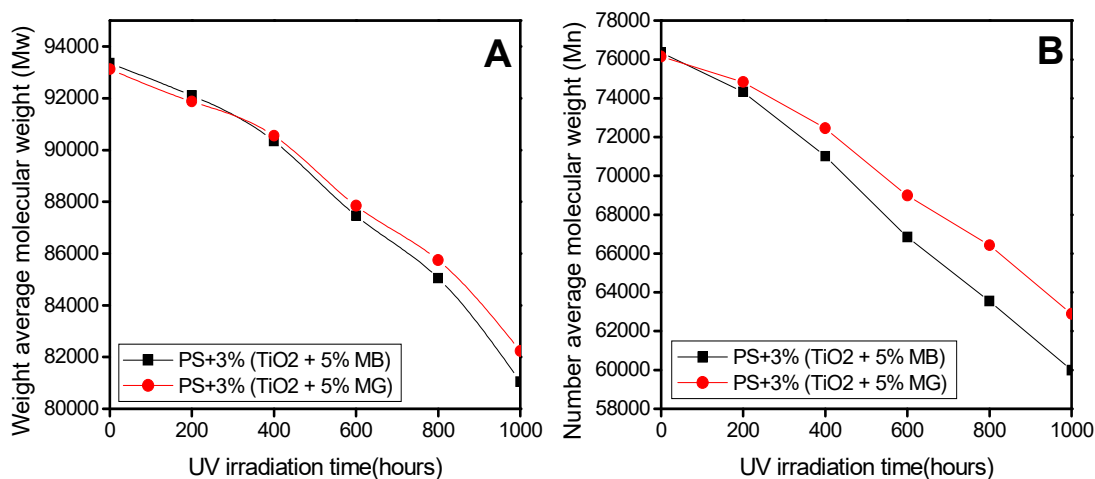
Figure 6.9.2. *A) Weight average ($\overline{M}_w$) and B) number average ($\overline{M}_n$) molecular weights of PS-TiO$_2$-dye composites under different UV irradiation time*

The plot of number of chain scission per molecule (S) and number of scission events per gram (N$_t$) versus time of UV irradiation of the composites clearly help us to visualize the variation in chain scission of the composites. It was clear that the polymer chain cleavage occurred more effectively in the PS-(TiO$_2$-4MOBP) followed

by PS-(TiO$_2$-2ClBP) among the PS-TiO$_2$-benzophenone based photosensitizer composites (Figure 6.9.3). The lowest extent of chain scission upon UV irradiation was found to be in PS-(TiO$_2$-2HO4MOBP) composites. PS-TiO$_2$-MB underwent better chain scission compared to PS-(TiO$_2$-MG) among the PS-TiO$_2$-dye composites (Figure 6.9.4).
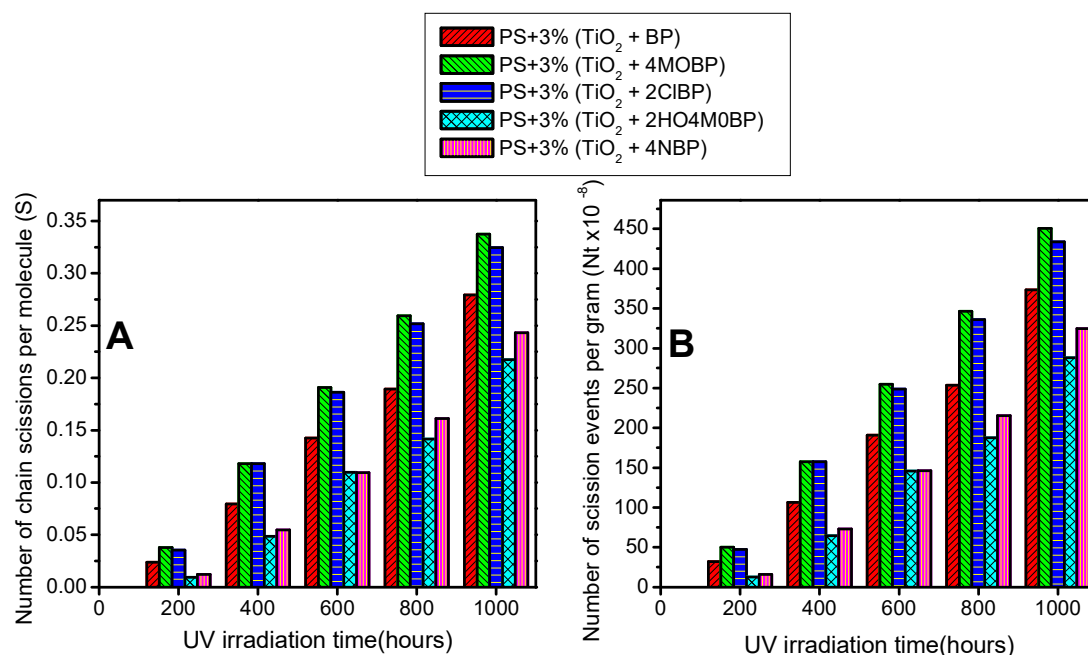
Figure 6.9.3. A) Number of chain scissions per molecule (S) and B) number of scission events per gram (N$_t$) of PS-TiO$_2$-benzophenone based photosensitizer composites under different UV irradiation
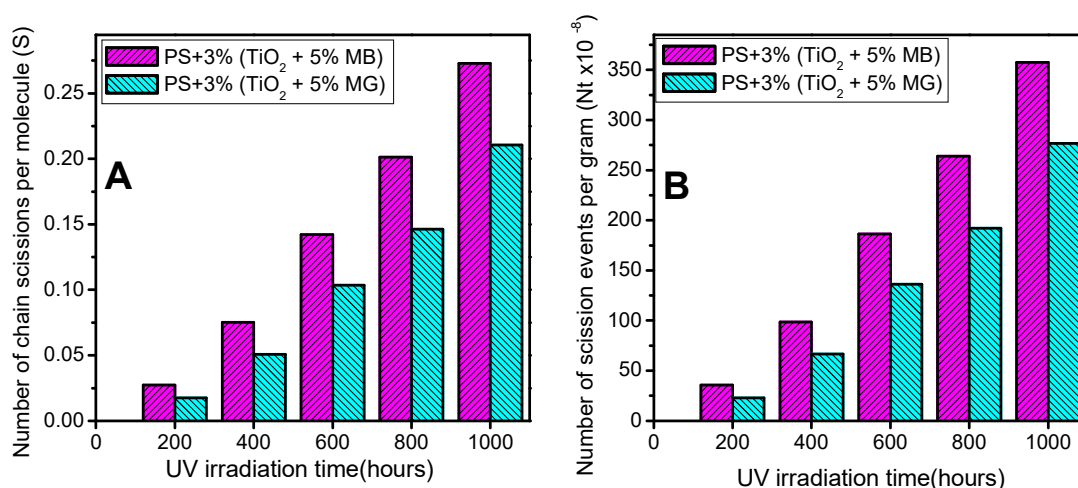
Figure 6.9.4. A) Number of chain scissions per molecule (S) and B) number of scission events per gram (N$_t$) of PS-TiO$_2$-dye composites under different UV irradiation

The polydispersity index (PDI) increased for all the composites with respect to UV irradiation time. The increase in randomness of chain scission (increase in PDI) was higher for the composites which underwent maximum chain scission upon UV irradiation (Figure 6.9.5). Among the PS-TiO$_2$-benzophenone based photosensitizer composites, we could see that the PDI of PS-(TiO$_2$-4MOBP) and PS-(TiO$_2$-2ClBP) have highest values at each UV irradiation intervals. Among the dye composites, the increase in PDI of PS-(TiO$_2$-5%MB) composites were better compared to PS-(TiO$_2$-5%MG).
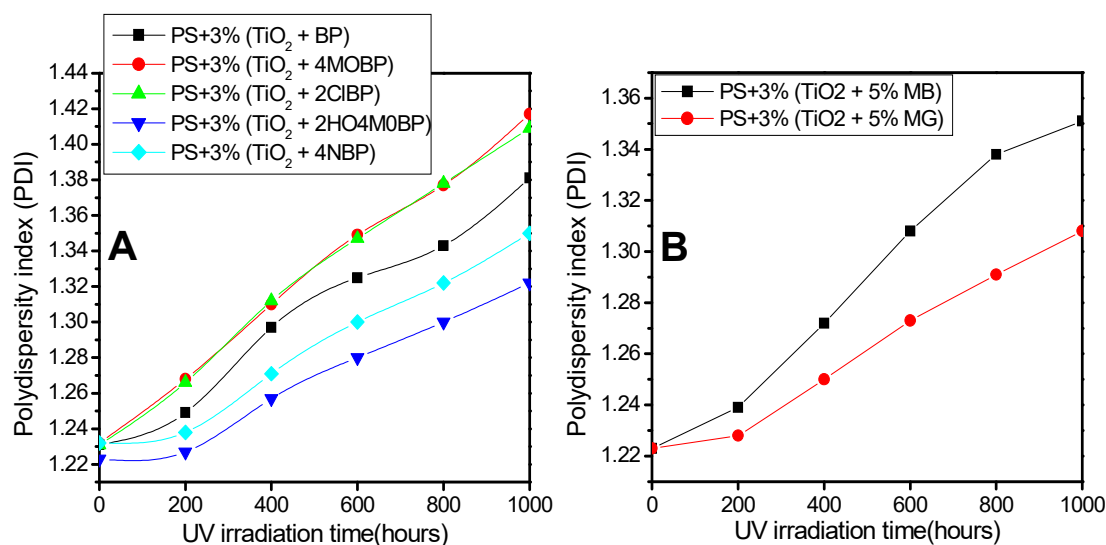
Figure 6.9.5. Polydispersity index (PDI) of PS –TiO$_2$- benzophenone based photosensitizer and PS-organic dye composite under various UV irradiation times.

6.4.2. FTIR spectroscopy

An appreciable increase in the intensities of absorption bands corresponding to >C=O, -OH/-OOH, >C=C< and conjugated double bonds were observed from the FTIR spectra of PS-TiO$_2$-benzophenone based photosensitizers upon UV irradiation (Figure 6.10.1). The extent of photo-oxidation of PS-TiO$_2$-photosensitizer composites was higher compared to PS-benzophenone based photosensitizer as well as PS-TiO$_2$ composites. PS-(TiO$_2$-4MOBP) composite underwent maximum photo-oxidation among the PS-TiO$_2$-benzophenone based photosensitizers followed by PS-(TiO$_2$-2ClBP). PS-(TiO$_2$-2HO4MOBP) composite underwent minimum photo-oxidation as expected.
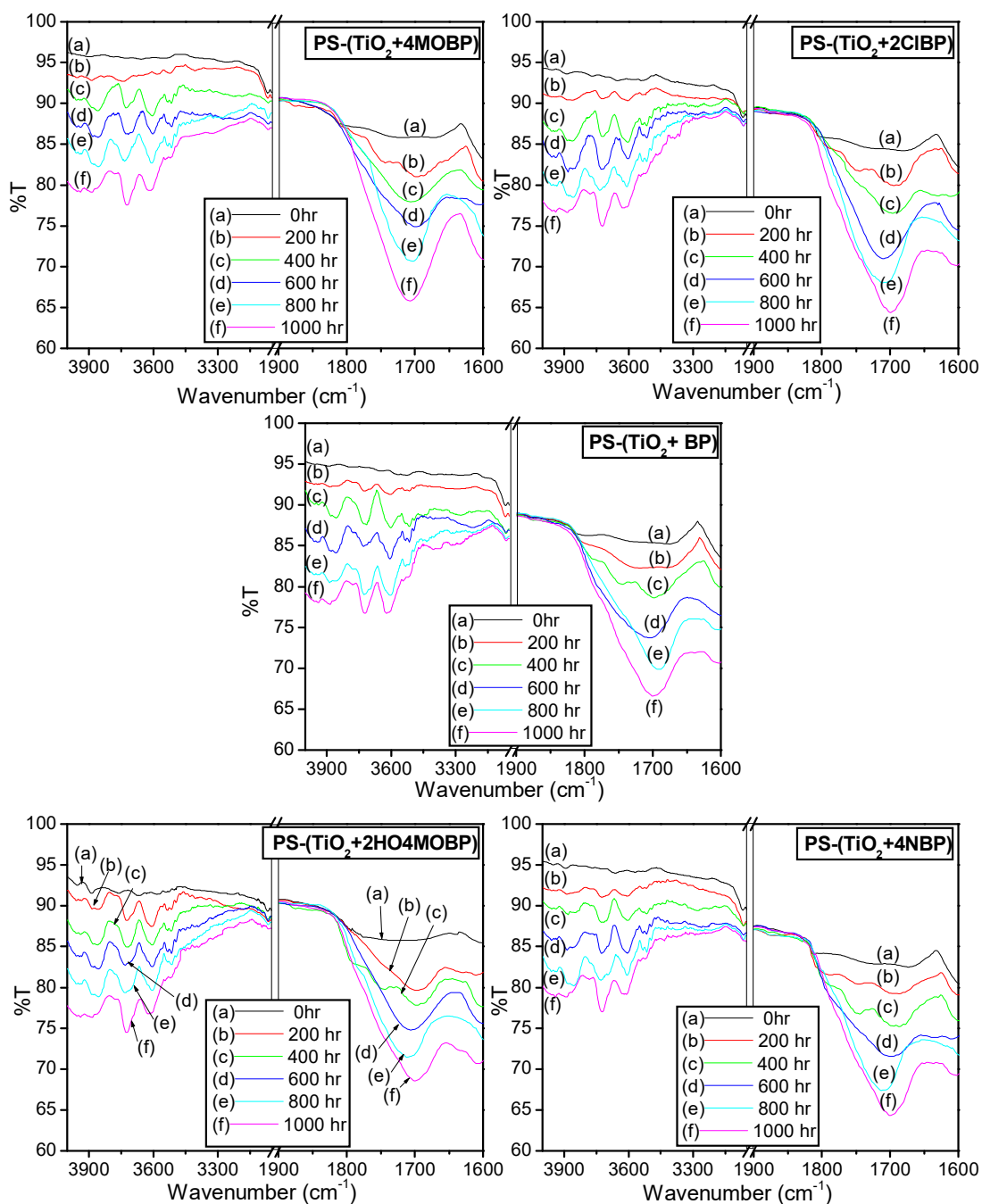
Figure 6.10.1. *FTIR spectra of PS-TiO₂-benzophenone based photosensitizer composites at different UV exposure time intervals ranging from 0 h to 1000 h.*

We have already seen that for PS-benzophenone based photosensitizer composites, the increase in intensity of absorption bands corresponding to >C=C< stretching vibrations (1700-1650 cm^{-1}) were more prominent than that of >C=O stretching bands (1740 -1700 cm^{-1}) upon UV irradiation. For PS-TiO₂ composites, the observation was vice versa where the increase in the bands corresponding to >C=O was better than that of >C=C< stretching. In the case of PS-TiO₂-benzophenone based

photosensitizer composites, the extent of increase in the bands corresponding to >C=O as well as >C=C< was equally more appreciable compared to PS-TiO$_2$ and PS-benzophenone based photosensitizer composites. The contribution of nano TiO$_2$ and benzophenone based photosensitizers for the photodegradation of PS was hence clear. The increase in the extent of photo-oxidation of these composites compared to PS-TiO$_2$ as well as PS-benzophenone based photosensitizers also suggests synergic effect of TiO$_2$ and benzophenone based photosensitizers.

An amazing observation was revealed from the FTIR spectra of PS-TiO$_2$-dye composites upon UV irradiation (Figure 6.10.2). The photocatalytic activity of nano TiO$_2$ coupled with organic dyes (MB and MG) increased to an appreciable extent for the photo-oxidation of PS. As already discussed, MG and MB alone were not efficient photocatalysts for the photodegradation of PS. TiO$_2$ coupled with these dyes acts as a good photocatalyst for PS degradation. Also, it was observed that the extent of photo-oxidation of the PS-TiO$_2$-dye composites were higher than that of PS-TiO$_2$ composites. This reveals the fact that MG and MB enhanced the photocatalytic activity of nano TiO$_2$ for the photodegradation of PS. It was also found that the photo-oxidation of PS-MB composite was higher than that of PS-MG composite.
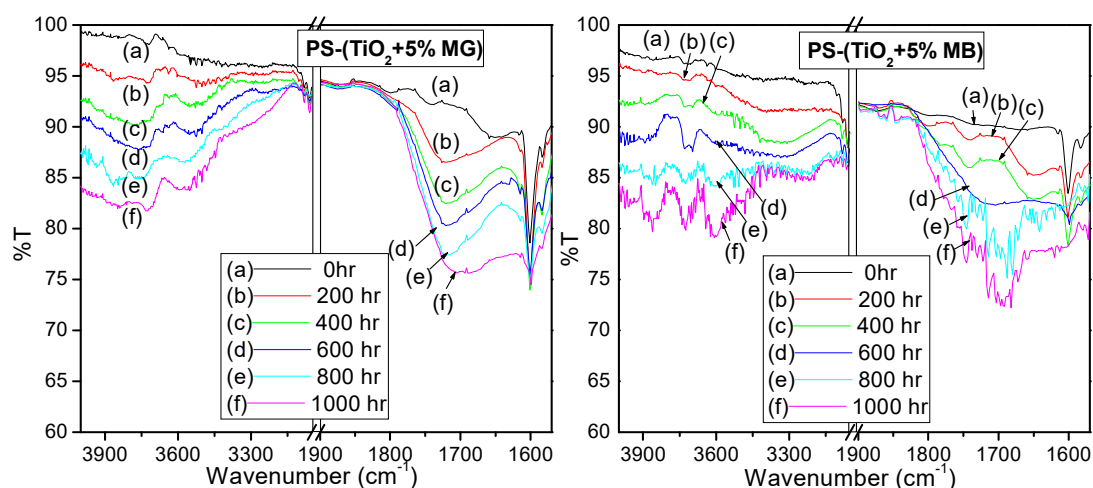
Figure 6.10.2. FTIR spectra of PS-TiO$_2$- benzophenone based photosensitizer composites at different UV exposure time intervals ranging from 0 h to 1000 h.

6.4.3. UV-visible diffused reflectance spectroscopy (UV-DRS)

Nano TiO$_2$-photosensitizer incorporated into PS matrix resulted in an appreciable decrease in the absorption bands observed in the UV region of the composites as observed in UV-DRS (Figure 6.11.1). The decrease in absorption bands suggests

photodegradation of PS-TiO$_2$-benzophenone based photosensitizer composites were higher than that of PS-benzophenone based photosensitizer and PS-TiO$_2$ composites discussed earlier. PS-TiO$_2$-4MOBP followed by PS-TiO$_2$-2ClBP composites underwent maximum decrease in the absorption bands upon UV irradiation. Minimum decrease in the absorption bands upon UV irradiation was observed for PS-TiO$_2$-2HO4MOBP.
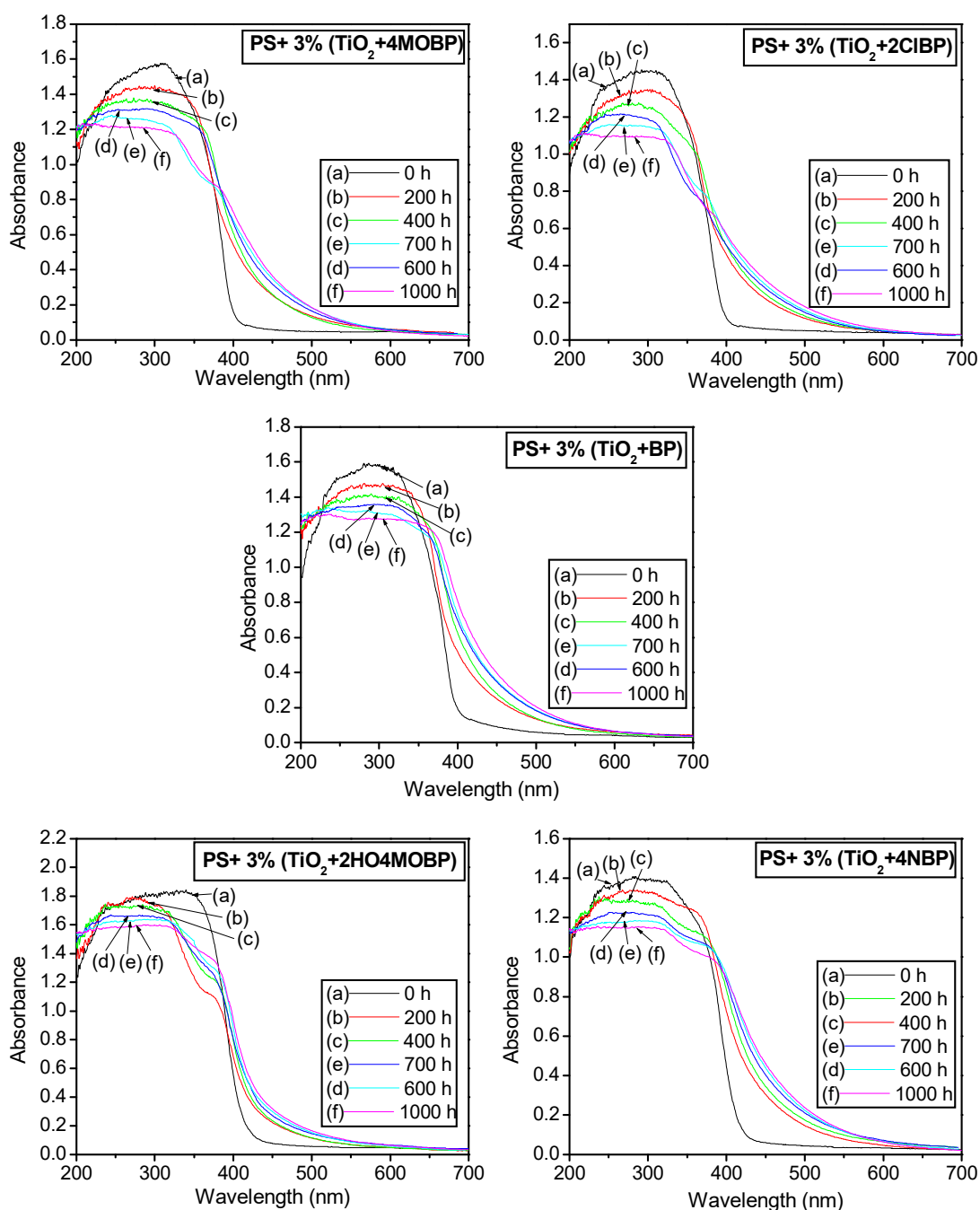
Figure 6.11.1. *UV-DRS of PS-TiO$_2$-benzophenone based photosensitizer composites with UV irradiation time intervals*

UV-DRS of PS-TiO$_2$-MB (Figure 6.11.2) composite looked different from that of PS-MB. The multiple bands observed in the UV region of the spectra for PS-MB was reconstructed into a single band resembling the UV region of the spectra of PS-TiO$_2$. Multiple bands observed in the visible region of PS-MB were also reconstructed entirely into a long tale like band in PS-TiO$_2$-MB composite extending to the far-red region. The interaction of nano TiO$_2$ with MB might have resulted in this peak tailing. The UV region of the UV-DRS of PS-TiO$_2$-MG on the other hand was similar to that of PS-MG composite (Figure 6.11.2). The visible region of PS-TiO$_2$-MG is reconstructed into a single broad band compared to the multiple peaks of PS-MG composites discussed above. The changes observed in the visible region of the spectra might have been an outcome of the interaction between nano TiO$_2$ and MG.

The increase in degradation efficiency of PS-TiO$_2$-BP, PS-TiO$_2$-4MOBP, PS-TiO$_2$-2HO4MOBP, PS-TiO$_2$-2ClBP and PS-TiO$_2$-4NBP with respect to pristine PS were 9.87, 13.41, 3.53, 14.53 and 8.25 respectively.
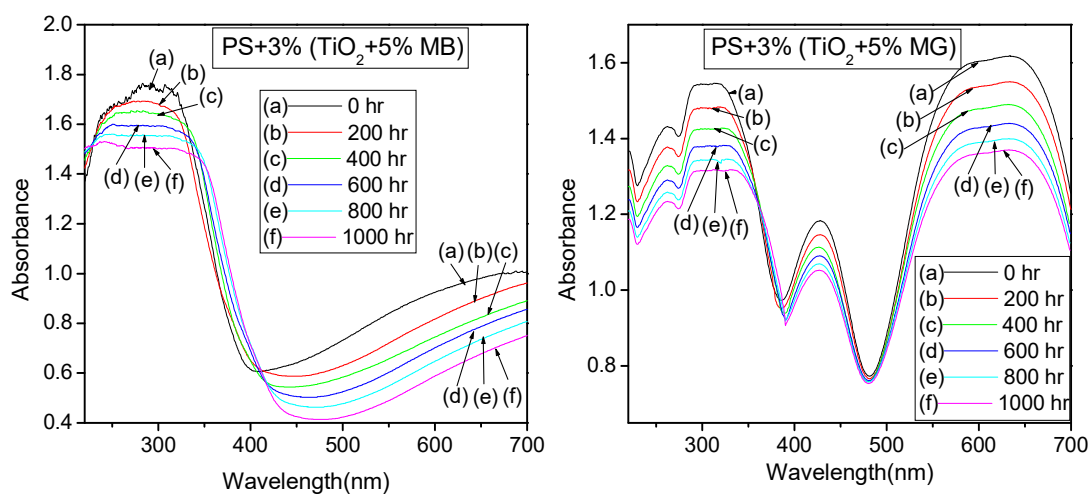
Figure 6.11.2*. UV-DRS of PS-TiO$_2$-dye composites at regular UV irradiation time intervals*

A considerable decrease in the absorption bands were observed in PS-TiO$_2$-MB as well as PS-TiO$_2$-MG composites upon UV irradiation. Slight bathochromic shift was also noticed for the bands in the UV region of the composites upon UV irradiation. The decrease in the absorption bands in the visible region supports photodegradation of PS as well as the organic dye. It could however be seen that the degradation of dye in the PS-TiO$_2$-dye composites was not as severe as that observed in PS-dye composites. The decrease in the absorption band intensities upon UV irradiation

observed in PS-TiO$_2$-dyes was higher compared to that of PS-dye as well as PS-TiO$_2$ composites. This observation highlights the fact that the organic dyes (MG and MB) act as a good photosensitizer by increasing the photocatalytic activity of nano TiO$_2$ for the photodegradation of PS under UV radiation. It was also noticed that the decrease in band intensities were higher for PS-TiO$_2$-MB composites compared to that of PS-TiO$_2$-MG composites. The increase in degradation efficiency of PS-(TiO$_2$-5%MB), PS-(TiO$_2$-5%MG) with respect to pristine PS were 5.13 and 5.25 respectively.

6.4.4. Mechanical properties
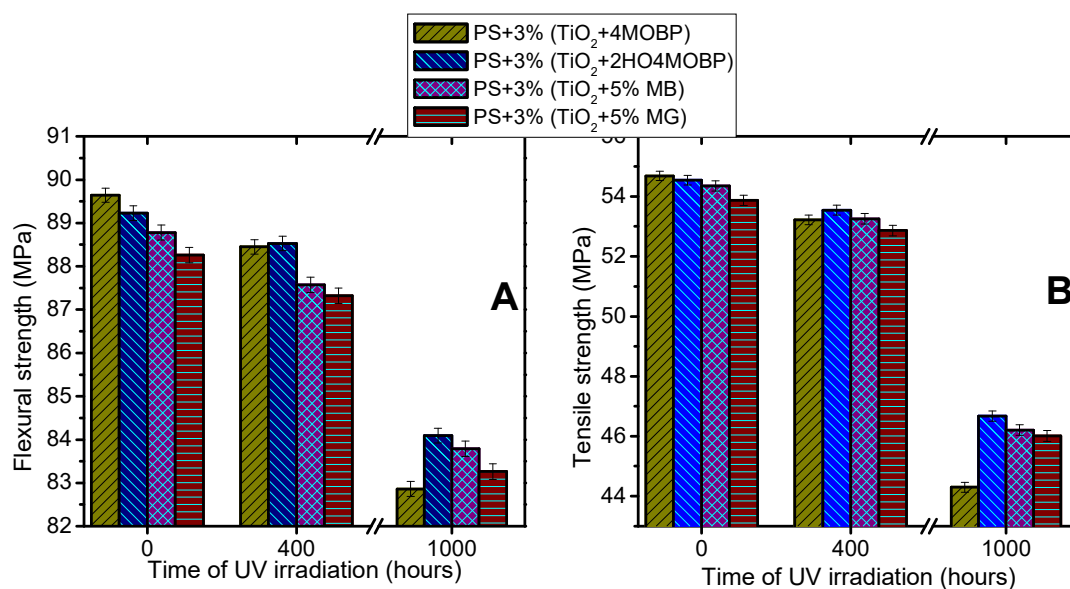
Figure 6.12. *Flexural (A) and tensile (B) strengths of PS-TiO$_2$-benzophenone based photosensitizer and PS- TiO$_2$-organic dye composites exposed to UV radiation for 0, 400 and 1000 h*

The mechanical properties of PS+3%(TiO$_2$+4MOBP) which exhibited maximum photodegradation and PS+3%(TiO$_2$+2H4MOBP) which exhibited minimum photodegradation among the PS-TiO$_2$-benzophenone based photosensitizer composites were studied after UV irradiation of 0, 400 and 1000 hours (Figure 6.12). The mechanical properties of PS+3%(TiO$_2$ + 5%MB) and PS+3%(TiO$_2$+ 5%MG) upon UV irradiation were also studied. The tensile and flexural strengths of all the composites decreased as the time of UV irradiation increased. PS+3% (TiO$_2$+4MOBP) exhibited better degradation compared to PS+3%(TiO$_2$+2H4MOBP) as expected among the PS-TiO$_2$-benzophenone based photosensitizer composites.

Even though PS+3%(TiO$_2$+5%MB) underwent better photodegradation compared to PS+3%(TiO$_2$+5%MG), the decrease in mechanical properties were significant in PS+3%(TiO$_2$+ 5%MG). This anomaly might have aroused as a consequence of poor dispersion of MG compared to that of MB in the PS-TiO$_2$-dye composites.

6.4.5. Electrical properties

The BDV of PS-3%(TiO$_2$+4MOBP), PS-3%(TiO$_2$+2ClBP) and PS-3%(TiO$_2$+5%MB) composites at varying UV irradiation time intervals (0, 400 & 1000 hours) were measured (Figure 6.13.1). All these composites underwent an appreciable decrease in the value of BDV as the time of UV irradiation increased. The decrease in BDV observed in PS-3%(TiO$_2$+2ClBP) was slightly greater than that of PS- 3%(TiO$_2$+4MOBP) after UV irradiation.
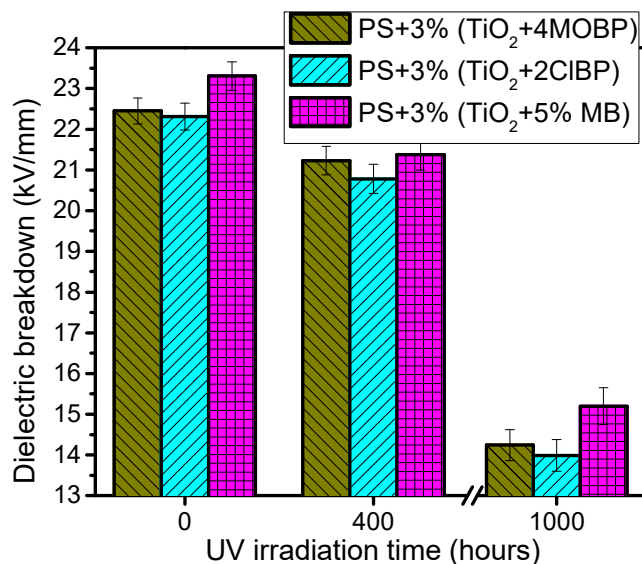
Figure 6.13.1. Dielectric breakdown (breakdown voltage) of PS-TiO$_2$-4MOBP, PS-TiO$_2$-2ClBP and PS-TiO$_2$-MB composites at varying UV irradiation time

Dielectric permittivity (ε_r) of PS-3%(TiO$_2$+4MOBP), PS-3%(TiO$_2$+2ClBP) (Figure 6.13.2), PS-3%(TiO$_2$+5% MB) and PS-3%(TiO$_2$+5% MG) (Figure 6.13.3) were measured at UV irradiation intervals of 0, 400 and 1000 hours. The ε_r of all the composites under study increased upon UV irradiation time. It is observed from the figure 6.13.2 that PS- 3%(TiO$_2$+2ClBP) underwent better increase in the values of ε_r on UV irradiation compared to PS-3%(TiO$_2$+4MOBP). Similarly PS-3%(TiO$_2$+5% MB) showed better increase in ε_r compared to PS-3%(TiO$_2$+5% MG) upon UV irradiation (Figure 6.13.3).
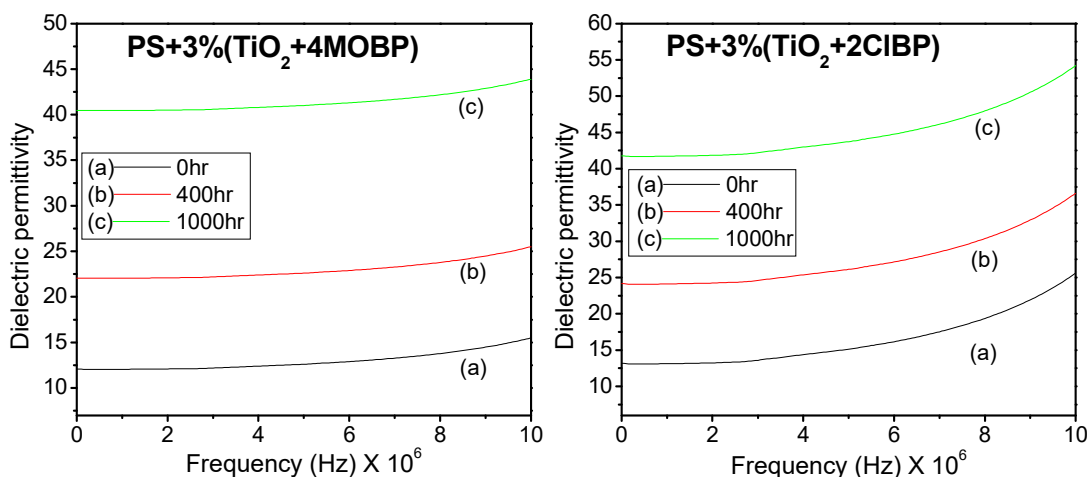
Figure 6.13.2. *Dielectric permitivity of PS-3% 4MOBP and PS-3% 2ClBP composites at UV irradiation intervals of 0, 400 and 1000 h*
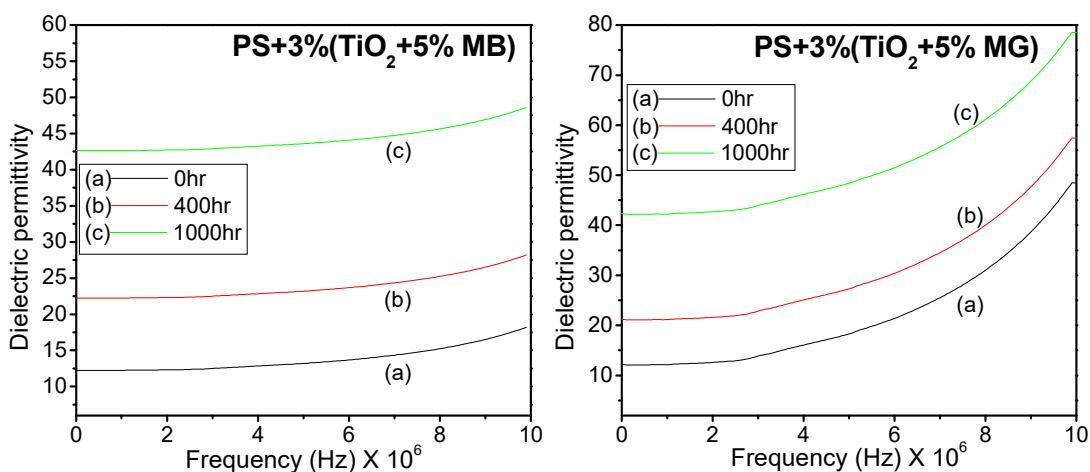
Figure 6.13.3. *Dielectric permittivity of PS-3% MB and PS-3% MG composites at UV irradiation intervals of 0, 400 and 1000 h*

6.4.6. Thermogravimetric Analysis (TGA)

The thermogram of PS-3%(TiO$_2$+4MOBP) (Figure 6.14 A) and PS-3% (TiO$_2$+5%MB) (Figure 6.14 B) obtained from TGA of the composites in nitrogen atmosphere gave two stages of weight loss curves representing the water desorption and decomposition of the composites respectively. Shift in decomposition temperature were observed in the composites upon UV irradiation. The decomposition temperature range of PS-3%(TiO$_2$+4MOBP) shifted from 293-423°C to 273-410°C on UV irradiation of 1000 hours. Similarly, a shift in decomposition temperature range for PS-3%(TiO$_2$+5%MB) was observed from 300-433°C to 287-424°C on UV irradiation of 1000 hours. Beyond the termination point of steep decomposition curve

of PS-3%(TiO_2+4MOBP) at 423°C (wt %=10) and PS-3%(TiO_2+5%MB) at 433°C (wt %=12.13), a slow decrease in weight percentage was observed. This represents the presence of inorganic residues that were quite thermally stable at these temperatures. UV irradiation of 1000 hours resulted to the decrease in the termination point of steep decomposition curves of the composites to lower temperature.
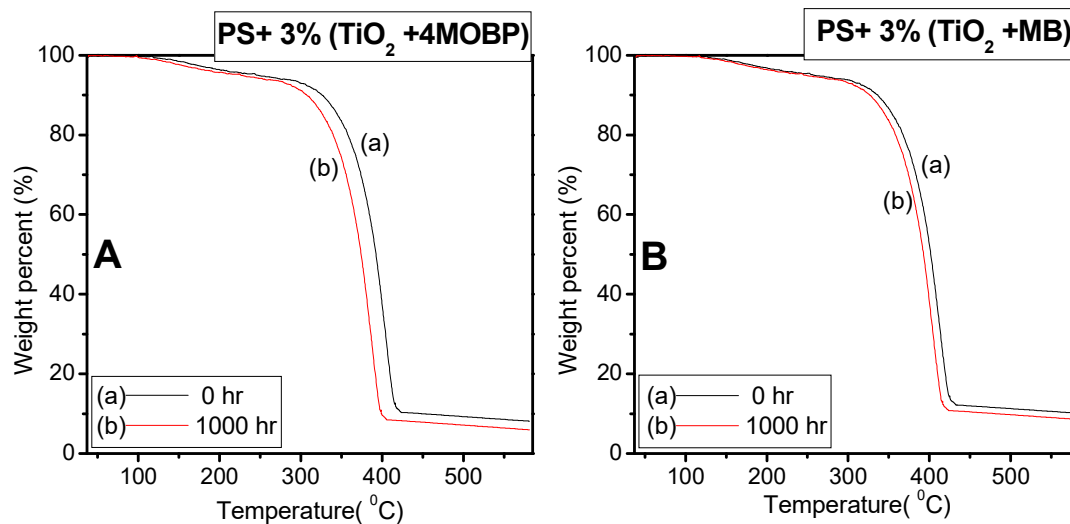
Figure 6.14. *TGA thermogram of PS-3% (TiO_2+4MOBP) **(A)** and PS-3% (TiO_2+5%MB) **(B)** composites before and after UV irradiation of 1000 h*

6.4.7. Weight loss
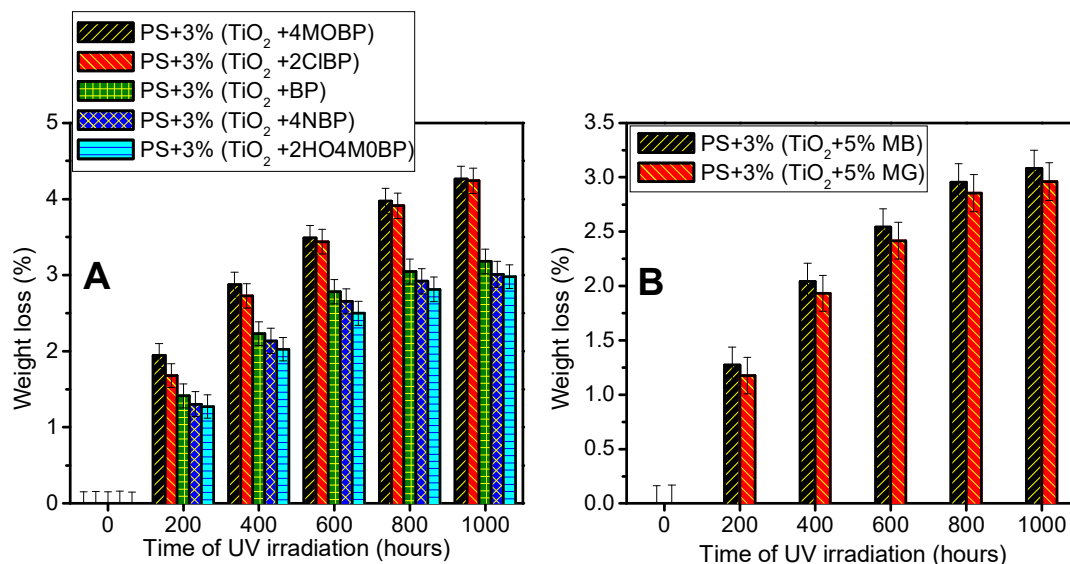
Figure 6.15. *Comparison of weight loss percentages of PS-3% (TiO_2+benzophenone based photosensitizer) **(A)** and PS-3% (TiO_2+dye) **(B)** composites at regular intervals of UV irradiation*

Significant weight loss was observed for PS-(TiO$_2$+benzophenone based photosensitizer) (Figure 6.15 A) and PS-(TiO$_2$+dye photosensitizer) (Figure 6.15 B) composites at regular intervals of UV irradiation. The order of weight loss percentage was PS-3%(TiO$_2$+4MOBP) > PS-3%(TiO$_2$+2ClBP) > PS-3%(TiO$_2$+BP) > PS-3%(TiO$_2$+4NBP) > PS-3%(TiO$_2$+2HO4MOBP). The weight loss percentage of PS-organic dye was found to be in the following order:- PS-3%(TiO$_2$+MB)> PS-3%(TiO$_2$+MG).

6.4.8. Scanning Electron Microscopy (SEM)
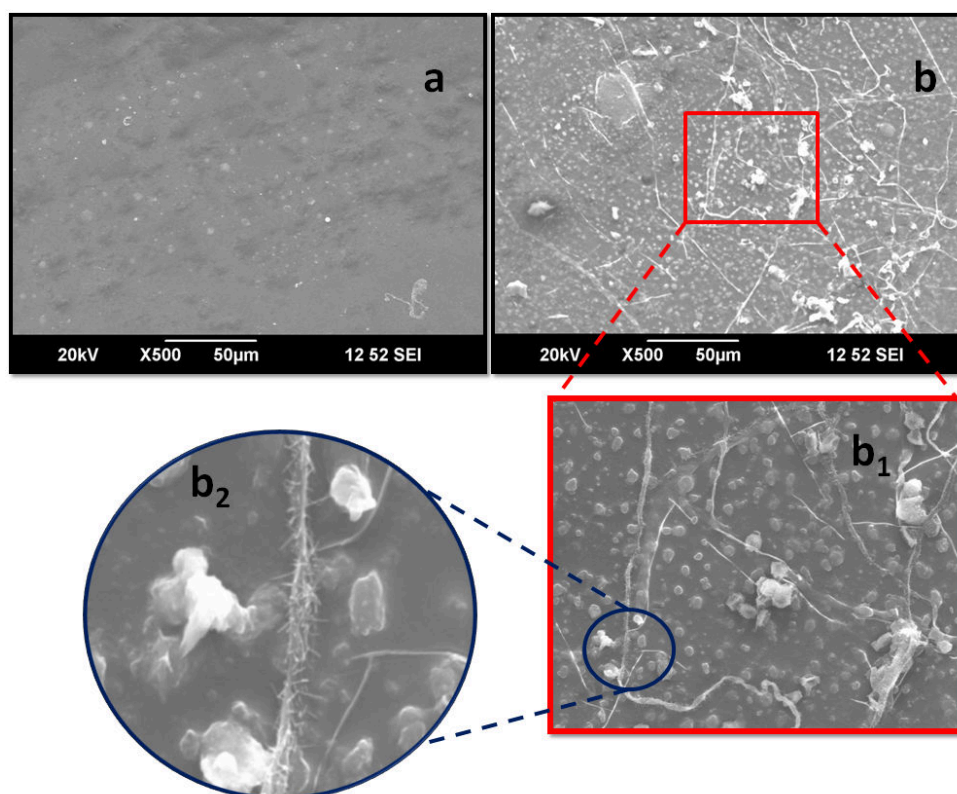
Figure 6.16. *SEM image of PS-3%(TiO$_2$+4MOBP) composite before (a) and after (b) UV irradiation of 1000 hours. 'b$_1$' and 'b$_2$' represents a portion of image 'b' in high resolution*

The SEM image of PS-3%(TiO$_2$+4MOBP) showed an increase in surface roughness after 1000 hours of UV exposure. Figure 6.16 a represents the polymer composite sheet before UV irradiation. After UV irradiation of 1000 hours (Figure 6.16 b) the polymer surface seemed to have increased roughness due to deterioration. Focused images of UV exposed sample (Figure 6.16 b$_1$ and b$_2$) revealed the

possibility that the surface of the polymer sheet might have degraded thereby exposing the catalysts over the surface.

6.5. Mechanism of photosensitized PS degradation

Based on the observations and discussions done so far, we could conclude that benzophenone derivatives act as a photosensitizer for the effective degradation of PS, harvesting UV radiation. The degradation efficiency of PS loaded with these compounds were however not as effective as nano TiO_2. When nano TiO_2 was coupled with benzophenone derivatives, their efficiency for the degradation of PS under UV light increased upto an appreciable level. The dyes, MB and MG on the other hand, had no appreciable photosensitizing efficiency by themselves, for PS degradation. They however acted as good photosensitizer when coupled with nano TiO_2. Both the benzophenone derivatives and organic dyes, MB and MG enhanced the photocatalytic activity of TiO_2.

An important observation made from the FTIR spectra of PS-benzophenone derivatives was the increased double bond formation upon UV irradiation. The possible mechanism for this is as depicted below.

- The π-bond belonging to the >C=O group in benzophenone may undergo homolytic cleavage in the presence of UV radiation to form singlet state diradicaloid. The diradicaloid is converted from singlet state to triplet state through inter system crossing (ISC) as given below.

Benzophenone   *Diradicaloid*   *Diradicaloid*
(Singlet state)   *(Triplet state)*
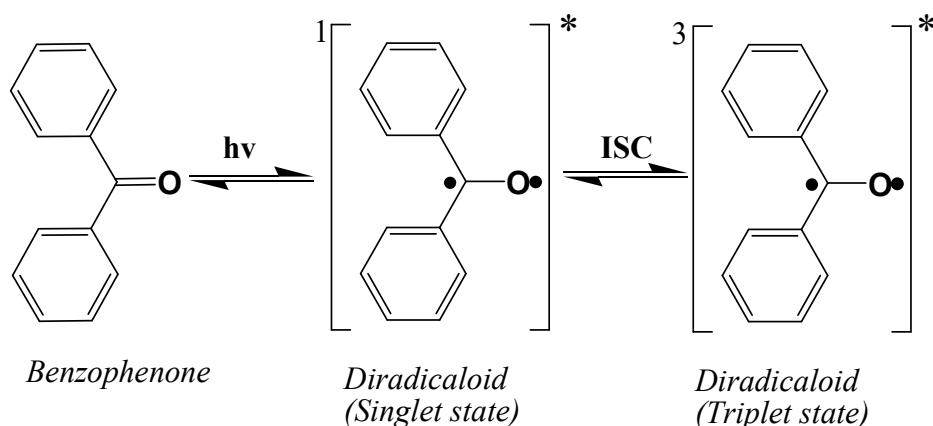
- The sigma bonds between C-C and/or C-H of PS may also undergo homolytic cleavage in the presence of UV radiation as given below to form macromolecular radicals.

Polystyrene

Polystyrene macromolecular radicals
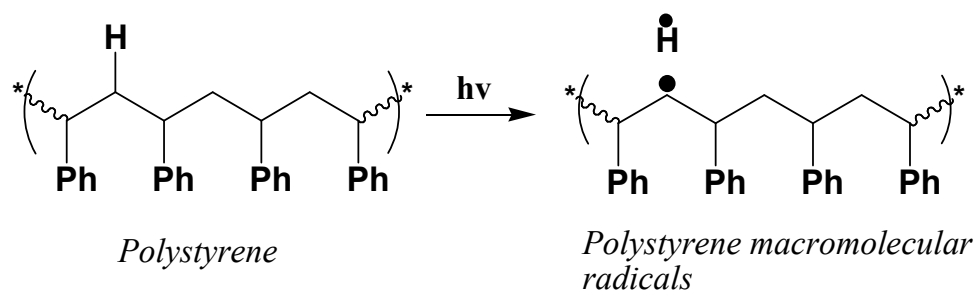
- Interaction between diradicaloid of benzophenone and PS radical takes place. The benzophenone diradicaloid abstracts hydrogen radical (H•) generated from PS to form ketyl radical. The ketyl radical can further abstract another H• from the adjacent carbon resulting in the formation of alkenic carbon–carbon double bond in the PS chain (as evident from FTIR of UV irradiated PS).

Diradicaloid (Triplet state)

Polystyrene macromolecular radicals

Ketyl radical

Diphenylmethanol   *Polystyrene with alkenic double bond*
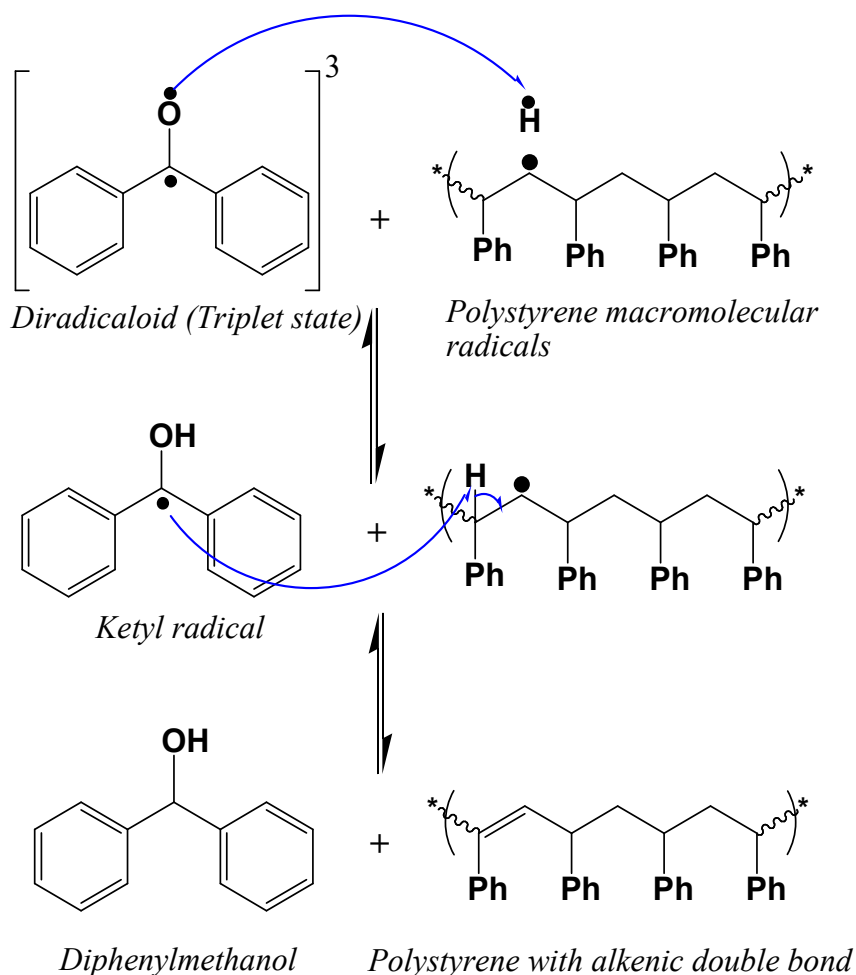
It should also be noted that the polystyrene macromolecular radicals may also react with oxygen or water from the atmosphere leading to -OH, -OOH as well as >C=O radicals in the PS chain (as evident from FTIR). The mechanism has been described in detail in chapter 3.

The above proposed mechanism depends mainly upon two aspects. Primarily the diradicaloid formed out of benzophenone should be stable without recombination and secondly the presence of PS macromolecular radicals should be in the vicinity of benzophenone diradicaloid for effective interaction. SEM image clearly revealed uniform dispersion of the composites where interaction among the PS and catalysts are possible. The diradicaloid are stable upto an extent as they are in conjugation with the two adjacent phenyl rings.

Observations made from the results of various analyses proved that the presence of various substituted groups on the phenyl rings of benzophenone influenced its photosensitizing activity. Loading PS with 4MOBP and 2ClBP resulted in a slight increase in the rate of photodegradation compared to BP, 4NBP and 2HO4MOBP.The exact reason for this observation has to be studied in detail. The decrease in the photocatalytical activity of 2HO4MOBP, however could be explained on the basis of photoenolization due to intra molecular hydrogen bond formation as depicted below.
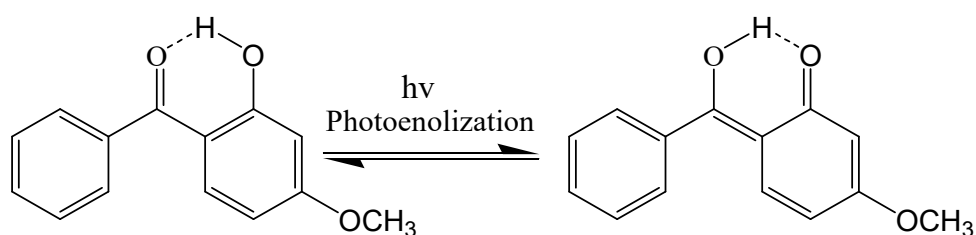
2-hydroxy-4-methoxybenzophenone

2HO4MOBP undergoes tautomerisation in the presence of UV light termed as photoenolization. The hydrogen bond existing between –OH and >C=O groups present in 2HO4MOBP also favours photoenolization. Due to the co-existence of hybrid structures as depicted in the above diagram of 2HO4MOBP as a result of photoenolization, the chance for the formation of diradicaloid is almost hindered. This results in the inefficiency of 2HO4MOBP to act as a photosensitizer for the photodegradation of PS[27,28].

6.6. Conclusion

Photodegradation of PS in the presence of benzophenone derivatives and triphenylmethane dyes as photosensitizers was studied. The combination of these dyes with nano TiO_2 for the photodegradation of TiO_2 was also investigated. All the PS-

benzophenone based photosensitizer composites showed accelerated degradation compared to pristine PS under UV irradiation. However the extent of degradation was not up to PS-TiO$_2$. Among the PS-benzophenone based photosensitizer composites, photodegradation followed the order: PS-4MOBP, PS-2ClBP, PS-BP, PS-NBP, PS-2H4MOBP. The decrease in the efficiency of 2H4MOBP for the photodegradation of PS could be explained due to photoenolization. The extent of photodegradation of PS-dye composites were not much appreciable. The combination of benzophenone based photosensitizer and dyes with nano TiO$_2$ showed an appreciable increase in the photodegradation efficiency even compared to PS-TiO$_2$ composites. Highest photocatalytic efficiency for the degradation of PS among TiO$_2$-benzophenone based photosensitizer composites was exhibited by TiO$_2$-4MOBP followed by TiO$_2$-2ClBP composite. PS-(TiO$_2$-MB) exhibited better photodegradation compared to PS-(TiO$_2$-MG) among the PS-TiO$_2$-dye composites. It can be concluded that the combination of benzophenone based photosensitizers or triphenylmethane dyes with TiO$_2$ serves as an efficient photocatalyst for the degradation of PS under UV irradiation.

References

1. Manangan, T., Shawaphun, S. & Wacharawichanant, S. Acetophenone and Benzophenone Derivatives as Catalysts in Photodegradation of PE and PP Films. in *Functionalized and Sensing Materials* **93**, 284–287 (Trans Tech Publications Ltd, 2010).
2. Barboiu, V. & Avadanei, M. I. Chemical reactions of benzophenone photoirradiated in 1,2-polybutadiene. *J. Photochem. Photobiol. A Chem.* **222**, 170–179 (2011).
3. Geuskens, G., Delaunois, G., Lu-Vinh, Q., Piret, W. & David, C. Photo-oxidation of polymers—VIII. The photo-oxidation of polystyrene containing aromatic ketones. *Eur. Polym. J.* **18**, 387–392 (1982).
4. Torikai, A., Takeuchi, T. & Fueki, K. Photodegradation of polystyrene and polystyrene containing benzophenone. *Polym. Photochem.* **3**, 307–320 (1983).
5. Lin, C. S., Liu, W. L., Chiu, Y. S. & Ho, S.-Y. Benzophenone-sensitized photodegradation of polystyrene films under atmospheric conditions. *Polym. Degrad. Stab.* **38**, 125–130 (1992).
6. Pinto, L. F. A., Goi, B. E., Schmitt, C. C. & Neumann, M. G. Photodegradation of polystyrene films containing UV-visible sensitizers. *J. Res. Updat. Polym. Sci.* **2**, 39–47 (2013).
7. Sikkema, K., Cross, G. S., Hanner, M. J. & Priddy, D. B. Photo-degradable polystyrene Part I: enhancing the photo-degradability of polystyrene by the addition of photosensitizers. *Polym. Degrad. Stab.* **38**, 113–118 (1992).
8. Cuquerella, M. C., Lhiaubet-Vallet, V., Cadet, J. & Miranda, M. A. Benzophenone Photosensitized DNA Damage. *Acc. Chem. Res.* **45**, 1558–1570 (2012).
9. Bayrakçeken, F. Triplet–triplet optical energy transfer from benzophenone to naphthalene in the vapor phase. *Spectrochim. Acta Part A Mol. Biomol. Spectrosc.* **71**, 603–608 (2008).
10. Bergamini, G. *et al.* Forward (singlet–singlet) and backward (triplet–triplet) energy transfer in a dendrimer with peripheral naphthalene units and a benzophenone core. *Photochem. Photobiol. Sci.* **3**, 898–905 (2004).
11. Si, Y., Liang, W. & Zhao, Y. Theoretical Prediction of Triplet–Triplet Energy Transfer

Rates in a Benzophenone–Fluorene–Naphthalene System. *J. Phys. Chem. C* **116**, 12499–12507 (2012).

12. Foote, C. S. DEFINITION OF TYPE I and TYPE II PHOTOSENSITIZED OXIDATION. *Photochem. Photobiol.* **54**, 659 (1991).

13. Aumaitre, C. *et al.* Visible and near-infrared organic photosensitizers comprising isoindigo derivatives as chromophores: synthesis{,} optoelectronic properties and factors limiting their efficiency in dye solar cells. *J. Mater. Chem. A* **6**, 10074–10084 (2018).

14. Nagarajan, B. *et al.* Novel ethynyl-pyrene substituted phenothiazine based metal free organic dyes in DSSC with 12% conversion efficiency. *J. Mater. Chem. A* **5**, 10289–10300 (2017).

15. Swanson, S. A. *et al.* Stable and Efficient Fluorescent Red and Green Dyes for External and Internal Conversion of Blue OLED Emission. *Chem. Mater.* **15**, 2305–2312 (2003).

16. Leung, M. *et al.* 6-N,N-Diphenylaminobenzofuran-Derived Pyran Containing Fluorescent Dyes: A New Class of High-Brightness Red-Light-Emitting Dopants for OLED. *Org. Lett.* **8**, 2623–2626 (2006).

17. Stolarski, R. & Fiksinski, K. J. Fluorescent perylene dyes for liquid crystal displays. *Dye. Pigment.* **24**, 295–303 (1994).

18. Grabchev, I., Moneva, I., Bojinov, V. & Guittonneau, S. Synthesis and properties of fluorescent 1{,}8-naphthalimide dyes for application in liquid crystal displays. *J. Mater. Chem.* **10**, 1291–1296 (2000).

19. Mitra, S. A polymeric triarylmethane dye as a sensitizer for photoconductivity. *J. Polym. Sci. Polym. Symp.* **74**, 165–169 (1986).

20. Tanielian, C., Mechin, R. & Shakirullah, M. Origin of dye bleaching and polymer degradation in the methylene blue-sensitized photo-oxygenation of polybutadiene. *J. Photochem. Photobiol. A Chem.* **64**, 191–199 (1992).

21. Chakrabarti, S., Chaudhuri, B., Bhattacharjee, S., Das, P. & Dutta, B. K. Degradation mechanism and kinetic model for photocatalytic oxidation of PVC–ZnO composite film in presence of a sensitizing dye and UV radiation. *J. Hazard. Mater.* **154**, 230–236 (2008).

22. Duxbury, D. F. The photochemistry and photophysics of triphenylmethane dyes in solid and liquid media. *Chem. Rev.* **93**, 381–433 (1993).

23. Baptista, M. & Indig, G. Effect of BSA Binding on Photophysical and Photochemical Properties of Triarylmethane Dyes. *J. Phys. Chem. B - J PHYS CHEM B* **102**, (1998).

24. Fleischmann, C., Lievenbrück, M. & Ritter, H. Polymers and dyes: developments and applications. *Polymers (Basel).* **7**, 717–746 (2015).

25. Nguyen, T. K. N. *et al.* Titanium dioxide-benzophenone hybrid as an effective catalyst for enhanced photochemical degradation of low density polyethylene. *e-Polymers* **18**, (2018).

26. Mishra, A., Fischer, M. K. R. & Bäuerle, P. Metal-Free Organic Dyes for Dye-Sensitized Solar Cells: From Structure: Property Relationships to Design Rules. *Angew. Chemie Int. Ed.* **48**, 2474–2499 (2009).

27. Placzek, M., Dendorfer, M., Przybilla, B., Gilbertz, K.-P. & Eberlein, B. Photosensitizing properties of compounds related to benzophenone. *Acta Derm. Venereol.* **93**, 30—32 (2013).

28. Allen, N. S., Luc-Gardette, J. & Lemaire, J. Photostabilising action of ortho-hydroxy benzophenones in polypropylene film: Influence of processing and wavelength of irradiation. *Polym. Photochem.* **3**, 251–265 (1983).

Chapter 7

Enhanced Photocatalytic Activity of Metal Doped TiO$_2$ for the UV degradation of Polystyrene

Abstract

UV degradation of PS was studied in the presence of metal doped TiO$_2$. Silver, iron and copper doped TiO$_2$ were prepared by sol-gel route in which the corresponding metal salts were added to the developing TiO$_2$ particles at pH 4. Metal doped TiO$_2$ with 3, 10 and 30 percentage of metals were prepared. XRD analysis revealed that as the percentage of metal doping increased, phase change occurred from anatase to rutile, easily at lower calcination temperature of 400°C. The photocatalytic activity of TiO$_2$ increased considerably upon metal doping, for the UV degradation of PS. Lower percentage metal doped TiO$_2$ acted as better photocatalyst compared to higher percent metal doped TiO$_2$. Ag doped TiO$_2$ showed enhanced photocatalytic efficiency compared to Fe or Cu doped TiO$_2$.

7.1. Introduction

The fate of photogenerated charges entirely determines the photocatalytic activity of TiO_2 which further depends upon its surface property. One of the methods employed for controlling the surface property of TiO_2 intrinsically is doping. Surface separation results as a consequence of doping where spatial trapping of photogenerated charge carriers take place. These spatially trapped charges are transferred to the associated substrates for redox reactions[1]. Metal doping has an advantage of introducing sub bands which are closer to the conduction band (CB) of TiO_2[2–4]. This is attained through the overlap of 3d orbital of titanium with suitable orbital of metals (*d*-orbitals in transition metals and *f*-orbitals in rare earth metals)[5]. An outcome of this interaction is the decrease in bandgap energies[6–8]. TiO_2 doped with noble metals including Pt[9], Pd[10], Ru[11], Rh[11], Ag[12], Au[13] etc have been reported to increase the photocatalytic efficiency by hindering the recombination of photogenerated electrons in conduction band (CB) and holes in valence band (VB). Schottky barrier that results at the interface of TiO_2 and metal explains the obstruction of these photogenerated charge recombination. Electrons from the CB of TiO_2 are captured by the noble metals which are stored and further transferred into another acceptor associated with it initiating photochemical reaction. TiO_2 doped with other transition metals including Fe[14–16], Cu[17], Cr[14], Mn[14,18], Co[14], Ni[14,19], V[20], Zn[21] etc., also have been reported with superior photocatalytic activity. Charge transfer between CB or VB of TiO_2 and the *d*-orbitals of the transition metals changed the electronic structure causing a red shift in the absorption from UV to visible region.

In this chapter, photodegradation of PS is studied using TiO_2 doped with Ag, Cu and Fe transition metals. TiO_2 doped with Ag, Cu and Fe as photocatalysts have already been used in various applications and satisfying results were obtained. Fe doped TiO_2 has been used as photocatalyst in the degradation of organic dyes like methyl orange[22,23], reactive blue 4[24], azo fuchsine[25], XRG[26], phenol[27] etc. Cu doped TiO_2 was reported to catalyse the degradation of methyl orange[28], nitrates[29] etc. The application of thin film of Cu doped TiO_2 which is super hydrophilic has been reported to exhibit anti-fogging property under sun light[30]. The antimicrobial activity of Cu doped TiO_2 photocatalyst has also been reported[31]. The degradation of dyes including azo dye[32], direct red 23[33], basic violet[34] etc has been reported using Ag

doped TiO_2 as photocatalyst. The degradation of chloroform and urea using Ag doped TiO_2 catalyst exhibited superior activity compared to pure TiO_2[35].

Section:I

Synthesis and characterisation of metal doped TiO_2

7.2. Experimental

7.2.1. Synthesis of Ag Doped TiO_2

Ag doped TiO_2 was prepared using sol-gel technique. Titanium (IV) isopropoxide (TTIP) was used as precursor of TiO_2 and silver nitrate ($AgNO_3$) for Ag. In order to prepare TiO_2 with 3 mole percentage of Ag, 2.463 g of TTIP (2.57 ml) was added to 14 ml ethanol and stirred at 4°C using a magnetic stirrer (solution I) for one hour. Meanwhile 0.054 g of $AgNO_3$ was dissolved in 4ml distilled water (solution II). Solution II was then added dropwise into solution I while stirring. The pH of the system was adjusted to 4 using drops of nitric acid. The system was stirred for three more hours. The colloidal solution hence obtained was filtered and washed using ethanol followed by distilled water. The resulting gel was dried at 120°C for 6 hours. The grey powder hence obtained was calcinated at 400°C for 5 hours[36].

In a similar way, TiO_2 doped with 10 and 30 mole percentages of Ag were also prepared. The composites were named as TiO_2-3% Ag, TiO_2-10% Ag and TiO_2-30% Ag depending on the mole percentage of Ag versus TiO_2 in the composites. Table 7.1.1 below represents the details of prepared Ag doped TiO_2 composites.

Table 7.1.1. TiO_2-Ag composites

Composite	TiO_2 Mole %	Ag Mole %	Weight of $AgNO_3$ (g)	Weight of TTIP (g)
TiO_2+3% Ag	97	3	0.0537	2.4630
TiO_2+10% Ag	90	10	0.1794	2.8206
TiO_2+30% Ag	70	30	0.5381	2.4619

7.2.2. Synthesis of Fe Doped TiO$_2$

Fe doped TiO$_2$ was prepared via sol-gel route. TTIP served as the precursor for TiO$_2$ and Iron (III) nitrate nonahydrate (Fe(NO$_3$)$_3$.9H$_2$O) for Fe in the composite. For the preparation of 3 mole percent Fe doped TiO$_2$, 2.872 g TTIP (2.99 ml) was dissolved in 14 ml ethanol and stirred at 4°C using a magnetic stirrer (solution I). Solution II consisting of 0.128 g Fe(NO$_3$)$_3$.9H$_2$O dissolved in 4 ml distilled water was added dropwise into solution I. pH of the solution was adjusted to 4 using nitric acid followed by three hours of stirring. The resulting product was filtered and washed using ethanol followed by water. The gel obtained was dried at 120°C for 6 hours. The reddish brown powder hence obtained was calcinated at 400°C for 5 hours[22,37].

10 and 30 mole percentages of Fe doped TiO$_2$ were also prepared in a similar manner to obtain TiO$_2$-10% Fe and TiO$_2$-30% Fe. The details of the prepared TiO$_2$-Fe composites are as tabulated below (Table 7.1.2).

Table 7.1.2. TiO$_2$-Fe composites

Composite	TiO$_2$ Mole %	Fe Mole %	Weight of Fe(NO$_3$)$_3$.9H$_2$O (g)	Weight of TTIP (g)
TiO$_2$+3% Fe	97	3	0.128	2.872
TiO$_2$+10% Fe	90	10	0.427	2.573
TiO$_2$+30% Fe	70	30	1.280	1.720

7.2.3. Synthesis of Cu Doped TiO$_2$

Preparation of Cu doped TiO$_2$ was also done via sol-gel method as discussed above. Copper sulphate pentahydrate (CuSO$_4$.5H$_2$O) was used as the precursor for Cu in TiO$_2$-Cu composites. In order to prepare 3 mole percentage Cu doped TiO$_2$ (namely TiO$_2$-3%Cu), 2.949 g TTIP (3.066 ml) was dissolved in 14 ml ethanol and stirred at 4°C using a magnetic stirrer (solution I). 0.051g CuSO$_4$.5H$_2$O dissolved in 4ml distilled water (solution II) was added to solution I, dropwise. The system was adjusted to pH 4 using nitric acid and stirred for three hours. The resulting product was filtered, washed and dried at 120°C for 6 hours. The pale blue solid powder was calcinated at 400 °C for 5 hours[8].

TiO$_2$ doped with 10 mole percentage and 30 mole percentage of Cu were also prepared (named as TiO$_2$-10% Cu and TiO$_2$-30% Cu). The details of the prepared TiO$_2$-Cu composites are as tabulated below (Table 7.1.3).

Table 7.1.3. *TiO$_2$-Cu composites*

Composite	TiO$_2$ Mole %	Cu Mole %	Weight of CuSO$_4$.5H$_2$O (g)	Weight of TTIP (g)
TiO$_2$+3% Cu	97	3	0.051	2.949
TiO$_2$+10% Cu	90	10	0.169	2.831
TiO$_2$+30% Cu	70	30	0.506	2.494

The prepared TiO$_2$-Cu, TiO$_2$-Ag and TiO$_2$-Fe composites were characterized using various techniques and results are discussed below.

7.3. Results and discussion

7.3.1. Powder XRD
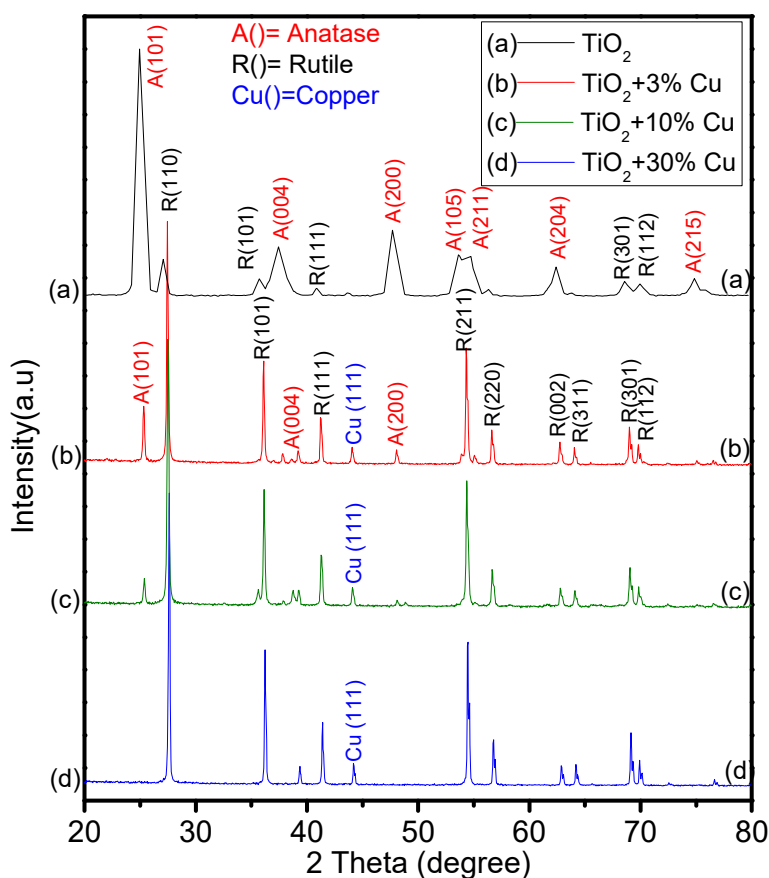
Figure 7.1.1. *XRD pattern of TiO$_2$ –Cu composites*

Higher percentage of metal doping in TiO_2 favoured its phase change from anatase to rutile at a calcination temperature of 400°C for 5 hours. The XRD pattern of metal doped TiO_2-3% Cu composite exhibited the peaks corresponding to anatase and rutile phases (Figure 7.1.1). The peaks observed at 2θ= 25.3° (101), 37.8° (004) and 48.05° (200) attributes to anatase phase and peaks at 2θ= 27.45° (110), 36.09° (101), 41.22° (111), 54.3 (211), 56.62 (220), 62.74 (002), 69.0 (301) and 69.79° (112) attributes to the rutile phase of TiO_2 existing in the composite. In addition to these, a new peak at 2θ= 44.05° corresponding to $C\overset{\circ}{u}$ (111) plane was also observed. On comparing the results with the XRD pattern of pristine TiO_2 (Figure 7.1.1 a), it is evident that the intensity of the peaks corresponding to the anatase phase decreased with an increase in the peak intensities of rutile phase. Some of the peaks corresponding to anatase phase were absent. On further increasing the metal doping percentage (TiO_2-10% Cu), the peak intensities corresponding to anatase phase decreased further. In TiO_2-30% Cu composite, TiO_2 existed almost in rutile phase.

Percentage of anatase and rutile phases of TiO_2 existing in the composites were determined by Spurr equations (equation 7.1 and 7.2)[38].

Percentage of anatase phase, $A\% = 100 \Big/ \{1 + 1.265 \left(\frac{I_R}{I_A}\right)\}$ (7.1)

Percentage of rutile phase, $R\% = 1 \Big/ \{1 + 0.8 \left(\frac{I_A}{I_R}\right)\}$ (7.2)

Where I_A represents the intensity of anatase (101) peak and I_R represents the rutile (110) peak. Table 7.2.1 represents the percentage of anatase and rutile phases of TiO_2-Cu composites.

Table 7.2.1. *Percentage of anatase and rutile phases in TiO₂-Cu composites*

	A% (101)	R%(110)
TiO_2	91.8	8.2
TiO_2+3% Cu	11.6	88.4
TiO_2+10% Cu	06.9	93.1
TiO_2+30% Cu	0	100

It should be noted that the values of A% and R% may not be accurate as the calculations were done considering only the anatase (101) and rutile (110) peaks observed in the XRD patterns.

Table 7.2.1 above clearly establishes the fact that the calcination temperature required for the phase transition from anatase to rutile phase of TiO$_2$ decreased upon Cu incorporation. Pristine TiO$_2$ which existed in ~91.8% anatase and ~8.2% rutile phase after calcination at 400° C for 5 hours have almost been converted into ~100% rutile form at the same calcination temperature upon 30% Cu incorporation.

Crystallite size of TiO$_2$-Cu composites calculated from the most prominent peak of the diffractogram was larger compared to that of pristine TiO$_2$ as determined through Debye Scherrer's equation (Table 7.2.2). The crystallite size increases as the percentage of Cu doping increases in the composites.

Table 7.2.2. Tabulated values of crystallite size of TiO$_2$-Cu composites

	Crystallite size (nm)
TiO$_2$	*18.9*
TiO$_2$+3% Cu	*47.0*
TiO$_2$+10% Cu	*50.7*
TiO$_2$+30% Cu	*56.2*

The observations made from the XRD pattern of TiO$_2$-Ag composites (Figure 7.1.2) were much similar to that of TiO$_2$-Cu composites. The increase in the percentage of Ag doping in TiO$_2$ leads to a gradual phase change from anatase to rutile at the calcination temperature of 400°C for 5 hours. In addition to the diffraction patterns corresponding to the predominant rutile and trace anatase phase, diffraction patterns were also observed at 2θ=38.3° and 44.4° which could be attributed to (111) and (200) planes of Ag$^{\circ}$. These peak intensities increased as the percentage of Ag doping in the composites increased. The percentage of anatase (A %) and rutile (R %) in the composites calculated using Spurr equations (equations 7.1 & 7.2) are tabulated in Table 7.2.3. The crystallite size of the composites was found to be larger than that of pristine TiO$_2$ as determined through Debye Scherrer's equation. An increase in the crystallite size among the composites was observed as the percentage of Ag doping increased (Table 7.2.4).
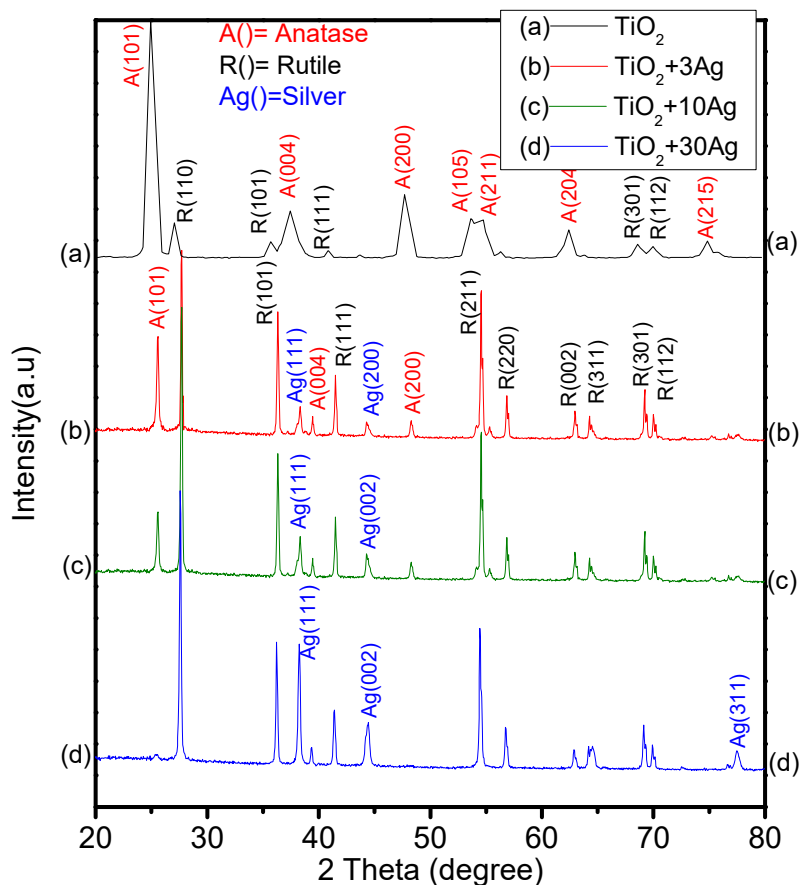
Figure 7.1.2. *XRD pattern of TiO₂ –Ag composites*

Table 7.2.3. *Percentage of anatase and rutile phases in TiO₂-Ag composites*

	A% (101)	R%(110)
TiO₂	91.8	8.2
TiO₂+3% Ag	29.3	70.7
TiO₂+10% Ag	15.6	84.4
TiO₂+30% Ag	0	100

Table 7.2.4. *Values of crystallite size of TiO₂-Ag composites*

	Crystallite size (nm)
TiO₂	18.9
TiO₂+3% Ag	46.6
TiO₂+10% Ag	51.1
TiO₂+30% Ag	62.7
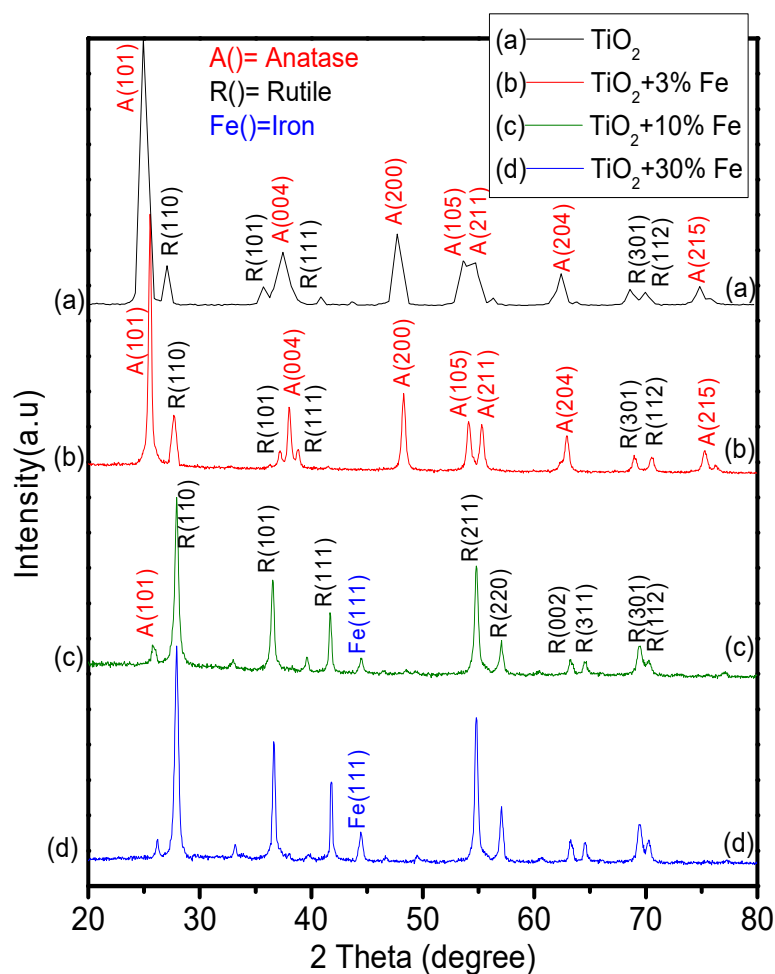
Figure 7.1.3. XRD pattern of TiO₂ –Fe composites

The diffraction patterns of the TiO₂-Fe composites (Figure 7.1.3) exhibited a slight variation from that of TiO₂-Cu and TiO₂-Ag composites. TiO₂-3% Fe exhibited similar diffraction patterns as observed in pristine TiO₂. Anatase phase is predominated over rutile phase here. Peaks corresponding to Fe were not observed. As the percentage of Fe is increased in the composites (ie, TiO₂-10% Fe & TiO₂-30% Fe) the phase change from anatase to rutile is observed. In addition to this, the peak corresponding to F$\overset{o}{e}$ (111) at 2θ=44.45° is also observed. The percentage of anatase (A%) and rutile (R %) calculated using Spurr equations are tabulated in table 7.2.5. The crystallite size of the TiO₂-Fe composites were larger compared to that of pristine TiO₂. Increased percentage of Fe doping further increases the crystallite size of the particles among the TiO₂-Fe composites which is tabulated below (Table 7.2.6).

Table 7.2.5. *Percentage of anatase and rutile phases in TiO₂-Fe composites*

	A% (101)	R%(110)
TiO₂	91.8	8.2
TiO₂+3% Fe	79.2	20.8
TiO₂+10% Fe	9.3	90.7
TiO₂+30% Fe	6.7	93.3

Table 7.2.6. *Values of crystallite size of TiO₂-Fe composites*

	Crystallite size (nm)
TiO₂	18.9
TiO₂+3% Fe	21.2
TiO₂+10% Fe	27.6
TiO₂+30% Fe	29.8

As discussed earlier, TiO₂-3% Fe composite existed predominantly in the anatase phase (~79.2% anatase and ~20.8% rutile) and the peak corresponding to Fe was absent. TiO₂-3% Cu and TiO₂-3% Ag composites, on the other hand, existed predominantly in the rutile phase. The peaks corresponding to Cu^{o} (111) and Ag^{o} (111) were present in the XRD pattern of their respective composites. This observation reveals the fact that more Fe^{3+} ions originating from $Fe(NO_3)_3.9H_2O$ precursor might have replaced the Ti^{4+} ions from the crystal frame work of anatase TiO₂ more actively compared to that of Ag^+ or Cu^{2+} ions originating from $AgNO_3$ or $CuSO_4.5H_2O$ precursors respectively. In such cases where Fe^{3+} ion replaces the Ti^{4+} ion from the anatase TiO₂ lattice, the phase remains unaltered and the diffraction patterns corresponding to Fe^{3+} may not be observed. Radius of Ti^{4+} ion (~0.64 Å) being almost similar to that of Fe^{3+} ion (~0.64Å), the latter can easily replace Ti^{4+} ions from its crystal lattice. As the percentage of Fe doping is increased from 10% to 30%, phase change of TiO₂ from anatase to rutile was enhanced without elevating the calcination temperature (400°C). The peak corresponding to Fe^{o} (111) was also observed. The observed peak for Fe could arise due to the reduction of agglomerated Fe^{3+} ions on the surface of TiO₂ [39].

7.3.2. FESEM-EDX analysis
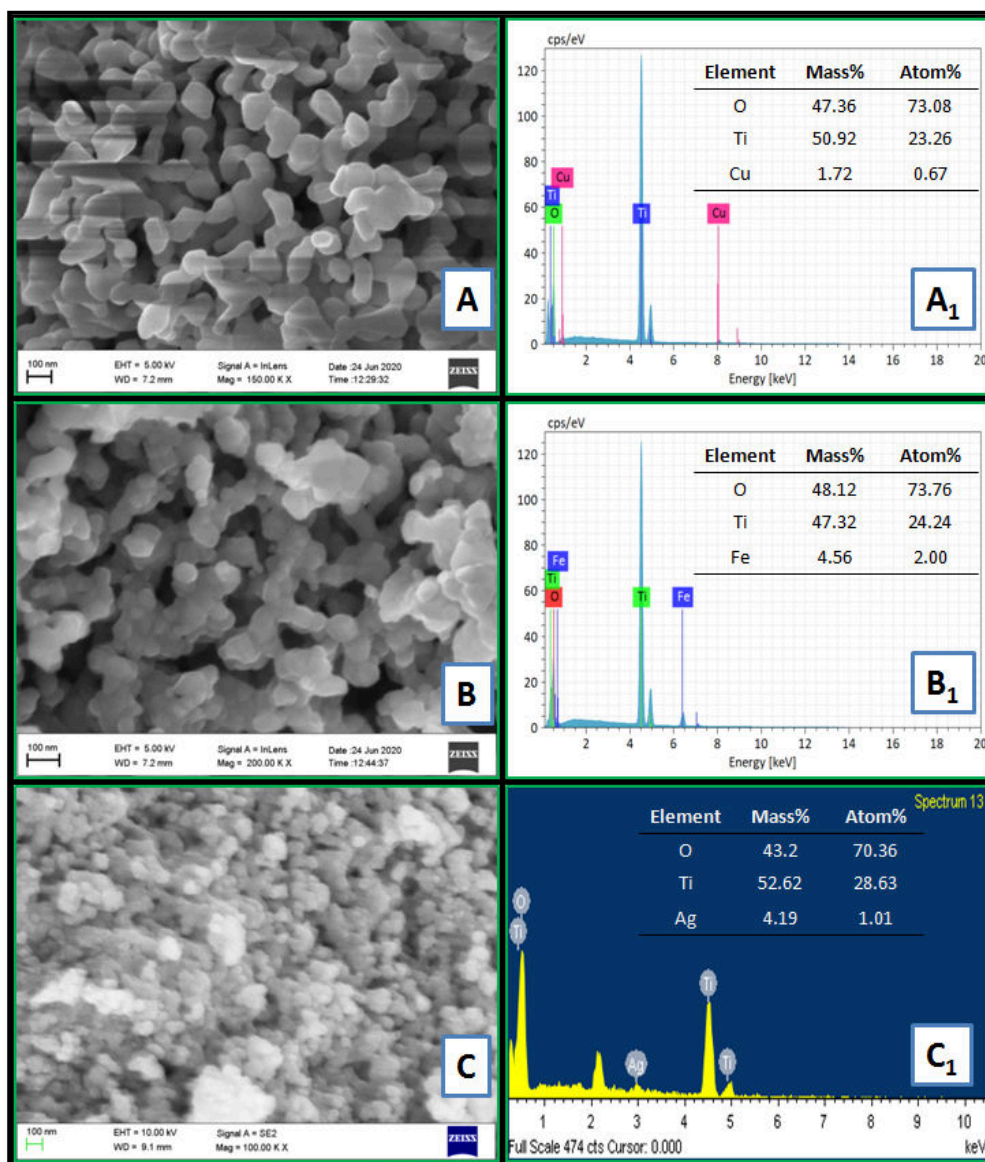
Figure 7.2*. FESEM image and EDX spectra of TiO$_2$ –3% Cu (A & A$_1$), TiO$_2$ –3% Fe (B & B$_1$) and TiO$_2$ –3% Ag (C & C$_1$) composites.*

FESEM image of TiO$_2$-3% Cu (Figure 7.2 A) revealed its sphere like particle morphology with average particle diameter ~125 nm. EDX pattern of the composite (Figure 7.2 A$_1$) showed the presence of titanium at 4.51 (Kα1), 4.93 (Kβ1) and 0.45 (Lα1) keV and oxygen at 0.53 (Kα1) keV. The presence of copper was observed at 0.93 (Lα1), 0.95 (Lβ1), 8.03 (Kα1), 8.05 (Kα2), 8.91 (Kβ1) and 8.98 (Kβ2) keV. The absence of other elements confirmed the purity of the composite. TiO$_2$-3% Fe composite too existed as sphere like particles with an average particle diameter of 85 nm (Figure 7.2 B). EDX pattern of TiO$_2$-3% Fe (Figure 7.2 B$_1$) showed the presence

of iron at 0.71 (Lα1), 0.72 (Lβ1), 6.4 (Kα1 and Kα2 overlap) and 7.16 (Kβ1) keV in addition to titanium and oxygen with no other impurities. TiO_2-3% Ag composite existed as spherical particles with particle diameter ~50 nm as evident from its FESEM (Figure 7.2 C). EDX spectra of TiO_2-3% Ag composite indicates the presence of Ag at around 3 keV (Lα1, Lβ1 and Lβ2 overlap) along with titanium and oxygen without the presence of other elements (Figure 7.2 C_1).

7.3.3. FTIR spectroscopy

FTIR spectra of all the composites looked alike irrespective of the metal doping percentage or the type of metal used. It could be seen that the bands between 950 and 500 cm^{-1} corresponding to Ti-O/ Ti-O-Ti vibrations shifted towards lower wave number in all the metal doped TiO_2 composites compared to pristine TiO_2. Bands between 3600 and 3000 cm^{-1} corresponding to -OH stretching as well as bands at around 1680 cm^{-1} attributing H-O-H bending vibrations could also be observed from the FTIR spectra of the composites.
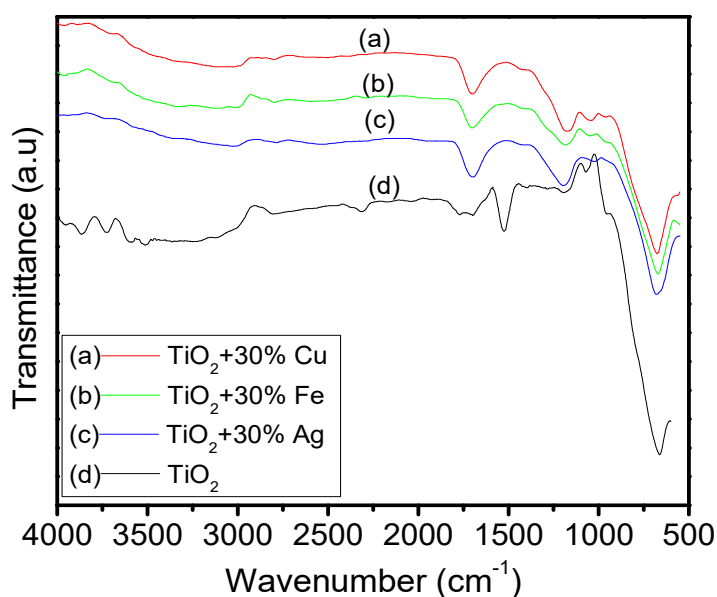
Figure 7.3. *FTIR image of TiO$_2$ –30% Cu (a), TiO$_2$ –30% Fe (b) and TiO$_2$ –30% Ag (c) composites.*

7.3.4. UV-visible diffused reflectance spectroscopy (UV-DRS)

Absorption spectra of TiO_2-Cu (Figure 7.4.1 A), TiO_2-Fe (Figure 7.4.2 A) and TiO_2-Ag (Figure 7.4.3 A) composites exhibited their absorption maxima in the UV region. Increased percentage of metal doping lead to an increase in the intensity of

absorption bands observed in the visible region. Optical bandgap energies (E_g) of the composites were determined by the application of Kubelka-Munk functions in Tauc plot.
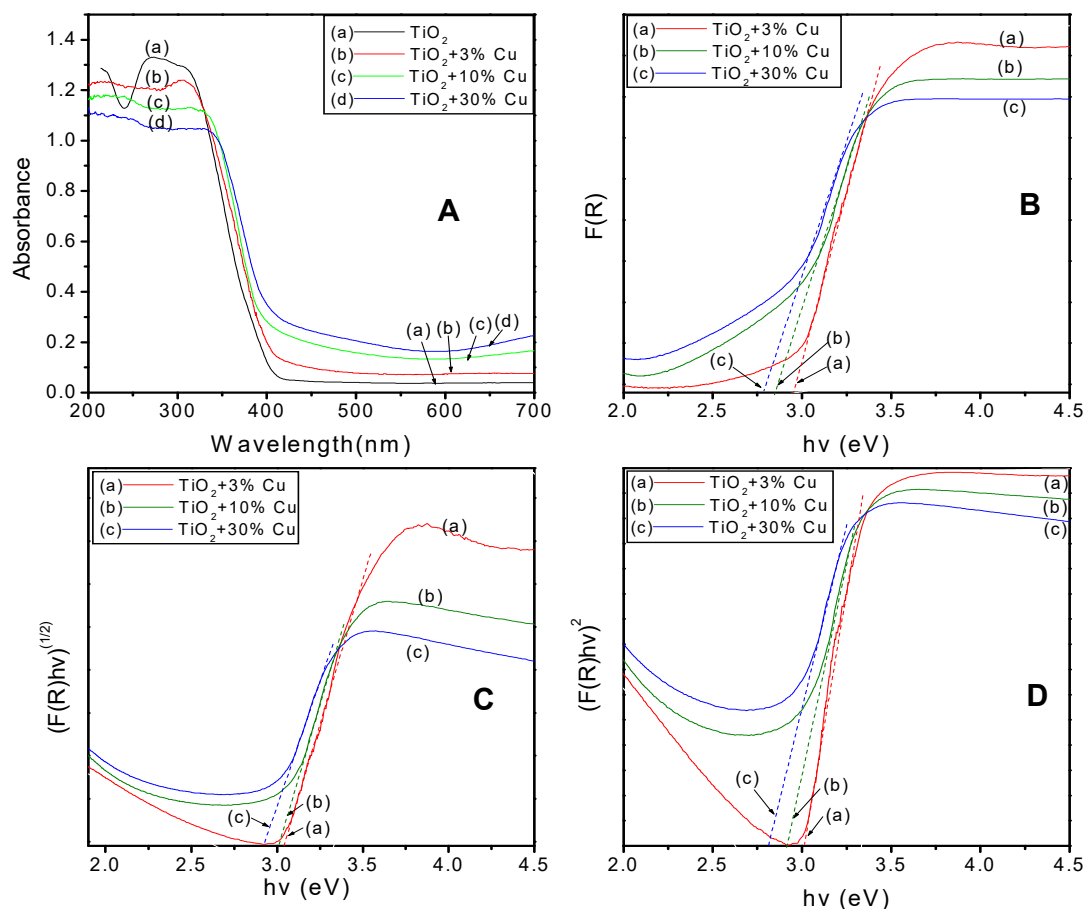
Figure 7.4.1. Absorption spectra (A), F(R) versus hυ (B), (F(R)hυ)$^{1/2}$ versus hυ (C) and (F(R)hυ)^2 versus hυ (D) of TiO$_2$-Cu composites.

Figure 7.4.1 B, C & D represents the E_g irrespective of transitions, indirect E_g and direct E_g of TiO$_2$-Cu composites respectively. Increase in the percentage of Cu doping lowered the E_g of the composites as represented in table 7.3.1.

Table 7.3.1. Optical bandgap energies (E$_g$s) of TiO$_2$–Cu composites

Method	Transition Type	Optical Bandgap energy in eV			
		TiO$_2$	TiO$_2$-3% Cu	TiO$_2$-10% Cu	TiO$_2$-30% Cu
F(R) vs hυ	Irrespective of transitions	3.16	2.97	2.85	2.78
(F(R)hυ)^2 vs hυ	Direct allowed	3.22	3.01	2.91	2.81
(F(R)hυ)$^{1/2}$ vs hυ	Indirect allowed	3.18	3.04	3.00	2.92
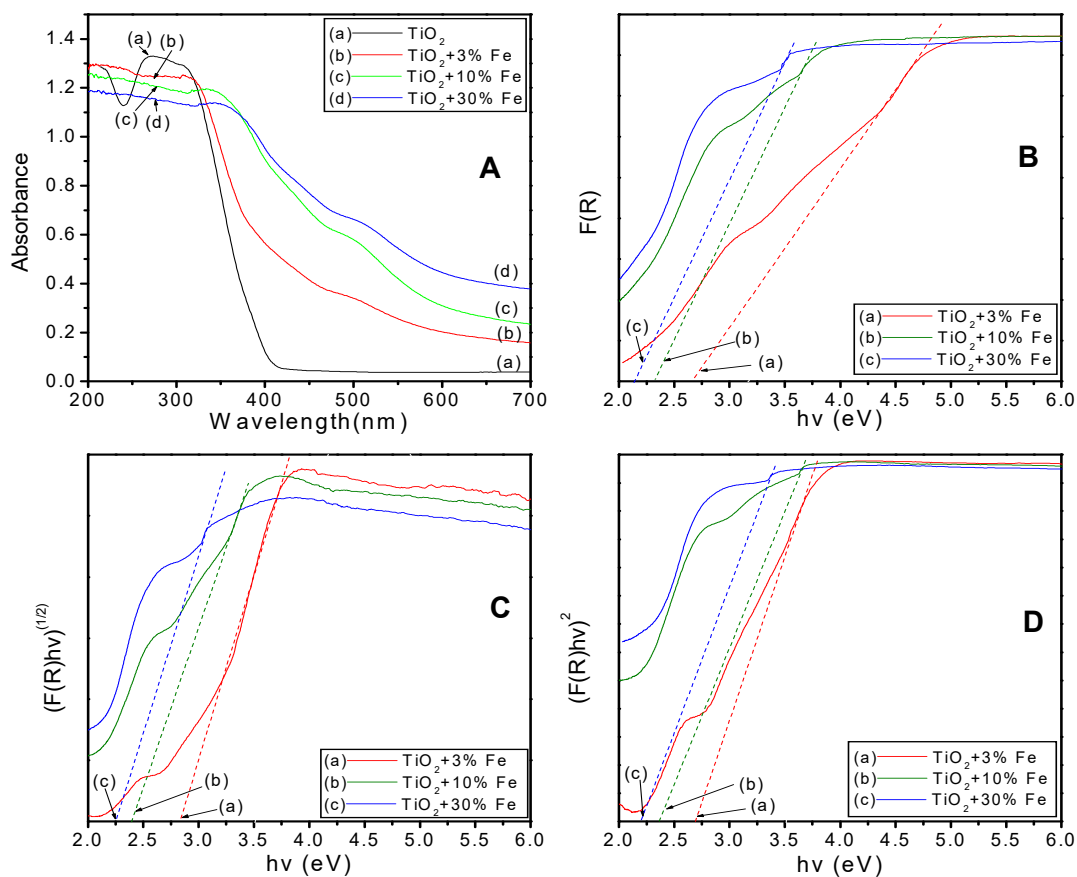
Figure 7.4.2. *Absorption spectra (A), F(R) versus hυ (B), (F(R)hυ)$^{1/2}$ versus hυ (C) and (F(R)hυ)^2 versus hυ (D) of TiO₂-Fe composites.*

The plots of E$_g$ irrespective of transitions (Figure 7.4.2 B), indirect E$_g$ (Figure 7.4.2 C) and direct E$_g$ (Figure 7.4.2 D) of TiO₂-Fe composites showed a decrease in the values of E$_g$ as the percentage of Fe doping increased. The values of Eg determined using the three methods are as tabulated in Table 7.3.2.

Table 7.3.2. *Optical bandgap energies (E$_g$s) of TiO₂ –Fe composites*

| Method	Transition Type	Optical bandgap energy in eV			
		TiO₂	TiO₂-3% Fe	TiO₂-10% Fe	TiO₂-30% Fe
F(R) vs hυ	Irrespective of transitions	3.16	2.67	2.32	2.14
(F(R)hυ)^2 vs hυ	Direct allowed	3.22	2.83	2.39	2.26
(F(R)hυ)$^{1/2}$ vs hυ	Indirect allowed	3.18	2.69	2.36	2.20
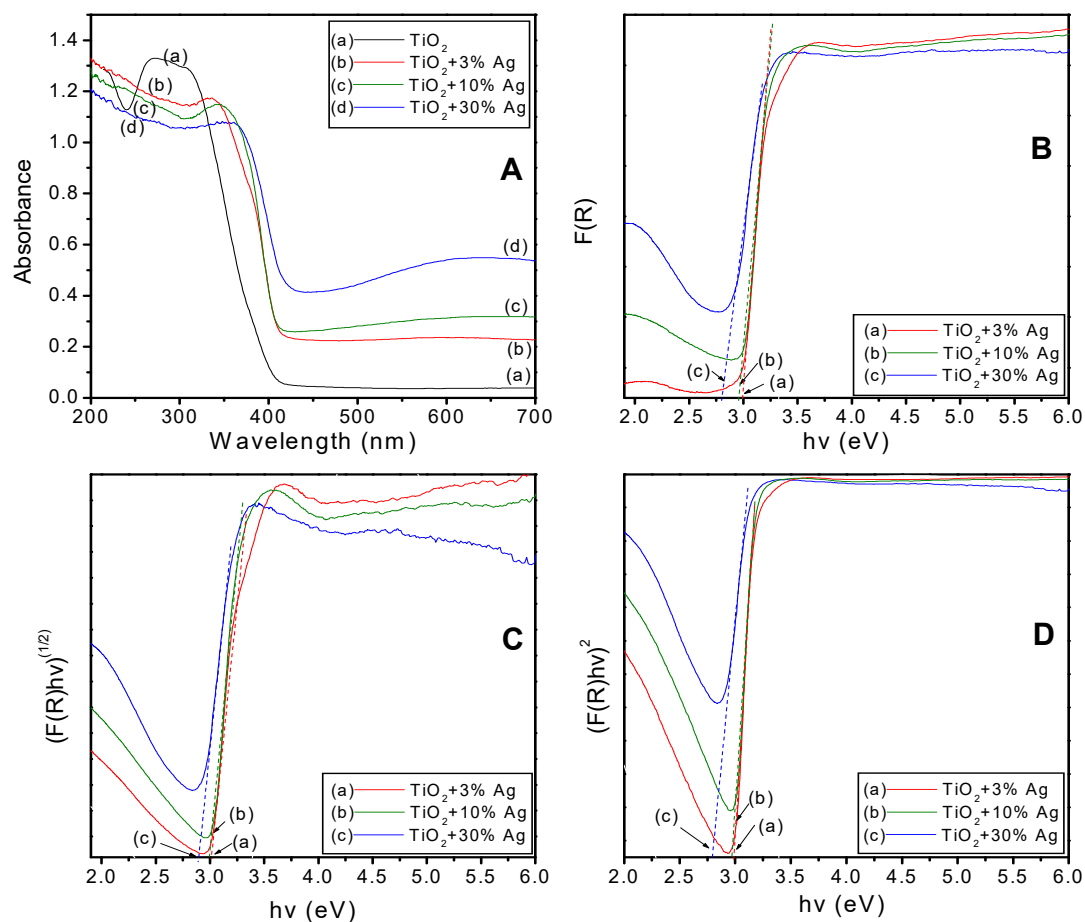
Figure 7.4.3. *Absorption spectra (A), F(R) versus hυ (B), (F(R)hυ)$^{1/2}$ versus hυ (C) and (F(R)hυ)^2 versus hυ (D) of TiO$_2$-Ag composites.*

The E$_g$ values of TiO$_2$-Ag composites also decreased as the percentage of Ag doped increases as evident from the plots (Figure 7.4.3 B, C & D) and Table 7.3.3

Table 7.3.3. *Optical bandgap energies (E$_g$s) of TiO$_2$–Ag composites*

Method	Transition Type	Optical bandgap energy in eV			
		TiO$_2$	TiO$_2$-3% Ag	TiO$_2$-10% Ag	TiO$_2$-30% Ag
F(R) vs hυ	Irrespective of transitions	3.16	2.99	2.96	2.80
(F(R)hυ)^2 vs hυ	Direct allowed	3.22	2.99	2.97	2.81
(F(R)hυ)$^{1/2}$ vs hυ	Indirect allowed	3.18	3.01	2.99	2.89

Section:II

Photodegradation of PS using metal doped TiO$_2$

7.4. Method

The synthesised, various metal doped TiO$_2$ were loaded into the PS matrix as discussed in chapter 2, and photodegradation of the resulting composites were studied. PS-TiO$_2$-metal composite specimens were also prepared for mechanical and electrical measurements. Photodegradation was monitored using various techniques and the obtained results are presented below.

7.5. Results and Discussion

Various monitoring techniques adopted in our study proved that PS-TiO$_2$-metal composites underwent better photodegradation in the presence of UV radiation compared to PS-TiO$_2$ composites. It was however noticed that increase in the percentage of metal doping in the composites could not increase the extent of photodegradation under UV light. Based on the results obtained, TiO$_2$ doped with 3 percentages of metals could be considered as better photocatalysts for the degradation of PS under UV radiation.

7.5.1. Gel permeation chromatography (GPC)

A decrease in the average molecular weights ($\overline{M}_w$ and $\overline{M}_n$) upon UV irradiation was observed in PS loaded with metal doped TiO$_2$ composites containing 3, 10 and 30% of metal compared to pristine TiO$_2$. PS-TiO$_2$-metal composites underwent better decrease in the average molecular weights in the presence of UV radiation compared to PS-TiO$_2$ composites. The extent of decrease in $\overline{M}_w$ and $\overline{M}_n$ of PS-TiO$_2$-Ag, PS-TiO$_2$-Fe and PS-TiO$_2$-Cu composites were almost similar. PS-TiO$_2$-Ag however underwent better decrease in $\overline{M}_w$ and $\overline{M}_n$ compared to PS-TiO$_2$-Fe and PS-TiO$_2$-Cu (Figure 7.5.1).
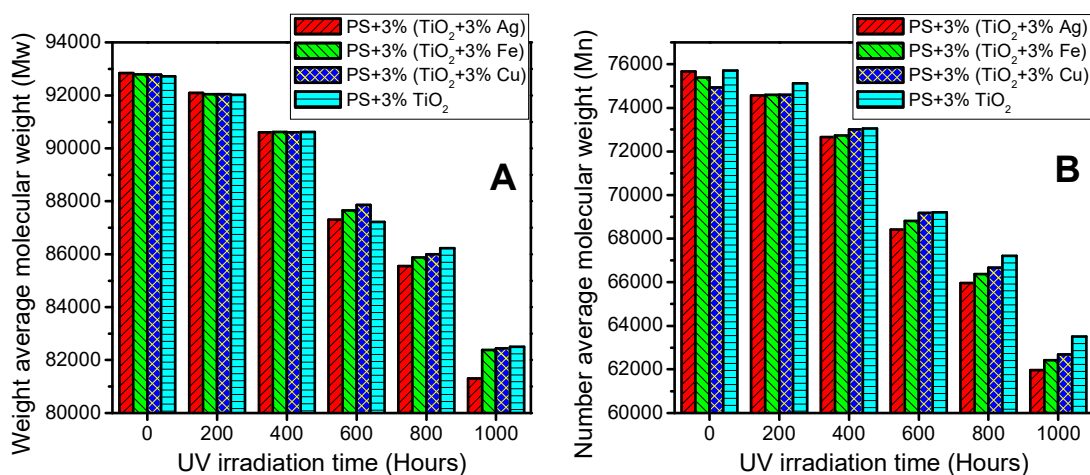
Figure 7.5.1. A) Weight average ($\bar{M}_w$) and **B)** number average ($\bar{M}_n$) molecular weights of PS-TiO₂-metal composites under different UV irradiation time
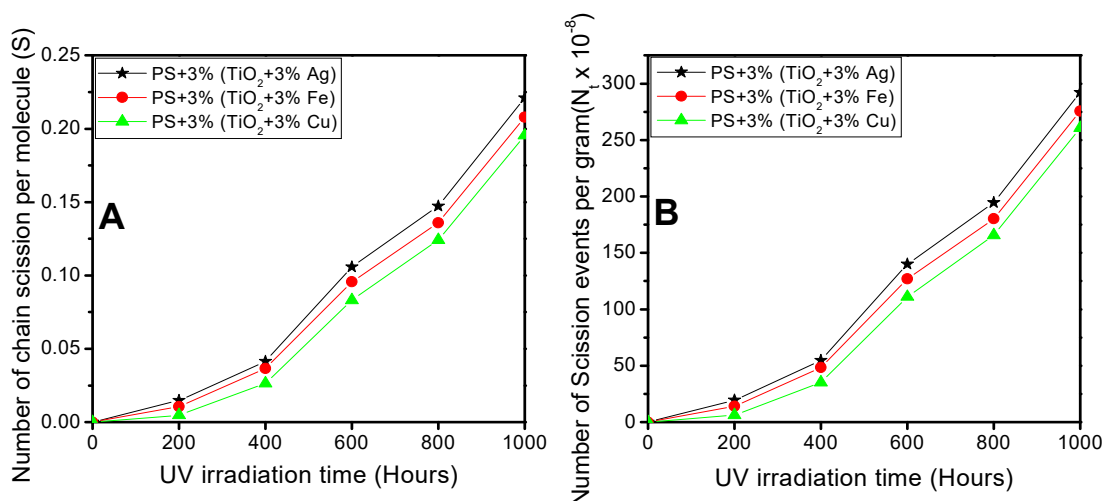
Figure 7.5.2. A) Number of chain scissions per molecule (S) and **B)** number of scission events per gram (N_t) of PS-TiO₂-metal composites under different UV irradiation time intervals

Number of chain scission per molecule (S) and number of scission events per gram (N_t) of the composites increased with UV irradiation time. From figure 7.5.2, it could be seen that the extent of chain scissions differed only by a very small value among PS-TiO₂-Ag, PS-TiO₂-Fe and PS-TiO₂-Cu composites. Extent of chain scission was however better in PS-TiO₂-Ag composite compared to others under study.
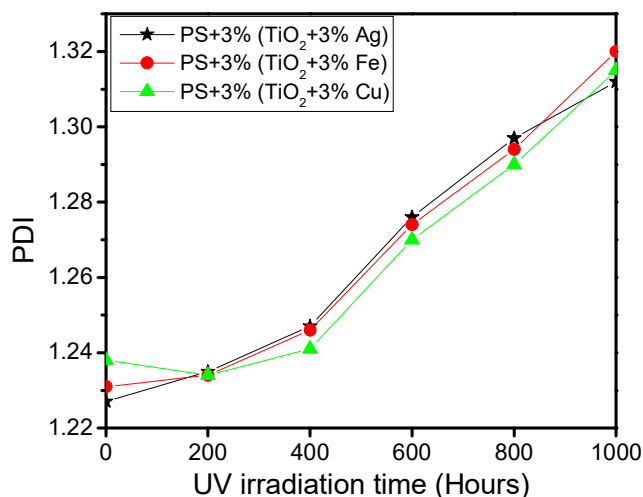
Figure 7.5.3. *Polydispersity index (PDI) of PS-TiO₂-metal composites under different UV irradiation time*

Polydispersity index (PDI) of all the PS-TiO₂-metal composites increased as the time of UV irradiation increases (Figure 7.5.3). The increase in the extent of random mannered chain scission due to photodegradation is evident here.

7.5.2. FTIR Spectroscopy
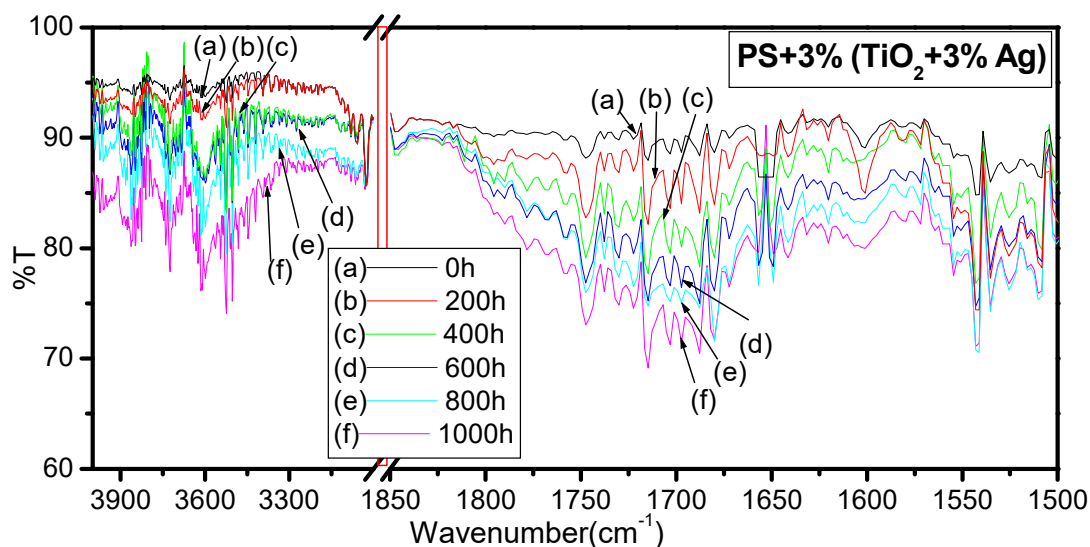
Figure 7.6. *FTIR spectra of PS-3%(TiO₂-3% Ag) at different UV exposure time intervals ranging from 0 h to 1000 h.*

FTIR spectra of all the PS-TiO₂-metal composites looked alike. An increase in the intensity of stretching vibrations corresponding to $>C=O$ (1740-1700 cm^{-1}), $-OH/-OOH$ (3700-3600 cm^{-1}), $>C=C<$ (1680-1650 cm^{-1}) etc were observed with the increase in UV irradiation time for all the composites. Photo-oxidation of the

composites taking place upon UV irradiation was evident. PS-TiO$_2$-metal composites underwent better photo-oxidation compared to PS-TiO$_2$ composites. Photo-oxidation taking place in PS-TiO$_2$-Ag composites (Figure 7.6) was slightly better compared to the other composites.

7.5.3. UV-visible diffused reflectance spectroscopy (UV-DRS)
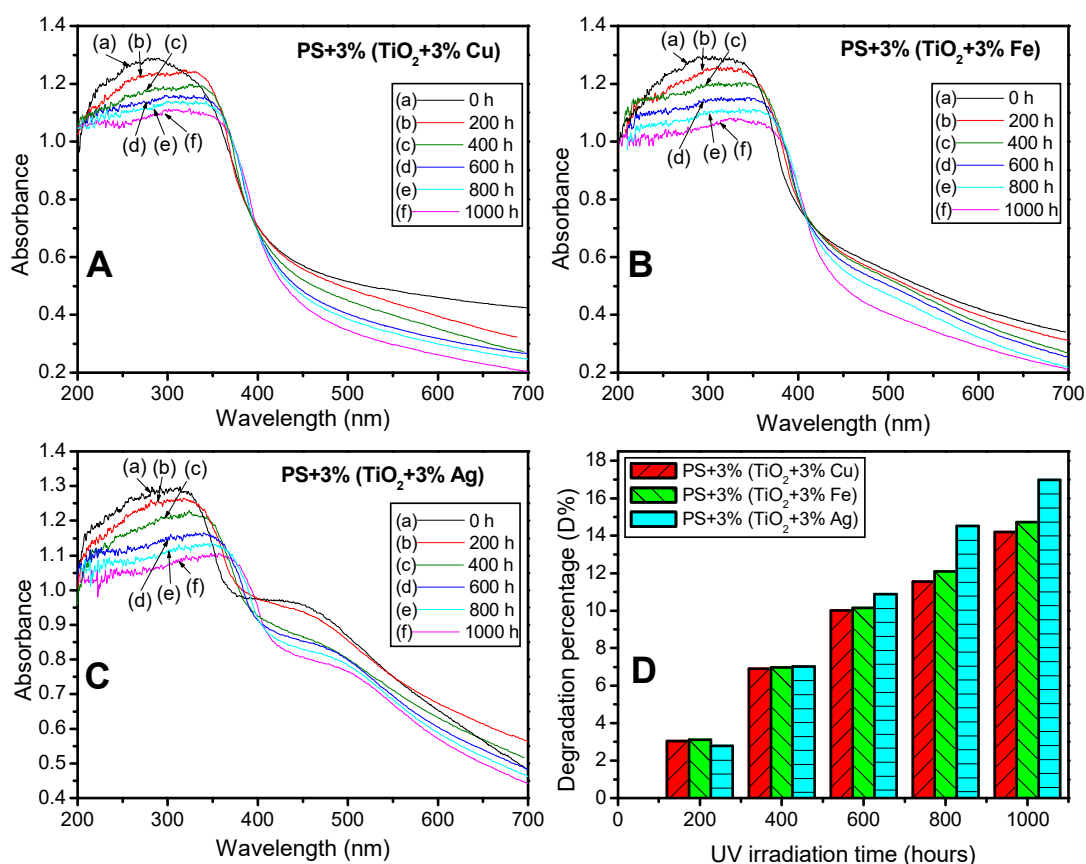
*Figure 7.7. UV-visible absorption spectra of PS-3%(TiO$_2$-3%Cu) **(A)**, PS-3%(TiO$_2$-3%Fe)*
*__(B)__, PS-3%(TiO$_2$-3% Ag) **(C)** and degradation percentages of PS-(TiO$_2$-3% metal)*
*composites **(D)** at different UV exposure time intervals ranging from 0 h to 1000 h*

PS-TiO$_2$-metal composites absorbed both in the UV and visible regions (Figure 7.7) unlike PS-TiO$_2$ composites which absorbed only in the UV region of the spectra. This indicates the possibility that the composites may utilise both UV and visible radiation to undergo photodegradation which has to be studied. The absorption maxima of the composites observed in the UV region decreased, as the time of UV irradiation increased pointing photodegradation possibility. A red shift was observed for the absorption bands in UV region indicating the formation of extended conjugation within the composites as a consequence of photodegradation. The

degradation percentage (D%) determined from UV-DRS were found to be maximum in PS-TiO$_2$-Ag composites compared to the PS composites with Fe or Cu doped TiO$_2$. The increase in degradation efficiency of PS-(TiO$_2$-3% Ag), PS-(TiO$_2$-3% Fe) and PS-(TiO$_2$-3% Cu) with respect to pristine PS were 7.37, 5.1 and 4.57 % respectively.

7.5.4. Mechanical Properties
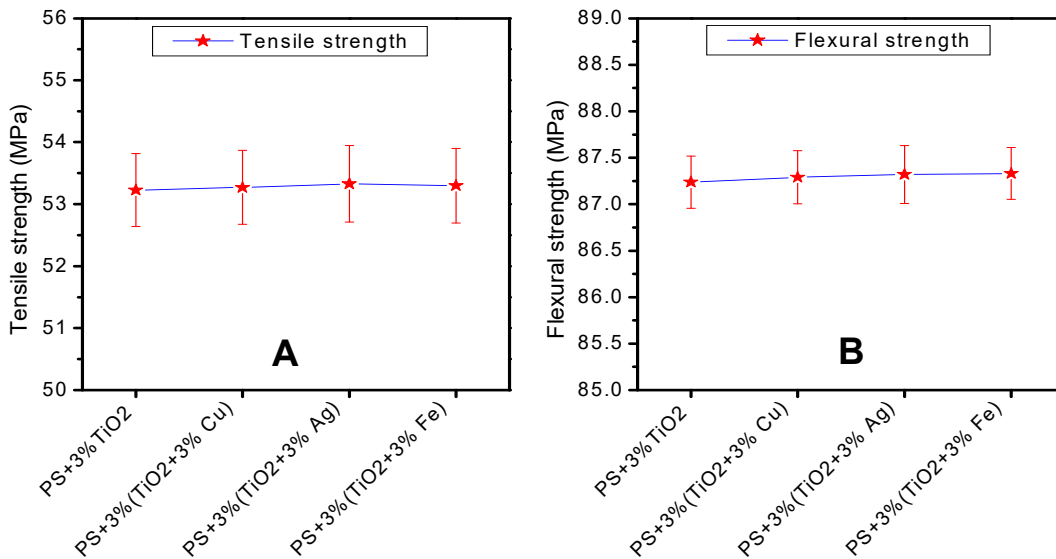
Figure 7.8.1. *Tensile (A) and flexural (B) strengths of PS-TiO$_2$-metal and PS-TiO$_2$ composites-a comparison*
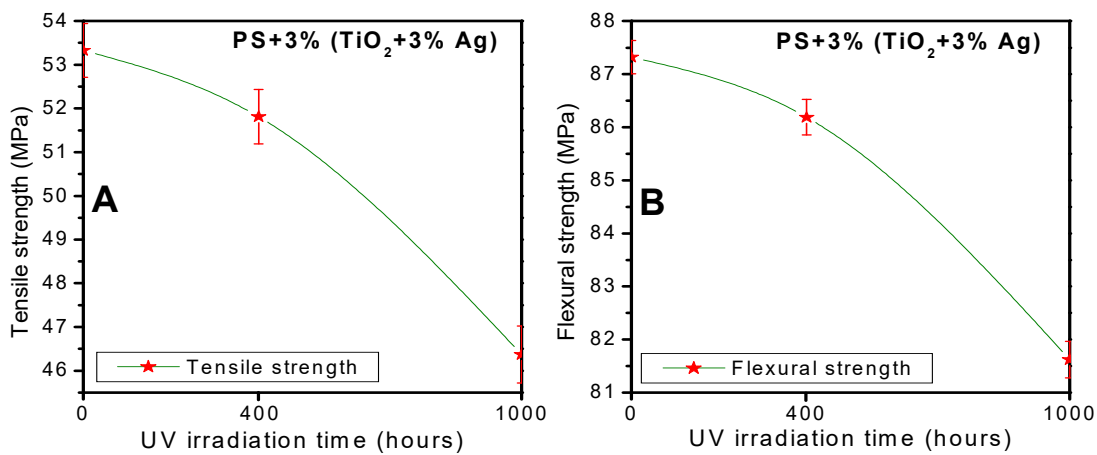
Figure 7.8.2. *Tensile (A) and flexural (B) strengths of PS-3%(TiO$_2$-3% Ag) composites exposed to UV radiation for 0, 400 and 1000 h.*

A comparison of tensile and flexural strengths of PS-TiO$_2$-metal and PS-TiO$_2$ composites are graphically represented in figure 7.8.1. It could be seen that the mechanical strengths of PS-TiO$_2$-metal composites were almost similar to that of PS-

TiO_2 composites. The mechanical strengths of PS-3%(TiO_2-3% Ag) were measured at UV irradiation time intervals of 0, 400 and 1000 hours (Figure 7.8.2). Tensile and flexural strengths of the composites decreased with the increase in UV irradiation time due to degradation.

7.5.5. Electrical properties

The value of dielectric breakdown (BDV) of PS-TiO_2-Ag was lower than that of PS-TiO_2 (Figure 7.9 A). Easier passage of electric charge across the polymer matrix in the presence of conducting Ag metal explains the observation. PS-TiO_2-metal composites can be used in such applications where enhanced electrical conductivity is demanded. From figure 7.9 A, the decrease in BDV with respect to the increase in UV irradiation time could also be observed. The decrease in BDV upon UV irradiation suggests that the free movement of charged species formed as a consequence of photodegradation is not hindered by Ag-doped TiO_2 across the polymer matrix.
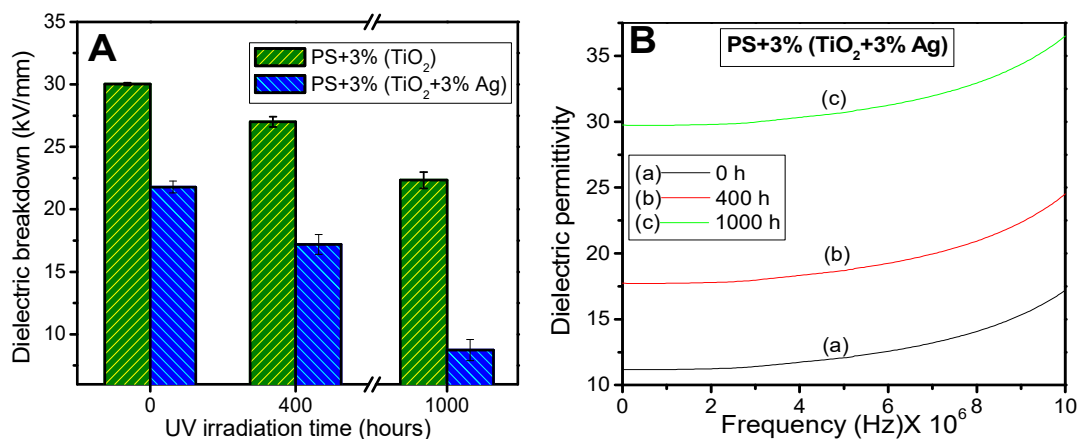
Figure 7.9. *Dielectric breakdown (A) and dielectric permittivity (B) of PS-(TiO_2-3% Ag) composite exposed to UV radiation for 0, 400 and 1000 h.*

Dielectric permittivity (ε_r) of PS-TiO_2-Ag composites was higher compared to that of PS-TiO_2 (Figure 7.9 B). The value of ε_r further increased upon UV irradiation. Formation of charged poles on UV irradiation is evident from this observation.

7.5.6. Thermogravimetric Analysis (TGA)

Thermogram of PS-(TiO_2-3% Ag) composite showed two stages of weight loss (Figure 7.10). The First stage of weight loss represents the water desorption of the composite. The second stage of weight loss resulting to a steep slope between 330 and

417° C represents the decomposition curve of the composite. The decomposition of the PS-(TiO$_2$-3% Ag) composite took place at an elevated temperature compared to that of PS-TiO$_2$ composite. This suggests that the thermal stability of PS-TiO$_2$-Ag composite was better compared to PS-TiO$_2$ composite. A decrease in the value of decomposition temperature was observed in the PS-(TiO$_2$-3% Ag) composite after 1000 hours of UV irradiation. The decomposition temperature was shifted to 311-396°C.
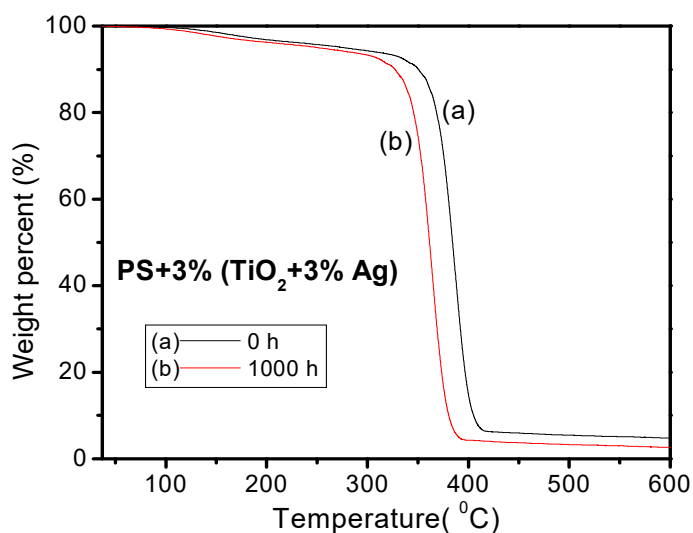
Figure 7.10. *TGA thermogram of PS-3%(TiO$_2$+3% Ag) composites before and after UV irradiation of 1000 h*

7.5.7. Weight loss
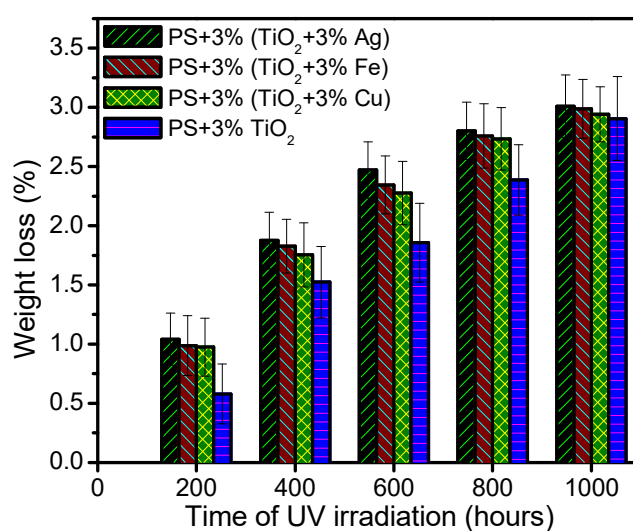
Figure 7.11. *Comparison of weight loss percentages of PS-TiO$_2$-metal composites at regular intervals of UV irradiation*

PS-TiO$_2$-metal composites underwent weight loss upon UV irradiation (Figure 7.11). All the PS-TiO$_2$-metal composites underwent enhanced weight loss compared to PS-TiO$_2$ composites. Maximum weight loss among the composites was observed in PS-TiO$_2$-Ag compared to others.

7.6.   Mechanism of photocatalysis of TiO$_2$-metal composites
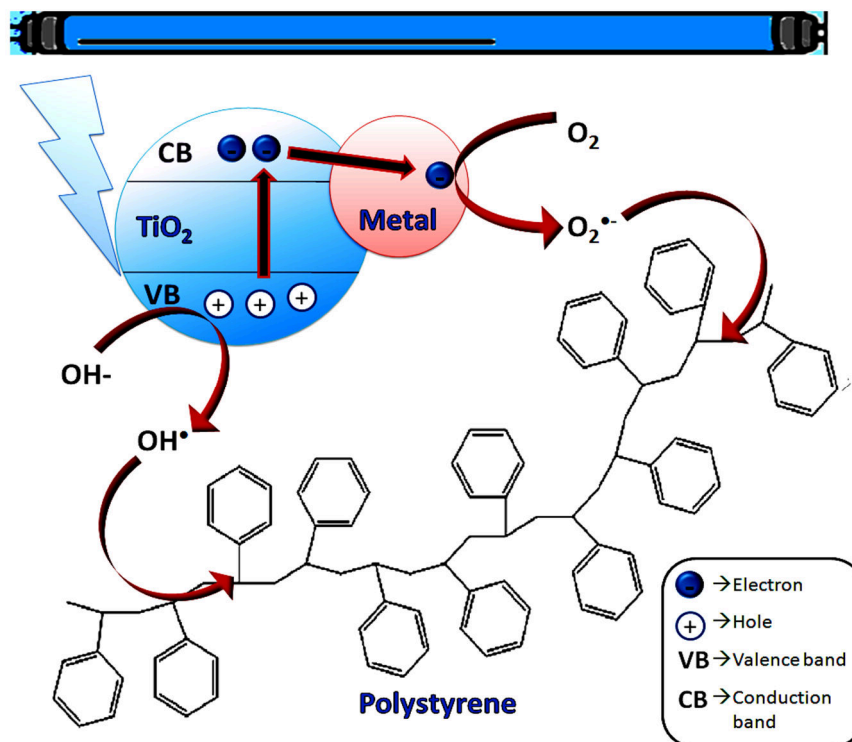
Figure 7.12. Pictorial representation of electron transfer from conduction band of TiO$_2$ to the doped transition metal, reducing the electron-hole recombination

An enhancement in the extent of photodegradation of PS-TiO$_2$-metal composites was observed compared to that of PS-TiO$_2$ composite. The increase in photocatalytic activity of TiO$_2$ upon metal doping was due to the fact that the transition metals block the recombination of photogenerated electrons and holes in TiO$_2$ upto an appreciable extent[40]. This charge pair separation efficiency is an outcome of improved charge transfer between the dopant metal and TiO$_2$[41].

Transition metal doping also reduces the bandgap of TiO$_2$ by altering the valence band maximum and conduction band minimum to new energy levels allowing the system to be photocatalytically active under radiations with lower energy[31]. The

decrease in bandgap energy was observed for Ag, Cu as well as Fe doped TiO_2 in our study as discussed earlier.

It was observed that Ag, Cu as well as Fe doped TiO_2 were all efficient photocatalyts for the degradation of PS even at low metal concentrations (3%). There was no expected improvement in the photocatalytic efficiency of these catalysts at higher concentration of metals (10% and 30%). Even though transition metals decreases the electron-hole recombination within TiO_2, higher concentration of metals may result in the formation of recombination centers which facilitate the charge recombination[42].

TiO_2-metal composites with higher metal doping percentages (10 and 30 mole percentages) existed predominantly in the rutile phase. Anatase TiO_2 is a better photocatalyst compared to rutile TiO_2[43]. PS loaded with TiO_2-10% and TiO_2-30% metals consisting of predominant rutile phase should not undergo better photodegradation compared to PS-(TiO_2-3% metal). This fact was in accordance with our observation. It has also been reported that even though anatase phase TiO_2 is photocatalytically more active than rutile phase, their mixed phase exhibited superior visible light induced photocatalytic activity. The heterojunctions formed as a result of mixing of the two phases is responsible for this[44,45]. In this point of view, the photodegradation of PS under visible light using TiO_2-metal composites with higher percentage of metal doping promises a future scope in research.

7.7. Conclusions

TiO_2 doped with 3, 10 and 30 mole percentages of Ag, Cu and Fe was prepared through sol-gel method. At a fixed calcination temperature of 400° C, the percentage of rutile phase increased and anatase phase decreased in the composites with respect to the increase in metal percentage. SEM images revealed that all the TiO_2-metal composites existed as spherical particles. The average diameters of TiO_2-3% Cu, TiO_2-3% Fe and TiO_2-3% Ag particles were ~125 nm, 85 nm and 50 nm respectively. The bandgap energies of all the composites decreased as the percentage of metal doping increased. PS loaded with TiO_2-metal composites underwent enhanced photo-oxidative degradation with deterioration in mechanical properties compared to PS-TiO_2 composites on UV exposure. The BDV of the PS-TiO_2-metal composites were

lower compared to PS-TiO$_2$ composites due to incorporation of conductive metals. Thermal stability of the composites was superior compared to PS-TiO$_2$. Dielectric permittivity of the PS-TiO$_2$-metal composites was higher compared to PS-TiO$_2$. UV irradiated PS-TiO$_2$-metal composites also showed decreased thermal stability. BDV of the composites decreased and the dielectric permittivity increased upon UV irradiation. A notable observation made from the photodegradation studies was that the PS-TiO$_2$-metal composites with 3% metal underwent better photodegradation compared to that of 10 and 30% metal. Out of Ag, Cu and Fe doped TiO$_2$ photocatalysts, better photodegradation of PS was exhibited by Ag doped TiO$_2$ under UV irradiation.

References

1. Huang, F., Yan, A. & Zhao, H. Influences of doping on photocatalytic properties of TiO2 photocatalyst. *Semicond. Photocatal. Mech. Appl. Cao, W., Ed* 31–80 (2016).
2. Fan, W.-Q. *et al.* Titanium dioxide macroporous materials doped with iron: synthesis and photo-catalytic properties. *CrystEngComm* **16**, 116–122 (2014).
3. Chang, S. & Liu, W. The roles of surface-doped metal ions (V, Mn, Fe, Cu, Ce, and W) in the interfacial behavior of TiO2 photocatalysts. *Appl. Catal. B Environ.* **156–157**, 466–475 (2014).
4. Umebayashi, T., Yamaki, T., Itoh, H. & Asai, K. Analysis of Electronic Structures of 3D Transition Metal-Doped TiO2 Based on Band Calculations. *J. Phys. Chem. Solids* **63**, 1909–1920 (2002).
5. Ishii, M. *et al.* Roles of Electrons and Holes in the Luminescence of Rare-Earth-Doped Semiconductors. *Electron. Commun. Japan* **96**, 1–7 (2013).
6. Li, X. Z., Li, F. B., Yang, C. L. & Ge, W. K. Photocatalytic activity of WOx-TiO2 under visible light irradiation. *J. Photochem. Photobiol. A Chem.* **141**, 209–217 (2001).
7. Song, H., Jiang, H., Liu, X. & Meng, G. Efficient degradation of organic pollutant with WOx modified nano TiO2 under visible irradiation. *J. Photochem. Photobiol. A Chem.* **181**, 421–428 (2006).
8. Khairy, M. & Zakaria, W. Effect of metal-doping of TiO2 nanoparticles on their photocatalytic activities toward removal of organic dyes. *Egypt. J. Pet.* **23**, 419–426 (2014).
9. Guayaquil-Sosa, J. F., Serrano-Rosales, B., Valadés-Pelayo, P. J. & de Lasa, H. Photocatalytic hydrogen production using mesoporous TiO2 doped with Pt. *Appl. Catal. B Environ.* **211**, 337–348 (2017).
10. Lavorato, C. *et al.* Pd/TiO2 doped faujasite photocatalysts for acetophenone transfer hydrogenation in a photocatalytic membrane reactor. *J. Catal.* **353**, 152–161 (2017).
11. Jin, C. *et al.* Effects of single metal atom (Pt, Pd, Rh and Ru) adsorption on the photocatalytic properties of anatase TiO2. *Appl. Surf. Sci.* **426**, 639–646 (2017).
12. Hossain, M. A. *et al.* Synthesis of Fe- or Ag-doped TiO2–MWCNT nanocomposite thin films and their visible-light-induced catalysis of dye degradation and antibacterial activity. *Res. Chem. Intermed.* **44**, 2667–2683 (2018).
13. Zou, Z., Zhou, Z., Wang, H. & Yang, Z. Effect of Au clustering on ferromagnetism in Au doped TiO2 films: theory and experiments investigation. *J. Phys. Chem. Solids* **100**, 71–77 (2017).
14. Inturi, S. N. R., Boningari, T., Suidan, M. & Smirniotis, P. G. Visible-light-induced photodegradation of gas phase acetonitrile using aerosol-made transition metal (V, Cr, Fe, Co, Mn, Mo, Ni, Cu, Y, Ce, and Zr) doped TiO2. *Appl. Catal. B Environ.* **144**, 333–

342 (2014).

15. Sood, S., Umar, A., Mehta, S. K. & Kansal, S. K. Highly effective Fe-doped TiO2 nanoparticles photocatalysts for visible-light driven photocatalytic degradation of toxic organic compounds. *J. Colloid Interface Sci.* **450**, 213–223 (2015).

16. Birben, N. C. *et al.* Application of Fe-doped TiO2 specimens for the solar photocatalytic degradation of humic acid. *Catal. Today* **281**, 78–84 (2017).

17. Choudhury, B., Choudhury, A. & Borah, D. Interplay of dopants and defects in making Cu doped TiO2 nanoparticle a ferromagnetic semiconductor. *J. Alloys Compd.* **646**, 692–698 (2015).

18. Tripathi, A. K. *et al.* Structural, optical and photoconductivity of Sn and Mn doped TiO2 nanoparticles. *J. Alloys Compd.* **622**, 37–47 (2015).

19. Yadav, H. M. *et al.* Synthesis and visible light photocatalytic antibacterial activity of nickel-doped TiO2 nanoparticles against Gram-positive and Gram-negative bacteria. *J. Photochem. Photobiol. A Chem.* **294**, 130–136 (2014).

20. Khan, H. & Berk, D. Synthesis, physicochemical properties and visible light photocatalytic studies of molybdenum, iron and vanadium doped titanium dioxide. *React. Kinet. Mech. Catal.* **111**, 393–414 (2014).

21. Kaviyarasu, K. *et al.* In vitro cytotoxicity effect and antibacterial performance of human lung epithelial cells A549 activity of Zinc oxide doped TiO2 nanocrystals: Investigation of bio-medical application by chemical method. *Mater. Sci. Eng. C* **74**, 325–333 (2017).

22. Deng, L. *et al.* Synthesis, Characterization of Fe-doped TiO2 Nanotubes with High Photocatalytic Activity. *Catal. Letters* **129**, 513–518 (2009).

23. Tong, T., Zhang, J., Tian, B., Chen, F. & He, D. Preparation of Fe3+-doped TiO2 catalysts by controlled hydrolysis of titanium alkoxide and study on their photocatalytic activity for methyl orange degradation. *J. Hazard. Mater.* **155**, 572–579 (2008).

24. Jamalluddin, N. A. & Abdullah, A. Z. Reactive dye degradation by combined Fe(III)/TiO2 catalyst and ultrasonic irradiation: Effect of Fe(III) loading and calcination temperature. *Ultrason. Sonochem.* **18**, 669–678 (2011).

25. Wang, J. *et al.* Preparation of Fe-doped mixed crystal TiO2 catalyst and investigation of its sonocatalytic activity during degradation of azo fuchsine under ultrasonic irradiation. *J. Colloid Interface Sci.* **320**, 202–209 (2008).

26. Zhu, J., Zheng, W., He, B., Zhang, J. & Anpo, M. Characterization of Fe–TiO2 photocatalysts synthesized by hydrothermal method and their photocatalytic reactivity for photodegradation of XRG dye diluted in water. *J. Mol. Catal. A Chem.* **216**, 35–43 (2004).

27. Ambrus, Z. *et al.* Synthesis, structure and photocatalytic properties of Fe(III)-doped TiO2 prepared from TiCl3. *Appl. Catal. B Environ.* **81**, 27–37 (2008).

28. Hamadanian, M., Reisi-Vanani, A. & Majedi, A. Synthesis, characterization and effect of calcination temperature on phase transformation and photocatalytic activity of Cu,S-codoped TiO2 nanoparticles. *Appl. Surf. Sci.* **256**, 1837–1844 (2010).

29. Li, L. *et al.* Photocatalytic nitrate reduction over Pt–Cu/TiO2 catalysts with benzene as hole scavenger. *J. Photochem. Photobiol. A Chem.* **212**, 113–121 (2010).

30. Wang, S., Meng, K. K., Zhao, L., Jiang, Q. & Lian, J. S. Superhydrophilic Cu-doped TiO2 thin film for solar-driven photocatalysis. *Ceram. Int.* **40**, 5107–5110 (2014).

31. Mathew, S. *et al.* Cu-doped TiO2: Visible light assisted photocatalytic antimicrobial activity. *Appl. Sci.* **8**, 2067 (2018).

32. Sobana, N., Muruganadham, M. & Swaminathan, M. Nano-Ag particles doped TiO2 for efficient photodegradation of Direct azo dyes. *J. Mol. Catal. A Chem.* **258**, 124–132 (2006).

33. Sobana, N., Selvam, K. & Swaminathan, M. Optimization of photocatalytic degradation conditions of Direct Red 23 using nano-Ag doped TiO2. *Sep. Purif. Technol.* **62**, 648–653 (2008).

34. Sahoo, C., Gupta, A. K. & Pal, A. Photocatalytic degradation of Crystal Violet (C.I. Basic Violet 3) on silver ion doped TiO2. *Dye. Pigment.* **66**, 189–196 (2005).

35. Kondo, M. M. & Jardim, W. F. Photodegradation of chloroform and urea using Ag-loaded titanium dioxide as catalyst. *Water Res.* **25**, 823–827 (1991).

36. Suwarnkar, M., Dhabbe, R., Kadam, A. & Garadkar, P. K. M. Enhanced photocatalyticactivityofAgdopedTiO2 nanoparticles synthesized byamicrowaveassistedmethod. *Ceram. Int.* **40(2014)**, 5489–5496 (2013).

37. Luu, C. L., Nguyen, Q. T. & Ho, S. T. Synthesis and characterization of Fe-doped TiO 2 photocatalyst by the sol – gel method. *Adv. Nat. Sci. Nanosci. Nanotechnol.* **015008**, 1–6

38. Byrne, C., Fagan, R., Hinder, S., McCormack, D. E. & Pillai, S. C. New approach of modifying the anatase to rutile transition temperature in TiO2 photocatalysts. *RSC Adv.* **6**, 95232–95238 (2016).

39. Mogal, S. I. *et al.* Single-Step Synthesis of Silver-Doped Titanium Dioxide : In fl uence of Silver on Structural , Textural , and Photocatalytic Properties. *Ind. Eng. Chem. Res.* **53**, 5749−5758 (2014).

40. Behnajady, M. A., Modirshahla, N., Shokri, M. & Rad, B. Enhancement of photocatalytic activity of TiO2 nanoparticles by silver doping: photodeposition versus liquid impregnation methods. (2008).

41. Bagheri, S., Ramimoghadam, D., Yousefi, A. T. & Hamid, S. B. A. Synthesis, characterization and electrocatalytic activity of silver doped-titanium dioxide nanoparticles. *Int. J. Electrochem. Sci* **10**, 3088–3097 (2015).

42. Sung-Suh, H. M., Choi, J. R., Hah, H. J., Koo, S. M. & Bae, Y. C. Comparison of Ag deposition effects on the photocatalytic activity of nanoparticulate TiO2 under visible and UV light irradiation. *J. Photochem. Photobiol. A Chem.* **163**, 37–44 (2004).

43. Luttrell, T. *et al.* Why is anatase a better photocatalyst than rutile? - Model studies on epitaxial TiO2 films. *Sci. Rep.* **4**, 4043 (2014).

44. El-Sheikh, S. M. *et al.* High performance sulfur, nitrogen and carbon doped mesoporous anatase–brookite TiO2 photocatalyst for the removal of microcystin-LR under visible light irradiation. *J. Hazard. Mater.* **280**, 723–733 (2014).

45. Etacheri, V., Seery, M. K., Hinder, S. J. & Pillai, S. C. Nanostructured Ti1-xSxO2-yNy Heterojunctions for Efficient Visible-Light-Induced Photocatalysis. *Inorg. Chem.* **51**, 7164–7173 (2012).

Chapter 8
Summary and Conclusion

Photodegradation could be considered as a suitable technique for the demolition of plastic debris compared to various other techniques practiced worldwide. The advantage of photodegradation over other remedial measures implemented for the waste plastic treatment is that the process is ecofriendly and cost effective. Photodegradation of plastics takes place naturally in the presence of sunlight but with a delayed time period which makes the process practically worthless. The entire plot of this thesis, focusing on the acceleration of PS photodegradation using various photocatalysts becomes relevant in this aspect. The metal oxide semiconductor TiO_2, as a photocatalyst showed better efficiency for the photodegradation of PS compared to ZnO under UV radiation. Throughout the study, we could arrive into the conclusion that the photocatalytic efficiency of TiO_2 and ZnO could be improved by modifying or coupling with various photosensitizers for the effective photodegradation of PS. Modifications have been done by associating TiO_2 and ZnO with PANI and GO. TiO_2 has been coupled with benzophenone derivatives and triphenylmethane dyes and doped with transition metals such as Fe, Cu and Ag. All these materials improved the photocatalytic efficiency of TiO_2 and ZnO for the photodegradation of PS under UV radiation. The compounds PANI, GO and triphenylmethane dyes and metals Fe, Cu and Ag were not acceptable photosensitizers in their uncoupled state. They could act as effective photosensitizers only when coupled with TiO_2 or ZnO. Derivatives of benzophenone however are better photosensitizers even in their uncoupled state.

The question "Which photocatalyst is the best for the photodegradation of PS?" has to be addressed at this point. This question however could only be answered accounting the mode of application of PS-photocatalyst composite system. From our investigations, PS-TiO_2-GO exhibited superior photocatalytic activity for UV initiated PS degradation compared to the other composites. PS-TiO_2-GO composites were mechanically stronger and thermally more stable compared to PS-TiO_2. This favours the use of PS-TiO_2-GO composite replacing pristine PS in several applications demanding better thermal stability and mechanical strength. Packing containers, toys or machine parts, for example, are made up of this composite. The products made out

of this composite undergo better degradation when thrown into the environment after their usage. TiO$_2$-GO, even though a better photocatalyst, cannot be considered as suitable filler for every application replacing other photocatalysts. The BDV values of PS-TiO$_2$-GO composites were lower compared to PS-TiO$_2$. This implies that the composite cannot be used for high voltage insulation applications. PS-TiO$_2$-PANI as well as PS-TiO$_2$-metal composites also showed lower BDV values even though they underwent appreciable extent of photodegradation. These composites also cannot withstand higher voltage similar to GO. Even though PS-TiO$_2$-metal can be used for food packing, PS-TiO$_2$-PANI and PS-ZnO-PANI are not suitable since the contact of PANI with edible materials is unhealthy. The PS-benzophenone derivative composites are transparent and mechanically stronger than pristine PS. The composites can substitute PS in applications where transparency is in demand. It should also be however noted that the compound 2-hydroxy-4-methoxybenzophenone does not sensitize PS for photodegradation as evident from the results obtained.

Practical significance of this work

- Photodegradation studies using an artificial UV lamp which has the power 30W and wavelength 253 nm have been conducted in this study. The photodegradation of PS was effective under this condition. It is estimated that UV radiation from sun striking the earth is around 32 W. This signifies that the efficiency of PS photodegradation, inside UV chamber, is certainly possible under natural sunlight too. Some of the composites of TiO$_2$ or ZnO with PANI or metals have the ability to be photocatalytically active even under visible light, as discussed in chapter 1. Exposure of PS under sunlight may increase the extent of photodegradation for such composites.

- Photodegradation might occur much easier and faster in our environment where the conditions are much harsher. Environmental weathering of the polymer may further assist its degradation process.

- Incorporation of optimum amount of photocatalysts also makes PS mechanically stronger and thermally more stable promising a wide range of applications.

- Photocatalysts can be loaded into PS during the moulding process and can be brought into commercial applications without much time consuming and complicated processes.

Eco friendliness in the photocatalysed degradation of PS and the relevance of this work

- Photodegradation occurs naturally under direct sunlight without any further requirements, making the process costless.
- No toxic gases are liberated during the process.
- The photocatalysts and sensitizers employed in this work, such as TiO_2, ZnO, GO, Fe, Cu and Ag are non-hazardous materials.
- Even though the photosensitizers like PANI, benzophenone derivatives and triphenylmethane dyes may be hazardous, their presence in PS doesn't matter much as they are loaded in very minute quantities.
- Photodegradation of PS composites would be effective in water bodies too. Interaction of water molecules with the catalysts or PS furnishes more OH• under sunlight that enhances photodegradation.

Way forward

UV-visible spectra of some of the PS composites especially composites consisting of PANI, GO, metals and dyes showed absorption in the UV as well as in the visible region. A thorough literature survey also supports the fact that these photosensitizers have the ability to extend the photocatalytic activity of TiO_2 and ZnO into the visible region. Replacing the UV light source with the visible light of sun can further extend the scope of PS photodegradation studies.

The electrical, mechanical and thermal properties of the PS-composites showed variations according to the type of photocatalysts used. A detailed study of various properties of these PS composites may explore the possible usages of these composites in several applications.

Publications and Conference Presentations

Journal papers

[1] **Dinoop lal S**, Sunil Jose T, Rajesh C, Anju Rose Puthukkara P, Savitha Unnikrishnan K, Arun K J, "Accelerated Photodegradation of Polystyrene by TiO_2-Polyaniline Photocatalyst under UV Radiation". *European Polymer Journal*, 2021, vol: 153, page: 110493. (Publisher: Elsevier). https://doi.org/10.1016/j.eurpolymj.2021.110493

[2] **Dinoop lal S**, Sunil Jose T, Rajesh C, Arun K J. "Accelerated Photodegradation of Solid Phase Polystyrene by Nano TiO2-Graphene Oxide Composite under Ultraviolet radiation". *Polymer Degradation and stability*, 2021, vol: 184, page: 109476. (Publisher: Elsevier). https://doi.org/10.1016/j.polymdegradstab.2020.109476

[3] **Dinoop lal S**, Sunil Jose T, Rajesh C. "Solid-phase photodegradation of polystyrene by nano TiO2 under ultraviolet radiation". *Environmental Nanotechnology, Monitoring & Management*, 2019, vol: 12, page: 100229. (Publisher: Elsevier). https://doi.org/10.1016/j.enmm.2019.10022

[4] Savitha Unnikrishnan K, Sunil Jose T, **Dinoop lal S,** Arun K J. "Glass fiber reinforced bismaleimide/epoxy $BaTiO_3$ nano composites for high voltage applications". *Polymer Testing*,2020, vol: 87, page:106505. (Publisher: Elsevier) https://doi.org/10.1016/j.polymertesting.2020.106505

[5] Anju Rose Puthukkara P, Sunil Jose T, **Dinoop lal S**. "Chitosan-Stabilized Fe/Ni Bimetallic Nanoparticles for the Removal of Cationic and Anionic Triphenylmethane Dyes from Water" *Environmental Nanotechnology, Monitoring & Management. 2020, vol: 14, page: 100295*. (Publisher: Elsevier). https://doi.org 10.1016/j.enmm.2020.100295

[6] Anju Rose Puthukkara P, Sunil Jose T, **Dinoop lal S**. "Plant mediated synthesis of zero valent iron nanoparticles and its application in water treatment" *Journal of Environmental Chemical Engineering*. (Publisher: Elsevier). 2020, page:104569. https://doi.org/10.1016/j.jece.2020.104569

[7] Savitha Unnikrishnan K, Sunil Jose T, **Dinoop lal S**. "Comparative studies of silane coupled e-glass fiber and e-glass fiber reinforced bismaleimide-epoxy hydroxylated BaTiO3 nanocomposites on the dielectric and mechanical properties". *Polymer Composites*. 2021. (Publisher: Wiley Online Library). https://doi.org/10.1002/pc.26057

Conference presentations

[1] **Dinoop Lal S,** Sunil Jose T, Rajesh C., "Photocatalytic Degradation of Solid Phase Polystyrene Using Nano TiO$_2$ and 2-Hydroxy-4-methoxybenzophenone*", International Conference on Molecular Spectroscopy-2017*, Mahatma Gandhi University, Kottayam

[2] **Dinoop Lal S,** Sunil Jose T, Rajesh C., "Photodegradation of Solid Phase Polystyrene by Nano Titanium dioxide and Photosensitizers under UV Radiation", *International Conference on Chemistry and Physics of Materials 2018*. St.Thomas' College (autonomous), Thrissur. (Best paper award)

[3] **Dinoop Lal S,** Sunil Jose T, Rajesh C., "Photodegradation of Solid Phase Polystyrene by Nano TiO$_2$-Polyaniline Photocatalyst under Ultraviolet Radiation", *International Conference on Energy & Environment 2019.* TKM college of Arts and Science, Kollam. **.**

[4] **Dinoop Lal S,** Sunil Jose T, Rajesh C., "Photodegradation of Solid Phase Polystyrene Plastics using Nano ZnO-Polyaniline Photocatalyst under UV Radiation", *14th International Conference on Ecomaterials 2020.* CSIR-NIIST, Thruvananthapuram.

[5] **Dinoop Lal S,** Sunil Jose T, Rajesh C., "Graphene Oxide Modified Nano TiO$_2$ Photocatalyst for Accelerated Photodegradation ff Polystyrene Plastics"*, 32nd Kerala Science Congress*. Palakkad.

[6] C. Rajesh, P. Divya, **S. Dinoop lal**, C. Seena, "Green Composites from Styrene Butadiene Rubber and Chicken feather fiber", International *Conference on Polymer Science and Technology (SPSI-MACRO-2018).*Pune, India.